Multilayer composites for magnetodielectric and magnetoelectric applications

Thesis Submitted to AcSIR for the Award of the Degree of

DOCTOR OF PHILOSOPHY in Physical Sciences

By

LEKSHMI D. R

Registration No: 10PP13A39015

Under the guidance of

Dr. K. P. SURENDRAN

Materials Science and Technology Division
National Institute for Interdisciplinary
Science and Technology (CSIR-NIIST)
Thiruvananthapuram-695 019
Kerala, India

December 2019

DECLARATION

I hereby declare that the matter embodied in the thesis entitled: **"Multilayer composites for magnetodielectric and magnetoelectric applications"** is the result of the investigations carried out by me at the Materials Science and Technology Division, CSIR-National Institute for Interdisciplinary Science and Technology (CSIR-NIIST), Thiruvananthapuram, under the supervision of Dr. K. P. Surendran and the same has not been submitted elsewhere for any other degree.

In keeping with the general practice of reporting scientific observations, due acknowledgments were made, wherever the work described is based on the findings of other investigators.

Lekshmi D. R.

COUNCIL OF SCIENTIFIC & INDUSTRIAL RESEARCH
NATIONAL INSTITUTE FOR INTERDISCIPLINARY SCIENCE AND TECHNOLOGY (CSIR-NIIST)
Industrial Estate P.O., Pappanamcode, Thiruvananthapuram-695 019, Kerala, INDIA
www.niist.res.in

Dr. K. P. Surendran
Senior Scientist
Materials Science and Technology Division

Off: +91-471-2515258
Fax: +91-471-2491712
E-mail: kpsurendran@niist.res.in

CERTIFICATE

This is to certify that the work incorporated in this Ph.D. thesis entitled **"Multilayer composites for magnetodielectric and magnetoelectric applications"** *submitted by* ***Ms. Lekshmi D. R.*** *to Academy of Scientific and Innovative Research (AcSIR), in fulfillment of the requirements for the award of the* ***Degree of Doctor of Philosophy in Physical Sciences****, embodies original research work under my supervision and guidance at the Materials Science and Technology Division of the CSIR-National Institute for Interdisciplinary Science and Technology (CSIR-NIIST), Thiruvananthapuram. I further certify that this work has not been submitted to any other University or Institution in part or full for the award of any degree or diploma. Research material obtained from other sources has been duly acknowledged in the thesis. Any text, illustration, table, etc., used in the thesis from other sources, have been duly cited and acknowledged.*

19.05.2020

Dr. K. P. Surendran
(Thesis Supervisor)

Lekshmi D. R.
(Student)

December, 2019
Thiruvananthapuram

ACKNOWLEDGEMENT

First and foremost, I must thank Dr. K. P. Surendran, Senior Scientist, Materials Science and Technology Division, CSIR-NIIST, my research supervisor for being my constant sources of motivation, support, and encouragement during the course of my research.

The unique guidance from Dr. K. P. Surendran was one of the main factors that helped me in successfully completing my research work. In spite of his hectic official routine as the Scientist, MSTD in CSIR-NIIST, he always managed to find time for frequent discussions. I am extremely thankful to him for the level of patience he showed when the progress of my work was dull, and for the effort he took to guide me through the right course. It has been a great pleasure and privilege to work under him. I could not have imagined having a better advisor and mentor for my Ph.D study.

I am particularly indebted to Dr. M. T. Sebastian, who was the head of division during the initial days of my research work and I am obliged to have his valuable inputs in my research topic which has been invaluable in helping me to learn how to do research, and to navigate some of the of the most challenging aspects of my work.

I am grateful to Dr. A. Ajayaghosh, Director of CSIR-NIIST, Dr. Suresh Das and Dr. Gangan Prathap, former directors of the institute for admitting and providing the necessary facilities and infrastructure to carry out this research investigation.

I express my sincere gratitude to Dr. Savithri S., Dr. Harikrishna Bhat, Dr. P. Prabhakar Rao, Dr. M. L. P. Reddy and Dr. M. T. Sebastian, former Heads of the division for their help rendered during the course of this work.

I am indebted to Dr. Suresh C. H., Dr. Luxmi Varma & Dr. Mangalam S. Nair, present and former co-ordinators of AcSIR for extending their support on my academic courses and its successful completion.

I gratefully acknowledge Dr. Manoj Rama Varma, Dr. U. S. Hareesh and Dr. Narayanan Unni, Doctoral Committee Members for their understanding, encouragement and personal attention which have provided good and smooth basis for my Ph.D. tenure and also for their helpful suggestions and comments during my presentations.

A special mention of thanks to Dr. Swapna S. Nair and Mr. Manikanda Pandibayal, Central University, Kasargod, for providing magnetodielectric measurements facility in

short notices despite of their hectic official routine and finding time for fruitful discussions regarding my work. I also thank Dr. Nadakumar Kalarickal and Dr. Anshida Mayeen, M G University, Kottayam for providing magnetoelectric measurements facility and their valuable suggestions. I acknowledge Dr. K. P. Jayachandran, Researcher IDMEC, Instituto Superior Tecnico (IST), University of Lisbon for providing the theoretical support.

Similar, overwhelming gratitude goes to Mr. Peer Mohammad for several characterizations related to my work and for being so supportive to me in personal level. I am also hugely appreciative to Mr. Kiran Mohan for HR-TEM studies related to my research work and for being one of my consistent support system by saving me from several pitfalls during the last days of my dissertation work. I appreciate Mr. Harish Raj, Mr. M. R. Chandran, Ms. Soumya, Mr. Prithvi Raj, Mr. Vibhu, Mr. Rejith, Ms. Aswathy K for their support in conducting various characterizations related to my work.

I am also pleased to say thank you to Dr. V. B. Manilal, Dr. B. Krishnankumar, Dr. Dileep Kumar, Mr. Dipin Raj and Mrs. Juby for CSIR 800 societal program. They have been very kind and patient and always willing to lend their service whenever I approached them and I acknowledge and appreciate each and everyone for all the efforts they put forward.

I also acknowledge the valuable suggestions and indispensable helps received from Dr. Subodh G. during the initial days of my research work for guiding me in the right path of the study. With a great admiration, I also remember the time spent by him for discussions and refinement techniques regardless of his hectic official schedule as Asst. Professor in University of Kerala. I wish to extend my special thanks to Dr. Abhilash, for being so dedicated to his roles as my senior, mentor and a good friend. He extended me rock steady support on my research work, which I am grateful to along with the endless deep conversations whenever I need one. Very special thanks to my colleague Mr. Adarsh S. Pillai for sharing constructive insights and worthwhile discussions with my research work and execution on these works.

I would like to express my deep sense of gratitude to all my seniors and labmates Dr. Manu, Dr. Chameswary, Dr. Jobin, Dr. Nina Joseph, Dr. Namitha, Dr. Induja, Dr. Gayathri, Dr. Angel, Dr. Dijith, Dr. Aiswarya, Mrs. Kanakangi S, Mrs. Aparna P N, Mrs. Bhavya A S, Ms. Revathi R, Ms. Ashitha, Ms. Aparna S, Ms. Sneha A K, Mr. Arun, Mrs. Roshni, Mr. Thomas Letang, Ms. Sabitha, Mr. Sikander, Ms. Heera, Mr. Praveen, Mr. Krishanakumar, Ms. Remya, Ms. Sneha, Mr. Alan, Mr. Bineesh, Mr. Anoop for all their advices, love and support. They always helped me out when I got any difficulties or queries regarding experiments and always stood by my side and sharing a great relationship as compassionate friends. I will always cherish the warmth shown by them.

A special mention of thanks to my friends in CSIR-NIIST and Material Science and Technology Division, especially in Magnetism and Polymer Group for their constant support and cooperation during my research period. Special mention to Mr. Arun B., Ms. Aswathy K. and Mr. Vipin G. Krishnan, Mr. Anoop in particular for the correction and proof reading of my dissertation work. Their timely help and friendship shall always be remembered.

I am indebted to my friends Dr. Sudheesh, Mrs. Deepthi, Mrs. Sijila, for their friendship and help during my work and constant emotional support which was crucial at times when I was down. I would always remember my fellow roommates Mrs. Daisymol K. B., Ms. Malini Abraham, Dr. Remya, Dr. Harsha for the fun-time we spent together, sleepless nights that gave me the courage to complete tasks before deadlines and for stimulating the discussions.

I must express my very profound gratitude to my better half Akhil Krishnan for providing me with unfailing support and continuous encouragement throughout my years of study and through the process of researching and writing this dissertation. His infallible love and eternal support has always been my strength. His patience and sacrifice will remain my inspiration throughout my life. Without his help, I would not have been able to complete much of what I have done and become who I am. I am immeasurably grateful to my son, Thanmay Krishna A, my Appus, for the tolerance and patience, and for putting up with me being a part-time mom for such a very long time and this accomplishment would not have been possible without him. Words cannot express the feelings I have for my parents, Rajendran Pillai and Deepa for their constant unconditional support in every aspect. My hardworking parents have sacrificed their lives for me and my child and provided unconditional love and care. I love them so much, and I would not have made it this far without them. My sister Oormila have been a great support ever and I owe her so much for the care and support shown to me as well as my son. I love her dearly and thank her for all her advice and support. Special thanks are also due to my in-laws for their amazing support to me and I know I always have them to count on when times are rough. I owe my invaluable debt to all family members, friends and teachers for their support, suggestions and co-operation without which I could not have executed this research work.

I would like to thank University Grants Commission, New Delhi for the financial support.

As a last byte, I would like to thank each and everyone for their integrity, sense of quality and mental assistance provided during this entire research work.

Lekshmi D. R.

CONTENTS

PREFACE

Multifunctional materials are a class of promising materials performing more than one function in a single system. These kinds of materials can be suitably engineered to realize dramatic and performance-tailorable properties. Integrating mutually exclusive functionalities into a single system is challenging but inevitable for realizing next generation electronic devices. Among different kinds of multifunctional materials, the present thesis is more focused on developing magnetodielectric as well as magnetoelectric multilayer materials.

Magnetodielectric materials form a genre of next generation multifunctional materials having controlled permittivity and permeability. These materials are potential candidates in electronic industry as efficient electronic band gap materials and also as substrate materials for antenna miniaturization, thanks to the compromising values of relative permittivity and magnetic permeability. On the other hand, magnetoelectrics are a subclass of multiferroic materials that combine ferroelectricity and ferromagnetism, thereby playing an important role in the development of efficient memory devices, sensors etc. These are materials that possess mutual control over electric polarization by magnetic field and magnetization by electric field. Both these multifunctional materials can be single phase or composite type. The present thesis focuses on layered composite type magnetoelectric and magnetodielectric materials that can be used for electronic and communication applications.

Electronic industry is frantically looking for novel materials with impressive energy efficiency and better functionality, capable of working at smaller dimensions. Scaling down is always a major challenge in the era of wireless communication where the biggest

roadblock is to reduce visual signature of antennas. Antenna miniaturization can be conveniently achieved by employing tailor-made magnetodielectric materials. In order to realize four state memory devices, magnetoelectric coupling between different ferroic materials should be explored. The subject matter of the thesis is to develop innovative magnetodielectric as well as magnetoelectric layered composites and understand the interesting science correlating individual properties. The present thesis has been organized into 6 chapters in which first two working chapters was dedicated for the development of (2-2) magnetodielectric layered composites and last two were designed for developing (2-2) thick film based ceramic magnetoelectric composites.

A general introduction to multifunctional materials with special emphasis on the science of magnetodielectric as well as magnetoelectric materials is presented in **Chapter 1**. This chapter also explains the theory, material requirement and applications of both classes of materials. Moreover, the commonly adopted techniques for realizing these multilayer structures are also explained in detail.

Chapter 2 outlines a novel kind of (2-2) magnetodielectric composite realized by screen printing a multiferroic layer on an LTCC substrate. The LTCC ceramic-glass composite based on $BiSmMoO_6$ (BSMO)-BBSZ ($40Bi_2O_3$:$49B_2O_3$:$6SiO_2$:5ZnO) was made into a tape which can be sintered at 875 ˚C. Meanwhile, a screen printable ink based on phase pure multiferroic, $BiFeO_3$ (BFO) was also developed in this research. The magnetodielectric composite was realized by screen printing BFO later on BSMO-BBSZ LTCC tape, a negative magnetocapacitance value of 15% was observed at 1 MHz under the application of 3 kOe magnetic field.

In another study as described in **Chapter 3**, an axially anisotropic magnetodielectric composite based on PMMA-$NiFe_2O_4$ was developed for realizing miniaturized antennas with wider bandwidth characteristics. The structural as well as ferromagnetic properties of developed $NiFe_2O_4$ were studied in detail in this chapter. Thin sheets of (0-3) composites were developed by adding different volume % of NFO in PMMA matrix (say 5, 10, 15, 20 vol.%). Interestingly high magnetocapacitance values were noticed for samples with higher solid loading. Further, an antenna operating at 830 MHz was theoretically modeled using this functionally graded anisotropic composite as substrate. An impressive miniaturization of 91% was observed for this particular antenna.

Chapter 4 of the thesis focuses on the development of all printed multilayer magnetoelectric (2-2) thick film composite based on $SrRuO_3$ (SRO) and Pr doped $SrTiO_3$ (Pr:STO). After exploring the structural as well as ferroic properties of the perovskite oxides, room temperature curable inks out of these materials were developed. Subsequently, a (2-2) composite was developed via screen printing one on top of other onto a platinized silicon substrate. Quasi-ferroelectric as well as ferromagnetic nature of the hetero structure was further confirmed. Magnetoelectric studies showed that the composite exhibited an unusual magnetoelectric coupling coefficient (MECC) value of 657 mV/cm.Oe and 655 mV/cm.Oe for ac and dc magnetic field respectively at room temperature. The unusual ME behavior associated with the present layered composite demonstrate its suitability in the fields of sensors, actuators, energy harvesters etc.

In **Chapter 5**, a (2-2) magnetoelectric composite based on Pr doped $SrTiO_3$ and $CoFe_2O_4$ was developed. fast curing inks were formulated out of the chemically derived nanopowders. Ink properties were tuned suitably for screen printing on hard and flexible

substrates. Layered magnetoelectric composites based on these materials having different functionalities were developed via screen printing. The magnetoelectric coupling studies reveal that developed (2-2) composite exhibit an enhanced MECC value of 780 mV/cm.Oe and 779 mV/cm.Oe for ac and dc magnetic field respectively. Ferroic and magnetoelectric properties of the composite was theoretically simulated using two-scale homogenization procedure employing finite element method that agree reasonably well with experimental results.

The overall conclusions of present investigation and future directions are summarized in **chapter 6** of the thesis.

Chapter 1

MULTIFUNCTIONAL MATERIALS: AN INSIGHT TO MAGNETODIELECTRIC AND MAGNETOELECTRIC MATERIALS

1.1 Introduction

We live in the golden age of materials, where exotic and smart materials are being emerged every day to quench the ever-growing demands of modern consumer electronics. Currently, multi-mission requirements of devices are achieved with the help multiple components and then integrate them into a single module. A new class of designer materials called multifunctional materials now take the central stage, that are able to perform multiple responsibilities through a judicious combination of different functional capabilities.[1] Typical examples include, an electronic skin that can sense mechanical strain, a coating that can change color on demand, a memory cell that can be written electrically but read out magnetically, a shell that can reconfigure its shape to suit surroundings etc. In such material systems, the designer functions can be performed concurrently or sequentially. Also this type of multifunctionality can be organized on the same length scale or can be organized hierarchically. However, integrating materials with independent functionality in one system is literally a scientific challenge but inevitable due to scaling of modern electronic devices.

Materials with specific properties such as electronic, magnetic, dielectric, thermal or other desirable characteristics can be performance-tailored suitably to satisfy some of the burning needs of modern electronics and communication.

1.2 Types of Multifunctional Materials

There are numerous kinds of multifunctional materials available in literatures. Some of them include:[2]

(i) Magnetoelectric materials: Materials that have mutual control over electric polarization under an external magnetic field or magnetization under the application of an external electric field.

(ii) Magnetostrictive materials: Ferromagnetic materials that will change their magnetization under the application of stress when subject to an external magnetic field.

(iii) Magnetocaloric materials: Class of materials that undergo reversible temperature change when exposed to an alternating magnetic field.

(iv) Magnetodielectric materials: These are a special genre of materials which consists of magnetic as well as dielectric components.

The present thesis envisages in development of magnetodielectric and magnetoelectric heterostructured materials by combining different dielectric, ferroelectric, ferromagnetic materials which will be detailed in following sections.

1.3 Magnetodielectric (MD) Materials

With the rapid proliferation of mobile phones, scaling of electronic components is the all-time relevant mantra in wireless communication. Unlike the electronic circuits which are highly scalable, the radiating element (say, antenna) invariably defies our efforts of miniaturization, leaving out a visual signature.[3] In fact, it is not easy to attain size reduction simply by structural design modification, without compromising its gain and bandwidth. A convenient strategy to attain size reduction is by improving material properties of antenna substrate.[4,5] Antenna miniaturization efforts are directed in two different ways. Primarily, high permittivity materials were attempted since antenna's

size is inversely proportional to $\sqrt{\varepsilon_r}$, where ε_r is the relative permittivity of the substrate.[6,7] Major drawback of using such kind of materials is that, electric field generated in the device will remain highly concentrated (field confinement) around high permittivity region only. This will result in low efficiency and narrow band operation in antenna characteristics.[8] Another shortcoming is due to low impedance for a high permittivity material which will affect impedance matching of antenna. In order to circumvent aforementioned problems, one can try using MD material as substrate.

MD materials are class of materials that possess dielectric permittivity (ε_r) and magnetic permeability (μ_r) in a compromising range. In such materials, the dielectric properties can be tailored by the application of suitable magnetic field and have the ability to reduce the impact of electromagnetic (EM) field confinement in regions near to the substrate. This substrate material will be less capacitive when compared with an all dielectric substrate. Further, the characteristic impedance of a MD material is close to the surrounding medium so that it enables better impedance matching over a wider bandwidth.[8]

1.3.1 Theory of Magnetodielectrics

Consider a MD material under an alternating EM field, wherein its dielectric as well as magnetic losses is assumed to be very small. Now the equation for transmission wavelength can be written as,

$$\lambda = \frac{c}{f\sqrt{\varepsilon_r \mu_r}} \qquad (1.1)$$

where λ is transmission wavelength, f is resonant frequency of antenna , c is speed of light in vacuum, ε_r is relative permittivity and μ_r is relative permeability of antenna substrate.[3] From equation (1.1), it is clear that improving the value of permeability of material has same effect as that of improving permittivity. This will eventually help in shortening the wavelength in dielectric medium and thereby reducing size of resultant antenna.

The characteristic impedance of an antenna has direct dependence with permittivity and permeability of substrate material, as given in equation,

$$Z = \sqrt{\frac{\mu_0 \mu_r}{\varepsilon_0 \varepsilon_r}} \approx \eta_0 \qquad (1.2)$$

where Z is impedance of antenna, η_0 is impedance of free space, ε_0 and μ_0 is the permittivity and permeability of free space ($\varepsilon_0 = 8.85x10^{-12}$ Fm^{-1} and $\mu_0 = 4\pi x10^{-7}$ $VsA^{-1}m^{-1}$) respectively.[9] For miniaturization of any electronic component, impedance matching is a crucial parameter since the real part of the antenna impedance actually represents radiated power. Follows from equation (1.2), the permittivity as well as permeability values of the substrate material should be nearly equal to attain impedance matching. This is a difficult task to achieve.

In layered laminate composites, individual dielectric layers with specific permittivity stacked with similar magnetic layers with specific permeability, are considered. If electric field is applied parallel and magnetic field is applied perpendicular to lamination planes, effective permittivity value of multilayer structure is given by,

$$\varepsilon_{eff} = \frac{1}{\sum\left(\frac{f_i}{\varepsilon_i}\right)} \quad (1.3)$$

where i is number of layers, $f_i = t_i/t$ where t=$\sum t_i$, while t_i is the thickness of i^{th} layer. Equation (1.3) can be used for finding effective permeability of the layered structure, by replacing ε with μ.

1.3.2 Material Requirements

As discussed before, the primary requirement for a MD material is to retain its magnetic as well as dielectric nature simultaneously. Unfortunately, naturally occurring materials having these properties are few and far between. There is a class of material named ferrites, which has high permittivity as well as permeability components in it. Thus, ferrites are considered to be an ideal host for producing low loss MD materials.[10,11]

As seen before, impedance matching is another stringent criterion for a MD material. Difference between values of ε_r and μ_r will result in impedance mismatch between material and system which will result in loss of signal due to reflection. If the criterion of impedance matching is satisfied, that will be advantageous for improving efficiency of scalable patch antennas.[12] But in practical terms, it is very difficult to satisfy this condition. Still, the main efforts so far are directed towards choosing materials having near values for ε_r and μ_r. Further, their magnetic as well as dielectric losses should be minimum for increasing the radiation efficiency of the antenna.

In the present thesis, we have developed two MD laminar composites in two different ways, as depicted in Figure 1.1. First type consists of a dielectric layer with permittivity value, ε_r and a magnetic layer on top of that having permeability value, μ_r as shown in Figure 1.1(a). In second type, different layers of MD materials having ε_r and μ_r values are thermo-laminated together, which in turn created anisotropy in the axis perpendicular to lamina's plane (Figure 1.1(b)). Each layer in this type of MD composite is made up of magnetic filler embedded in a dielectric (polymer) matrix as shown in Figure 1.1(c). So each layer will have a distinct value for ε_r and μ_r.

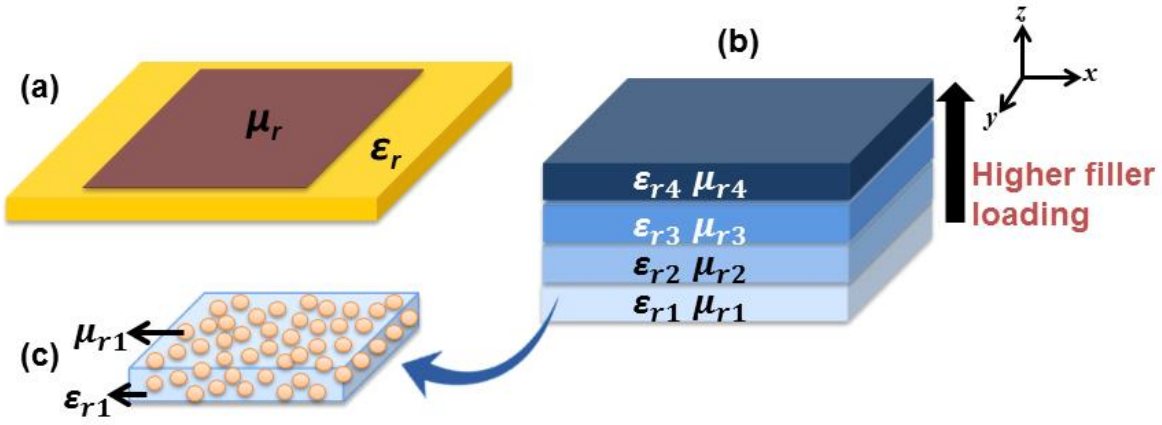

Figure 1.1: Schematic of MD composite materials used in present thesis.

1.3.3 Applications of Magnetodielectric Materials

The viability in designing a MD material is useful in radio frequency and wireless communication applications. There are two specific applications namely (i) electromagnetic band gap structures (EBG) and (ii) miniaturization of antenna.

EBG materials are usually 3 dimensional (3D) periodic structures that are used for blocking the propagation of EM waves in a specific band of frequency for all

polarization states. EBG structures are ample in number which always exhibit interesting characteristics like band gap, frequency stop band and pass band.[13] But in real scenario, it is hard to get a complete band gap structure, only partial band gaps can be accomplished. In a work done by Ho *et al.*, a periodic structure that is capable of producing complete transmission band gap was developed by using dielectric material only.[14] Later, the results derived in that investigation was compared with some new MD materials and discussed.[8] They concluded that, one can obtain a band gap structure that can yield better band gap rejection levels than using an all dielectric material in EBG.

Size reduction of microstrip patch antenna is another interesting application, as hinted above. The main characteristics of an antenna in mobile communication are wider bandwidth and high efficiency, to be realized at smaller dimensions. But the stronger capacitive coupling between antenna and its ground plane limits the performance of the device.[7] In order to solve this, one can use MD materials as substrate for antenna having moderate values for permittivity and permeability. Here miniaturization can be achieved by reducing the coupling between antenna and its ground plane. This means that, capacitive property is decreased by introducing inductance effect that will eventually counteract capacitive nature with improved efficiency as well as band width.[8]

1.4 Magnetoelectric (ME) Materials

In the contemporary information era, the demand is huge for high performance next generation memory devices.[15] Ferroelectric Random Access Memory (FeRAM) is a memory device in which information is stored by the principle of spontaneous

polarization (*P*) of the ferroelectric material. This is a very promising and mature non-volatile memory due to its low power consumption, fast reading/writing speed, high durability etc.[16,17] Despite of having so many advantages, there exist umpteen practical hurdles in the working of FeRAM, mainly in its data reading mechanism. Here, reading is performed by applying a bias voltage to the ferroelectric capacitor and sensing the corresponding *P* switching current. But this process is a destructive one and rewrite step is necessary. Besides, the employed reading method requires a minimum capacitor size, as the current generated will be high for sensing the circuit.[18] This can be resolved by engineering magnetization direction using an electric field, thereby taking the advantage of ME effect.[19-21] Hence, ME effect is suggested as a convenient way to read and write in future information storage systems.[22]

Multiferroic materials have certain advantages in achieving efficient information storage.[18,19,23] They are class of materials that simultaneously show ferroelectricity and ferromagnetism which is termed as ME materials. In other words, they show mutual control of electric polarization, *P* over magnetic field, *H* (which is called direct magnetoelectric effect, DME) or conversely, control magnetization, M by electric field, E (which is called converse magnetoelectric effect, CME). The ME effect is stemmed from the cross interaction between ferromagnetic (magnetostrictive) and ferroelectric (piezoelectric) phases in the material, which can either be in single phase or composite. When magnetic field is applied in ME composites, a strain is produced in the magnetostrictive phase which will be mechanically transferred to the peizoelectric phase, thereby an electric current is created. This elastic interaction mainly depends on

the microstructure of composite material and coupling interaction at interfaces between corresponding phases.[24,25]

1.4.1 Theory of Magnetoelectrics

From application perspective, the significance of ME materials lies in the prospect of strong ME coupling. As ME effect originates from coupling between electric and magnetic fields, the phenomenological description of ME coupling arise from the series expansion of free energy.[26]

Consider free energy density,[27]

$$dF = -SdT - P.dE_0 - MdB_0 \tag{1.4}$$

where S is entropy, T is temperature, P is electric moment, M is magnetic moment, E_0 and B_0 are external electric and magnetic field. Here, $B_0 = \mu_0 H_0$

For single phase ME, free energy up to quadratic order, at constant temperature is given by,[28,29]

$$-F(E_0, B_0) = P_S.E_0 + M_S.E_0 + \frac{\varepsilon_0}{2}\sum_{ij}\chi^e_{ij}E_{0i}E_{0j} + \frac{1}{2\mu_0}\sum_{ij}\chi^m_{ij}B_{0i}B_{0j} + \frac{1}{\mu_0}\sum_{ij}\alpha_{ij}E_{0i}B_{0j} + \cdots \tag{1.5}$$

where P_S and M_S are electric and magnetic spontaneous polarizations, χ^e and χ^m are electric and magnetic susceptibility tensors, α is linear ME coupling tensor and ε_0 is permittivity of free space. Here, α describes the outbreak of a magnetic (electric) field induced electric (magnetic) polarization. Equation (1.5) implies that, for fulfilling the time reversal or space inversion symmetry, the ME material should be invariant under

inversion reflection, as indicated by term containing α in the expression.[29] This will certify that for occurrence of linear ME effect, magnetic ordering in crystal is a stringent but necessary criteria.[30,31]

In case of composite ME materials, magnetic and electric terms in the expression for free energy (see equation (1.4)) corresponds to ferromagnetic and ferroelectric components. The ME term defines effectual interaction between order parameters for the corresponding phases. This coupling usually originates at the interface between respective phases. This interface breaks symmetry in materials which will further allow the presence of ME coupling in case of composite.[32]

Comparing equations (1.4) and (1.5), electric as well as magnetic inductions can be expressed as,

$$P_i = \frac{\partial F}{\partial E_{0i}} = P_{Si} + \varepsilon_0 \sum_j \chi^e_{ij} E_{0j} + \frac{1}{\mu_0} \sum_j \alpha_{ij} B_{0j} + \cdots \quad (1.6)$$

$$M_i = \frac{\partial F}{\partial B_{0i}} = M_{Si} + \frac{1}{\mu_0} \sum_j \chi^m_{ij} B_{0j} + \frac{1}{\mu_0} \sum_j \alpha_{ij} E_{0j} + \cdots \quad (1.7)$$

From these two equations, it is clear that, there is a component for cross polarization irrespective of spontaneous and induced terms.

The linear ME effect is given by,

$$\alpha_{ij} = \frac{\partial P_i}{\partial B_{0j}} = \mu_0 \frac{\partial M_i}{\partial E_{0j}} \quad (1.8)$$

For an isotropic material,

$$\alpha^2 = \varepsilon_0 \mu_0 \chi^e \chi^m \quad (1.9)$$

This result suggests that, large ME coupling can be observed in materials with large electric and magnetic susceptibility values.

In case of composite materials, ME response is measured in capacitor type device structures. Hence, the distance between capacitor plates should be taken into account when ME response is studied.

1.4.2 Material Requirements

The selection of suitable material is the key challenge in obtaining a large ME response. There are two possible platforms to explore the coupling between magnetic and electronic orders of matter: single phase ME materials and composite ME materials.[33] The major obstacle in using this single phase ME materials in technological applications is that they show ME coupling usually beneath room-temperature, that too with relatively low coupling coefficients.[34] In contrast, composite ME material, consisting of separate ferroelectric and ferromagnetic phases, exhibits a higher value for ME coupling coefficient at room temperature. This ME property which is of many orders higher than the single phase ones, makes them attractive candidates in device applications.[35] These composites can be broadly classified into ceramic based or polymer based.[36] Among them, ceramic based ME composites show better ME coupling than polymer based ones.[33,37] In past decades, various ceramic composites consisting of piezoelectric and magnetic oxide ceramics were investigated.[38-40]

In general, two-phase composites can either be a particle reinforced composite (0-3), laminate composite (2-2), or fiber reinforced composite (1-3), where the classification is done using the concept of phase connectivity, as shown in Figure 1.2. Usually, (0-3) particulate composites consist of ferroelectric and ferromagnetic oxide grains, whereas (2-2) type laminate composites consist of ferroelectric and

ferromagnetic layers developed using a thin film technology, thick paste or ink. On the other hand, (1-3) type fiber/rod composite comprises of fiber/rod of one phase that is embedded in the matrix of another phase.[41] Figure 1.3 gives an idea of the evolution of development of ME materials in due course of time. In 1894 first theoretical prediction of intrinsic ME effect was done by Pierre Curie and was experimentally observed in Cr_2O_3 single crystal in 1961.[42,43] From the view point of material constituents and dimensionalities, evolution of ME materials happened from single to particulate, to laminate and now to micro/nano thin films.[44]

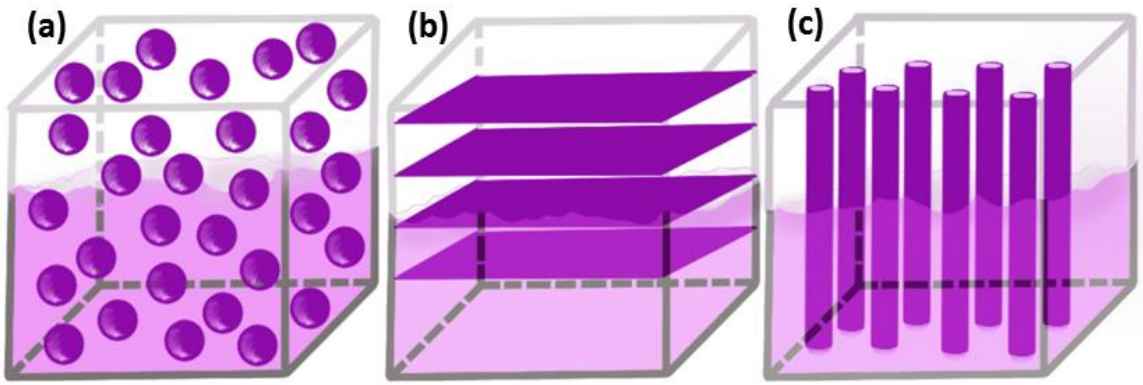

Figure 1.2: Commonly used ME composites namely (a) 0-3 particle reinforced, (b) 2-2 laminate, (c) 1-3 fiber reinforced.

As seen thus far, coexistence of magnetic and electric dipoles is the basic requirement for ME effect. The conditions for occurrence of ferroelectricity and magnetic ordering in a material are often accompanied by ferroelasticity. This demands the following: (a) presence of sufficient structural building blocks that allows ferroelectric-type ionic movements, (b) magnetic interaction pathways, usually of the super exchange type, and (c) actualization of symmetry conditions.[45] In composite materials, the interfacial bonding between two phases has a strong influence on elastic coupling in composite

material and hence its ME response too. So a good mechanical bonding at interface is need for efficient strain transfer to happen.[25] As the laminate composite preserve properties of both components, individual characteristics of ferroelectric as well as ferromagnetic parameters have to be taken into account. This means, better individual ferroic property may lead to better ME response for the composite.

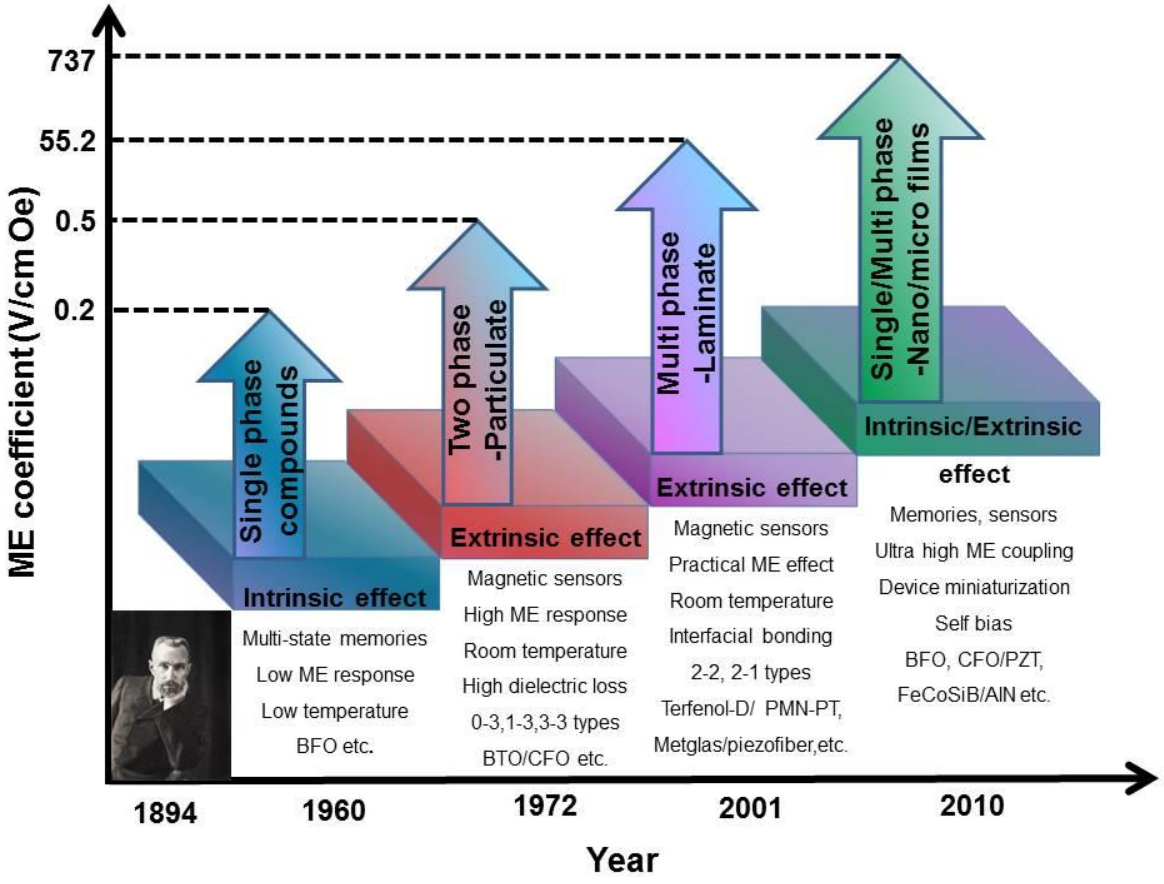

Figure 1.3: Evolution of ME materials from single phase to micro/nano thin films.

1.4.3 Applications of Magnetoelectric Materials

As far as bulk and film based ME composites are concerned, a variety of applications have been proposed that includes magnetic/electric sensors, energy

harvesters, ME random access memory, biomedical applications etc. ME based devices are promising substitute for Hall Effect sensors and giant magnetoresistive devices. They can replace superconducting quantum interface devices (SQUIDs) due to their passive nature combined with self- powered operation at room temperature. In the last decade, a galaxy of laminate based ME sensors have been reported in literature, that find various applications in medical applications as well as oil prospecting.[46-50] Energy harvesting from ambient sources is a hot area that was set to improve life time of devices and thereby addressing the limitations of conventional batteries. Magneto-mechano-electric (MME) mechanism has the potential to solve this problem, where any mechanical vibration in the composite will result in an electric voltage and hence can harvest energy.[51-55]

ME composites were also suggested to be used in biomedical field that includes wireless endoscopy, stimulation of living cells etc.[56] They also find its applications in drug release as carries and for stimulating neural activities in brain.[57,58] As mentioned earlier, there exists a mutual control over the ferromagnetic phase and ferroelectric phase in ME composites. Hence this coupling can be creatively exploited to combine the essence of FeRAM and MRAM, to create a novel type of magnetoelectric random access memory (MERAM) with multiple memory states. This has got the advantages of large memory capacity, low power consumption, improved thermal stability.[19,59,60]

1.5 Commonly Adopted Methods for Making Magnetodielectric and Magnetoelectric Composites

There are umpteen ways to develop composite materials. The current section is devoted for explaining various methods that are widely used to make MD and ME composite materials for various applications. For any particle application, the developed composite may either be a thick film, thin film or else in bulk form.

1.5.1 Thick Film Hybrid Technology

Conventionally silicon monoliths were used as mechanical supporter for bearing active and passive components in an electronic circuit. But in applications like military, automotive, avionics etc., integrated circuits have to deal with stringent conditions such as high temperature, pressure as well as humidity. In such cases, conventionally used silicon based monoliths fails to deliver the desired performance. Also, silicon monoliths fail to board large value capacitors, crystal oscillators, metallic inductors etc. In this scenario, a series of ceramic substrates have been evolved. In line with scaling trends, there emerges the need for 3D integrated circuit that can withstand extreme conditions by maintaining its electrical as well as mechanical properties. Hybrid circuits or multilayer ceramic technology (MLC) is a concept where active components like transistors, diodes etc. and passive components like resistors, capacitors, inductors, transformers etc., are bonded into a ceramic substrate or printed circuit board (PCB). The main advantage of MLC technology is that, it can combine passive components like microstrips, antennas, filters, resonators, inductors, capacitors, phase shifters, dividers into a monolith and are fired in a furnace to get a single module.[61]

High packing densities of any electronic circuits can be achieved by increasing circuit density, reducing number of interconnects and by shortening conductor lengths.

Here comes the concept of cofired technology. This cofired ceramic technology has an intense role in 3D circuit board development. Multilayer cofired technology is broadly classified into three categories: high temperature cofired ceramics (HTCC), low temperature cofired ceramics (LTCC), ultra-low temperature cofired ceramics (ULTCC). The basic difference between these three technologies is the choice of electrode materials used as well as the cofiring temperature employed. These three technologies are elaborated in following sections.

1.5.1.1 High Temperature Cofired Ceramics (HTCC)

Multilayer capacitors are the simplest form of hybrid circuits which were first developed in late 1940s. Ten years later, Radio Corporation of America (RCA) first developed multilayer ceramic technology and was named as HTCC.[62] In 1961, IBM endorsed this technology for development of multilayer packages for microprocessor applications. They enabled hermitic packages containing large number of electrical feeds within small chip spaces.[63] The important characteristics of HTCC technology are,

(i) Excellent mechanical stability

(ii) High temperature stability

(iii) High thermal conductivity

The fabrication of a typical HTCC module involves several stages of processing. This starts from the judicious selection of starting materials, slurry preparation, green tape development using tape casting technique, via punching, screen printing, lamination of multiple layers, cofiring followed by post firing operations like sawing, machining, brazing etc.[61] The cofiring temperature used in HTCC technology is greater

than 1500 ˚C and hence the electrodes chosen are molybdenum (Mo) and tungsten (W) which can stand these high temperatures. But the main disadvantage of using these highly resistive materials is that they will contribute conductor loss in the module while using in high frequencies. Alumina (Al_2O_3) is the most frequently used HTCC substrate for electronic utilizations due to its excellent dielectric, thermal and mechanical properties.[64,65] Other commonly used HTCC substrates are aluminium nitride (AlN) and zircon ($ZrSiO_4$).[61]

1.5.1.2 Low Temperature Cofired Ceramics (LTCC)

Size reduction of electronic packages is the current trend followed by microelectronic industries. This will result in more complex packages with high interconnect density, smaller component sizes along with greater reliability.[66] This continuous effort for size reduction with improved performance will lead to the usage of finer wiring techniques, which will eventually result in increasing electrical resistance that causes signal attenuation.[62] At this juncture, there arises the need of using a high electrical conducting material as wiring interconnects in hybrid circuits. The well-known low resistivity materials are silver (Ag), gold (Au) and copper (Cu). But the major disadvantage of using them is their comparatively low melting temperature, i.e, <1050 ˚C. This necessitated replacing the known HTCC materials with designer glass-ceramic materials known as Low Temperature Cofired Ceramics (LTCC). Currently LTCC is the leading technology for ceramic packaging. The main characteristics of LTCC include:

(i) Passive integration and 3D design

(ii) High circuit density

(iii) High conductivity (low resistivity) metallization

(iv) Low thermal conductivity

High circuit density can be achieved by integration of numerous components within a single package. Figure 1.4 shows the schematic cross section of an LTCC module. LTCC has got a distinctive ability to integrate a large amount of passive components into a very compact arrangement and thereby leaving valuable circuit surface area for active components.[67]

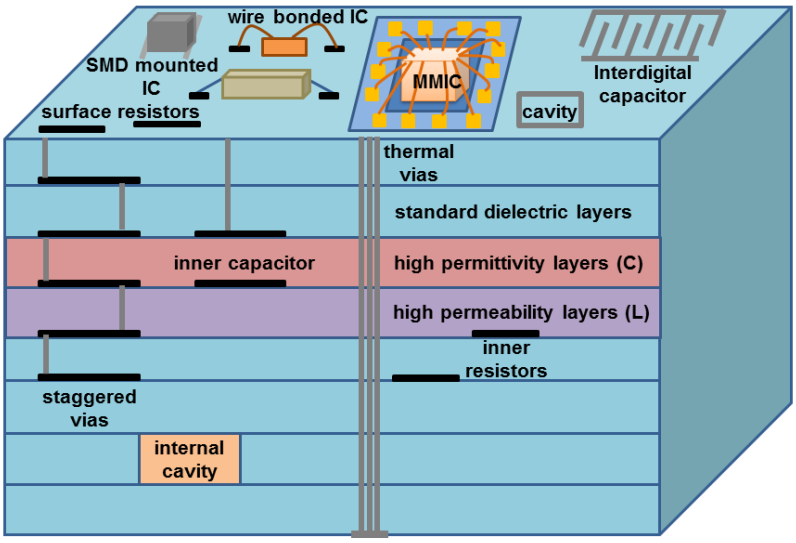

Figure 1.4: Schematic showing cross section of an LTCC multilayer module.

The process followed in LTCC is exactly the same as that for HTCC except ceramics and electrode materials. Some of the commercial suppliers of LTCC tapes are Dupont, Heraeus, ESL, Ferro etc.[68]

1.5.1.2.1 Material Requirements

In order to produce an LTCC module, the material should be cofired with concerned electrodes; as a consequence, the sintering temperature of material should be lower than that of the electrode. Even though so many low resistivity materials are available for using as inner electrode in LTCC technology, silver (Ag) is the usual choice for electrode which means the sintering temperature of LTCC material should be below 961 ˚C (melting temperature of Ag).[66,69-72] Usually, materials having good dielectric property are having a very high sintering temperature, which limits their applications in LTCC. There are only handful of methods used for diminishing the sintering temperature like use of low melting glasses, due to its low cost and easiness in application.

Essentially, there are two different protocols adopted for using glass-ceramic composite preparation. First method is glass-ceramic route, in which one can start with a glass system with suitable composition and then it is allowed to crystallize to obtain maximum density after heating. Here, the physical properties of the composition are inhibited by the degree of crystallization which is mainly due to the addition of small amount of crystalline phase that acts as nucleating agent. A typical example is MgO-Al_2O_3-SiO_2 glass system having cordierite as the principal crystalline phase.[73,74] The second method is glass + ceramic route, in which contain a vitreous promoting low loss glass and ceramic powder that can be sintered near 900 ˚C. Here, liquefaction of glass and its viscous flow mechanism through the constituent ceramic particles occurs, which play key role in densification behavior of the whole system. The prerequisite for liquid phase sintering is that the liquid phase (glass) should wet the ceramic grains. Over the years, there are a lot of reports in glass + ceramic LTCC composites.[75-82] But the major

disadvantage of using glass + ceramics is that high content of glassy phase will deteriorate microwave dielectric property of LTCC material. Also, the presence of different phases will result in some undesirable chemical reaction between the electrode materials, leading to the formation of secondary phases. Due to foresaid reasons, researchers are looking for LTCC compositions with the lowest glass content. Our efforts to qualify an ideal LTCC ceramic material is described in chapter 2 of this thesis, where the designer material is with a very low amount of glassy phase, with good microwave dielectric properties.

Multilayer ceramic substrates (hard substrates) are developed using a process known as ”tape casting”, which is also called doctor blade technique. This method was introduced for ceramic materials in 1947 by Glenn Howatt. Ever since, it has been used for the production of multilayer capacitors and ceramic substrates for HTCC as well as LTCC systems.[83] The main advantage of using this technique is that it can produce flexible, self- supporting green ceramic sheets with a wide thickness range of 10-100 μm.[84] Suitably casted tape layers act as building blocks in many multilayer ceramic packages.[85] The detailed description for tape casting technique is given in the following section.

1.5.1.2.1.1 Tape Casting

Tape casting is a fluid forming process in which a ceramic powder is converted into well stabilized slurry by the addition of different components like solvent, binder, plasticizers, homogenizer etc. The process flowchart of a typical tape casting procedure is depicted in Figure 1.5.

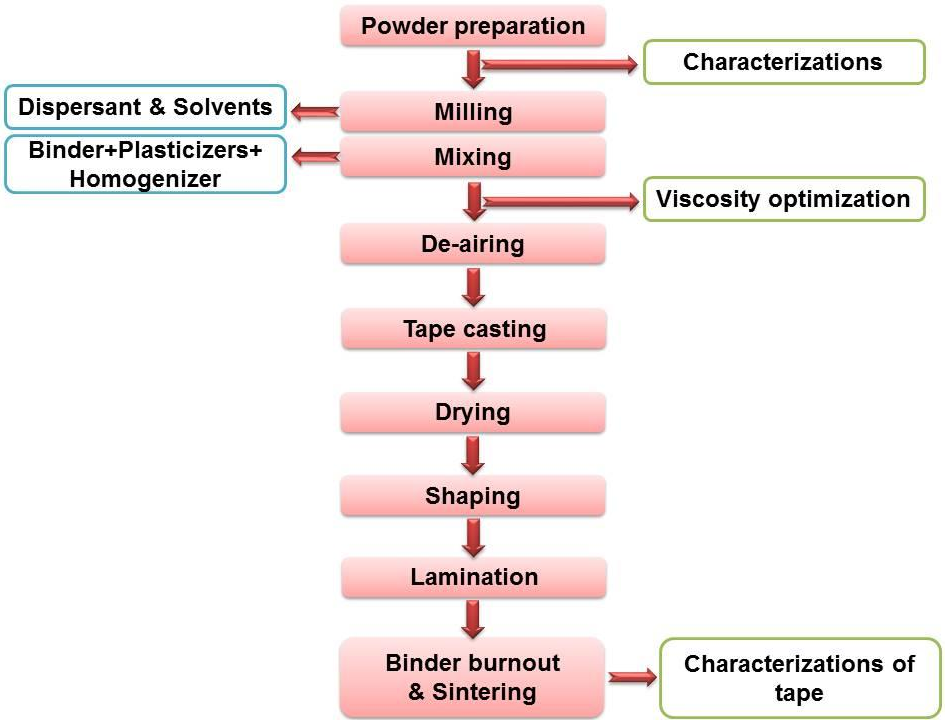

Figure 1.5: Process flowchart of tape casting.

The basic formula for tape casting slurry comprises of ceramic powder, solvents and suitable organic additives like binders, dispersants and plasticizers. These ingredients other than ceramic powder are added only to ease the fabrication of tape and to make a mechanically strong tape enough for subsequent processing. So after firing, solvents and organic additives will be removed and ceramic material will remain in a dense form.[62] Usually binary solvent systems are used in tape casting process due to their ability to solvate different polymeric binders and functional additives. Additional advantages of having greater control over rheology of slurry prepared and faster drying speed are shown by binary solvent system. The function of each component used in tape casting technique is summarized in Table 1.1.

Table 1.1: Different components and their functions in tape casting slurry.

Component		Functions
Part 1		
Ceramic powder		Provide desirable material properties
Solvents		Dissolve different organic additives, disperse powder particles, provide suitable viscosity for the slurry
Dispersant		Disperse powder particles, controls degree of agglomeration of ceramic powder
Part 2		
Binder		Binding the ceramic particles together, provide strength for green tapes, guarantees laminate formation
Plasticizer	Type I	Softens polymeric chains present in binder and thereby making the green tape more stretchable without fracture
	Type II	Provides flexibility by lubricating the tape matrix
Homogenizer		Prevent skin formation, makes the powder and additives uniform throughout the slurry

The amount of solvents and other organic additives should be kept to a minimum level, because excess amount will lead to their burnout difficulties which may result in a damaged tape with low firing density. After slurry preparation, it is spread over a flexible substrate by letting them to pass through a gap kept for attaining accurate width and thickness, using a doctor blade. This is the deciding factor for

thickness of green tape. In tape casting process, the thickness of green tape is controlled by four parameters viz. slurry viscosity, carrier speed, blade gap and reservoir height.

The most important pre-requisites of a tape casting slurry include (i) well dispersed homogenous stable system (ii) minimum viscosity (iii) shear thinning behavior etc.[86]

1.5.1.2.1.2 LTCC Module Fabrication

The process flowchart of LTCC module fabrication is shown in Figure 1.6. After drying the casted tape in air, it is further processed to form multilayer components, as shown. The tape is first cut to desired size and required vias were formed using punching or drilling. After via filling and screen printing of conductor patterns on individual layers separately, they are stacked and laminated together. The laminate is then cofired. Subsequently, post firing testing and validation of the fabricated LTCC module will be carried out.

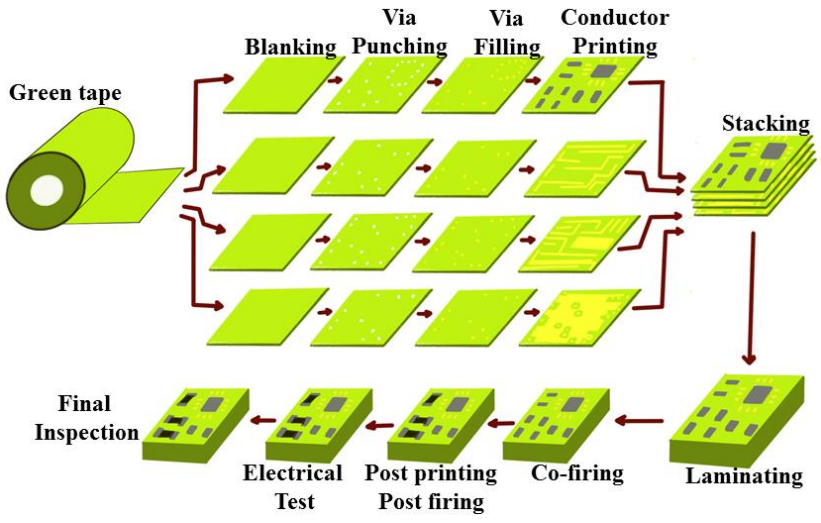

Figure 1.6: Flow chart of LTCC module fabrication process.

The mechanical stability and flexibility ensures the manageability of the developed tape. Printing of patterns on top of tape surface is controlled by surface

smoothness. Sinterability and good binder burnout behavior dictates the density of the cofired tape. In LTCC production, the process parameters have to be defined separately in each glass-ceramic composition and therefore they have been a proprietary secret for commercial materials.

1.5.1.2.2 Applications of LTCC

LTCC technology finds wide range of application in every aspect of our day-to-day life which includes consumer electronics, automotive, home appliances, biomedical and so on. In addition to dielectric properties, LTCC materials are supposed to possess superior mechanical properties too, in sintered state. This will extend their applications in the field of sensors, actuators, microsystems that can work in extreme harsh conditions like humidity and temperature.[69,87,88] Microwave antenna is another domain where LTCC technology is found to be useful, especially in Bluetooth, global positioning system (GPS) and wireless local area network (WLAN). With the advent of mobile telecommunication, LTCC based antennas gain more attention due to their multifunctionality and performance.[89]

1.5.1.3 Ultra-Low Temperature Cofired Ceramics (ULTCC)

The demand of dielectric materials that can be sintered at low temperatures (<700 ˚C), has been increased recently. The advantages of using such kind of materials in multilayer ceramic packaging are their cost effectiveness, less energy consumption and reduced processing time.[90] In ULTCC technology, firing temperature can be tuned to temperatures below 400 ˚C (Category I ULTCC) or 700 ˚C (Category II ULTCC) which allows the integration of structures using nano silver or aluminum respectively. In

2010, Valant et al. reported the first ULTCC material sillenite based $Bi_{12}Mo_{20-d}$ compounds.[91] Nowadays, there are scores of reports are available in literature, dealing with electroceramic that can sinter well below 600 ˚C.[92-98]

1.5.2 Polymer Ceramic Composites

Polymers play a vital role in the microelectronic industry due to their optimum dielectric properties at microwave frequency region, as substrates and packaging applications. The globe is inundated with polymers due to their low cost, large area and low temperature processability. But low thermal conductivity and high thermal expansion coefficient limits their single phase usage in electronic applications. Complimentarily, there are many ceramics having high processing temperature but excellent dielectric properties and low thermal expansivity. Modern electronic industry requires diverse and specific functional properties in materials which cannot be met in single material alone.[99] Hence, individual properties of polymers and ceramics can be tailored together in a composite approach, in order to obtain a combination with excellent dielectric, thermal and mechanical properties. In recent decades, a huge variety of polymer-ceramic composites have been launched for applications in the field of telecommunication, medical and microelectronics.[100] In these composites, polymer is termed as matrix and ceramic is categorized as filler material. The ceramic filler can be a dielectric, magnetic or any kind of material depending on the application. Here in one of the chapters (chapter 3), we plan to make a composite by adding magnetic filler into a polymer matrix which will result in MD composite with tailor-made properties.

1.5.2.1 Connectivity

Connectivity is a key feature in the evolution of multiphase solids since the physical properties are greatly depending on the connection between individual particles.[101] The concept of connectivity was first introduced by Newnham.[102] The interspatial relationship in a multiphase composite is of great significance because this controls the mechanical, dielectric, magnetic and thermal fluxes between the phases. In a two phase composite, there are ten number of connectivity as shown in Figure 1.7. Here, the first digit amount to inclusions and the second one stands for host. The commonly studied composites among these varieties of connectivity are, (0-3), (2-2) and (1-3) configurations. Polymer ceramic composites with (0-3) connectivity are suitable for producing functional packages.[103] In a typical (0-3) composite system, zero dimensional (0D) particulate fillers will be distributed in a 3D host polymer matrix. Here in principle, the filler particles should not be connected to each other, whereas the polymer matrix will be self-connected in all directions.[104] When compared to other configurations, 0-3 connectivity can be achieved at relatively low cost.[105] Preparation of (0-3) MD composite is planned in the thesis with the aim of developing miniaturized microstrip patch antenna.

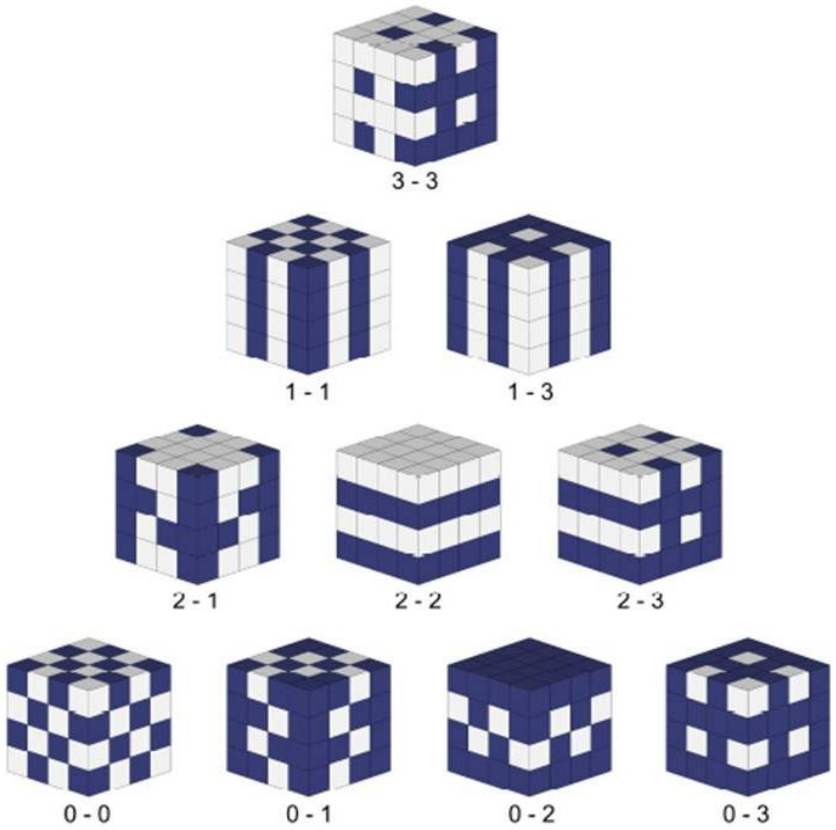

Figure 1.7: Connectivity patterns in two phase composite system.[102]

1.5.2.2 Material Requirements

Polymer ceramic composites are developed for fulfilling diverse applications in electronic industry. As they are the combination of polymer and ceramic materials, they should be blessed with the advantages of both the constituents. The present thesis plans to develop a MD composite with (0-3) connectivity, where the magnetic part acts as the filler and the polymer acts as the matrix. Since the developed composites are intended to use in microelectronic devices, they have to fulfill certain stringent criteria like low dielectric as well as magnetic loss, and agreeing values for dielectric permittivity and magnetic permeability over the desired frequency range. The filler

particle size, interfacial properties, percolation level and porosity play key roles in the composite properties.

Thermal properties of composites are very crucial since ceramic and polymers differ largely. The properties that are significant in enduring life cycle profiles of resultant devices include thermal conductivity and thermal expansion coefficient. High value for thermal conductivity is required to dissipate heat generated during operation of the device. Low thermal expansion is also a mandatory property for composite since it is related to dimensional compatibility and thermal stability when used with other elements in the device. Usually, low or matching thermal expansion coefficient close to that of silicon (~ 4 ppm/°C) chips is acceptable to curtail thermal failure.

Mechanical properties are also important for a polymer ceramic composite since the developed one has to sustain flexural loading during operation. The mechanical properties of composites are strongly affected by size and shape of ceramic filler, matrix properties and interfacial adhesion between them. The mechanical properties are critical because during manufacturing as well as assembling stages, the composites have to undergo thermo mechanical stresses, shocks and vibrations. Different forms of composites are known to research world, where functional ink which is essentially a mixture of functional filler and a vehicle, is also a composite.

1.5.3 Formulation of Functional Inks

Printed electronics is a revolutionizing domain in next generation electronics which finds lot many advantages than silicon technology by means of its low temperature processability, low production cost, mask less as well as additive manufacturing process. Functional inks are usually used in printed electronics aiming

the development of different functionalities in a single device. There are different kinds of functional inks that are being used in current state of art. Figure 1.8 gives a brief idea of different types of ink and the components used to make an ink.

Figure 1.8: Different types of ink and components in each type of ink.

As shown, various kinds of inks are currently available for printed electronic purposes. They include dielectric, conducting, magnetic and semiconducting inks. The difference between these inks is their functionalities that are being offered after printing in for a purpose. In multilayer circuits, dielectric inks are often used for providing electrical insulation between the conducting layers and thereby avoiding short circuits.[106] Magnetic, conducting as well as semiconducting inks can be used for printing components of specific applications. Moreover, magnetic ink finds its application in banking industry in clearance of cheques as magnetic ink character recognition (MICR) code.[107]

Any ink is comprised of filler colloidally dispersed in a solvent system along with binder and dispersant. Different functionalities can be obtained by suitable selection of

filler material. More careful choice of solvent system has to be done since the filler should be soluble (or dispersible) in the same. A polymeric binder is used in order to bind the filler particles together in the printed pattern. The role of dispersant is to disperse filler particle in the system for obtaining a stable suspension of ink, while remaining soluble in the solvent.

There are lot many methods available for transferring the ink to a substrate. Semiconductor industry uses printing technologies like inkjet printing, micro contact printing, screen printing, flexographic printing etc. Among them screen printing offers cost effective as well as easy technology for depositing functional inks. This method can be used to print large area patterns in a matter of few seconds. A schematic representation of screen printing process is shown in Figure 1.9.

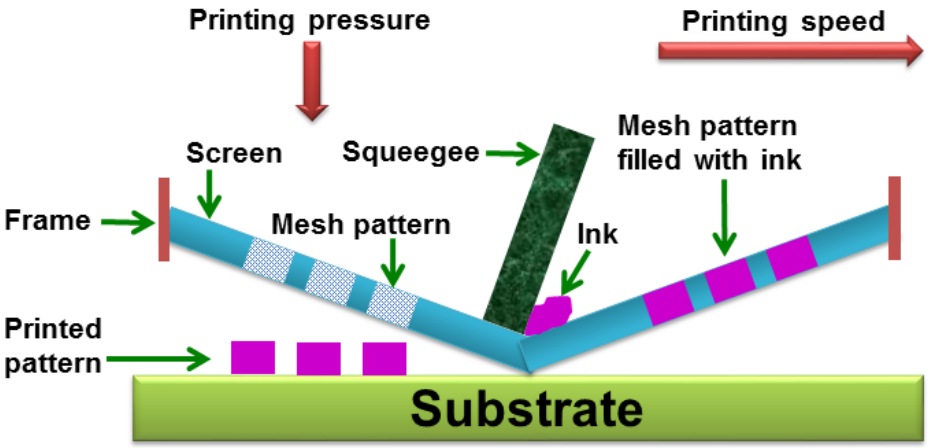

Figure 1.9: Schematic representing screen printing process.

The essential elements in screen printing technique are screen, ink and a squeegee. Screen printing requires a highly viscous ink (viscosity ~10 Pa.s or more), which is squeezed through a finely woven mesh on to a substrate using a squeegee (see

Figure 1.9). Screen is usually made up of porous fabric or stainless steel which is tightly held onto a wooden/metallic frame. The pattern to be printed is usually defined in the mesh through photochemically or manually. Squeegee is a flexible blade used to flow ink into the mesh and to wipe off excess ink from the screen. During screen printing, squeegee moves against the screen and presses ink through mesh opening and register over the surface of substrate. The important parameter that determines the flow of ink through mesh is the viscosity of ink, which is a measure of inner friction of the fluid when subjected to mechanical pressure. Wetting behavior of ink as well as mesh parameters also play important role in determining the resolution of printed pattern.

1.6 Testing of Magnetodielectric and Magnetoelectric Properties

The developed MD and ME composites have to be measured for getting an idea for exploring them in practical applications. A variety of characterization techniques are to be used for measuring the individual as well as combined properties of materials synthesized and also for developing various composites discussed in the present thesis. Some of the popular characterization techniques used in the present study are briefly described below.

1.6.1 Radio Frequency and Microwave Measurements

The dielectric properties of the developed materials were studied in low radio frequency (1 Hz to 1 MHz) as well as microwave frequency (> 1 GHz) regions and are detailed in the following sections.

1.6.1.1 LCR Meter

LCR meter is a device used to measure inductance, capacitance, resistance and dissipation factor of a dielectric ceramic, generally in radio frequency region. Under the application of an ac voltage across the device, LCR meter will measure the impedance of the same under test. LCR meter uses the well-known parallel plate capacitor method for elucidating parameters like capacitive, inductive and resistive components of the ac field in interaction with the dielectric, beside the dielectric dissipation factor. The parallel plate method comprises of sandwiching a sheet of dielectric material between two electrodes in the form a capacitor. Here we use silver paste as conductive electrode for measuring. The capacitance of parallel plate capacitor measured in vacuum is compared with the one measured in presence of material for which the dielectric property is to be measured. The permittivity of the sample is calculated from measured capacitance as per the equation,

$$C = \frac{\varepsilon_r \varepsilon_o A}{d} \qquad (1.10)$$

where C is capacitance, and ε_r and ε_o are permittivity of material and free space, A is area and d is thickness of sample.

Here in the thesis, we used an instrument Hioki model 3532-50 (Japan) whose accuracy for the impedance measurement is ±0.12 % at 10 kHz. The accuracy of capacitance is ±0.009.

1.6.1.2 Microwave Characterization

The complete knowledge about microwave dielectric properties of the material is required to qualify novel low loss dielectric materials for microwave applications. The measurement of these properties classified into two categories according to the methods used: resonant and non-resonant methods. Resonant method provides meticulous knowledge about the dielectric properties at a particular frequency or at discrete frequencies. In non-resonant method, the accurate knowledge of properties will be obtained over a frequency range.

1.6.1.2.1 Measurement of Permittivity

The permittivity of a material used in microwave applications is measured using the method developed by Hakki and Coleman and modified by Courtey.[108] In this method, sample in the form of a cylindrical puck is end shorted between two conducting plates made up of copper whose surface is already coated with silver/gold. In this method, TE_{011} resonant mode is used for measurements since this mode is least the perturbed one in frequency domain, and is capable of propagating inside dielectric sample and is evanescent outside the same. Hence, a large quantity of electrical energy will be stored in high Q resonators.[109] For easily identifying the TE_{011} mode from adjacent modes, the aspect ratio (sample diameter to height ratio) should be maintained to two. The permittivity of the sample is measured using the relation,[110]

$$\varepsilon_r = 1 + [\frac{c}{\pi D f_0}]^2(\alpha^2 + \beta^2) \qquad (1.11)$$

where D is diameter of sample, f_o is resonant frequency, α and β are resonant wavelengths inside and outside the resonator.

1.6.1.2.2 Measurement of Quality Factor

Transmission mode cavity proposed by the Polish scientist Jersey Krupka, was used in the present study for measuring unloaded quality factor (Q_u) of dielectric material.[111] Resonant cavity is a hollow metallic cylinder made of copper and inner sides are coated with silver in order to reduce the radiation loss. When microwave is fed using loop coupling, cavity excites infinite number of modes. $TE_{01\delta}$ mode is identified when the cavity volume is adjusted properly. After identifying the foresaid mode, fine tuning has to be made for getting maximum separation between $TE_{01\delta}$ and any nearby cavity modes, to attain maximum possible accuracy in quality factor measurement. The loaded Q factor is calculated using,

$$Q_L = \frac{f_0}{\Delta f} \qquad (1.12)$$

where f_0 is the $TE_{01\delta}$ mode frequency and Δf is the half power (3dB) bandwidth.

Practically, the unloaded quality factor will be nearly equal to the loaded Q value for extremely loose coupling (for low loss samples). In microwave frequency region, the dielectric loss increases with increase in frequency. That means, there exist an inverse relationship with quality factor and frequency. So the quality factor of a dielectric resonator is conventionally represent in units of $Q_u \text{x} f$, rather than Q_u.

1.6.1.2.3 Split Post Dielectric Resonator (SPDR)

Split Post Dielectric Resonator method is a resonant technique, which is used to characterize thin sheet like samples. It provides accurate measurement of complex permittivity and dielectric loss at single frequency point.[112] Here the resonator consists of a dielectric split into two thin equal discs inside the metal enclosure. SPDR is designed in such a way that, air gap will not affect measurement of dielectric properties of material under test. SPDR usually operates with $TE_{01\delta}$ mode, which only has the component of azimuthal electric field. Hence, the electric field will remain continuous throughout interfaces of the dielectric. But the field distribution gets affected by the introduction of sample, which in effect will change resonant frequency as well as unloaded quality factor. The dielectric properties are thus derived from the changes in values of resonant frequency and Q_u, due to perturbation happened by the insertion of respective sample. The permittivity is obtained as an iterative solution to the following equation,

$$\varepsilon_r = 1 + \frac{f_0 - f_s}{h f_0 K_\varepsilon(\varepsilon_r, h)} \qquad (1.13)$$

where h is thickness of the sample, where f_0 and f_s are resonant frequency of resonant fixture without and with sample, K_ε is a function of ε_r and h will be evaluated using Rayleigh-Ritz technique.[111] The loss tangent is calculated using the equation,

$$tan\delta = \frac{{Q_u}^{-1} - {Q_{DR}}^{-1} - {Q_C}^{-1}}{\rho_{es}} \qquad (1.14)$$

where Q_u is a parameter dependent on the unloaded quality factor of resonant fixture, Q_{DR} is quality factor depending on the dielectric losses in dielectric resonators and Q_C is quality factor depending on the metal enclosure losses.

The overall uncertainty associated with measurements using SPDR is about 0.3%. The accuracy level of loss tangent that can be achieved through this method is $2x10^{-5}$ and a 1% error for Q-factor measurements.[111]

1.6.1.2.4 Transmission Waveguide Technique

The main disadvantage of cavity resonant method is its unsuitability for measuring the dielectric parameters of relatively lossy samples. The resonant curves for lossy samples will be widened as the loss of the samples increase. Transmission wave guide technique is a non-resonant method which employs two port transmission/reflection over a wide range of frequencies. This is based on transmission line theory, where the properties can be determined from phase and amplitude of a microwave signal reflected from the sample itself. Here the real and imaginary part of both permittivity and permeability can be obtained over the respective band of frequencies. Rectangular block samples that fit in the exact dimensions of waveguides is used. Herein, the dominant TE_{01} transverse electric mode is identified which propagates through discontinuity created by sample under test in respective waveguide. This method involves the measurement of the reflected (S_{11} or S_{22}) and transmitted signals (S_{12}or S_{21}). These scattering parameters are closely related to the complex permittivity and permeability of the material.[113] Uncertainty in the measurement is greatly depends on the thickness of the samples used for measurement.

The average resolution for loss tangent in waveguide method is approximately 10^{-2} for the waveguide used in this investigation (Agilent, USA).

1.6.2 Magnetic Characterization

Magnetic measurements of the samples were studied with the aid of a Vibrating Sample Magnetometer (VSM) attached to a Physical Property Measurement System (PPMS, Quantum Design, San Diego, USA). VSM is a measurement tool that measures the magnetic moment of a material with very high accuracy based on Faraday's law of electromagnetic induction. This law states that, an emf is induced when placed in a varying magnetic field and the induced emf is equal to the rate of change of flux associated with it. On measuring this emf, one can get information about the changing magnetic field. VSM measures the magnetic moment of a sample when it is being vibrated perpendicular to a uniform magnetic field.

In a typical VSM testing, the sample is placed in a constant magnetic field. If the material is magnetic responsive, then this field will magnetize the material by aligning the magnetic domains or individual magnetic spins along the field direction. A stray magnetic field is developed around the sample due to this magnetic dipole moment. When the sample is vibrated in an up and down direction, this stray field will vary as a function of time, which is detected using a set of pickup coils. The corresponding change in magnetic field will induce an emf into the pickup coil, which is directly proportional to magnetic moment of the sample. The time dependent voltage induced in the coil is given by,

$$V_{coil} = \frac{d\Phi}{dt} = (\frac{d\Phi}{dz})(\frac{dz}{dt}) \quad (1.15)$$

where Φ is magnetic flux enclosed by the pickup coil, z is vertical position of sample with respect to coil and t is time. For sinusoidally oscillating sample, the voltage is given by the equation,

$$V_{coil} = 2\pi f C m A sin(2\pi f t) \quad (1.16)$$

where C is coupling constant, m is DC magnetic moment of sample, A is amplitude of oscillation and f is frequency of oscillation. By measuring coefficient of sinusoidal voltage response, magnetic moment can be calculated.

1.6.3 Ferroelectric Characterization

All ferroelectric materials will have its own characteristic hysteresis loop, which is known as the fingerprint of that material. Remanent polarization is the signature of ferroelectricity (FE). The easiest and most frequently used approach is the inspection of Polarization (P) -Electric field (E) hysteresis loop. In order to characterize a ferroelectric material, a sinusoidal voltage is applied across the sample made in the MIM capacitor form and the corresponding polarization as well as displacement is recorded. Leakage current is another important parameter that can deteriorate the property of a ferroelectric material. The presence of lattice defects giving rise to space charges, injection of electrons into the sample due to low work function of electrode materials etc. are some of the factors that give rise to leakage current in a material. Current across the dielectric is investigated by the application of electric field that will

give an idea about leakage current of that material. For both hysteresis loop and leakage current, the samples have to be modeled like a parallel plate capacitor.

All ferroelectric testing in the present thesis is done with the help of Ferroelectric Test & Measurement System (TF Analyser 3000) from Aixacct System GmbH, Aachen, Germany) provided with 10 KV external voltage amplifier. Here, a triangle waveform is applied to the FE capacitor in a Sawyer-Tower circuit. Then the number of charge generation is estimated across couple capacitors, and is plotted as a function of the applied polarization voltage. This testing set up is capable of electrical measurements to be performed at submicron level with high precision.

1.6.4 Magnetodielectric Measurement

The existence of magnetocapacitance is a measure of dielectric properties of a material can be tailored under magnetic field. The existence of MD property has been attributed to the coexistence of magnetic as well as insulating grains in the same material. Herein MD testing, permittivity (ε_r) is measured as a function of magnetic field (H).[114] Multiferroicity contributed by the coupling between electric and magnetic orders is a major cause of MD effect. However, there are other reasons as well. For example, Maxwell-Wagner (M-W) type relaxation process is observed in several MD systems.[115,116] In magnetocapacitive materials, the applied magnetic field will decrease the magnetic ordering and charge ordering in a material, which in turn changes the magnetocapacitance.[114,117,118] It is possible to calculate magnetocapacitance with the help of M-W equations and is defined as,

$$MC\ (\%) = \frac{\varepsilon'(H) - \varepsilon'(0)}{\varepsilon'(0)}\, x\ 100 \qquad (1.17)$$

where $\varepsilon'(H)$ and $\varepsilon'(0)$ are the permittivity values of material at magnetic field H and zero magnetic field respectively.

The magnetocapacitance (MC) measurement was performed using Wayne Kerr Impedance Analyzer (Model 6500B) which is used for dielectric measurements, together with electromagnet that can provide a maximum field upto 5 kOe at a pole gap of around 2 cm.

1.6.5 Magnetoelectric Measurement

In ME testing, the ME coupling coefficient can be conveniently estimated by measuring the voltage ME coefficient using a dynamic lock-in amplifier, since voltage is easily measurable than electric polarization. This method provides a measure of voltage generation as a result of magnetic field induced magnetostrictive strain. The induced polarization under an applied magnetic field is monitored using a Hall probe setup. The ac field is produced by using a set of Helmholtz coils and dc bias using a set of permanent magnets. Here the induced voltage is measured with the aid of lock-in amplifier in differential mode, in order to subtract the common mode induction contribution. The experiment involves the measurement of induced voltage as a function of variable amplitude of applied ac magnetic field at a fixed frequency which was produced by Helmholtz coils. According to theory, induced voltage is having a linear relationship with amplitude of ac applied field. Here, the ME coupling coefficient is given by the equation,

$$\alpha = \frac{1}{t}\left(\frac{dV}{dH_{ac}}\right) \quad (1.18)$$

where V is induced voltage, H_{ac} is amplitude of applied ac magnetic field and t is thickness of the sample.

This measurement was performed using a Magnetoelectric coefficient measurement setup by Marine India. This tracer instrument was developed for characterizing multiferroic materials. It measures voltage in presence of ac as well as dc magnetic fields. Alternating magnetic field measurements are performed at 850 Hz sinusoidal signal.

1.7 Scope of Present Thesis on Multilayer Multifunctional Research

With the progressing scaling down of wireless communication systems, there is a critical need to reduce size and volume of antenna. It is realized that the trademark dimension of an antenna is mainly controlled by transmission wavelength. In this way, for low-frequency applications, an antenna must undergo greater miniaturization in terms of its dimensions. MD materials are potential candidate for this application. Two chapters in the present thesis are dedicated for developing MD substrates that will help in satisfying the demand of miniaturization of antennas. ME materials have a coexistence of ferroelectric and ferromagnetic parameter that could be exploited in developing novel types of memory. The harmony between magnetization and polarization can allow realization of four state logic memories in a single device. Such kind of ME composites were developed in the present thesis by novel, cost-effective method.

1.8 References

(1) Lendlein, A.; Trask, R. S. Multifunctional Materials: Concepts, Function-Structure Relationships, Knowledge-Based Design, Translational Materials Research. *Multifunct. Mater.* **2018**, *1* (1), 010201.

(2) Ferreira, A. D. B. L.; Nóvoa, P. R. O.; Marques, A. T. Multifunctional Material Systems: A State-of-the-Art Review. *Compos. Struct.* **2016**, *151*, 3–35.

(3) Su, H.; Tang, X.; Zhang, H.; Jing, Y.; Bai, F. Low-Loss Magneto-Dielectric Materials: Approaches and Developments. *J. Electron. Mater.* **2014**, *43* (2), 299–307.

(4) Ji, J. K.; Ahn, W. K.; Kum, J. S.; Park, S. H.; Kim, G. H.; Seong, W. M. Miniaturized T-DMB Antenna with a Low-Loss Ni-Mn-Co Ferrite for Mobile Handset Applications. *IEEE Magn. Lett.* **2010**, *1*, 0–3.

(5) Lee, J.; Hong, Y. K.; Lee, W.; Abo, G. S.; Park, J.; Neveu, N.; Seong, W. M.; Park, S. H.; Ahn, W. K. Soft M-Type Hexaferrite for Very High Frequency Miniature Antenna Applications. *J. Appl. Phys.* **2012**, *111* (7), 109–112.

(6) Mongia, R. K.; Ittibipoon, A.; Cuhaci, M. Low Profile Dielectric Resonator Antennas Using a Very High Permittivity Material. *Electron. Lett.* **1994**, *30* (17), 1362–1363.

(7) Colburn, J. S. Patch Antennas on Externally Perforated High Dielectric Constant Substrates. *IEEE Trans. Antennas Propag.* **1999**, *47* (12), 1785–1794.

(8) Mosallaei, H.; Sarabandi, K. Magneto-Dielectrics in Electromagnetics: Concept and Applications. *IEEE Trans. Antennas Propag.* **2004**, *52* (6), 1558–1567.

(9) Teo, M. L. S.; Kong, L. B.; Li, Z. W.; Lin, G. Q.; Gan, Y. B. Development of Magneto-Dielectric Materials Based on Li-Ferrite Ceramics. I. Densification Behavior and Microstructure Development. *J. Alloys Compd.* **2008**, *459* (1–2), 557–566.

(10) Moon, K. S.; Wong, C. P.; Kim, S. H.; Choi, H. Do; Han, S.; Yoon, H. G.; Suh, K. S. Ferrite Polymer Composite for Improving the Electromagnetic Compatibility of Semiconductor Packaging. *J. Electron. Mater.* **2007**, *36* (12), 1711–1718.

(11) Kavanlooee, M.; Hashemi, B.; Maleki-Ghaleh, H.; Kavanlooee, J. Effects of Annealing on Phase Evolution, Microstructure, and Magnetic Properties of Nanocrystalline Ball-Milled LiZnTi Ferrite. *J. Electron. Mater.* **2012**, *41* (11), 3082–3086.

(12) Kong, L. B.; Li, Z. W.; Lin, G. Q.; Gan, Y. B. Magneto-Dielectric Properties of Mg-Cu-Co Ferrite Ceramics: I. Densification Behavior and Microstructure Development. *J. Am. Ceram. Soc.* **2007**, *90* (10), 3106–3112.

(13) Rahmat-Samii, Y. Electromagnetic Band-Gap Structures: Classification, Characterization, and Applications. *11th lntemational Conf. Antennas Propag.*

2005, 480, 560–564.

(14) Ho, K. M.; Chan, C. T.; Soukoulis, C. M.; Biswas, R.; Sigalas, M. Photonic Band Gaps in Three Dimensions: New Layer-by-Layer Periodic Structures. *Solid State Commun.* **1994**, *89* (5), 413–416.

(15) Zhai, K.; Shang, D. S.; Chai, Y. S.; Li, G.; Cai, J. W.; Shen, B. G.; Sun, Y. Room-Temperature Nonvolatile Memory Based on a Single-Phase Multiferroic Hexaferrite. *Adv. Funct. Mater.* **2018**, *28* (9), 1–5.

(16) Hu, J. M.; Li, Z.; Chen, L. Q.; Nan, C. W. Design of a Voltage-Controlled Magnetic Random Access Memory Based on Anisotropic Magnetoresistance in a Single Magnetic Layer. *Adv. Mater.* **2012**, *24* (21), 2869–2873.

(17) Roy, A.; Gupta, R.; Garg, A. Multiferroic Memories. *Adv. Condens. Matter Phys.* **2012**, *2012*, 1–12.

(18) Shen, J.; Cong, J.; Shang, D.; Chai, Y.; Shen, S.; Zhai, K.; Sun, Y. A Multilevel Nonvolatile Magnetoelectric Memory. *Sci. Rep.* **2016**, *6*, 1–6.

(19) Bibes, M.; Barthélémy, A. Towards a Magnetoelectric Memory. *Nat. Mater.* **2008**, *7* (6), 425–426.

(20) Hambe, M.; Petraru, A.; Pertsev, N. A.; Munroe, P.; Nagarajan, V.; Kohlstedt, H. Crossing an Interface: Ferroelectric Control of Tunnel Currents in Magnetic Complex Oxide Heterostructures. *Adv. Funct. Mater.* **2010**, *20* (15), 2436–2441.

(21) Hu, J. M.; Li, Z.; Wang, J.; Nan, C. W. Electric-Field Control of Strain-Mediated Magnetoelectric Random Access Memory. *J. Appl. Phys.* **2010**, *107* (9), 093912.

(22) Shi, Z.; Wang, C.; Liu, X.; Nan, C. A Four-State Memory Cell Based on Magnetoelectric Composite. *Chinese Sci. Bull.* **2008**, *53* (14), 2135–2138.

(23) Scott, J. F. Data Storage: Multiferroic Memories. *Nat. Mater.* **2007**, *6* (4), 256–257.

(24) Jayachandran, K. P.; Guedes, J. M.; Rodrigues, H. C. Solutions for Maximum Coupling in Multiferroic Magnetoelectric Composites by Material Design. *Sci. Rep.* **2018**, *8* (1), 1–9.

(25) Palneedi, H.; Annapureddy, V.; Priya, S.; Ryu, J. Status and Perspectives of Multiferroic Magnetoelectric Composite Materials and Applications. *Actuators* **2016**, *5* (1), 9.

(26) Martin, L. W.; Crane, S. P.; Chu, Y. H.; Holcomb, M. B.; Gajek, M.; Huijben, M.; Yang, C. H.; Balke, N.; Ramesh, R. Multiferroics and Magnetoelectrics: Thin Films and Nanostructures. *J. Phys. Condens. Matter* **2008**, *20* (43), 434220.

(27) Vaz, C. A. F.; Hoffman, J.; Ahn, C. H.; Ramesh, R. Magnetoelectric Coupling Effects in Multiferroic Complex Oxide Composite Structures. *Adv. Mater.* **2010**, *22* (26–27), 2900–2918.

(28) Rado, G. T. Statistical Theory of Magnetoelectric Effects in Antiferromagnetics. *Phys. Rev.* **1962**, *128* (6), 2546–2556.

(29) Rado, G. T.; Folen, V. J. Magnetoelectric Effects in Antiferromagnetics. *J. Appl. Phys.* **1962**, *33* (3), 1126–1132.

(30) Smolenskii, G. A.; Chupis, I. E. Ferroelectromagnets. *Soviet Physics Uspekhi* **2011**, *137* (7), 415.

(31) Landau, L. D.; Lifshitz, E. . *Electrodynamics of Continuous Media*, Vol. 8.; Pergamon Press, **1960**.

(32) Rondinelli, J. M.; Stengel, M.; Spaldin, N. A. Carrier-Mediated Magnetoelectricity in Complex Oxide Heterostructures. *Nat. Nanotechnol.* **2008**, *3* (1), 46–50.

(33) Martins, P.; Kolen'Ko, Y. V.; Rivas, J.; Lanceros-Mendez, S. Tailored Magnetic and Magnetoelectric Responses of Polymer-Based Composites. *ACS Appl. Mater. Interfaces* **2015**, *7* (27), 15017–15022.

(34) Henrichs, L. F.; Cespedes, O.; Bennett, J.; Landers, J.; Salamon, S.; Heuser, C.; Hansen, T.; Helbig, T.; Gutfleisch, O.; Lupascu, D. C.; et al. Multiferroics: Multiferroic Clusters: A New Perspective for Relaxor-Type Room-Temperature Multiferroics. *Adv. Funct. Mater.* **2016**, *26* (13), 2110–2110.

(35) Kulkarni, A.; Meurisch, K.; Teliban, I.; Jahns, R.; Strunskus, T.; Piorra, A.; Knöchel, R.; Faupel, F. Giant Magnetoelectric Effect at Low Frequencies in Polymer-Based Thin Film Composites. *Appl. Phys. Lett.* **2014**, *104* (2), 022904.

(36) Zhang, J.; Li, P.; Wen, Y.; He, W.; Yang, A.; Lu, C. Giant Self-Biased Magnetoelectric Response with Obvious Hysteresis in Layered Homogeneous Composites of Negative Magnetostrictive Material Samfenol and Piezoelectric Ceramics. *Appl. Phys. Lett.* **2013**, *103* (20), 202902.

(37) Kulawik, J.; Szwagierczak, D.; Guzdek, P. Magnetic, Magnetoelectric and Dielectric Behavior of $CoFe_2O_4$-$Pb(Fe_{1/2}Nb_{1/2})O_3$ Particulate and Layered Composites. *J. Magn. Magn. Mater.* **2012**, *324* (19), 3052–3057.

(38) Srinivasan, G.; Rasmussen, E. T.; Hayes, R. Magnetoelectric Effects in Ferrite-Lead Zirconate Titanate Layered Composites: The Influence of Zinc Substitution in Ferrites. *Phys. Rev. B - Condens. Matter Mater. Phys.* **2003**, *67* (1), 1–10.

(39) Srinivasan, G.; Rasmussen, E. T.; Gallegos, J.; Srinivasan, R.; Bokhan, Y. I.; Laletin, V. M. Magnetoelectric Bilayer and Multilayer Structures of Magnetostrictive and Piezoelectric Oxides. *Phys. Rev. B - Condens. Matter Mater. Phys.* **2001**, *64* (21), 1–6.

(40) Laletin, V. M.; Paddubnaya, N.; Srinivasan, G.; De Vreugd, C. P.; Bichurin, M. I.; Petrov, V. M.; Filippov, D. A. Frequency and Field Dependence of Magnetoelectric Interactions in Layered Ferromagnetic Transition Metal-Piezoelectric Lead

Zirconate Titanate. *Appl. Phys. Lett.* **2005**, *87* (22), 1–3.

(41) Nan, C. W.; Bichurin, M. I.; Dong, S.; Viehland, D.; Srinivasan, G. Multiferroic Magnetoelectric Composites: Historical Perspective, Status, and Future Directions. *J. Appl. Phys.* **2008**, *103* (3), 031101.

(42) Fiebig, M. Revival of the Magnetoelectric Effect. *J. Phys. D. Appl. Phys.* **2005**, *38* (8), R123–R152.

(43) Folen, V. J.; Rado, G. T.; Stalder, E. W. Anisotropy of the Magnetoelectric Effect in Cr_2O_3. *Phys. Rev. Lett.* **1961**, *6* (11), 607–608.

(44) Wang, Y.; Li, J.; Viehland, D. Magnetoelectrics for Magnetic Sensor Applications: Status, Challenges and Perspectives. *Mater. Today* **2014**, *17* (6), 269–275.

(45) Schmid, H. Multi-Ferroic Magnetoelectrics. *Ferroelectrics* **1994**, *162* (1), 317–338.

(46) Dong, S.; Zhai, J.; Bai, F.; Li, J. F.; Viehland, D. Push-Pull Mode Magnetostrictive/Piezoelectric Laminate Composite with an Enhanced Magnetoelectric Voltage Coefficient. *Appl. Phys. Lett.* **2005**, *87* (6), 3–5.

(47) Das, J.; Gao, J.; Xing, Z.; Li, J. F.; Viehland, D. Enhancement in the Field Sensitivity of Magnetoelectric Laminate Heterostructures. *Appl. Phys. Lett.* **2009**, *95* (9), 10–13.

(48) Gao, J.; Das, J.; Xing, Z.; Li, J.; Viehland, D. Comparison of Noise Floor and Sensitivity for Different Magnetoelectric Laminates. *J. Appl. Phys.* **2010**, *108* (8), 084509

(49) Gao, J.; Gray, D.; Shen, Y.; Li, J.; Viehland, D. Enhanced Dc Magnetic Field Sensitivity by Improved Flux Concentration in Magnetoelectric Laminates. *Appl. Phys. Lett.* **2011**, *99* (15), 2–5.

(50) Li, M.; Wang, Z.; Wang, Y.; Li, J.; Viehland, D. Giant Magnetoelectric Effect in Self-Biased Laminates under Zero Magnetic Field. *Appl. Phys. Lett.* **2013**, *102* (8), 8–11.

(51) Patil, D. R.; Zhou, Y.; Kang, J. E.; Sharpes, N.; Jeong, D. Y.; Kim, Y. Do; Kim, K. H.; Priya, S.; Ryu, J. Anisotropic Self-Biased Dual-Phase Low Frequency Magneto-Mechano-Electric Energy Harvesters with Giant Power Densities. *APL Mater.* **2014**, *2* (4), 046102.

(52) Ryu, J.; Kang, J. E.; Zhou, Y.; Choi, S. Y.; Yoon, W. H.; Park, D. S.; Choi, J. J.; Hahn, B. D.; Ahn, C. W.; Kim, J. W.; et al. Ubiquitous Magneto-Mechano-Electric Generator. *Energy Environ. Sci.* **2015**, *8* (8), 2402–2408.

(53) Zhou, Y.; Apo, D. J.; Priya, S. Dual-Phase Self-Biased Magnetoelectric Energy Harvester. *Appl. Phys. Lett.* **2013**, *103* (19), 192909.

(54) Liu, G.; Ci, P.; Dong, S. Energy Harvesting from Ambient Low-Frequency Magnetic Field Using Magneto-Mechano-Electric Composite Cantilever. *Appl. Phys. Lett.*

2014, *104* (3), 032908.

(55) Lasheras, A.; Gutiérrez, J.; Reis, S.; Sousa, D.; Silva, M.; Martins, P.; Lanceros-Mendez, S.; Barandiarán, J. M.; Shishkin, D. A.; Potapov, A. P. Energy Harvesting Device Based on a Metallic Glass/PVDF Magnetoelectric Laminated Composite. *Smart Mater. Struct.* **2015**, *24* (6), 065024.

(56) Paluszek, M.; Avirovik, D.; Zhou, Y.; Kundu, S.; Chopra, A.; Montague, R.; Priya, S. *Magnetoelectric Composites for Medical Application*; Woodhead Publishing: Cambridge, UK, **2015**.

(57) Guduru, R.; Liang, P.; Runowicz, C.; Nair, M.; Atluri, V.; Khizroev, S. Magneto-Electric Nanoparticles to Enable Field-Controlled High-Specificity Drug Delivery to Eradicate Ovarian Cancer Cells. *Sci. Rep.* **2013**, *3*, 1–8.

(58) Yue, K.; Guduru, R.; Hong, J.; Liang, P.; Nair, M.; Khizroev, S. Magneto-Electric Nano-Particles for Non-Invasive Brain Stimulation. *PLoS One* **2012**, *7* (9), 1–5.

(59) Vopson, M. M. Fundamentals of Multiferroic Materials and Their Possible Applications. *Crit. Rev. Solid State Mater. Sci.* **2015**, *40* (4), 223–250.

(60) Liu, M.; Lou, J.; Li, S.; Sun, N. X. E-Field Control of Exchange Bias and Deterministic Magnetization Switching in AFM/FM/FE Multiferroic Heterostructures. *Adv. Funct. Mater.* **2011**, *21* (13), 2593–2598.

(61) Sebastian, M. T.; Ubic, R and Jantunen, H. *Microwave Materials and Applications*; M T Sebastian, R. U. and H. J., Ed.; John Wiley & Sons: Chichester, UK, **2017**.

(62) Imanaka, Y. *Multilayered Low Temperature Cofired Ceramics Technology*; Springer: US, Boston, **2005**.

(63) Barlow, F. D.; Elshabini, A. *Ceramic Interconnect Technology Handbook*; CRC Press, Inc.: Boca Raton, FL, USA, **2007**.

(64) Sano, H.; Itoh, H.; Tate, H.; Fukuchi, K. Key Materials and Components for Mobile Information Devices for Supporting Highly Information-Oriented Society. *Hitachi Rev.* **2006**, *55* (1), 26–31.

(65) Roshni, S. B.; Sebastian, M. T.; Surendran, K. P. Can Zinc Aluminate-Titania Composite Be an Alternative for Alumina as Microelectronic Substrate. *Sci. Rep.* **2017**, *7*, 1–13.

(66) Sebastian, M. T.; Jantunen, H. Low Loss Dielectric Materials for LTCC Applications: A Review. *Int. Mater. Rev.* **2008**, *53* (2), 57–90.

(67) Sprague, J. L. Multilayer Ceramic Packaging Alternatives. *IEEE Trans. Components, Hybrids, Manuf. Technol.* **1990**, *13* (2), 390–396.

(68) Prudenziati, M.; Hormadaly, J. *Printed Films: Materials Science and Applications in Sensors, Electronics and Photonics*; Woodhead Publishing Limited: UK, 2012.

(69) Golonka, L. J. Technology and Applications of Low Temperature Cofired Ceramic (LTCC) Based Sensors and Microsystems. *Bull. Polish Acad. Sci. Tech. Sci.* **2006**, *54* (2), 221–231.

(70) Abhilash, P.; Roshni, S. B.; Mohanan, P.; Surendran, K. P. A Facile Development of Homemade Substrate Using 'Quench Free' Glass-Ceramic Composite and Printing Microstrip Patch Antenna on It. *Mater. Des.* **2018**, *137*, 38–46.

(71) Lekshmi, D. R.; Kuzhichalil Peethambharan, S. Ultra-Low Dielectric Loss $BiSmMoO_6$ Flexible Tapes for Hybrid Integrated Circuits. *J. Eur. Ceram. Soc.* **2019**, *39* (5), 1819–1826.

(72) Induja, I. J.; Abhilash, P.; Arun, S.; Surendran, K. P.; Sebastian, M. T. LTCC Tapes Based on Al_2O_3-BBSZ Glass with Improved Thermal Conductivity. *Ceram. Int.* **2015**, *41* (10), 13572–13581.

(73) Son., Y. B.; Kim., C. H.; Jang., S. D.; Liu., J.; Sarikaya., M.; Aksay, I. A. Crystallization Behavior of Cordierite-Based Glass with Excess SiO_2 and Al_2O_3 at Initial Stage.

(74) TUMMALA, R. R. ChemInform Abstract: Ceramic and Glass-Ceramic Packaging in the 1990s. *ChemInform* **2010**, *22* (32), 895–908.

(75) Zhou, Z.; Su, H.; Tang, X.; Zhang, H.; Xu, F.; Zhang, S.; Jing, Y. Microwave Dielectric Properties of LBBS Glass Added $(Zn_{0.95}Co_{0.05})_2SiO_4$ for LTCC Technology. *Ceram. Int.* **2016**, *42* (9), 11161–11164.

(76) Dernovsek, O.; Naeini, A.; Preu, G.; Wersing, W.; Eberstein, M.; Schiller, W. A. LTCC Glass-Ceramic Composites for Microwave Application. *J. Eur. Ceram. Soc.* **2001**, *21* (10–11), 1693–1697.

(77) Gangwar, R. K.; Singh, S. P.; Choudhary, M.; Kumar, D.; Lakshmi Narayana Rao, G.; James Raju, K. C. Experimental Study on LTCC Glass-Ceramic Based Dual Segment Cylindrical Dielectric Resonator Antenna. *J. Ceram.* **2013**, *2013*, 1–8.

(78) Induja, I. J.; Varma, M. R.; Sebastian, M. T. Preparation, Characterization and Properties of Alumina-Lithium Aluminium Borosilicate Glass Based LTCC Tapes. *J. Mater. Sci. Mater. Electron.* **2017**, *28* (19), 14655–14663.

(79) Park, Z. H.; Yeo, D. H.; Shin, H. S. Effect of Ca-Al-Si-O Common Glass on Dielectric Properties of Low-Temperature Co-Fired Ceramic Materials with Different Fillers. *Biotechnol. Biotechnol. Equip.* **2014**, *28* (1), S1–S5.

(80) Wu, J.; Li, Z.; He, H.; Huang, Y.; Wu, H. Preparation of Forsterite-Based Glass Ceramics for LTCC from Potassium Feldspar. *J. Mater. Sci. Mater. Electron.* **2013**, *24* (7), 2271–2276.

(81) Yu, H.; Ju, K.; Wang, K. A Novel Glass-Ceramic with Ultra-Low Sintering Temperature for LTCC Application. *J. Am. Ceram. Soc.* **2014**, *97* (3), 704–707.

(82) Zhou, J. Towards Rational Design of Low-Temperature Co-Fired Ceramic (LTCC) Materials. *J. Adv. Ceram.* **2012**, *1* (2), 89–99.

(83) Jantunen, H. A Novel Low Temperature Co-Firing Ceramic (LTCC) Material for Telecommunication Devices, **2001**.

(84) Dhanesh, T. Phosphate Based Dielectric Ceramics and Composites for Microwave Applications, The University of Kerala, **2012**.

(85) Albano, M. P.; Garrido, L. B. Influence of the Slip Composition on the Properties of Tape-Cast Alumina Substrates. *Ceram. Int.* **2005**, *31* (1), 57–66.

(86) Vasanthakumari, K. G.; Natarajan, R. Dispersion and Rheological Behaviour of SiC Tape Casting Slurry. *Adv. Appl. Ceram.* **2005**, *104* (2), 73–78.

(87) Golonka, L.; Bembnowicz, P.; Malecha, K. Low Temperature Co-Fired Ceramics (LTCC) Microsystems. *Opt. Appl.* **2011**, No. May 2014.

(88) Kulke, R.; Rittweger, M.; Uhlig, P.; Gunner, C. LTCC-Multilayer Ceramic for Wireless and Sensor Applications. *Plus* **2001**, *12*, 2131–2136.

(89) Ullah, U.; Ain, M. F.; Mahyuddin, N. M.; Othman, M.; Arifin Ahmad, Z.; Abdullah, M. Z.; Marzuki, A. Antenna in LTCC Technologies: A Review and the Current State of the Art. *IEEE Antennas Propag. Mag.* **2015**, *57* (2), 241–260.

(90) Sebastian, M. T.; Ubic, R.; Jantunen, H. Low-Loss Dielectric Ceramic Materials and Their Properties. *Int. Mater. Rev.* **2015**, *60* (7), 392–412.

(91) Matjaz Valant; Suvorov, D. Processing and Dielectric Properties of Sillenite Compounds $Bi_{12}MO_{20-\delta}$.Pdf. *J. Am. Ceram. Soc.* **2001**, *84* (12), 2900–2904.

(92) Zhai, X. L.; Zheng, X.; Xi, H. H.; Li, W. B.; Han, J.; Zhou, D. Microwave Dielectric Properties of $LiKSm_2(MoO_4)_4$ Ceramics with Ultralow Sintering Temperatures. *J. Am. Ceram. Soc.* **2015**, *98* (9), 2716–2719.

(93) Zhang, G. Q.; Guo, J.; He, L.; Zhou, D.; Wang, H.; Koruza, J.; Kosec, M. Preparation and Microwave Dielectric Properties of Ultra-Low Temperature Sintering Ceramics in K_2O-MoO_3 Binary System. *J. Am. Ceram. Soc.* **2014**, *97* (1), 241–245.

(94) Dhanya, J.; Basiluddeen, A. V.; Ratheesh, R. Synthesis of Ultra Low Temperature Sinterable $Na_2Zn_5(MoO_4)_6$ Ceramics and the Effect of Microstructure on Microwave Dielectric Properties. *Scr. Mater.* **2017**, *132*, 1–4.

(95) Zhang, G. Q.; Wang, H.; Guo, J.; He, L.; Wei, D. D.; Yuan, Q. Bin. Ultra-Low Sintering Temperature Microwave Dielectric Ceramics Based on Na_2O-MoO_3 Binary System. *J. Am. Ceram. Soc.* **2014**, *98* (2), 528–533.

(96) Zhou, D.; Li, W. B.; Guo, J.; Pang, L. X.; Qi, Z. M.; Shao, T.; Xie, H. D.; Yue, Z. X.; Yao, X. Structure, Phase Evolution, and Microwave Dielectric Properties of $(Ag_{0.5}Bi_{0.5})(Mo_{0.5}W_{0.5})O_4$ Ceramic with Ultralow Sintering Temperature. *Inorg.*

Chem. **2014**, *53* (11), 5712–5716.

(97) Zhou, D.; Li, W.-B.; Pang, L.-X.; Guo, J.; Qi, Z.-M.; Shao, T.; Yue, Z.-X.; Yao, X. Sintering Behavior and Dielectric Properties of Ultra-Low Temperature Fired Silver Molybdate Ceramics. *J. Am. Ceram. Soc.* **2014**, *97* (11), 3597–3601.

(98) Zhou, D.; Pang, L. X.; Xie, H. D.; Guo, J.; He, B.; Qi, Z. M.; Shao, T.; Yao, X.; Randall, C. A. Crystal Structure and Microwave Dielectric Properties of an Ultralow-Temperature-Fired $(AgBi)_{0.5}WO_4$ Ceramic. *Eur. J. Inorg. Chem.* **2014**, No. 2, 296–301.

(99) Batra, A. K.; Aggarwal, M. D.; Edwards, M. E.; Bhalla, A. Present Status of Polymer: Ceramic Composites for Pyroelectric Infrared Detectors. *Ferroelectrics* **2008**, *366* (1), 84–121.

(100) Taya, M. *Electronic Composites Modeling, Characterization, Processing, and MEMS Applications*; Cambridge University Press, UK, 2005.

(101) McLachlan, D. S.; Blaszkiewicz, M.; Newnham, R. E. Electrical Resistivity of Composites. *J. Am. Ceram. Soc.* **1990**, *73* (8), 2187–2203.

(102) Newnham, R. E., Skinner, D. P., Cross, L. E. Connectivity and Piezoelectric Pyroelectric Composites. *Mater. Res. Bull* **1978**, *13* (5), 525–536.

(103) Sebastian, M. T.; Jantunen, H. Polymer-Ceramic Composites of 0-3 Connectivity for Circuits in Electronics: A Review. *Int. J. Appl. Ceram. Technol.* **2010**, *7* (4), 415–434.

(104) Tressler, J. F.; Alkoy, S.; Dogan, A.; Newnham, R. E. Functional Composites for Sensors, Actuators and Transducers. *Compos. Part A Appl. Sci. Manuf.* **1999**, *30* (4), 477–482.

(105) Dias, C. J.; Das Gupta, D. K. Inorganic Ceramic / Polymer Ferroelectric Composite Electrets. *IEEE Trans. Dielectr. Electr. Insul.* **1996**, *3* (5), 706–734.

(106) Varghese, J.; Sebastian, M. *Microwave Materials and Applications 2V Set*; Sebastian, M., Ubic, R., Jantunen, H., Eds.; John Wiley & Sons, Ltd, 2017.

(107) International, T. S. *MICR Basics Handbook*; United States of America, 2000.

(108) W, H. B.; Coleman P. D. A Dielectric Resonator Method of Measuring the Inductive Capacitance in the Millimeter Range. *IRE Trans. Microw. Theory Tech* **1960**, *8*, 402–410.

(109) Kobayashi, Y.; Tanaka, S. Resonant Modes of a Dielectric Rod Resonator Short-Circuited at Both Ends by Parallel Conducting Plate. *IEEE Trans. Microw. Theory Tech* **1980**, *28*, 1077–1085.

(110) Courtney, E. W. Analysis and Evalluation of a Method of Measuring the Complex Permittivityand Permeability of Microwave Insulators. *IEEE Trans. Microw.*

Theory Tech. **1970**, *18*, 476–485.

(111) Krupka, J.; Gregory, A. P.; Rochard, O. C.; Clarke, R. N.; Riddle, B.; Baker-Jarvis, J. Uncertainty of Complex Permittivity Measurements by Split-Post Dielectric Resonator Technique. *J. Eur. Ceram. Soc.* **2001**, *21* (15), 2673–2676.

(112) Chen, L. F.; Ong, C. K.; Neo, C. P.; Varadan, V. V; K, V. V. *Microwave Electronics: Measurement and Materials Characterization*; John Wiley & Sons: England, 2004.

(113) Tereshchenko, O. V.; Buesink, F. J. K.; Leferink, F. B. J. An Overview of the Techniques for Measuring the Dielectric Properties of Materials., *30th URSI Gen. Assem. Sci. Symp. URSIGASS 2011* **2011**, 1–4.

(114) Catalan, G. Magnetocapacitance without Magnetoelectric Coupling. *Appl. Phys. Lett.* **2006**, *88* (10), 102902 (1-3).

(115) Sebald, J.; Krohns, S.; Lunkenheimer, P.; Ebbinghaus, S. G.; Riegg, S.; Reller, A.; Loidl, A. Colossal Dielectric Constants: A Common Phenomenon in $CaCu_3Ti_4O_{12}$ Related Materials. *Solid State Commun.* **2010**, *150* (17–18), 857–860.

(116) Arumugam, S.; Sivaprakash, P.; Dixit, A.; Chaurasiya, R.; Govindaraj, L.; Sathiskumar, M.; Chatterjee, S.; Suryanarayanan, R. Complex Magnetic Structure and Magnetocapacitance Response in a Non-Oxide NiF_2 System. *Sci. Rep.* **2019**, *9* (1), 1–8.

(117) Mamin, R. F.; Egami, T.; Marton, Z.; Migachev, S. A. Giant Dielectric Permittivity and Colossal Magnetocapacitance Effect in Complex Manganites with High Conductivity. *Ferroelectrics* **2007**, *348* (October 2014), 7–12.

(118) Mamin, R. F.; Kabanov, V. V. Giant Dielectric Permittivity and Magneto-Capacitance Effects in Low Doped Manganites. *New J. Phys.* **2014**, *16*, 073011..

Chapter 2

NOVEL MAGNETODIELECTRIC STRUCTURES USING $BiFeO_3$ SCREEN PRINTED ON $BiSmMoO_6$ TAPES INSPIRED BY LTCC TECHNOLOGY

2.1 Abstract

Thus far, magnetodielectric (MD) structures have never been realized on Low Temperature Cofired Ceramic (LTCC) tapes. In this chapter, an all ceramic MD substrate was developed for miniaturized printed antenna applications. For this, LTCC tapes based on $BiSmMoO_6$ (added with 2 wt.% BBSZ glass) were developed. The tape sintered at 875 ˚C, possesses an ultra-low dielectric loss of the order of $9x10^{-4}$ when measured at 5 GHz. Meanwhile, room temperature curable ink based on the well-known multiferroic, $BiFeO_3$ (BFO) was developed. The ferroelectric, ferromagnetic and dielectric properties of the developed ink in the bulk and printed form were discussed. A MD composite was developed by screen printing BFO ink on top of developed LTCC tape. The variation of capacitance in presence of magnetic field was studied at different frequencies. An impressive negative magnetocapacitance variation upto 15% was observed under 3 kOe magnetic field at 1MHz, which can be posed as an ideal substrate for ceramic patch antenna miniaturization.

2.2 Introduction

All across the globe, hand held mobile devices have become ubiquitous, with India holding over 80 crore mobile phone users in 2019 and counting. In portable wireless mobile communication, people are always looking for thinner and lighter devices with multifunctionality. This in turn, prompts engineers to look for ideas that could help in achieving integration of several components into a single device, at reduced size. Antennas are the critical components in every modern mobile communication gadgets and different antennas are used in different applications like Global System for Mobile Communications (GSM), 3G, 4G ,WiFi, Bluetooth, Global

Positioning System (GPS) etc.[1] The microstrip antennas are ideal choice in miniaturized devices since they can be realized on the same printed circuit board (PCB) where other electronic components are integrated, thereby optimizing the available compact space.

Attaining reduced size without compromising antenna's performance is a tedious task, since antenna parameters like radiation efficiency, band width and gain have direct dependence with antenna size.[2] Using a high permittivity material will result in poor antenna performance like narrow bandwidth and low efficiency, which can be compensated only by increasing the antenna size.[3] So the best known strategy for achieving miniaturization is possible by loading a high refractive index (n=$\sqrt{\varepsilon_r \mu_r}$) material in the antenna design.[4] The MD materials are widely used in electromagnetic band gap designs, where they can provide high band rejection levels, besides miniaturization. In patch antennas, the central idea is that a MD material having permittivity (ε_r) and permeability (μ_r) greater than unity, provide less capacitive coupling, and avoid the imminent field confinement around the substrate. Moreover, they can provide better impedance matching since the characteristic impedance $\eta = \eta_o \sqrt{\varepsilon_r / \mu_r}$ of the substrate is close to that of the surrounding medium.[5,6] In all microwave communication applications, the impedance mismatch is an undesirable but critical parameter which exacerbates when difference between ε_r and μ_r is more where the loss increases due to higher reflection loss. This problem is solved best with MDs.

In simplest terms, an ideal MD material upon the application of a magnetic field shows variation in the dielectric properties. In fact, intrinsic MD materials are not readily available in nature and have to be realized through engineered material

synthesis. In general, composites are being largely explored as MD materials. Several composite strategies such as (0-3), (1-3), (2-2) etc. are available for developing such heterostructures.

In laminate (2-2) MD composites, there are loads of literature reports available, where a magnetic layer is in intimate contact with a dielectric layer.[7-10] Usually, these layers are developed using tape casting technique which invariably involves a high temperature treatment. In the present research, the concept of 'hybrid microcircuits' is introduced to develop MD structures. An emerging protocol under hybrid microcircuits is the LTCC hybrid circuit technology that enables passive components to be embedded within the layers of multilayer ceramic substrates, and cofiring them below 900 ˚C. Inspired by this concept, we have chosen a pre-fired, low loss dielectric layer as an LTCC substrate, on top of which a magnetic layer was coated using screen printing. Usual post printing heating of the MD composite may eventually lead to delamination, owing to the difference in thermal expansion of layers and all. Since the magnetic layer is a ceramic ink, it need not have to be heated at all, after printing. This method of printing the ferromagnetic component over dielectric is advantageous than multilayer tape lamination pressing of LTCC heterostructures, due to its simplicity and versatility to make any desired shaped MD structures. Also in the present case, the magnetic layer will be a few microns thick which will further reduce overall thickness of the module.

In this chapter, the dielectric layer chosen is $BiSmMoO_6$ based LTCC composition. In 2009, Zhou et al. reported the microwave dielectric properties of Bi_2MoO_6, sinterable at 750 ˚C. The ceramic has got a relative permittivity value of ~31 with a $Q_u$xf value of ~16,700.[11] With the intention to develop for LTCC applications, we have attempted the

substitution of samarium (Sm) in one of its Bi-site, to form $BiSmMoO_6$ (abbreviated as BSMO). In 2017, Li et al. reported the microwave dielectric properties of $BiSmMoO_6$ sintered at 1000 ˚C.[12] Here in our case, though the properties got improved compared to the parent compound, which is detailed in the discussion section, the sintering temperature was 975 ˚C. For the purpose of LTCC applications that demands sintering temperature less than 900 ˚C, we have qualified a glass additive, $40Bi_2O_3$: $49B_2O_3$: $6SiO_2$: 5ZnO (abbreviated as BBSZ). This glass system had a proven record of promoting liquid phase sintering in a lot of low firing low loss systems investigated in recent times.[13-16] With an addition of 2 wt.% of BBSZ glass, we found that the sintering temperature of BSMO was reduced to 875 ˚C. So, in the first part of this chapter, we outline the development of the LTCC tape based on BSMO-BBSZ, its structural, microstructural, thermal, mechanical and dielectric properties, as a hybrid microcircuit component suitable for MD circuits.

The magnetic part chosen in the present investigation is the well-known multiferroic material, $BiFeO_3$ (BFO) which is described in the subsequent section. Here, the chosen material stands out as a unique choice since it simultaneously possesses ferroelectricity and magnetism at room temperature. It has got a ferroelectric Curie temperature of 1103 K and has a G-type antiferromagnetic Neel transition at 647 K.[17] These properties permit the usage of BFO for various applications at room temperature. It is very difficult to synthesis single phase BFO through solid state reactions and hence chemical methods are been widely employed.[18-20] In the present study, a sol-gel technique was used for synthesizing phase pure BFO which was then further developed

in ink form to make a MD (2-2) layered composite. Our efforts to develop a MD composite inspired LTCC concept is described in the following section.

2.3 Experimental Section

2.3.1 Materials

Bismuth oxide (Bi_2O_3, 99.9%, Sigma Aldrich), Samarium oxide(Sm_2O_3, 99%, Indian Rare Earth), Molybdenum trioxide (MoO_3, 99+%, Sigma Aldrich), Boron trioxide (B_2O_3, 99%, Sigma Aldrich), Silicon dioxide (SiO_2, 99.6%, Sigma Aldrich), (Zinc oxide (ZnO, 99.9%, Sigma Aldrich), Bismuth nitrate (($Bi(NO_3)_3.5H_2O$, Merck), Iron nitrate (($Fe(NO_3)_3.9H_2O$), Sigma Aldrich), Xylene (Sigma–Aldrich), Ethanol (Merck), Fish oil (Arjuna Natural Extracts, Kerala, India), Ethylene glycol (Merck), Triton X-100 (TCI, Tokyo, Japan), Ethyl cellulose (Sigma Aldrich), Polyvinyl butyral (PVB, Butvar B-98, Sigma Aldrich), Butyl benzyl phthalate (SigmaAldrich), Polyethylene glycol (SigmaAldrich), Cyclohexanone (Sigma Aldrich).

2.3.2 Sample Preparation

2.3.2.1 BSMO-BBSZ Ceramic

$BiSmMoO_6$ ceramic was prepared using conventional solid state ceramic route. Stoichiometric amount of powders was weighed and ball milled together in water medium using yittria stabilized zirconia balls for 24 h. The slurry thus obtained was dried in a hot air oven at 100 ˚C. The resultant powder was then kept for calcination at 900 ˚C for 4 h. The properties of BSMO ceramics were tested after they were formed into cylindrical pellets at 150 MPa (Carver Inc., USA) and sintered at 975 ˚C for 2 h.

For the preparation of BBSZ glass, stoichiometric amount of reagents were weighed and mixed. The resultant powder was splash quenched at 750 ˚C and then made into fine powder using a high energy planetary ball mill (Fritsch Pulverisette 5, Germany). The finely ground BSMO ceramic was then added with 2 wt.% of BBSZ glass and ball milled in water medium for 24 h in order to get a homogeneous mixture of ceramic-glass.

2.3.2.2 BSMO-BBSZ Tape

The tape casting process for BSMO-BBSZ was carried out using an organic solvent based technique. A mixture of xylene and ethanol in the ratio 50:50 was used as solvent for the procedure. In order to optimize the dispersant amount, ceramic slurry was prepared with varying amounts of dispersant. In this case, fish oil was chosen as dispersant and the amount was varied from 0.5–2.0 wt.% with respect to powder. The powder loading was fixed at a constant value of 69.96 wt.% for the dispersant optimization.

2.3.2.3 BFO Ink

Stoichiometric amount of precursor salts were weighed out and mixed in about 12 ml acetic acid, in separate beakers respectively at 80 ˚C for 1 h under constant stirring. After mixing, Bi and Fe solutions were allowed to mix together for a couple of hours at the same temperature. About 15 ml ethylene glycol was then added and mixed at 120 ˚C. The sample was then allowed to dry at an elevated temperature until all the solvents evaporate completely.

For ink formulation Triton X 100 was mixed in an ultrasonicator for 30 min after which the filler particles, BFO was added. This was kept for mixing in a magnetic stirrer under vigorous stirring. After 4 h of stirring, binder was added to the mixture and was kept continued stirring for another 24 h at room temperature. The obtained ink was used for making MD sample.

2.3.2.4 BSMO-BBSZ-BFO Magnetodielectric Structures

MD composite was made by screen printing BFO ink, using a semiautomatic screen printer (XPRT 2, Ekra GmbH, Germany) over developed BSMO based LTCC tape sintered at 875 ˚C for 2 h.

2.3.3 Characterization

2.3.3.1 BSMO and its LTCC Composition

The phase purity of as prepared BSMO and BSMO-BBSZ ceramics were characterized by Bruker D8 Advance diffractometer using CuKα radiation (Karlsruhe, Germany). The coefficient of thermal expansion (CTE) of BSMO and BSMO-BBSZ was analyzed using a thermo mechanical analyzer (TMA SS7300, SII Nano Technology Inc, Northridge, CA, USA). The thermal conductivity (TC) of sintered samples of BSMO and BSMO-BBSZ was directly measured by a xenon flash technique using a laser flash thermal properties analyzer (FlashLine2000, Anter Corporation, Pittsburgh, USA). The bulk density of sintered samples was measured using Archimedes method. A scanning electron microscope (JEOL JSM 5600LV, Tokyo, Japan) was used to study microstructural morphology of the green and sintered tape samples. The microwave dielectric properties were measured using a vector network analyzer (Model No.

E5071C ENA series; Agilent Technologies, Santa Clara, CA). The relative permittivity (ε_r) of the sintered BSMO samples was measured by the Hakki–Coleman method modified by Courtney.[21] The unloaded quality factor and temperature coefficient of resonant frequency (τ_f) were measured by the resonant cavity method (QWED, Warsaw, Poland). Temperature variation of relative permittivity (τ_ε) of the sample was measured using an LCR Meter (Hi-Tester, Hioki 3532-50) at 1 MHz, using a thin densified, properly electroded pellet in the form of a MIM capacitor.

2.3.3.2 BSMO-BBSZ Tapes

The viscosity of slurry was periodically measured by cone and plate method using a rheometer (Rheo plus32, Anton Paar, USA). The sedimentation analysis was performed out in a 10 ml graduated measuring cylinder. The packed bed density of the slurry was investigated from the ratio of the sediment's initial height (H_o) and sediment height (H) as a function of time, at regular intervals.

Tape casting slurry was formulated in two stages; in the first stage, mixing of BSMO-BBSZ powder with optimized dispersant concentration in the binary solvent mixture was performed. In second stage, other essential vehicle components like binder, plasticizers and a homogenizer were added. The LTCC tapes were casted using a double doctor blade tape casting machine (Keko equipment, Zuzemberk, Slovenia) onto silicon coated Mylar® films, using the final optimized slurry. The casted tape was allowed to dry at room temperature. The mechanical strength of green tape was measured using a universal testing machine (Hounsfield, H5K-S UTM, Redhill, UK). The thermogravimetric analysis (TGA) of the green tape was conducted using a thermogravimetric analyzer (Perkin Elmer, Waltham, USA), in order to construct the

sintering profile. The lamination of individual green tapes was done in an isostatic lamination press (Keko equipment, Haikutech, Maastricht, Netherlands) by applying a pressure of 10 MPa and a temperature of 60 ˚C for 8 min. These tapes were sintered at 875 ˚C for 2 h, employing constrained sintering technique, by keeping the thermo-laminate tape in between two macroporous alumina plates that helps to avoid warping. The microstructure of green and sintered tapes was analyzed using scanning electron microscope, as described earlier. The surface roughness of the green tape was determined using an atomic force microscope (AFM) (Bruker Nano, Inc., USA), being operated at tapping mode. Passive circuits were screen printed on top of green tapes using Ag ink with the aid of a semi-automatic screen printer, as described before, and were cofired at 875 ˚C. The surface homogeneity and quality of the post-printed tape were characterized using optical microscopy (MRDX, Leica Microsystems, Wetzlar, Germany). The micro hardness of sintered tapes was measured using Vickers microindentation hardness test (Shimadzu HMV-2TAW, Kyoto, Japan). The microwave dielectric properties were measured using a split post dielectric resonator (SPDR, QWED, Warsaw, Poland) operating at 5 GHz with the aid of a vector network analyzer.

2.3.3.3 $BiFeO_3$

Thermogravimetry/ differential thermal analysis (TG/DTA) of the BFO was carried out from room temperature upto 600 ˚C in air atmosphere using a thermogravimetric analyzer (TGA/DTA instrument, Shimadzu, Japan). Phase purity of the calcined powder was analyzed using X-ray diffraction (XRD) analysis with Cu Kα radiation (X'Pert PRO diffractometer, PANalytical, Almelo, The Netherlands). The particle size of ceramics prepared was performed using high-resolution transmission

electron microscopy (HRTEM) (FEI Tecnai G2 30S-TWIN, FEI Co., Hillsboro, OR, USA). Rheo plus32 rheometer was used for measured using viscosity of developed ink slurry (Anton Paar, Ashland, VA, USA). Screen printing of developed ink was performed under optimal conditions. Microstructural analysis of the printed film was identified using a scanning electron microscopy (SEM) using a JSM 5600LV instrument (JEOL, Tokyo, Japan). Atomic force microscopy (AFM) (Multimode, Bruker, Germany), in tapping mode is used for getting an idea regarding the surface roughness of printed sample. The ferroelectric property was analyzed using a ferroelectric tester (aixACCT-TF2000E, GmbH, Aachen, Germany). Magnetic properties were measured using an oven setup which can go upto 900 K attached to Physical Property Measurement System (PPMS Quantum Design, USA).

2.3.3.4 Magnetodielectric Composite

The microstructural analysis was done using scanning electron microscopy (SEM) using a JSM 5600LV instrument (JEOL, Tokyo, Japan). Elemental mapping was performed using an EDAX technique associated with SEM. The multiferroic studies were done using a ferroelectric tester and oven setup attached to PPMS as discussed in 2.3.3.3. Magnetocapacitance measurement was performed using a WayneKerr Impedence Analyser as discussed in 1.6.4.

2.4 Results and Discussion

2.4.1 $BiSmMoO_6$ based LTCC Tape

An earlier study has shown that, the effect of rare earth ion, Sm with strongly localized *f* shell electrons influences the dielectric loss quality of $BiSmMoO_6$ significantly.[12]

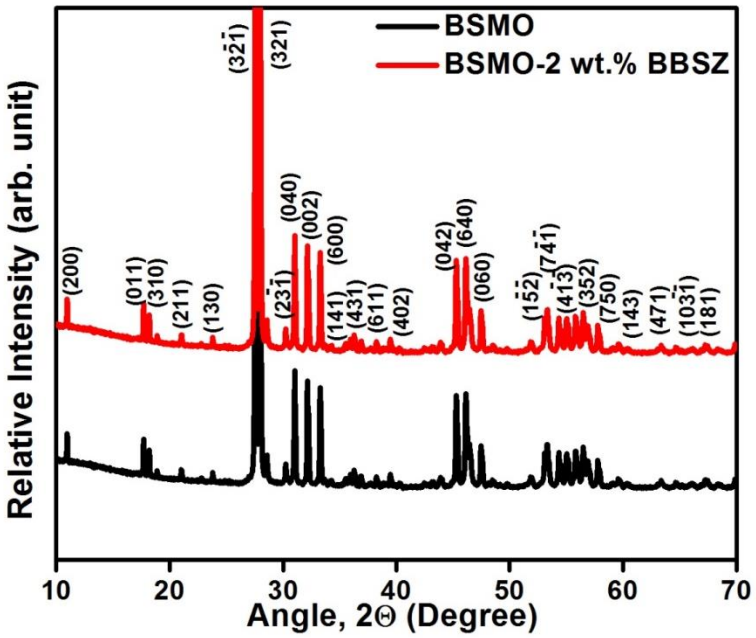

Figure 2.1: XRD of BSMO and BSMO-2 wt.% BBSZ ceramic sintered at 975 ˚C and 875 ˚C for 2 h respectively (prominent peaks are indexed).

The crystal structure of $BiSmMoO_6$ ceramics was identified as monoclinic. As shown in Figure 2.1, the XRD pattern obtained for pure BSMO sintered at 975 ˚C and 2 wt.% BBSZ glass added BSMO samples sintered at 875 ˚C, remains identical without any additional phases which confirms that the glass phase has no apparent reactivity with the ceramic powder, other than providing a low melting medium for vitreous sintering. In order to elucidate the crystal structure of BSMO ceramic, a detailed Rietveld analysis of the powder diffraction pattern was done using TOPAS software. The quality of refinement data was accessed by several parameters like Profile factor (R_p), weight profile factor (R_{wp}), expected weight profile factor (R_{exp}) and Goodness of fit (χ^2). The best fitted refinement parameters along with the lattice constant values were represented in Table 2.1. The crystallite size of the chemically derived powder can be estimated using the XRD profile with the help of Debye-Scherrer equation,

$$d = \frac{K\lambda}{\beta Cos\theta} \qquad (2.1)$$

where d is the crystallite size, K defines the shape factor (K~0.9), λ is the wavelength of Cu-Kα radiation used, β is the full width at half maximum. Most of the crystals that are oriented along $(3\bar{2}\bar{1})$ and (321) planes having an average crystallite size of around 91±3 nm.

Table 2.1: Refinement data of BSMO.

Material	Lattice Constants (Å)		Refinement Parameters (%)	
BSMO Structure: Monoclinic Space Group: *I*12/c1	a	16.1412(2)	R_p	2.63
	b	11.5214(1)	R_{wp}	3.42
	c	5.5606(2)	R_{exp}	2.32
	α=γ=90°, β=91.6°		χ^2	1.47

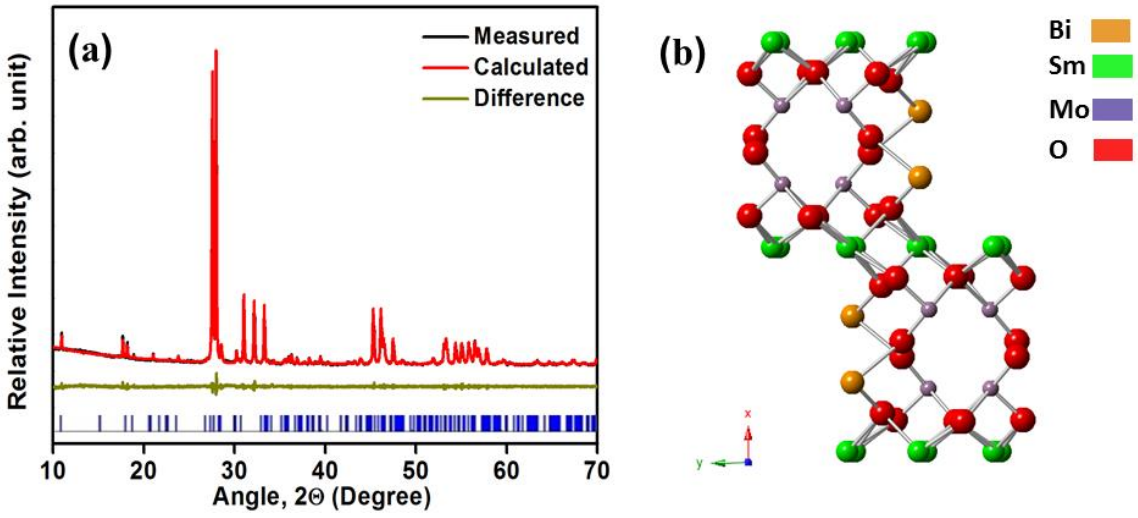

Figure 2.2: (a) Refinement of XRD pattern of BSMO and (b) its schematic crystal structure in ball and stick model.

Figure 2.2(a) represents the refinement pattern obtained for pure BSMO which clearly distinguishes the observed, calculated and difference plot along with the Bragg's diffractions. Based on refinement data, the crystal structure of BSMO was elucidated

using Crystal Maker software as shown in Figure 2.2(b). The crystal structure is found to be monoclinic with *I*12/c1 space group.

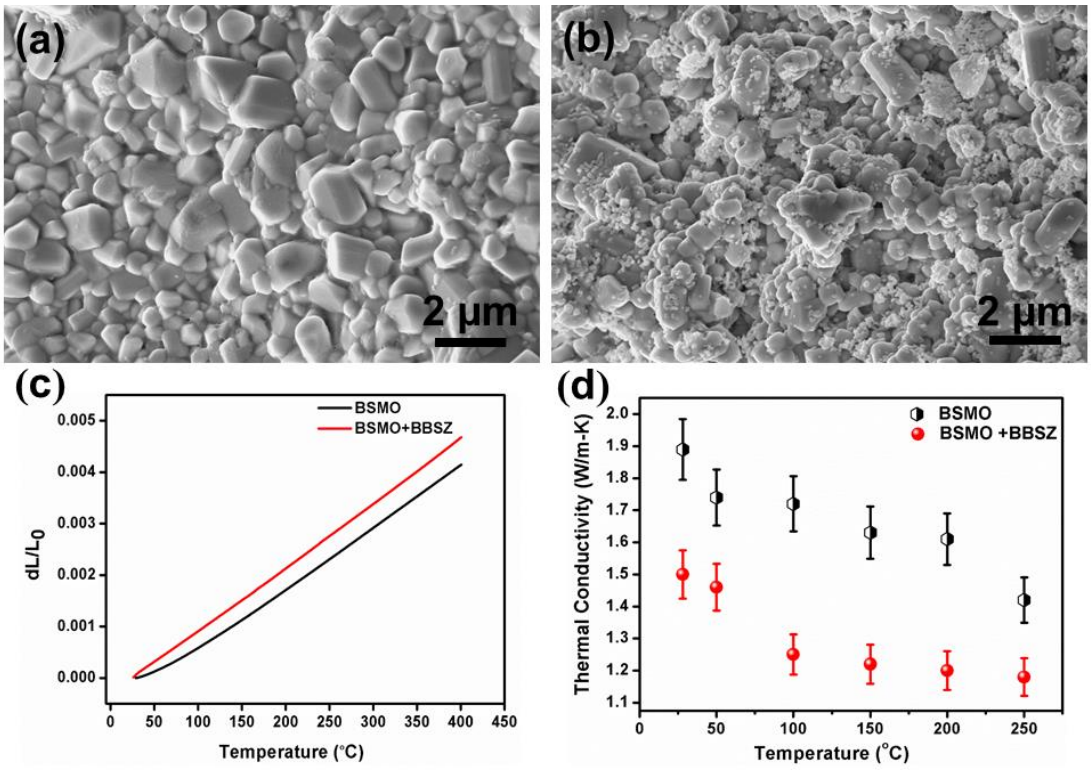

Figure 2.3: Cross sectional SEM images of (a) BSMO ceramic sintered at 975 ˚C, (b) BSMO-2 wt.% BBSZ glass sintered at 875 ˚C, (c) thermal expansion characteristics and (d) temperature variation of thermal conductivity of BSMO alone and BSMO-BBSZ composite.

The SEM micrographs of thermally etched BSMO ceramic sintered 975 ˚C/2h as well as BSMO-2 wt.% BBSZ sintered at 875 ˚C/2h were recorded. Figure 2.3(a) shows the cross sectional SEM image of BSMO ceramic where we can see a dense microstructure with minimal porosity. BSMO ceramic shows non homogenous particle size which were appeared to be polygonal in shape, but all the particles possess a size less than 2 μm. The cross sectional SEM image of 2 wt.% BBSZ glass loaded BSMO ceramic was recorded and shown as Figure 2.3(b). From Figure 2.3(b), it is clear that the morphology of particles is similar to that of intrinsic BSMO ceramic. Some uniformly

distributed additional nanoparticle clusters are also observed throughout the surface. This is believed to be recrystallized BBSZ glassy phase in the ceramic. The average size of BSMO particles is less than 2 μm while size of grains corresponding to glassy phase is in the range of 100 nm.

In multilayer thick film devices, thermal properties of substrate are highly critical because during cofiring, the thermodynamical and physicochemical interactions inside subsystems result in mechanical strain that would destabilize the module. Figure 2.3(c) shows the expansion of BSMO and BSMO-BBSZ ceramic as a function of temperature (30 ˚C-400 ˚C). It is clear from the figure that samples show a quasi-linear variation of length with respect to temperature. The mean coefficient of thermal expansion (CTE) of the samples was computed using the equation,

$$CTE = \frac{l_2 - l_1}{l_1(T_2 - T_1)} \qquad (2.2)$$

where l_1 and l_2 are the changes in lengths of the samples at temperatures T_1 and T_2 respectively. Usually in ceramic materials, the coefficient of linear thermal expansion is very low due to strong inter-atomic bonding compared to polymers and metals. During cofiring in hybrid circuits, the thermal delamination and cracks occur due to expansivity mismatch between embedded passives and substrate package. A convenient way to circumvent this risk is to employ a ceramic with matching CTE as that of the electrode, Ag. Commercial LTCC materials possess CTE values in the range 2-5 ppm/˚C which is close to the value of silicon. But in LTCC hybrid circuits, highly conductive metals like Au, Ag are used which are having very high CTE values (> 10 ppm/˚C). Literatures are scarce on such materials which are thermally matching but non-reactive to electrodes. In 2011, Chen et al. reported a higher CTE value of 11.7

ppm/˚C for an LTCC system based on quartz added with BaO-Al_2O_3-SiO_2-B_2O_3 glass composite.[22] In 2017, Arun et al. also reported LZT+LMZBS composite possess a higher CTE value of 11.97 ppm/˚C.[23] Recently, Xiang et al. reported an ultra-low loss $CaMgGeO_4$ microwave ceramic for LTCC application having a CTE value of 12.4 ppm/˚C.[24] Herein for pure BSMO ceramic, it exhibited a CTE value of 11.2 ppm/˚C while BSMO-BBSZ composite possess even higher CTE value of 12.3 ppm/˚C. This apparent high CTE value is also acceptable to LTCC substrates that can be cofired with high conductive silver, without any visible thermo-delamination.

Heat is inevitably developed in all active circuits including hybrids, which has to be efficiently dissipated from the devices for their smooth functioning. Figure 2.3(d) represent the variation of thermal conductivity of BSMO-BBSZ composite, from room temperature to 250 ˚C, as estimated using Xe flash technique. Here, thermal conductivity of ceramics was computed using the relation[25]

$$TC = \lambda * Cp * \rho \qquad (2.3)$$

where λ is thermal diffusivity, C_p is specific heat capacity at room temperature and ρ is density of the sample. It is clearly seen from figure that thermal conductivity shows a decreasing trend with increase in temperature which is typical for a polycrystalline ceramic. With the addition of 2 wt.% of BBSZ glass to BSMO, the room temperature thermal conductivity value decreases marginally from 1.8 W/m-K to 1.54 W/m-K. Usually, glass addition deteriorates the thermal conductivity value, since glass is poor in heat conduction.[26] Further, glass fluxing invites entrapped porosity which is commonly observed in glass-ceramic composites. Usually thermal conductivity value for most of the commercial LTCC materials fall in the range of 2-3 W/m-K.[27]

The microwave dielectric properties of BSMO and BSMO-2 wt.% BBSZ were measured. The intrinsic BSMO has a densification over 96% which is in support with the SEM analysis. The material has got a relative permittivity of 11.5 and $Q_u$xf value of 44,300 (at 11 GHz). The temperature coefficient of resonant frequency measured within the temperature range of 25-100 ˚C, is -35.7 ppm/ ˚C. However, these values are different from the previous report of Li et al., who also investigated the microwave dielectric properties of $BiSmMoO_6$.[12] They obtained a relative permittivity value of 8.5 with $Q_u$xf value of 43,700 and τ_f value of -27.1. The exact reason for this discrepancy is unknown, but can be attributed to the lower values of densification in the earlier report, purity of raw materials used, sintering and measurement conditions etc. When 2 wt.% BBSZ glass was added to the ceramic, the sintering temperature was brought down to 875 ˚C. It is interesting to note that, the relative permittivity has a marginal increase to 11.9 with a slight reduction of $Q_u$xf (~ 40,600 GHz). The τ_f for the LTCC composition is calculated to be -40.2 ppm/ ˚C.

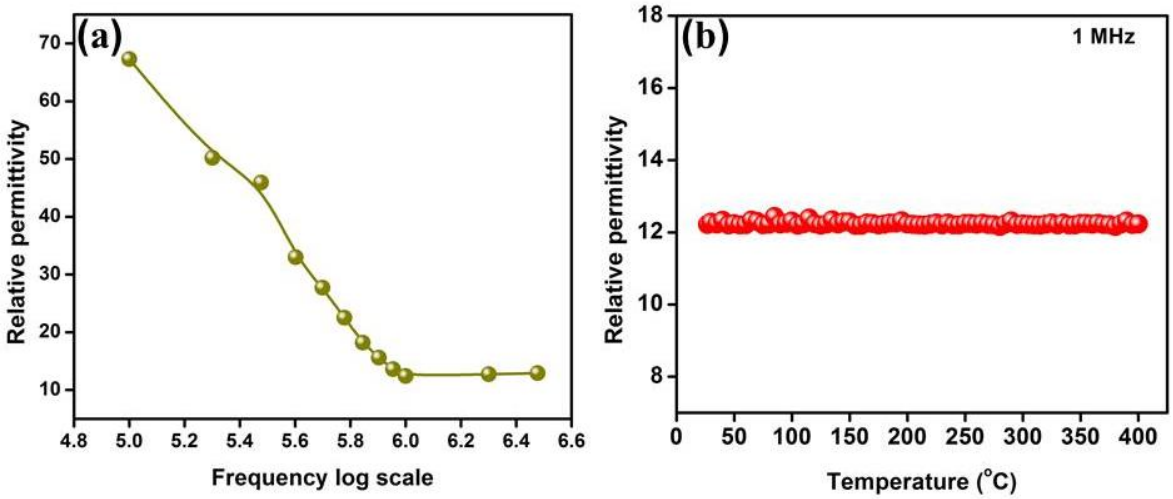

Figure 2.4: (a) Variation of relative permittivity with frequency, (b) temperature dependence of ε_r measured at 1 MHz for the BSMO-BBSZ sample sintered at 875 ˚C.

The variation of relative permittivity with frequency for BSMO-BBSZ was recorded and is shown in figure 2.4(a). The value of relative permittivity at 1 MHz is observed to be 12.4. In order to estimate thermal stability of dielectric properties, the temperature coefficient of relative permittivity at 1 MHz of BSMO-2 wt.% BBSZ was also measured. Invariance of relative permittivity with temperature is a critical factor that determines its practical applicability, since hybrid LTCC modules are supposed to function at harsh conditions like high temperature and humidity. The variation of relative permittivity (ε_r) with respect to temperatures ranging from 25 ˚C-400 ˚C recorded at 1 MHz is plotted in Figure 2.4(b). The temperature coefficient of relative permittivity (τ_ε) was calculated as 106 ppm/˚C using the relation,

$$\tau_\varepsilon = \frac{(\varepsilon_2 - \varepsilon_1)}{\varepsilon_1 (T_2 - T_1)} \qquad (2.4)$$

where ε_1 and ε_2 corresponds to the relative permittivity at T_1 and T_2 temperatures. For most commercial LTCC materials, τ_ε is usually not given in the data sheets, but a lower values are always desirable.

From this value of τ_ε, one can calculate the temperature coefficient of resonant frequency (τ_f) of the tape, which otherwise could be done only in the ceramic puck form, using the relation,

$$\tau_f = \frac{-\tau_\varepsilon}{2} - CTE \qquad (2.5)$$

where *CTE* is the coefficient of thermal expansion. Given the CTE of BSMO-BBSZ as 12.3 ppm/˚C (see Figure 2.3(c)), the value of τ_f was calculated from the equation (2.4) and obtained as -65.3 ppm/˚C. There are earlier reports available for LTCC compositions with large negative τ_f values.[28] However, being a substrate, the negative τ_f values of

LTCC tapes will not critically affect the performance of the multilayer hybrid module. The difference in τ_f value of tape with its ceramic counterpart is attributed to the variation of densification in tapes which suffers differential shrinkage along x, y and z directions. Interestingly, from the Figure 2.4, one can infer that the relative permittivity is invariant with respect to temperature ranging from 25 ˚C - 400 ˚C.

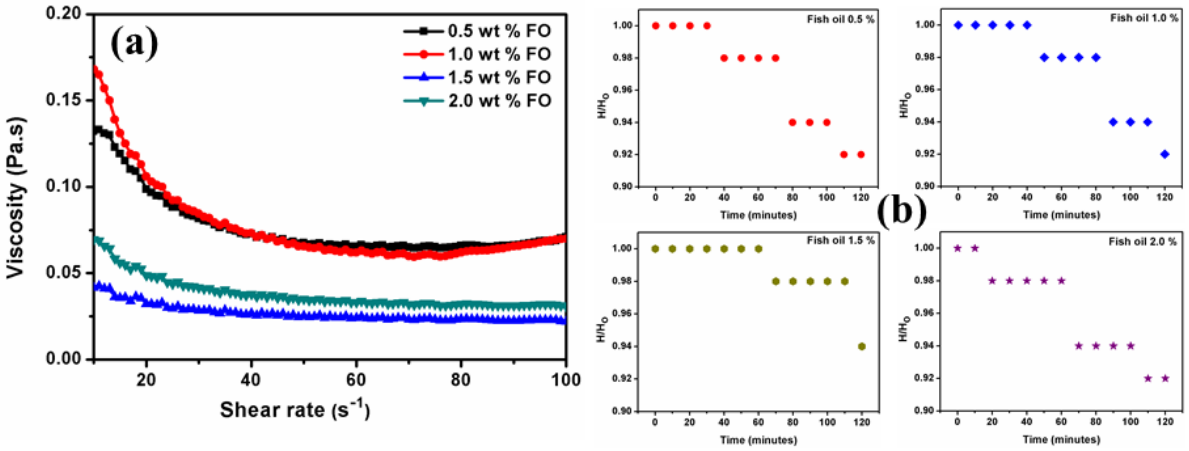

Figure 2.5: (a) Variation of viscosity and (b) sedimentation analysis of slurry with different wt.% of dispersant.

In non-aqueous tape casting, besides fast drying of the volatile organic solvents, the imminent hydration of ceramic particles can be conveniently avoided.[29,30] An optimum amount of dispersant is required in the slurry for electrostatically dispersing ceramic particles and thereby making the suspension homogeneous throughout the process.[31,32] The flow characteristics of slurry were optimized using rheological measurements which includes viscosity and sedimentation analysis. The variation of viscosity as a function of shear rate for different wt.% of fish oil (FO) is depicted in Figure 2.5(a). From the figure, it is evident that viscosity decreases with the increase in dispersant content up to 1.5 wt.% and thereafter increases. The decrease in viscosity with dispersant addition can be attributed mainly to the formation of fluid

interparticulate layer between the ceramic particles which tend to improve the particle mobility.[31] Beyond this concentration of dispersant, the viscosity increases due to bridging flocculation.[33,34] The colloidal stability of the slurry was investigated using sedimentation analysis. In this study the sedimentation height (H) was observed at regular intervals as a function of time against the initial height of the slurry (H_0). In principle, a well deflocculated slurry should have a slow settling rate and a higher packed bed density than partially flocculated one.[31] From the sedimentation results depicted in Figure 2.5(b), one can infer that the slurry with 1.5 wt.% of dispersant with respect to the powder loading shows a slower rate of sedimentation and higher packing density. Hence it can be concluded that 1.5 wt.% of fish oil with respect to the ceramic powder loading is the optimum amount needed to obtain a well dispersed suspension.

Table 2.2: Final composition of tape casting slurry.

Component	Composition (wt.%)	Function
PART I		
BSMO+2 wt.% BBSZ	69.96	Filler
Fish Oil	1.05	Dispersant
Xylene	11.66	Solvent
Ethanol	11.66	Solvent
PART II		
Polyvinyl butyral	1.21	Binder
Butyl benzyl phthalate	1.43	Plasticizer (Type I)
Polyethylene glycol	1.80	Plasticizer (Type II)
Cyclohexanone	0.42	Homogenizer

To begin with the two-stage slurry synthesis procedure, ceramic filler with optimized amount of dispersant was mixed and later binder, plasticizer etc. were added and optimized. The second stage of optimization was performed using trial and error method by a microscopic careful inspection of the resultant green tape. The final optimized composition of the ready-to-cast slurry is given in Table 2.2. From the Table 2.2, it is clear that a maximum powder loading achieved was 69.96% with respect to the total composition which will indirectly dictate drying speed and packing density the green tape. High loading, in turn, reduces the drying stress that can be evolved in the green tape, which may result in a crack free microstructure of the dried tape.[35-,37] The final viscosity plot of the ready-to-cast tape is shown in Figure 2.6.

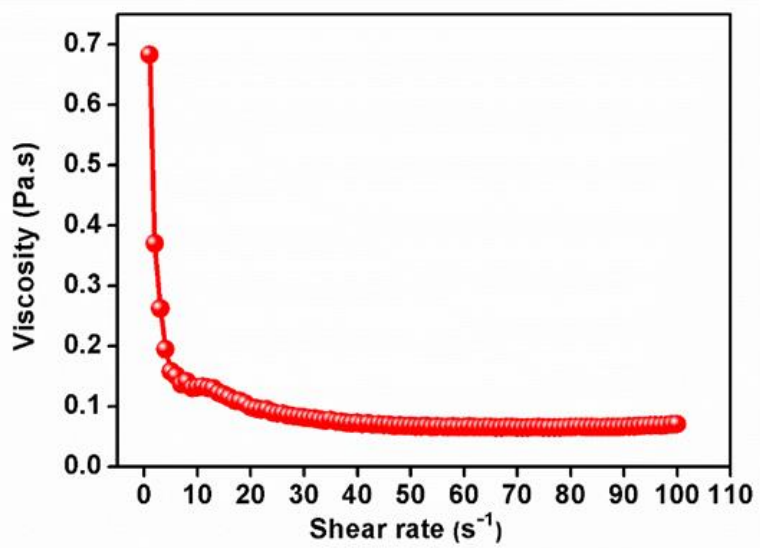

Figure 2.6: Rheological behaviour of the ready to cast slurry.

The viscosity curve shows a typical pseudo plastic behaviour which is a pre-requisite for an ideal tape casting slurry. This can be explained as the tendency of decreasing viscosity with respect to increase in shear rate which in turn favors smooth

flow of slurry through the doctor blade. Once casting is done, the viscosity will increase that will halt the undesired flow of slurry through the carrier film (Mylar® (polyethylene terephthalate)).[30]

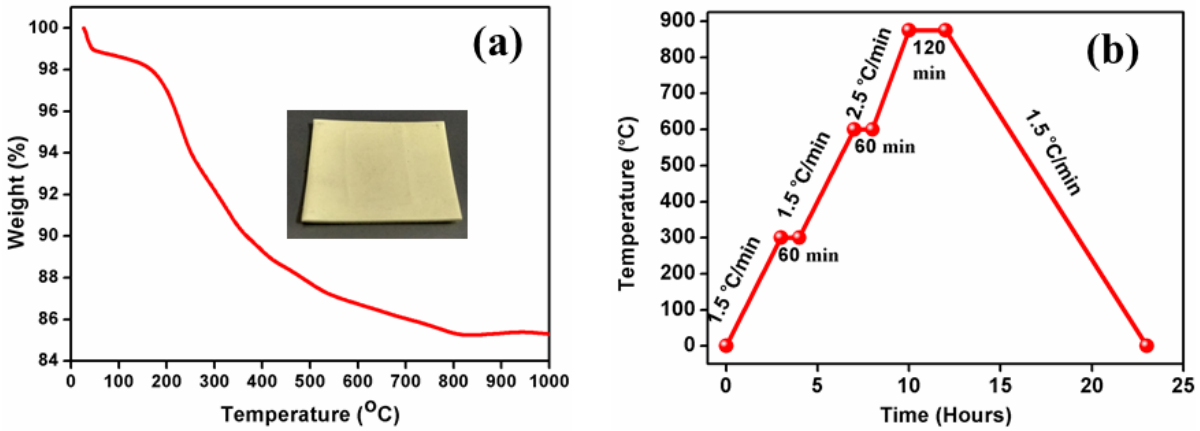

Figure 2.7: (a) Thermo-gravimetric curve of green tape with the inset showing sintered tape, and (b) optimized sintering profile of the BSMO-BBSZ tape.

The green tape obtained after tape casting contains a lot of organic constituents used at the time of slurry preparation. So, a clear understanding of the thermal decomposition of organic matters in the green tape is essential to reduce undesirable defects like delamination of layers, cracks, anisotropic shrinkage etc. during sintering. Ideally, all the organic additives present in the green tape should be removed prior to sintering, failing which will adversely affect the shrinkage as well as material properties of the sintered ceramic. Hence, the TG analysis of the resultant green tape was carried out in the oxygen atmosphere up to 1000 ˚C with a heating rate of 10 ˚C/minute which is shown in Figure 2.7(a). The tape showed a low weight loss of around 1.75% up to 150 ˚C. This weight loss may be due to the volatilization of organic solvents used in the procedure. A maximum weight loss of 9.8% was noted during 150-450 ˚C which implies that most of the organic additives used in the tape casting process decompose in this

regime. A small weight loss of around 2% was happening up to 800 ˚C which may be due evaporation of low melting glass component present in the tape. After 800 ˚C, the weight loss is almost constant. Inset of the TG curve shows the sintered tape of BSMO-BBSZ. Based on the TG curve, a sintering profile for the BSMO-BBSZ tape was constructed as shown in Figure 2.7(b). In order to remove all the organic additives, two intermediate binder burn out steps were included in the sintering profile at 300 ˚C and 600 ˚C. The sintered tape was observed to have shrinkage of 7%, 9% and 12% in x, y and z axes respectively.

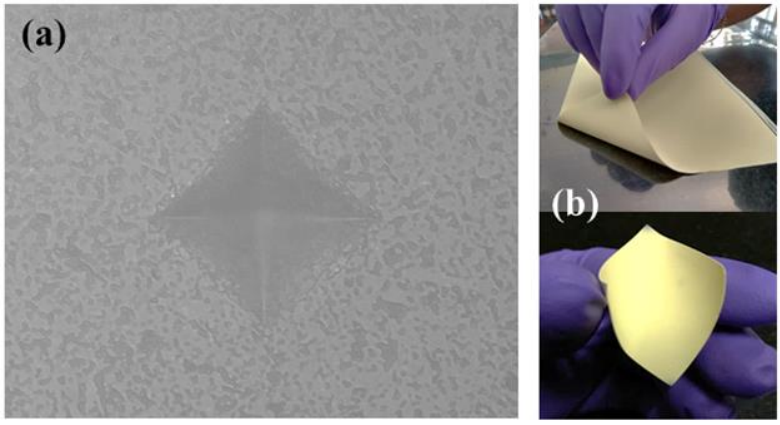

Figure 2.8: (a)Optical microscopic image of the indentation produced by Vicker's indenter on the surface of BSMO-BBSZ tape sintered at 875 ˚C and (b) photographs of developed green tape showing its flexibility.

As well known, glass was added to ceramic for bringing down its sintering temperature, but at the expense of its mechanical strength. Obviously, even little glass content will deteriorate its hardness which delimit the machinability like via punching, trimming etc.[38] The micro hardness measurement is a versatile tool for getting mechanical strength of a densified sample by Vickers hardness test. The optical microscopic image of the surface of indented BSMO-BBSZ substrate sintered at 875 ˚C is

shown in Figure 2.8(a). The average value Vicker's hardness number (VHN) after five measurements was obtained as 478.12 ± 7.67. Hence the hardness of BSMO-BBSZ glass sintered tape was estimated as 4.69 ± 0.07 GPa. The images shown in figure 2.8(b) are the photographs of the green tapes that is a testimonial of their flexibility. Mechanical strength of green tapes was measured by tensile measurement, using a single layer of green tape with a thickness of ~109 ±2 μm. The results indicate that single layer of unsintered tape has a tensile strength of about 0.37 MPa which is good agreement with the previous reports.[27,30,35]

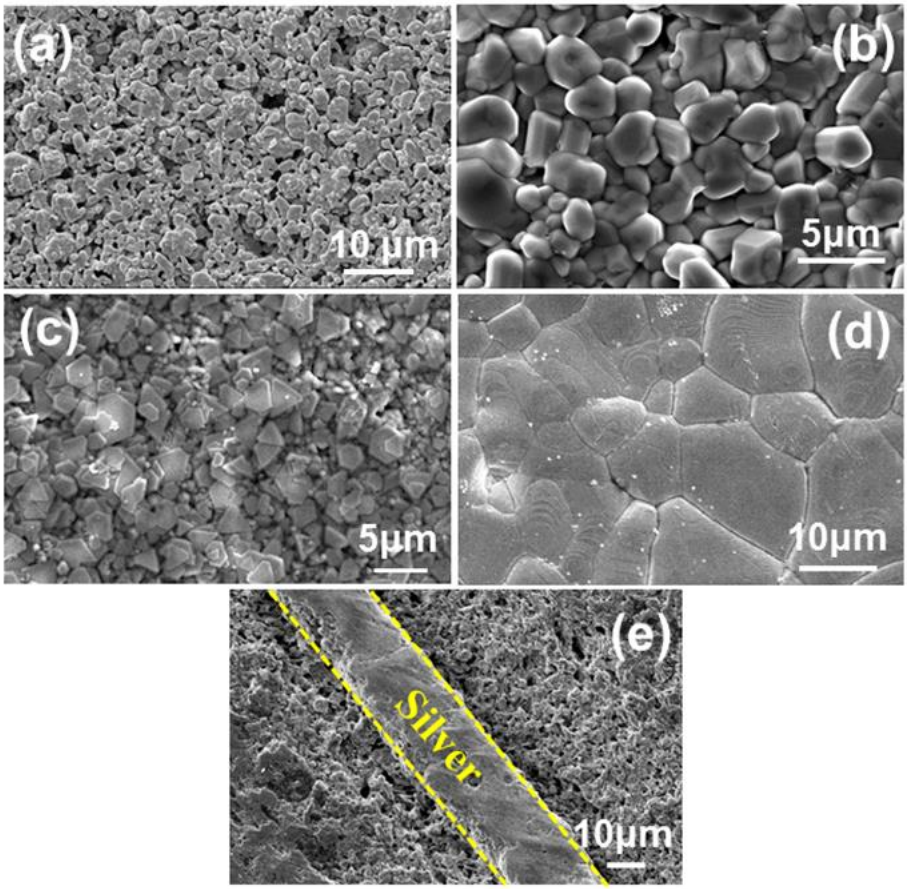

Figure 2.9: (a) Surface of BSMO-BBSZ green tape, (b) fractured surface of tape sintered at 875 ˚C, (c) topography of Ag printed on top of green tape, (d) surface of Ag screen printed tape after co-firing at 875 ˚C for 2 h and (e) cross section of stacked tape with embedded Ag pattern between tapes, after thermo-lamination and cofiring.

Surface morphological studies of BSMO-BBSZ tape is given in Figure 2.9. Figure 2.9(a) represents a dense and homogeneous microstructure with minimum porosity for the green tape surface. Here one can observe that the ceramic particles with an average particle size less than 1 μm, are covered and bonded to each other efficiently by the polymeric binder. Minimal porosity in the green tape is attributed to the higher powder loading achieved in the first stage of slurry preparation. Figure 2.9(b) represents a typical fractogram of tapes sintered at 875 ˚C for 2 h. A dense and more closely packed microstructure is observed for the sintered tape with an average particle size comes around 1-3 μm.

In LTCC technology, the key challenges facing while cofiring the ceramic with Ag are its diffusion into the substrate material and its partial evaporation from the material surface. In order to test the compatibility of prepared BSMO-BBSZ tape with electrode material, Ag was first screen printed on top of the prepared green tape. Figure 2.9(c) represents the micrograph of Ag screen printed surface of BSMO-BBSZ green tape. One can observe a plate like microstructure throughout the surface with most of the silver particle possessing triangular morphology. The screen-printed surface was then taken for sintering at 875 ˚C for 2 h and the microstructure was recorded as given in Figure 2.9(d). Here, it can be inferred that Ag paste has undergone a transformation from triangle like morphology to a well densified polyhedral microstructure. In order to test the diffusion of Ag into tape matrix, Ag paste was blanket printed on top of two green tapes and then they were thermo-laminated together, embedding the metal between ceramics. The sample was then sintered at desired temperature whose cross-sectional SEM was recorded (Figure 2.9(e)). The microstructure obtained for the cross-

section reveals the fact that no visible diffusion of Ag was observed towards the interior of LTCC tape even after sintering. More importantly, there is no visible proof of delamination resulting from thermal stress in the heterostructure, since their CTEs are in good agreement. From these tests, one can summarize that the developed BSMO-BBSZ based LTCC tape can be conveniently cofired with Ag based passive components in hybrid electronic devices.

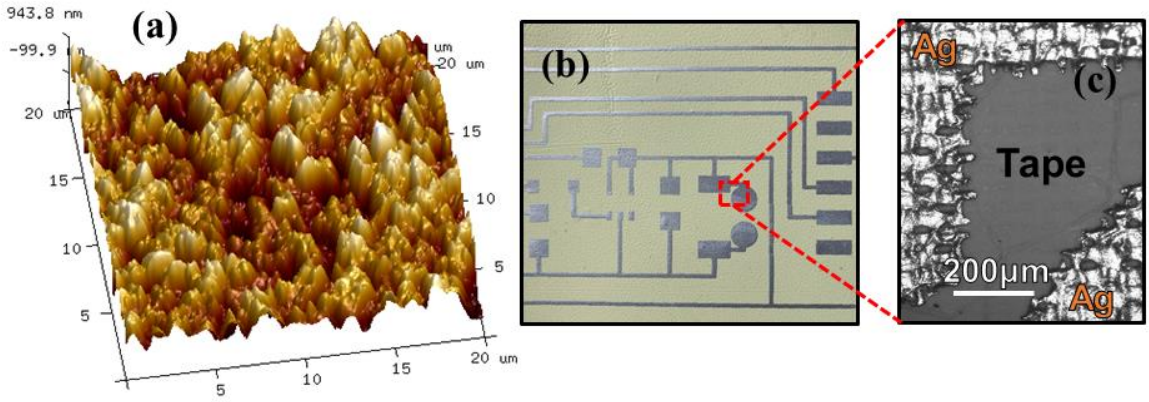

Figure 2.10: (a) 3D AFM image of the developed green tape, (b) photograph of the passive circuit screen printed using Ag ink on LTCC green tape and (c) optical microscopic image.

Surface roughness plays an important role in printing patterns on top of LTCC tapes.[39] For obtaining better results in pattern printing over LTCC tapes, an optimal roughness is necessitous since it promotes adhesion between the printing ink and tape surface. Figure 2.10(a) represents 3D AFM image of the developed BSMO-BBSZ green tape surface. Average surface roughness (R_a), Kurtosis and skewness values of the developed green tape were observed to be 229±5nm, 3.49 and -0.38 respectively. The value of kurtosis was found to be >3 which indicates that the surface has more peaks than valleys. Negative skewness value reveals the presence of longer tails below the reference plane.[35,40] The foresaid values clearly indicate that the surface of the green

tape has finite roughness estimated within experimental error limits, which makes the printing of passive circuits easy. In order to confirm this, a passive circuit was printed on the green tape using screen printing with Ag ink. The photograph of the printed pattern and its optical image are shown in Figures 2.10(b) and (c) respectively.

Table 2.3: Microwave dielectric properties of green, laminated and sintered tape.

Material	No. of Layers	Thickness (μm)	Density (g/cm^3)	5 GHz		10 GHz	
				ε_r	tanδ	ε_r	tanδ
Green Tape	1	108	5.91	8.24	$1x10^{-2}$	8.12	$1x10^{-2}$
Laminated tape	6	650	6.23	8.78	$3x10^{-3}$	8.51	$2x10^{-3}$
Sintered tape	6	583	6.82	9.27	$9x10^{-4}$	9.03	$8x10^{-4}$

The microwave dielectric property of the parent material as well as the LTCC material was studied in bulk ceramic form. When the material was modified into an LTCC tape, Q factor measurements were possible only as loss tangent (tanδ) since the testing was done using SPDR technique. The microwave dielectric properties of the green, stacked and sintered tapes measured at 5 GHz and 10 GHz are given in Table 2.3. It is clear from the table that green tapes show low permittivity and relatively higher dielectric loss values. This is due to the presence of organic additives like dispersant, plasticizer etc. that were present in the tape. Most of the organic additives are having low relative permittivity and high dielectric loss due to their strong covalent bonds and low atomic polarizabilities.[31] During thermo-lamination, polymer chains get weakened and bind well with ceramic particles making the composite denser and thereby a marginal variation in values of dielectric properties can be observed.[30,41] Improvement

in the value of relative permittivity and decreased value of dielectric loss were observed after sintering of thermo-laminated tape. This can be attributed to facts that, at elevated temperature, the organic moieties present in the tape were burnt out, which in turn resulted in removal of pores. Further, at higher temperature grain growth occurs and thereby strong bonding between the ceramic particles happens to form which will help in achieving higher densification of the sample.[42] The microwave dielectric properties of the tapes were measured both in 5 GHz as well as in 10 GHz, using SPDR technique and are given in Table 2.3.

After studying properties of $BiSmMoO_6$ tape, the properties of $BiFeO_3$ was studied in detail in the section 2.4.2

2.4.2 $BiFeO_3$ based Ink

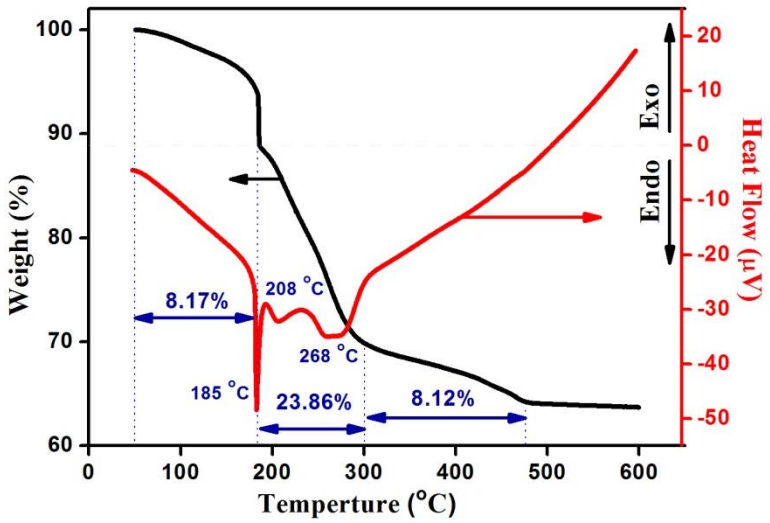

Figure 2.11: TG/DTA of BFO precursor powder.

The chemically derived BFO powder was dried well, prior to structural elucidation. In order to get clear information about the calcination temperature, TG-

DTA analysis was carried out on BFO precursor powder. Figure 2.11 shows the resultant TG-DTA obtained up to 600 ˚C in oxygen atmosphere. In the first stage, the weight loss starts from 50 ˚C and shows a decrease up to 185 ˚C which can be attributed to the evaporation of planar water as well as ethylene glycol in the precursor. A sharp endothermic peak at 185 ˚C is observed in the DTA curve corresponding to this weight loss. The second stage, a major weight loss of about 23.86 % occurs in the range of 185 ˚C- 300 ˚C. Two endothermic peaks are observed at 208 ˚C and 268 ˚C that imply the decomposition of nitrates and carbonaceous matters present in the precursor powder. A small weight loss of around 8% was observed in 300 ˚C to 480 ˚C which can be attributed to the crystalline perovskite phase formation of BFO from the amorphous component. No significant weight loss was observed after 500 ˚C which confirms the formation of stabilized perovskite type BFO powder. From the TG-DTA plot the calcination temperature was optimized to be at 500 ˚C/ 4h.

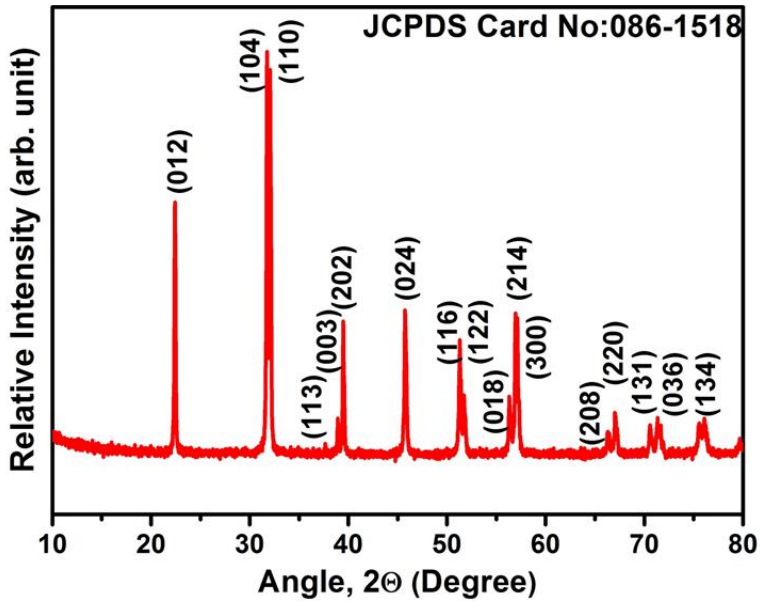

Figure 2.12: XRD pattern of BFO powder calcined at 500 ˚C/ 4 h.

A key parameter to be controlled in BFO's powder processing is its phase purity, since satellite phases like $Bi_2Fe_4O_9$ are very likely to form. In this regard, XRD pattern was recorded for the BFO sample that was meticulously calcined at 500 ˚C/ 4h which is shown in Figure 2.12. All the peaks corresponding to XRD results were indexed using a standard JCPDS card no. 086-1518 for $BiFeO_3$ with a rhombohedral crystal structure having R3c (161) space group. According to Debye-Scherrer, most of the crystals that are oriented along (104) and (110) planes having an average crystallite size of around 68±2 nm.

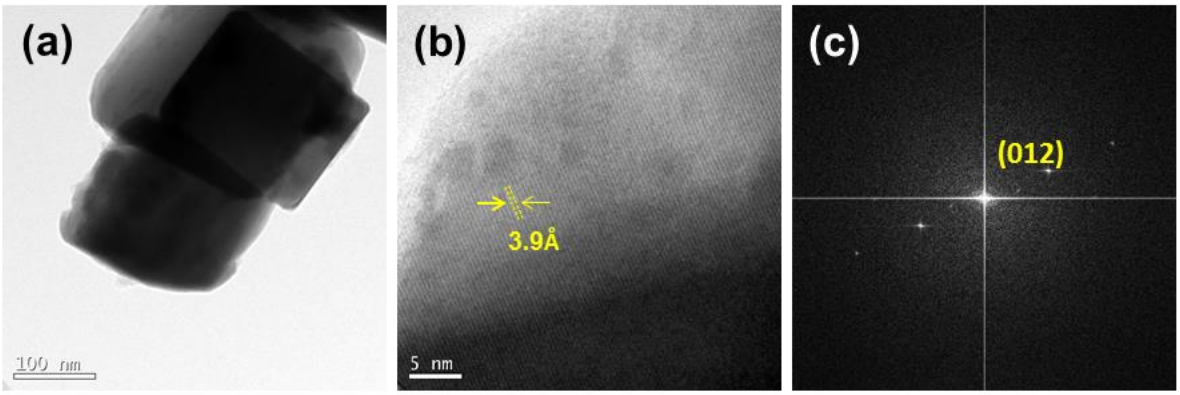

Figure 2.13: (a), (b) HRTEM images of BFO and (c) FFT pattern of BFO.

In ink formulation, particle size plays a crucial role along with rheology and microstructure of the printed thick film, since bigger particles rattle the ink's colloidal stability and result in settling. Smaller particle size have an additional advantage of better dispersion contributed by organic dispersant, improved flow characteristics, and higher printability.[43] In screen printing technique, a combination of smaller size with uniform size is more desirable. This will provide homogeneous microstructure and accuracy to the printed film. For obtaining similar sized particles, the calcined particles

were again re-milled for 4 h to avoid flocculation. The particle size of the ball milled BFO powder was determined from TEM analysis. Figure 2.13(a) represents the morphology as well as particle size of the calcined BFO powder. It is clear from the TEM image that structure obtained are more like cuboid with an average size of 115nm. This particle size is understandable since the powder is already calcined at 500 ˚C. In figure 2.13(b), the lattice fringes of the crystal are visible which indicates the high crystallinity of the BFO powder. The d-spacing value of two adjacent fringes was measured to be 3.9 Å which corresponds to (012) plane. The Fast Fourier Transform (FFT) pattern (Figure 2.13(c)) specifies the reflections from the (012) crystal plane.

$BiFeO_3$ is a well-known room temperature multiferroic material.[44] Here, the magnetic properties have been investigated by the field dependent magnetization (M-H) measurements and also the zero-field-cooled (ZFC), field-cooled (FC) temperature dependent magnetization measurements. Figure 2.14(a) shows the room temperature magnetic hysteresis loop for $BiFeO_3$. The enlarged portion of the hysteresis loop is shown in the inset of figure 2.14(a). From the figure it is clear that BFO exhibits a remnant magnetization (M_r) value of 0.195 emu/g with a coercive field (H_c) of 263 Oe. This confirms the weak ferromagnetic behavior of BFO at room temperature. $BiFeO_3$ is well known for its G type anti-ferromagnetic ordering where spin pinning at the domain boundaries between antiferromagnetic and ferromagnetic domains is very likely. This is because, each Fe^{3+} spin is surrounded by six antiparallel spins of nearest Fe neighbours. Since these spins are not perfectly antiparallel, there exist a weak canting moment. That is, it has got a residual magnetic moment originated from the weak ferromagnetic nature.[45,46]

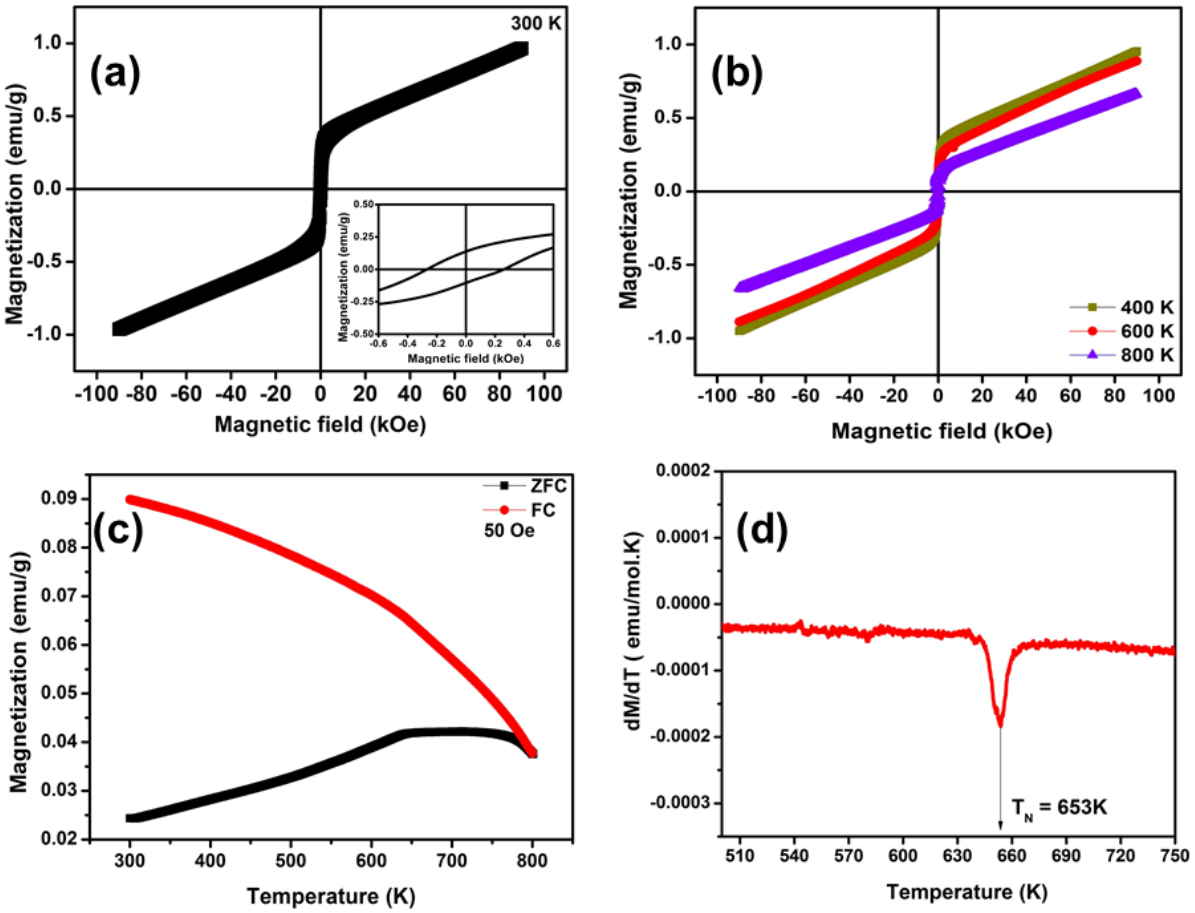

Figure 2.14: (a) Room temperature M-H curve of BFO, (b) M-H plot of BFO at different temperatures, (c) M-T plot of BFO at a magnetic field of 50 Oe and (d) dM/dT plot to determine T_N.

Figure 2.14(b) shows the M-H loops at 400 K, 600 K and 800 K. It is clear from the graph that as temperature increases, the M_r value as well as H_c decrease. Usually in ferromagnetic materials, magnetization tends to align along its crystallographic easy axis due to magnetocrystalline anisotropy. The anisotropic constant K is greatly temperature dependent. For K>0, as the temperature increases, M_r as well as H_c value will decrease and the material will shift from ferromagnetic state to paramagnetic state.[47] The FC and ZFC temperature dependent magnetization was taken at 50 Oe and is shown in figure 2.14(c). One can observe a bifurcation between the FC and ZFC

curves in the figure. This bifurcation shows randomness which usually decreases by the application of external magnetic field. When the applied magnetic field is greater, the magnetic moments associated with the particles will get aligned in the direction of the field and hence the bifurcation reduces.[48] Here, the field applied is 50 Oe which resulted in large bifurcation between FC and ZFC curves. From the M-T plot obtained here only gives an idea about the antiferromagnetic Neel transition of BFO. From the dM/dT plot (figure 2.14(d)), we could obtain T_N value as 653 ˚C, which is exactly equal to what is reported in literature.[49]

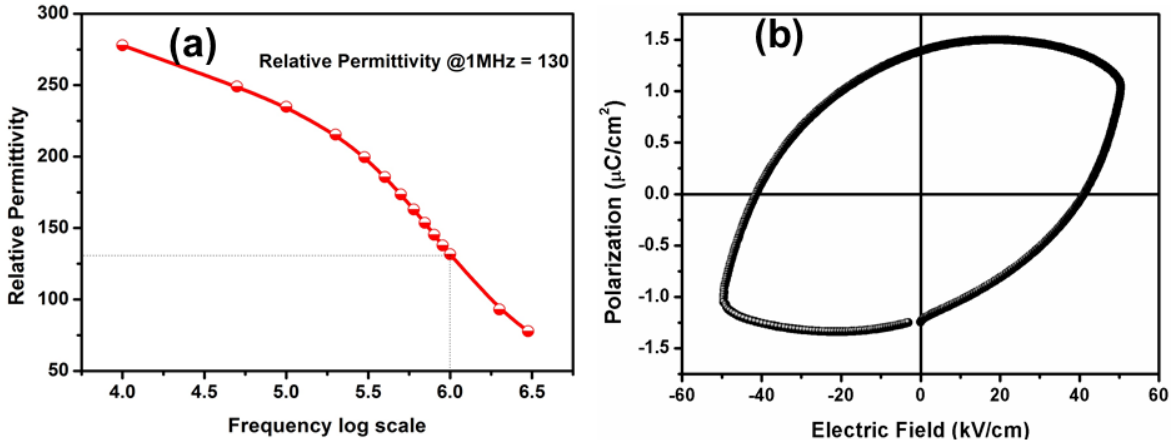

Figure 2.15: (a) Variation of relative permittivity with frequency for BFO and (b) room temperature P-E loop of BFO.

Figure 2.15(a) represents the variation of relative permittivity with respect to frequency of $BiFeO_3$. It is clear from the graph that relative permittivity decrease with increase in frequency. The relative permittivity obtained at 1 MHz (corresponding to $\log_{10}(f) = 6$, as marked in the graph) is 130. This value is small compared with some typical perovskite ferroelectric materials such as $BaTiO_3$. This ε_r is not unreasonable for $BiFeO_3$, since its ferroelectric Curie temperature is relatively higher and has a long

range magnetic order, in sharp contrast to $BaTiO_3$. The dielectric loss obtained for BFO at 1 MHz is 0.25.

Figure 2.15(b) shows the room temperature variation of polarization (P) with respect to electric field (E). The P-E hysteresis loop of BFO indicates their ferroelectric nature but with signature of a lossy dielectric. The sample was able to bear an electric field up to 50 kV/cm without any break down, but it was observed that even with the application of such a high electric field, the P-E loop obtained is not saturated. The remnant polarization (P_r) and coercive field (E_c) obtained are 1.03 μC/cm^2 and 39.8 kV/cm respectively. Beyond 50 kV/cm the sample undergoes break down. The high value of coercive field may be responsible for unsaturated P-E loop and low value of polarization.[50,51]

Multiferroic properties of chemically derived BFO powder were studied in detail. Ongoing efforts are to transcend the above said properties into a practical application, either in thin or thick film form. For realizing thick film devices, the popular coating methods are screen printing or dip coating. In screen printing, the prepared nanomaterial has to be formulated into a stable printable ink suspension. Preferably, screen printable inks require greater control over their rheological properties for facilitating smooth printing and efficient functioning of the end devices.[40] The quality and quantity of different organic additives needed for ink formulation such as solvents, dispersant and binder must be chosen judiciously, in order to control the rheology of ready-to-print ink within the printable range (> 1.0 Pa.s).

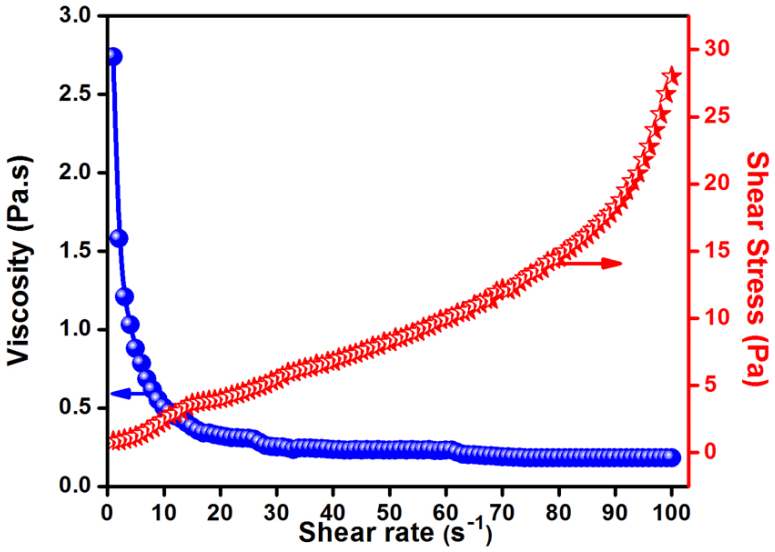

Figure 2.16: Viscosity curve of ready-to-print BFO ink.

The rheological behavior of the formulated BFO ink is shown in figure 2.16. An ideal screen printing ink should exhibit pseudoplastic behaviour. From figure, it is clear that as shear stress increases, viscosity decreases (pseudoplastic) which will eventually help in bringing out high resolution of printed patterns without smudging.[52,53] This is due to the fact that, when shear rate by the squeegee increases, ink becomes thinner that will help the ink to flow freely. Usually in conventional screen printing process, ink is pushed through the mesh opening with the aid of rubber squeegee, where the latter can handle considerable pressure and less prone to wear and tear.[54] The shear stress curve in figure also shows a pseudoplastic behaviour which helps in preventing the ink to flow beyond the assigned boundaries after printing.

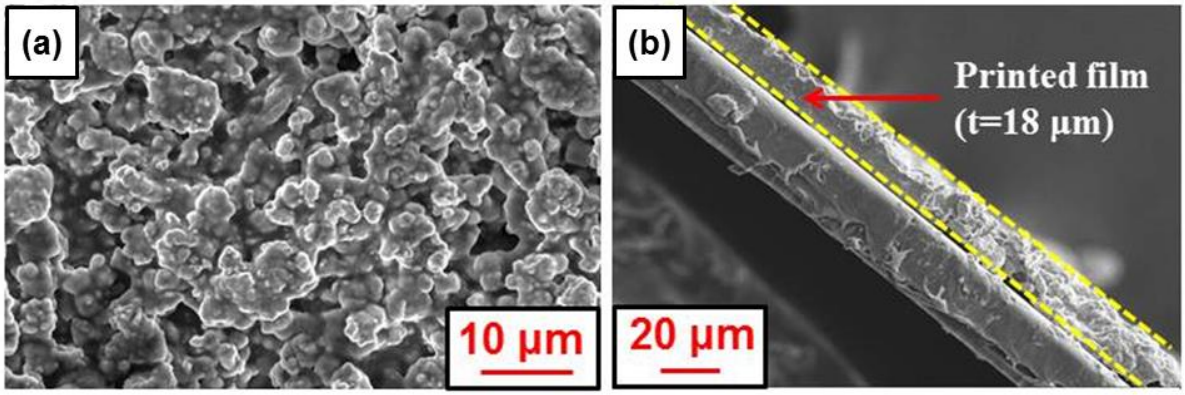

Figure 2.17: (a) Surface SEM micrograph of BFO printed on Mylar® substrate and (b) cross sectional SEM of printed pattern.

The surface SEM was recorded for double stroke printed BFO ink on Mylar® substrate and is shown in figure 2.17(a). A uniform distribution of BFO powder was observed with minimum porosity was observed. This minor amount of porosity arises due to the obvious volatilization of solvents which were used in ink formulation. The cross sectional SEM micrograph of BFO ink printed over Mylar® substrate is shown in figure 2.17(b). The printed pattern is clearly distinguishable from the Mylar® in the figure. A more or less uniform thickness of around 18 ±0.03 µm is observed for printed pattern throughout the SEM image.

Surface roughness is tested here as an important parameter in post print analysis, which mainly depends on the particle size of the filler, porosity evolved due to the volatilization of organic constituents as well as leveling nature of ink during printing.[40]

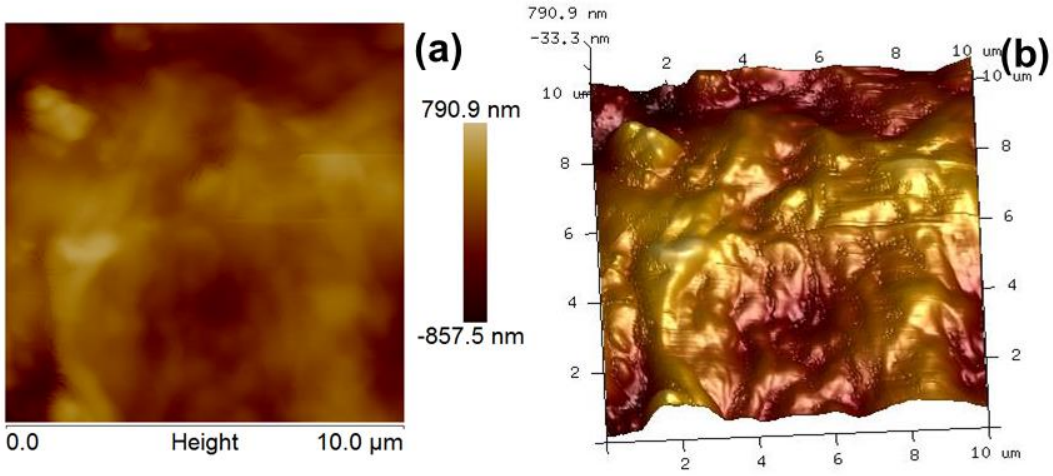

Figure 2.18: (a) 2D and (b) 3D AFM images of screen printed BFO.

The 2D and 3 D AFM images are shown in figure 2.18(a) and (b) respectively. The average surface roughness (R_a) of BFO film is around 112±5 nm and root mean square deviation of surface roughness (R_q) is around 156±5 nm respectively. In printed patterns, skewness is a measure of asymmetry of the surface and was obtained to be -0.28. The negative value of skewness indicates that the surface distribution has a greater number of longer tails at the measurement areas when compared to the reference plane. This means that an uneven surface distribution of BFO particles is observed with a greater amount of porosity on the Mylar® substrate. Kurtosis is a measure of unevenness of the printed film. If the kurtosis value is less than 3, it is usually called "platykurtoic". Here the value obtained for kurtosis is around 2.67, which means that the surface has relatively few high mountains and low valleys.[55] These bumbs and valleys arises due to the volatilization of organic solvents present in the ink, as discussed before. But this has no direct effect on the quality of printed pattern due to the comparatively lower surface roughness value obtained. Nonetheless, the observed surface parameters are good enough for screen printing applications.

Figure 2.19(a) shows the M-H curve for printed BFO ink. One can clearly notice a visible decrease in M_r value in this case, when compared to bulk. This is due to the presence of extra organic components present in the ink formulation. Vehicle of inks typically contain solvents, binder and dispersant whose evaporation transforms the printed surface into a porous one.

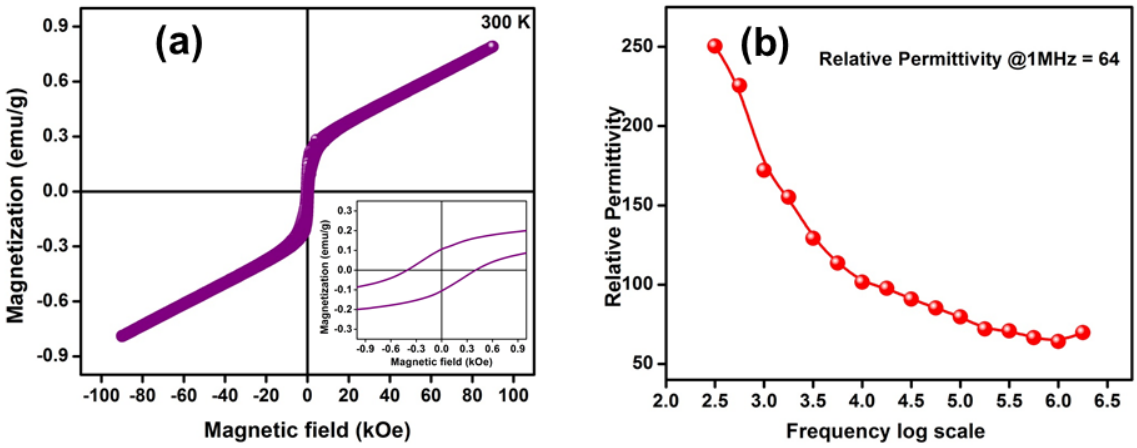

Figure 2.19: (a) M-H curve for BFO in ink form and (b) variation of relative permittivity (ε_r) as a function of frequency for screen printed BFO.

G.F. Dionne, in 1969 itself proved that nonmagnetic inclusion like porosity, and grain boundaries can detrimentally affect the magnetic hysteresis of polycrystalline materials.[56] According to this assumption, 90° spike domains or closure domains will appear on opposite sides of the pores. When the material is saturated, the spike domains would nucleate about pores and grow. As a consequence, the remanence ratio (ratio of remanence to saturation magnetization) diminishes considerably, by closure domains.[56] This diminishing can be seen on comparing figure 2.14(a) with 2.19(a). The variation of relative permittivity with frequency for screen printed ink pattern is shown in figure 2.19(b). For the bulk BFO, ε_r at 1 MHz was measured to be 130 (see figure

2.15(a)). But for BFO ink the value of ε_r is found to be 64 (see figure 2.18(b)). The main reason for the decrease in value of ε_r can also be attributed to the porosity, that decreases relative permittivity since ε_r of air is 1.0.

Since the properties of BFO ink was studied in detail, it can be qualified as the printable magnetic component in a MD layered composite. Here a 2-2 layered composite of $BiSmMoO_6$ and $BiFeO_3$ was developed by screen printing BFO ink over the LTCC dielectric layer. The schematic of composite is shown in figure 2.20(a). The developed composite is shown in figure 2.20(b).

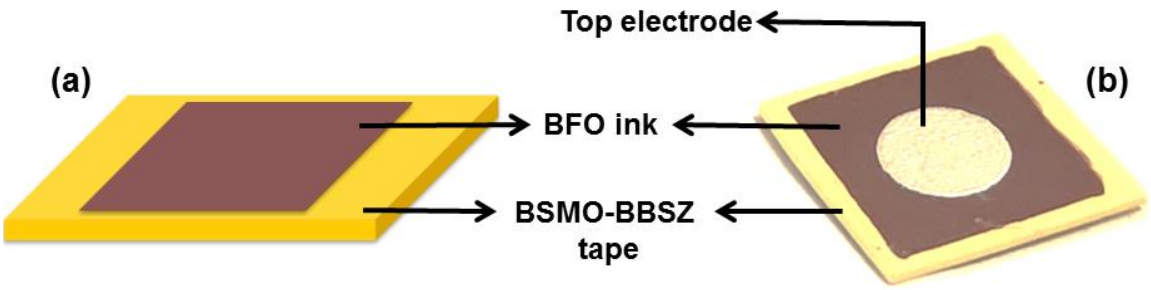

Figure 2.20: (a) Schematic of MD composite and (b) photograph of developed MD composite.

2.4.3 $BiSmMoO_6$-$BiFeO_3$ Magnetodielectric Composite

As per the schematic shown in figure 2.20, a MD composite was developed by flatbed screen printing BFO on glass doped, pre-fired BSMO tapes. The cross sectional SEM image of the composite was taken and is shown in figure 2.21. Here, one can see a thick layer of BSMO which has thickness of several hundred microns. The screen printed BFO layer on top of BSMO tape has a thickness of around 64±0.03 μm.

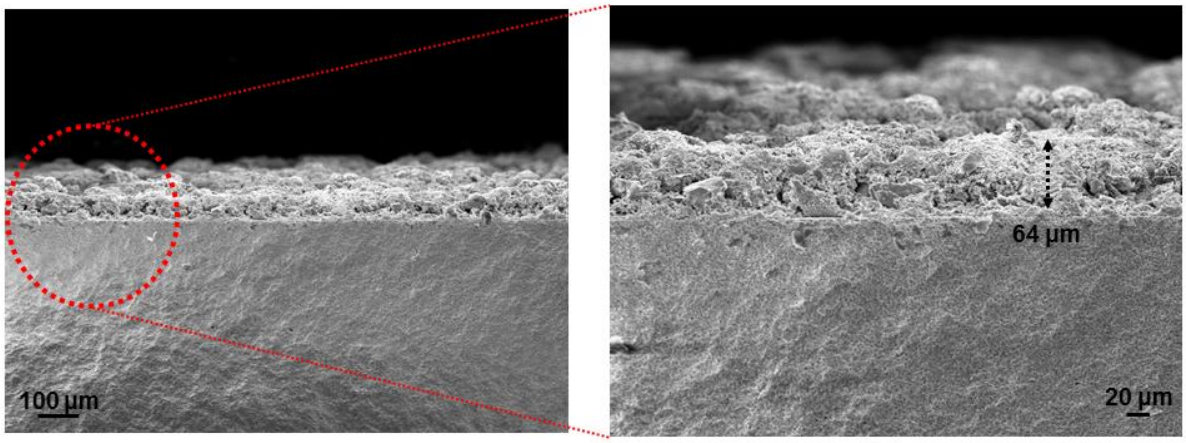

Figure 2.21: Cross sectional SEM image of MD composite developed.

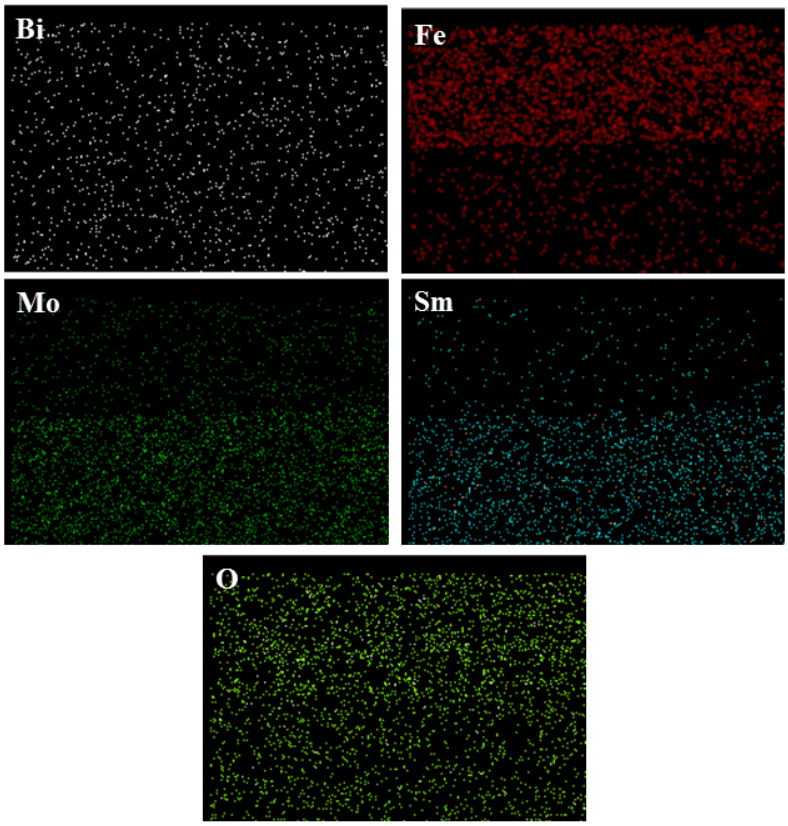

Figure 2.22: Elemental mapping of sectional image of BSMO-BFO composite films.

Elemental composition of the developed composite has been reviewed with the help of elemental mapping associated with SEM and EDAX technique as shown in figure

2.22. Bi and O are observed throughout the sample, obviously. Fe, Sm and Mo concentrations can be observed at the areas were their compositional dominant layers are present (see figure 2.22).

The magnetic as well as ferroelectric nature of the MD composite (containing a multiferroic component) was studied and is shown in figure 2.23. Figure 2.23(a) shows the room temperature M-H curve for the developed composite. The composite shows a ferromagnetic nature with even feebler hysteresis characteristics, than figure 2.19(a). The suppression of magnetic properties can be attributed to the presence of a relatively thick layer of BSMO which will restrict the spins in BFO layer to align in the field direction.

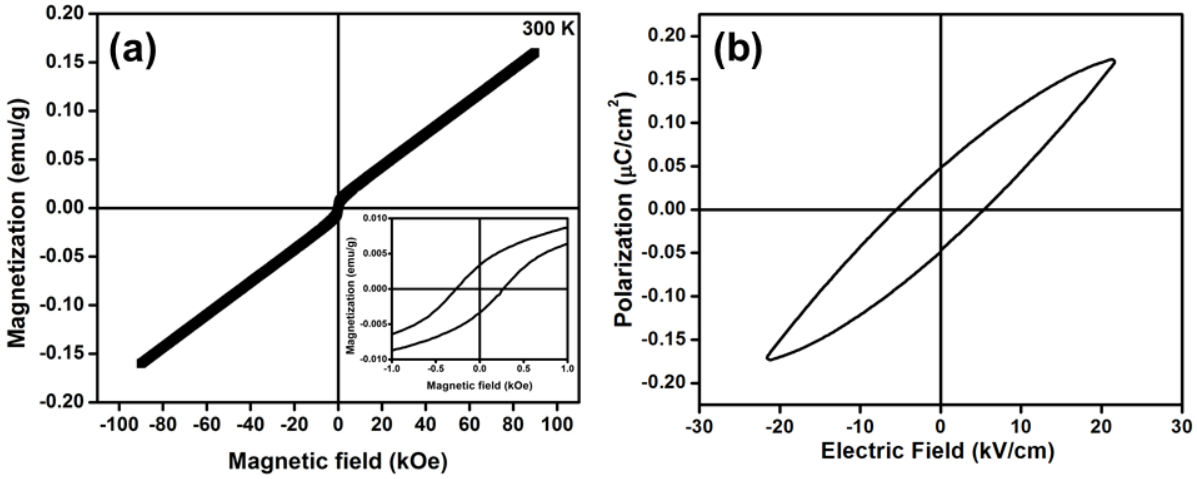

Figure 2.23: (a) M-H curve and (b) P-E curve of MD composite measured at room temperature.

The P-E curve for the MD composite was measured at 99 V and 100 Hz (see figure 2.23(b)). A seemingly leaky dielectric response was observed for the composite with a very low value of P_r (0.05 μC/cm^2). The inherent porosity associated with the evaporation of solvents from BFO layer will be the main reason for the decreased P_r

value. However, the samples were able to bear a voltage of 20 kV/cm, without any break down.

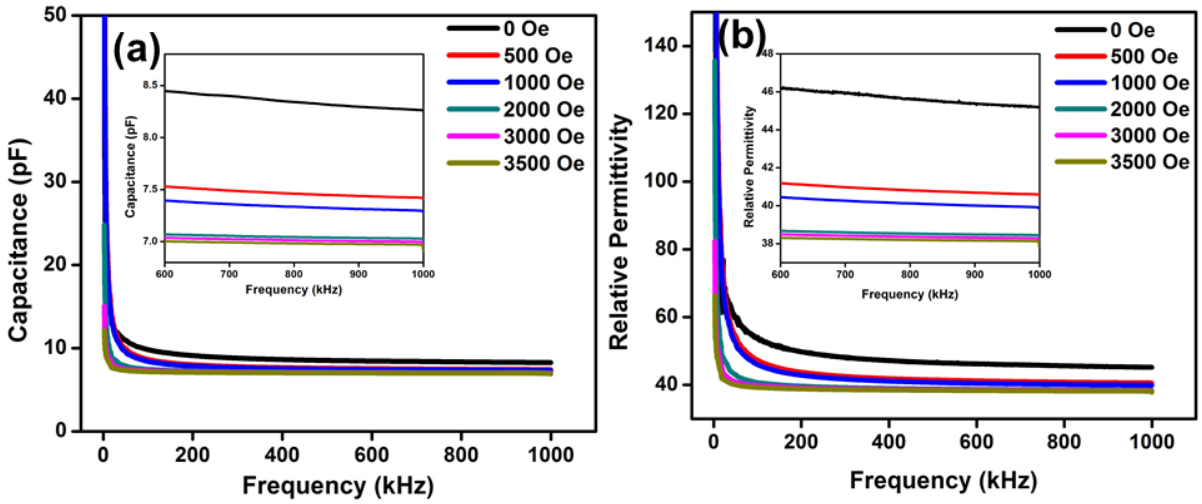

Figure 2.24: (a) Variation of capacitance and (b) variation of relative permittivity as a function of frequency, with and without the application of magnetic field.

In order to study the MD property of developed composite, the variation of capacitance with and without magnetic field is studied which is shown in figure 2.24(a). Evidently, the capacitance shows a decrease in value when an external magnetic field is applied. When the intensity of magnetic field increases, capacitance further decreases which is clearly seen from the enlarged image in the inset of 2.24(a). Since relative permittivity has direct dependence with capacitance ($C \propto \varepsilon_r$), this variation will reflect in its values too. The variation of relative permittivity with frequency is represented in figure 2.24(b). At low frequencies, relative permittivity shows high values which decreases as a function of frequency. The high value of ε_r at low frequencies can be attributed to the net effect of four types of polarizations namely, interfacial, dipolar, ionic and electronic, where interfacial polarization dominates. But as frequency

increases, other polarization will separate out sequentially, leaving out ionic and electronic polarization at frequencies above conventional radio frequency range. Here in this range, the rapid fall in ε_r is unseen, which assumes steady values, even though decreasing. Enlarged portion from 600 kHz to 1 MHz is shown at the inset of figure 2.24(b). From the graph, it is clear that when no magnetic field is applied, the relative permittivity of composite comes around 45, which decreases when the magnetic field is increased. This shows that magnetic field has a strong dependence on the dielectric counterpart in the composite which will eventually give rise to MD coupling. Usually MD coupling is expressed in terms of magnetocapacitance and is described in equation 1.17.

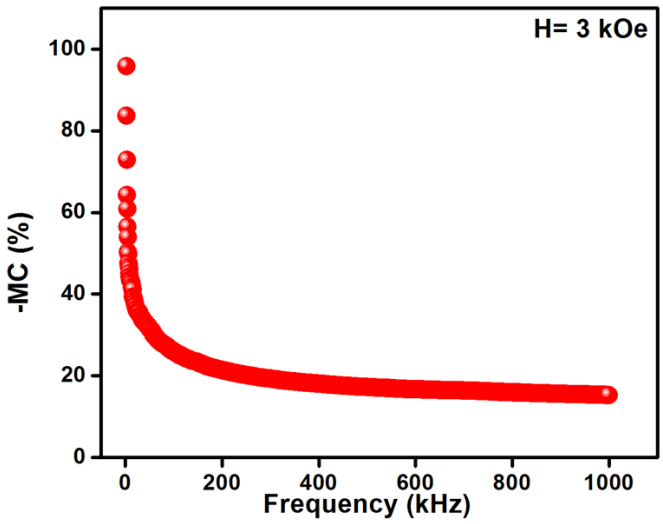

Figure 2.25: Variation of magnetocapacitance with frequency at 3 kOe magnetic field.

In the present case, the variation of magnetocapacitance is noted at 3 kOe magnetic field and is shown in figure 2.25. The variation of magnetocapacitance shows a similar decreasing trend with respect to frequency. One can observe a negative value for magnetocapacitance as the relative permittivity decreases under the application of

magnetic field. At 1 MHz, the magnetocapacitance is observed as -15%. The observance of MD property in $BiFeO_3$ screen printed on $BiSmMoO_6$ based LTCC substrate at room temperature is a promising result towards the generation antenna miniaturization, where the (2-2) laminar composite can serve as the substrate with higher bandwidth, more impedance matching and ease of miniaturization. Further, these kind of structures are also useful in creating electromagnetic band gap structure (EBG), which is supposed to exhibit efficient band rejection at lower frequencies.[6]

2.5 Conclusions

This chapter deals with developing a novel kind of MD substrate, assimilating the concepts of LTCC technology. The core idea is to make a tape castable–printable layered (2-2) composite, whose dielectric properties vary under magnetic field. For that, an ultra-low loss dielectric material was qualified and we reduced its sintering temperature by adding a little amount of BBSZ glass, aimed to broaden its applicability to LTCC. The glass-ceramic based on $BiSmMoO_6$-2 wt.% BBSZ was sintered at 875 ˚C. The developed substrate has got good thermal and mechanical properties. The microwave dielectric properties showed that the LTCC composition posses an ultra-low loss of the order of $9x10^{-4}$ at 5 GHz. The magnetic component chosen was a well known single phase multiferroic, $BiFeO_3$. After exploring its structural, microstructural, ferrroelectric and magnetic characteristics, we tried making a room temperature curable ink out of the developed BFO nanopowder. The printed BFO ink shown a relative permittivity value of 64 where as for bulk, the value is 130, at 1 MHz. This BFO ink was later screen printed on the LTCC substrate, to form a laminate type composite.

Under the applicationof 3 kOe magnetic field, we could observe a negative magnetocapacitance value upto 15%. The developed composite possesses multiferroicity along with magnetoelectric coupling which can be utilized in the field of antenna miniaturization and electronic bandgap applications.

2.6 References

(1) Han, K. H. Magneto-Dielectric Material Characterization and RF Antenna Design, Georgia Institute of Technology, **2015**.

(2) Han, K.; Swaminathan, M.; Pulugurtha, R.; Sharma, H.; Tummala, R.; Rawlings, B. M.; Nair, V. RF Characterization of Magnetodielectric Material Using Cavity Perturbation Technique. *IEEE Trans. Components, Packag. Manuf. Technol.* **2015**, *5* (12), 1850–1859.

(3) Colburn, J. S. Patch Antennas on Externally Perforated High Dielectric Constant Substrates. *IEEE Trans. Antennas Propag.* **1999**, *47* (12), 1785–1794.

(4) Ikonen, P.; Rozanov, K. N.; Osipov, A. V; Tretyakov, S. A. Magneto-Dielectric Substrates in Antenna Miniaturization : Potential and Limitations. *IEEE Trans. Antennas Propag.* **2006**, *54* (11), 3391–3399.

(5) Ikonen, P. M. T.; Rozanov, K. N.; Osipov, A. V.; Alitalo, P.; Tretyakov, S. A. Magnetodielectric Substrates in Antenna Miniaturization: Potential and Limitations. *IEEE Trans. Antennas Propag.* **2006**, *54* (11), 3391–3399.

(6) Mosallaei, H.; Sarabandi, K. Magneto-Dielectrics in Electromagnetics: Concept and Applications. *IEEE Trans. Antennas Propag.* **2004**, *52* (6), 1558–1567.

(7) Yang, H.; Bai, L.; Lin, Y.; Wang, F.; Wang, T. Magneto-Dielectric Laminated $Ba(Fe_{0.5}Nb_{0.5})O_3$-$Bi_{0.2}Y_{2.8}Fe_5O_{12}$ Composites with High Dielectric Constant and High Permeability. *Ceram. Int.* **2017**, *43* (3), 2903–2909.

(8) Lin, Y.; Liu, X.; Yang, H.; Wang, F.; Liu, C.; Wang, X. Laminated $SrTiO_3$-$Ni_{0.8}Zn_{0.2}Fe_2O_4$ Magneto-Dielectric Composites for High Frequency Applications. *J. Alloys Compd.* **2016**, *688*, 571–576.

(9) Lin, Y.; Liu, X.; Yang, H.; Wang, F.; Liu, C. Magnetic and Dielectric Properties of Laminated $Ca(Zn_{1/3}Nb_{2/3})O_3$-$Ni_{0.8}Zn_{0.2}Fe_2O_4$ Magneto-Dielectric Composites. *Mater. Res. Bull.* **2017**, *86*, 101–106.

(10) Yao, Y. P.; Hou, Y.; Dong, S. N.; Li, X. G. Giant Magnetodielectric Effect in Terfenol-

DPZT Magnetoelectric Laminate Composite. *J. Appl. Phys.* **2011**, *110* (1).

(11) Zhou, D.; Wang, H.; Pang, L. X.; Randall, C. A.; Yao, X. Bi_2O_3-MoO_3 Binary System: An Alternative Ultralow Sintering Temperature Microwave Dielectric. *J. Am. Ceram. Soc.* **2009**, *92* (10), 2242–2246.

(12) Li, H.; Huang, Z.; Cheng, L.; Kong, S.; Liu, S. Structure and Dielectric Properties of Novel Low Temperature Co-Fired Bi_2O_3-RE_2O_3-MoO_3(RE=Pr, Nd, Sm, and Yb) Based Microwave Ceramics. *Ceram. Int.* **2017**, *43* (5), 4570–4575.

(13) Hsiang, H. I.; Chen, T. H. Electrical Properties of Low-Temperature-Fired Ferrite-Dielectric Composites. *Ceram. Int.* **2009**, *35* (5), 2035–2039.

(14) Thomas, S.; Sebastian, M. T. Effect of B_2O_3-Bi_2O_3-SiO_2-ZnO Glass on the Sintering and Microwave Dielectric Properties of $0.83ZnAl_2O_4$-$0.17TiO_2$. *Mater. Res. Bull.* **2008**, *43* (4), 843–851.

(15) Dernovsek, O.; Naeini, A.; Preu, G.; Wersing, W.; Eberstein, M.; Schiller, W. A. LTCC Glass-Ceramic Composites for Microwave Application. *J. Eur. Ceram. Soc.* **2001**, *21* (10–11), 1693–1697.

(16) Hsiang, H.-I.; Chen, T.-H. Dielectric and Magnetic Properties of Low-Temperature-Fired Ferrite–Dielectric Composites. *J. Am. Ceram. Soc.* **2008**, *91* (6), 2043–2046.

(17) Yuan, J.; Hou, Z.; Yang, H.; Li, Y.; Kang, Y.; Song, W. High Dielectric Loss and Microwave Absorption Behavior of Multiferroic $BiFeO_3$ Ceramic. *Ceram. Int.* **2013**, 1–6.

(18) Kayani, Z. N.; Riaz, S.; Naseem, S. Preparation of $BiFeO_3$ Films By Sol-Gel Technique and Their Characterization. *Sci. Int.* **2011**, *23* (4), 255–258.

(19) Liu, T.; Xu, Y.; Zhao, J. Low-Temperature Synthesis of $BiFeO_3$ via PVA Sol-Gel Route. *J. Am. Ceram. Soc.* **2010**, *93* (11), 3637–3641.

(20) Sinha, R. R.; Sinha, S. K.; Mursaleen, M.; Bera, S.; Mahta, J.; Kumar, A. Synthesis of Bismuth Ferrite Nano Particles by Sol-Gel Method and Their Characterization. *IOSR J. Appl. Phys.* **2015**, *7* (1), 44–47.

(21) Hakki, B. W.; Coleman, P. D. A Dielectric Resonator Method of Measuring Inductive Capacities in the Millimeter Range. *IRE Trans. Microw. Theory Tech.* **1960**, *MTT-8* (4), 402–410.

(22) Chen, S.; Zhang, S.; Zhou, X.; Li, B. Thermal and Dielectric Properties of the LTCC Composites Based on the Eutectic System BaO-Al_2O_3-SiO_2-B_2O_3. *J. Mater. Sci. Mater. Electron.* **2011**, *22* (3), 238–243.

(23) Arun, S.; Sebastian, M. T.; Surendran, K. P. $Li_2ZnTi_3O_8$ Based High κ LTCC Tapes for Improved Thermal Management in Hybrid Circuit Applications. *Ceram. Int.* **2017**, *43* (7), 5509–5516.

(24) Xiang, H.; Li, C.; Jantunen, H.; Fang, L.; Hill, A. E. Ultralow Loss $CaMgGeO_4$ Microwave Dielectric Ceramic and Its Chemical Compatibility with Silver Electrodes for Low-Temperature Cofired Ceramic Applications. *ACS Sustain. Chem. Eng.* **2018**, *6*, 6458–6466.

(25) Parker, W. J.; Jenkins, R. J.; Butler, C. P.; Abbott, G. L. Flash Method of Determining Thermal Diffusivity, Heat Capacity, and Thermal Conductivity. *J. Appl. Phys.* **1961**, *32* (9), 1679–1684.

(26) Induja, I. J.; Abhilash, P.; Arun, S.; Surendran, K. P.; Sebastian, M. T. LTCC Tapes Based on Al_2O_3-BBSZ Glass with Improved Thermal Conductivity. *Ceram. Int.* **2015**, *41* (10), 13572–13581.

(27) Abhilash, P.; Sebastian, M. T.; Surendran, K. P. Glass Free, Non-Aqueous LTCC Tapes of $Bi_4(SiO_4)_3$with High Solid Loading. *J. Eur. Ceram. Soc.* **2015**, *35* (8), 2313–2320.

(28) Li, C.; Xiang, H.; Xu, M.; Tang, Y.; Fang, L. Li_2AGeO_4 (A = Zn , Mg): Two Novel Low-Permittivity Microwave Dielectric Ceramics with Olivine Structure. *J. Eur. Ceram. Soc.* **2017**, No. October, 0–1.

(29) Hotza, D.; Greil, P. Aqueous Tape Casting of Ceramic Powders. *Mater. Sci. Eng. a-Structural Mater. Prop. Microstruct. Process.* **1995**, *202* (1–2), 206–217.

(30) Thomas, D.; Abhilash, P.; Sebastian, M. T. Casting and Characterization of $LiMgPO_4$ glass Free LTCC Tape for Microwave Applications. *J. Eur. Ceram. Soc.* **2013**, *33* (1), 87–93.

(31) Mistler, R. E.; Twiname, E. R. *Tape Casting: Theory and Practice*; The American Ceramic Society, **2000**.

(32) Ceylan Ali, A.; Suvaci, E.; Mandal, H. Role of Organic Additives on Non-Aqueous Tape Casting of SiAlON Ceramics. *J. Eur. Ceram. Soc.* **2011**, *31* (1–2), 167–173.

(33) Albano, M. P.; Garrido, L. B. Influence of the Slip Composition on the Properties of Tape-Cast Alumina Substrates. *Ceram. Int.* **2005**, *31* (1), 57–66.

(34) Bulatova, R.; Jabbari, M.; Kaiser, A.; Della Negra, M.; Andersen, K. B.; Gurauskis, J.; Bahl, C. R. H. Thickness Control and Interface Quality as Functions of Slurry Formulation and Casting Speed in Side-by-Side Tape Casting. *J. Eur. Ceram. Soc.* **2014**, *34* (16), 4285–4295.

(35) Abhilash, P.; Roshni, S. B.; Mohanan, P.; Surendran, K. P. A Facile Development of Homemade Substrate Using 'Quench Free' Glass-Ceramic Composite and Printing Microstrip Patch Antenna on It. *Mater. Des.* **2018**, *137*, 38–46.

(36) Gurauskis, J.; Baudín, C.; Sánchez-Herencia, A. J. Tape Casting of Y-TZP with Low Binder Content. *Ceram. Int.* **2007**, *33* (6), 1099–1103.

(37) Seal, A.; Chattopadhyay, D.; Das Sharma, A.; Sen, A.; Maiti, H. S. Influence of Ambient Temperature on the Rheological Properties of Alumina Tape Casting Slurry. *J. Eur. Ceram. Soc.* **2004**, *24* (8), 2275–2283.

(38) Pushkarev, O. I. Study of the Surface Strength and Crack Resistance of Very Hard Ceramic Materials bythe Microintendation Method. *Refract. Ind. Ceram.* **2002**, *43*, 295–298.

(39) Monika, D.; N. Suri; P. K. Khanna. Optimization of Shrinkage and Surface-Roughness of LTCC Tape. *Int. J. Res. Eng. Technol.* **2013**, *2* (9), 2319–1163.

(40) Pullanchiyodan, A.; Surendran, K. P. Formulation of Sol-Gel Derived Bismuth Silicate Dielectric Ink for Flexible Electronics Applications. *Ind. Eng. Chem. Res.* **2016**, *55* (26), 7108–7155.

(41) Roshni, S. B.; Sebastian, M. T.; Surendran, K. P. Can Zinc Aluminate-Titania Composite Be an Alternative for Alumina as Microelectronic Substrate. *Sci. Rep.* **2017**, *7*, 1–13.

(42) Rosidah Alias. Structural and Dielectric Properties of Glass – Ceramic Substrate with Varied Sintering Temperatures. *INTECH Open Access Publ.* **2013**.

(43) Kunjappu, J. . *Essays in Ink Chemistry*; Nova Science Publishers: New York, **2001**.

(44) Catalan, B. G.; Scott, J. F. Physics and Applications of Bismuth Ferrite.*Adv. Mater.* **2009**, *21*, 2463–2485.

(45) Song, J.; Choi, K. S.; Yoon, S.; Sohn, W.; Hong, S. P.; Lee, T. H.; An, H.; Cho, S. Y.; Kim, S. Y.; Kim, D. H.; et al. Enhancement of Ferroelectric Properties of Superlattice-Based Epitaxial $BiFeO_3$ Thin Films via Substitutional Doping Effect. *J. Phys. Chem. C* **2019**, *123* (18), 11564–11571.

(46) Lebeugle, D.; Colson, D.; Forget, A.; Viret, M.; Bataille, A. M.; Gukasov, A. Electric-Field-Induced Spin Flop in $BiFeO_3$ Single Crystals at Room Temperature. *Phys. Rev. Lett.* **2008**, *100* (22), 1–4.

(47) Castillo, M. E.; Shvartsman, V. V.; Gobeljic, D.; Gao, Y.; Landers, J.; Wende, H.; Lupascu, D. C. Effect of Particle Size on Ferroelectric and Magnetic Properties of $BiFeO_3$ Nanopowders. *Nanotechnology* **2013**, *24* (35).

(48) Revathy, R.; Varma, M. R.; Surendran, K. P. *Effect of Morphology and Ageing on the Magnetic Properties of Nickel Nanowires*; *Mater.Res.Bull.*, **2019**; *120.* ,110576.

(49) Kiselev, S. V. .; Ozerov, R. P. .; Zhdanov, G. S. Detection of Magnetic Order in Ferroelectric BiFeO3 by Neutron Diffraction. *Sov. Phys. Dokl.* **1963**, *7* (8), 742–744.

(50) Palai, R.; Schmid, H.; Scott, J. F.; Katiyar, R. S. Raman Spectroscopy of Single-Domain Multiferroic $BiFeO_3$. *Phys. Rev. B - Condens. Matter Mater. Phys.* **2010**, *81* (6), 1–7.

(51) Godara, S.; Sinha, N.; Ray, G.; Kumar, B. Combined Structural, Electrical, Magnetic and Optical Characterization of Bismuth Ferrite Nanoparticles Synthesized by Auto-Combustion Route. *J. Asian Ceram. Soc.* **2014**, *2* (4), 416–421.

(52) Bonaccorso, F.; Bartolotta, A.; Coleman, J. N.; Backes, C. 2D-Crystal-Based Functional Inks. *Adv. Mater.* **2016**, *28* (29), 6136–6166.

(53) Joseph, A. M.; Nagendra, B.; Gowd, E. B.; Surendran, K. P. Screen-Printable Electronic Ink of Ultrathin Boron Nitride Nanosheets. *ACS Omega*, **2016**,*1*, 1220-1228.

(54) Hsu, C. P.; Guo, R. H.; Hua, C. C.; Shih, C. L.; Chen, W. T.; Chang, T. I. Effect of Polymer Binders in Screen Printing Technique of Silver Pastes. *J. Polym. Res.* **2013**, *20* (10).

(55) Varghese, J.; Teirikangas, M.; Puustinen, J.; Jantunen, H.; Sebastian, M. T. Room Temperature Curable Zirconium Silicate Dielectric Ink for Electronic Applications. *J. Mater. Chem. C* **2015**, *3* (35), 9240–9246.

(56) Dionne, G. F. Effect of Pore Size on Remanence Ratios of Magnetic Materials. *J. Appl. Phys.* **1969**, *40* (1), 431–432.

Chapter 3

FUNCTIONALLY GRADED MAGNETODIELECTRIC SUBSTRATES FOR ANTENNA MINIATURIZATION

3.1 Abstract

Miniaturization of electronic devices is the need of present hour, owing to the increasing demand of portable devices in the fields of telecommunication, consumer electronics etc. In wireless communication, one of the biggest hurdles for scaling is size reduction of antennas, since that can eventually result in direct reduction in the efficiency and bandwidth of antenna. Tailor made magnetodielectric materials can be used for the purpose of scaling in microstrip patch antennas. Polymer-ceramic composite, especially (0-3) type is suitable for this purpose, where polymer is chosen as matrix and a magnetic component as filler. Here, in the present chapter, an axially anisotropic magnetodielectric (MD) composite based on polymethyl methacrylate (PMMA)-$NiFe_2O_4$ (NFO) was developed for realizing miniaturized antennas. The structural as well as ferromagnetic properties of developed $NiFe_2O_4$ via polymer pyrolysis method were studied in detail. Thin sheets of (0-3) composites were developed by adding different volume % of NFO (say 5, 10, 15, 20 vol.%) in PMMA matrix. Structural, dielectric, magnetic as well as magnetocapacitance measurements were done on individual composites. A micro strip patch antenna operating at 830 MHz was theoretically modelled by stacking differently loaded MD wafers to form functionally graded anisotropic composite, used as the substrate. An impressive miniaturization of 91% was observed for this MD antenna when compared to normal dielectric substrates with permittivity and permeability value equals unity.

3.2 Introduction

Over the past few decades, researchers in the domain of condensed matter physics actively pursue on multifunctional materials at nanoscale, aimed to miniaturize electronic devices. One visible effort towards miniaturization is seen in wireless communication systems where antenna size reduction can be successfully achieved by choosing a high permittivity material as antenna substrate. However, strong capacitive coupling between high permittivity substrate and base plane will diminish radiation performance of the antenna. The best alternative is to choose a magnetodielectric (MD) substrate material with moderate values of relative permittivity (ε_r) and permeability (μ_r). As seen in chapter 2, magnetodielectric materials are defined as a class of multifunctional materials which are mainly composite dielectrics with magnetic particles as the filler. So under the application of magnetic field, the dielectric properties will vary, thereby enabling simultaneous ease of impedance matching and miniaturization in patch antennas. Here, high miniaturization factor ($n=\sqrt{\varepsilon_r \mu_r}$) can be reached while diminishing the strong capacitive coupling between the antenna and ground plane. In this way, the capacitive nature of the resonant patch antenna is mitigated by inductance that can further counteract the former, and thereby improving both the bandwidth and efficiency of microstrip patch antenna.[1]

Tuning of dielectric properties of a material under the application of magnetic field has been both scientifically admissible and technologically demanding.[2] Two main strategies to magnetically control the dielectric or capacitive property of a material are, (a) controlling interface physics in multilayer systems and (b) amplifying MD

effect in ferromagnetic materials near its ferromagnetic transitions.[3,4] Usually single phase MD materials possess weak magnetodielectric effect (MDE) at room temperature due to materials symmetry restrictions which will further restrict their implementation in technological applications.[5] Developing composites composed of dielectric and magnetic materials is a promising approach to generate large MDE near room temperature.[6,7] Two main mechanisms that leads to large MDE in composite materials are,[8,9]

(i) combination of magnetoresistance (MR) and Maxwell-Wagner effects.

(ii) magnetic field induced strain transfer through interface coupling.

In the first case, selection of materials for MR related MDE is broad.[10] But in the latter case, a magnetic and dielectric material coexists in the system. When magnetic field is applied, a strain will be induced in the magnetostrictive phase of composite. This generated stress at interface can induce dielectric polarization in respective component of composite system, which will eventually result in strong MDE response.[11,12]

Generally, ceramic based materials were used for developing MD composites, but they possess several disadvantages. Primarily, ceramic MDs require high temperature processing. On top of this, poor machinability of ceramics causes difficulty in designing components of desired shape. These problems can be circumvented by using polymer based composites by filling dielectric polymers with magnetic components. They possess advantages of low temperature processing, wide range of versatility, low cost, high dielectric break down field etc.[13] Following this, efforts have been made by researchers to develop polymer nanocomposites because of their

synergic and tunable properties. This chapter deals with developing a polymer nanocomposite based MD substrate for antenna miniaturization.

Here, PMMA was used as the dielectric component, which is one among the major functional polymers having low dielectric loss over wide frequency range, at room temperature.[14-16] Soft spinel ferrites based on $M^{2+}Fe^{3+}{}_2O_4$ (M=Co, Ni, Zn, Mn etc.) exhibit high saturation magnetization, low eddy current loss and high electrical conductivity.[17] Among them, $NiFe_2O_4$ has inverse spinel structure with $Fd\bar{3}m$ space group. It shows ferrimagnetism that originates from magnetic moment of anti-parallel spins between Fe^{3+} ions at tetrahedral sites and Ni^{2+} ions at octahedral sites, formed by cubic close packing of oxygen (O^{2-}) ions.[18] The present work focuses on developing (0-3) composite based on PMMA–$NiFe_2O_4$ with varying magnetic filler loading. An axially anisotropic substrate was developed by stacking the developed (0-3) composite, aimed to make MD substrates, ideal for antenna miniaturization application.

3.3 Experimental Section

3.3.1 Materials

Nickel nitrate ($Ni(NO_3)_2.6H_2O$, Sigma Aldrich), Iron nitrate ($Fe(NO_3)_3.9H_2O$, Sigma Aldrich), Ammonium persulfate ($(NH_4)_2S_2O_8$, Sigma Aldrich), Acrylic acid (Sigma Aldrich), PMMA, *N,N*-dimethylformamide (DMF, HPLC)

3.3.2 Synthesis of NFO

Polymer pyrolysis method was employed to synthesis NFO nanoparticles. This method possesses so many advantages when compared to other wet chemical synthesis

procedures, including easy operation, scaling up in the form of batch and production of highly homogeneous nanocrystalline spinel ferrites. $NiFe_2O_4$ with well-defined structure was prepared by pyrolysis of Ni-Fe polyacrylate precursors, via in situ polymerization.

Chemical reagents like $Ni(NO_3)_2.6H_2O$, $Fe(NO_3)_3.9H_2O$, $(NH_4)_2S_2O_8$ and acrylic acid were used without further purification. Initially, ferric nitrate and nickel salt were dissolved in 10 g of acrylic acid aqueous solution where acrylic acid:H_2O=70:30 wt.%, under constant stirring. Then, 0.5 g of initiator ($(NH_4)_2S_2O_8$) was added to the mixed solution in order to promote polymerization. The mixed solution was kept at 70 ˚C under constant stirring to form well distributed polyacrylate salt. The so obtained polyacrylate was dried in an oven at 100 ˚C. After drying, it was taken to calcination at different temperatures in a furnace, in O_2 atmosphere.

3.3.3 Synthesis of PMMA-NFO Composites

The polymer nanocomposites were synthesized through an in-situ method. First, PMMA was dissolved in DMF under continuous sonication. At the same time, required amount of NFO was also dissolved in DMF. After complete dissolution, both the filler and matrix were mixed together and sonicated for many hours. Finally, the composite was precipitated out from DMF by filtration and dried in a hot air oven. A series of composites were developed using this technique, namely NFO5 (5 vol.% NFO/0.05V_f NFO), NFO10 (10 vol.% NFO/0.1V_f NFO), NFO15 (15 vol.% NFO/0.15V_f NFO) and NFO20 (20 vol.% NFO/0.2V_f NFO). Various characterizations were performed using samples developed through hot pressing technique.

3.3.4 Characterization

Thermogravimetry/ differential thermal analysis (TG/DTA) of Ni-Fe precursor powder was carried out from room temperature upto 600 ˚C in air atmosphere using a thermogravimetric analyzer (TGA/DTA instrument, Shimadzu, Japan) at a rate of 10 ˚C/min. Phase purity of the calcined powders at different temperatures were analyzed using X-ray diffraction (XRD) analysis with Cu Kα radiation (X'Pert PRO diffractometer, PANalytical, Almelo, The Netherlands). The particle size of calcined NFO was characterized using high-resolution transmission electron microscopy (HRTEM) (FEI Tecnai G2 30S-TWIN, FEI Co., Hillsboro, OR, USA) by drop casting it in ethanol medium. Magnetic properties of NFO as well as composites developed were measured using a oven measurement attached to Physical Property Measurement System (PPMS Quantum Design, USA). Wide angle XRD (WAXD) was used for characterizing the phase formation of PMMA and NFO loaded samples using a Genix micro source from Xenocs operated at 50 kV and 0.6 mA. Similar to XRD analysis, here also Cu Kα radiation (λ = 1.54 Å) was used. To understand the thermal stability of PMMA and its composites, TG analysis was performed using thermogravimetric analyzer TA Q50 under N_2 atmosphere, at a heating rate of 10 ˚C/min. Thermal conductivity of samples were measured using a laser flash thermal property analyzer, Flash Line 2000 (Anter corporation, Pittsburgh). Thermomechanical analyzer (TMA/SS7300, SII NanoTechnology Inc.Tokyo, Japan) was used for characterizing the coefficient of thermal expansion for all the samples from room temperature to 80 ˚C under the application of 0.1 N force. Microstructural analysis was performed for the fractured surface of composites using an EDS coupled SEM, Zeiss EVO 18 Cryo SEM, Germany. The

magnetocapacitance (MC) measurement was performed using Wayne Kerr Impedance Analyzer (Model 6500B) which is mentioned in section 1.6.4. The theoretical simulation of proposed antenna was done using Ansys High Frequency Structure Simulator (HFSS) software.

3.4 Results and Discussion

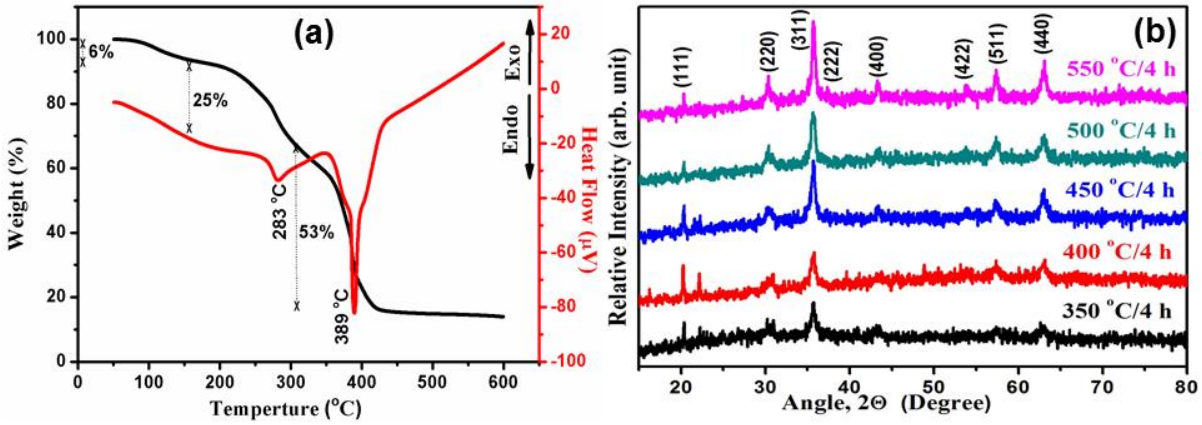

Figure 3.1: (a) TG/DTA of prepared NFO precursor powder and (b) XRD pattern of NFO calcined at different temperatures for 4 h.

Figure 3.1(a) represents TG/DTA curve of co-polymeric Ni-Fe precursors. A small weight loss of 6% is happening up to 100 ˚C, which corresponds to the removal of planar water from the powder. A minor endothermic peak is observed at 283 ˚C corresponding to a weight loss of 25% between 100 ˚C-300 ˚C, which is due to the elimination of residual solvents in the precursor. A major weight loss of around 53% is observed between the temperature range of 300 ˚C to 420 ˚C and the sharp endothermic peak at 389 ˚C corresponds to the same. This can be attributed to the thermal decomposition of polymer chains and nitrates to form oxides.[19] Figure 3.1(b) represents the XRD of NFO calcined at various temperatures ranging from 350 ˚C-550 ˚C

for 4 h. The peak intensity increases with increase in calcination temperature. The diffraction pattern obtained at 550 ˚C matches well with JCPDS file number 86-2267. Calcining at temperature ≥ 550 ˚C shows the sign of single phase spinel ferrite formation, without any impurity phase.

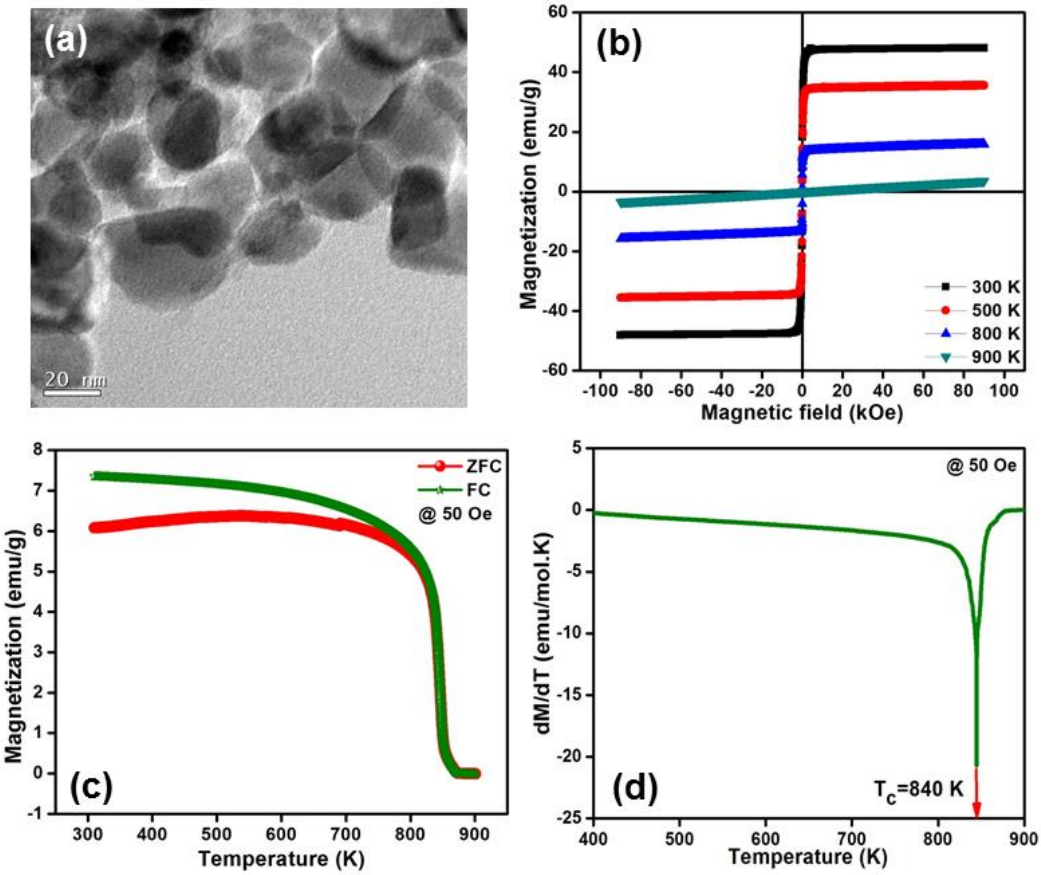

Figure 3.2: (a) TEM micrograph of NFO calcined at 550 ˚C, (b) M-H curves for NFO taken at different temperatures, (c) ZFC and FC curves taken at 50 Oe and (d) dM/dT plot showing the curie transition temperature (T_c) of developed NFO powder.

The microstructure of developed powder was characterized using TEM and is shown in figure 3.2(a). It is found that particles are possessing nanometric scale morphology ranging from 20-50 nm. In order to elucidate the magnetic behavior of synthesized NFO in an accurate manner, the variation of magnetization with respect to

magnetic field was studied at various temperatures ranging from 300 K to 900 K. The result is presented in figure 3.2(b). The M-H curve at 300 K shows negligible value for remanence and coercivity that suggests the paramagnetic behavior of developed nanocrystalline NFO particles, at temperature above T_c. The saturation magnetization (M_s) at 300 K is around 48 emu/g which is lower when compared to that of bulk NFO.[20,21] As temperature increases from 300 K to 900 K, the saturation magnetization decreases and at 900 K, it eventually became zero (paramagnetic). The magnetization vs temperature (M-T) plot gives an insight into the ferromagnetic curie temperature of a material. The M-T plot of NFO at 50 Oe is presented in figure 3.2(c). When the applied field is less, all the spins may not align in the direction of applied field, which will result in bifurcation in zero field cooled (ZFC) and field cooled (FC) curves. The point in which ZFC meets FC is called Curie temperature (T_c). For accurately determining the T_c value, dM/dT is plotted against temperature for ZFC curve, as shown in figure 3.2(d). The transition from ferromagnetic to paramagnetic nature is indicated by the sharp decrease in magnetization in this figure. The Curie temperature of NFO is found to be 840 K, which is in good agreement with the previously reported values.[22]

After studying the structural, thermal and magnetic properties of pristine NFO powder, its composites with PMMA were developed. Four composites namely, NFO5, NFO10, NFO15 and NFO20 were used for determining their suitability for application in the field of antenna miniaturization. The structural, thermal magnetic properties were studied in detail for all composites, which is discussed below.

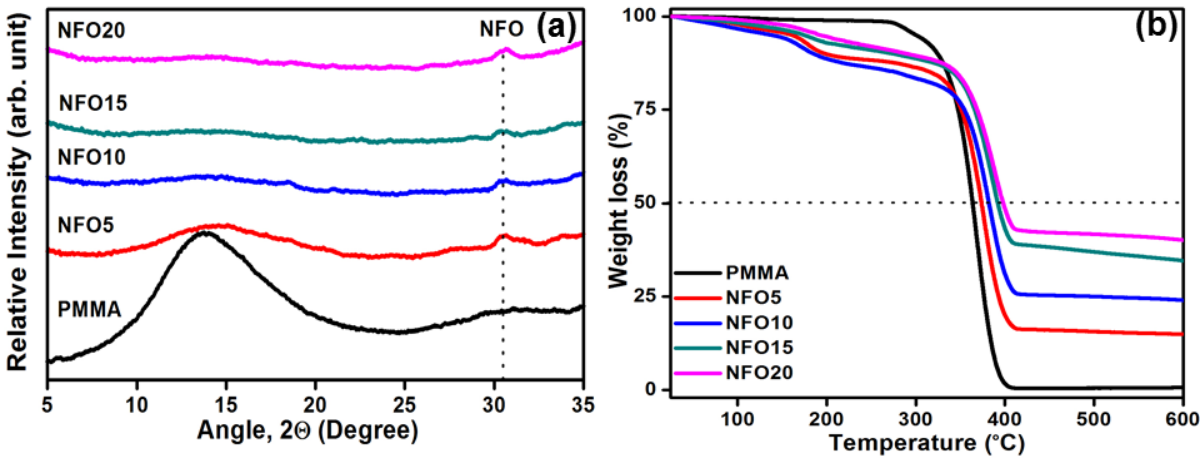

Figure 3.3: (a) WAXD of pristine PMMA along with the developed composites, (b) TG profile of PMMA and composites.

Figure 3.3(a) represents the WAXD of pristine PMMA and its composites. While scanning through the image, it is seen that PMMA is amorphous in nature. When NFO content in the composite is increased from 5 vol.% to 20 vol.%, intensity of PMMA is diminishing and a peak at 31.5˚ starts appearing. This peak corresponds to the (220) plane of NFO. Figure 3.3(b) shows the TGA thermograms for the samples. The TGA plot reveals the enhancement in thermal stability of developed composites when compared to the pure polymer. This plot clearly indicates that the decomposition temperature of composites have been progressively improved as a function of NFO content. At 50% weight loss temperature, there is an enhancement of 35 ˚C in the decomposition temperature of NFO20 when compared to pristine PMMA. This is due to the presence of high thermal conducting material NFO which results in the formation of carbonaceous char that will further act as a barrier for mass transport and delays decomposition process in composites.[23]

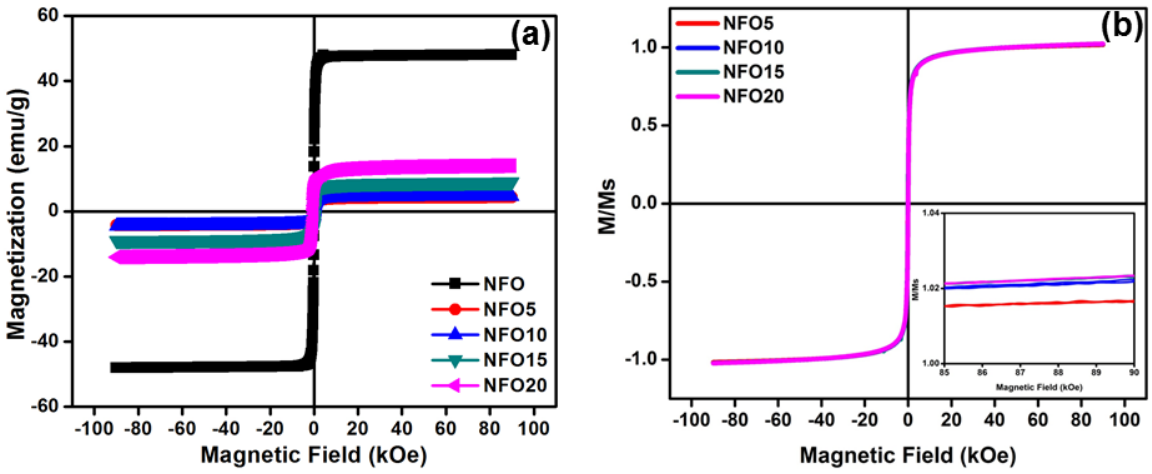

Figure 3.4: (a) M-H curves for the developed composites compared with that of pristine NFO powder, (b) normalized plot showing the increase in M/M_s value with increase in NFO content.

Figure 3.4(a) represents the magnetic characterization of PMMA-NFO composites. The M-H curve indicates that when NFO content increases, the saturation magnetization (M_s) also increases due to obvious reasons. From figure 3.4(b), it is clear that the value of M/Ms is increasing as NFO concentration (5 wt.%-20 wt.%).

Table 3.1: Remanent magnetization (M_r) and saturation magnetization (M_s) values obtained for different composites developed.

Composition	M_r (emu/g)	M_s (emu/g)
NFO5	0.5	3.9
NFO10	0.8	4.7
NFO15	1.3	8.8
NFO20	2.7	14.1
NFO	6	48

Table 3.1 shows the values of M_s and remanent magnetization (M_r) of composites and pure NFO. When compared to pure NFO, the M_s value of composites is less which is due to the presence of polymeric chains that restrict the NFO spins to align when magnetic field is applied externally. Also the content of NFO is less in the case of composites. However, the ferromagnetic nature is retained in all composites due to magnetic inclusion (see figure 3.4).

In order to identify the practical application of any polymer ceramic composite in electronic industry, its thermal properties plays a crucial role. For polymers, generally thermal conductivity (TC) will be less and coefficient of thermal expansion (CTE) is likely to be very high. However, to dissipate away the heat generated in electronic devices, the materials should be of high thermal conductivity. Hence researchers are looking forward to improve thermal conductivity of polymers. Here, thermal conductivity of PMMA-NFO composites was measured and shown in figure 3.5.

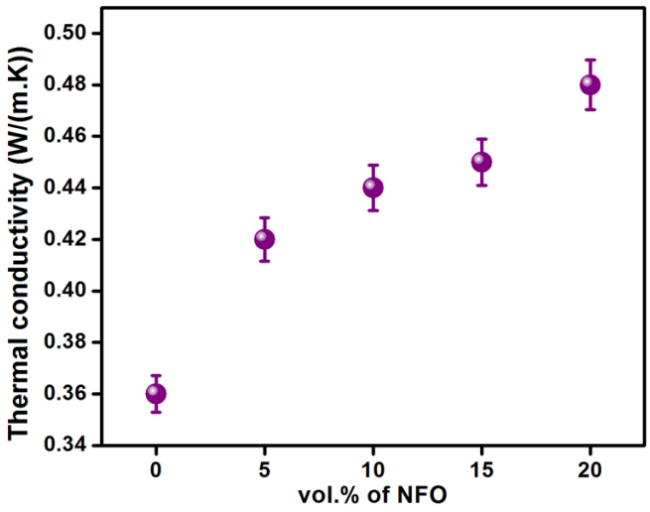

Figure 3.5: Variation in thermal conductivity with respect to filler loading.

Pure PMMA possesses a TC value of 0.36 W/m.K at room temperature, which is common in amorphous polymers. The TC starts increasing as a function of increase in NFO content and with 20 vol.%, the value obtained is 0.48 W/m.K. Usually, thermal conductivity of a material can be elevated by suppressing the phonon scattering through strong interfacial interactions.[24] For pure NFO, the reported thermal conductivity is 10 W/m.K.[25] The underlying mechanism for the enhanced thermal conductivity can be attributed to the ability of NFO particles to create pathways/continuity for conducting energy through the polymers and thereby reducing the thermal resistance.[26]

Large CTE of polymers is one of their handicaps for electronic applications. Usually polymer ceramic composites find a suitable substitute for polymers and can be used without compromising the merits of polymers. Here the CTE of PMMA, NFO and their composites were measured and values are tabulated in table 3.2.

Table 3.2: Coefficient of thermal expansion (CTE) values of samples developed.

Composition	CTE (ppm/°C)
PMMA	87.3
NFO5	84.5
NFO10	72.1
NFO15	68.1
NFO20	65.6
NFO	13.4

The thermal expansion coefficient of PMMA is reduced from 87.3 ppm/˚C to 65.6 ppm/˚C, with the addition of 20 vol.% NFO. The pure filler has got a CTE value of 13.4 ppm/˚C which is concurrent with the previous reports.[25] Interestingly, this relatively low CTE filler will restrict the growth of polymer chains which will eventually lead to low CTE value for higher filler loaded composites. As the filler content is increased, they will arrest the polymer chains to expand, when they get enough thermal energy.[27,28] This will eventually reduce the CTE value of composites with higher filler loading.

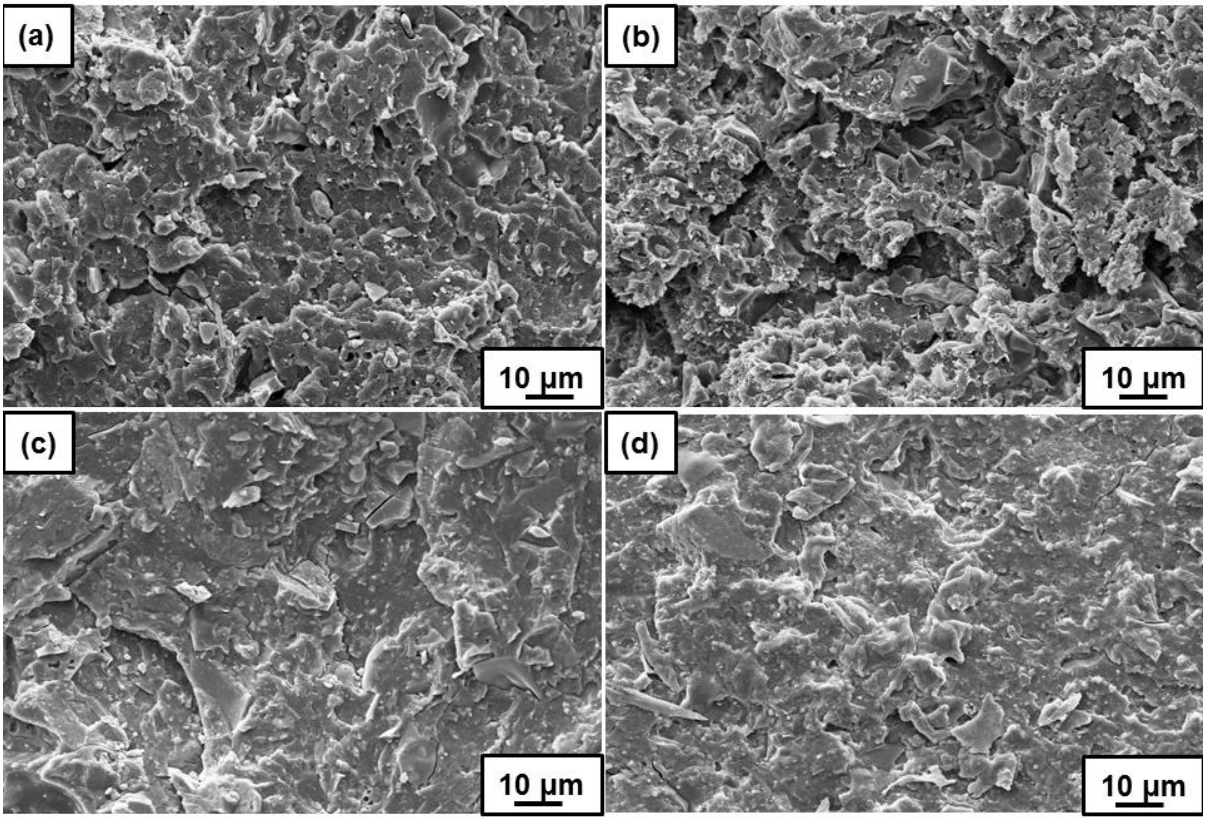

Figure 3.6: SEM micrographs of (a) NFO5, (b) NFO10, (c) NFO15 and (d) NFO20.

The SEM fractograms of all the composites are shown in figure 3.6. When the volume fraction (v_f) of NFO is increased from 0.05 to 0.2, the connectivity between the ceramic particles seemingly increases as evidenced from the figure. Higher filler loading

will lead to agglomeration in the composite. This will eventually increase the connectivity which will in turn improve the properties of composite.[27]

After studying the chemico-physical properties, the MD coupling of composites was studied. As the composite contains magnetic filler evenly dispersed in a dielectric matrix, there will be variation in relative permittivity under the application of an external magnetic field. Variation of relative permittivity as a function of frequency under zero field (without magnetic field) is shown in figure 3.7.

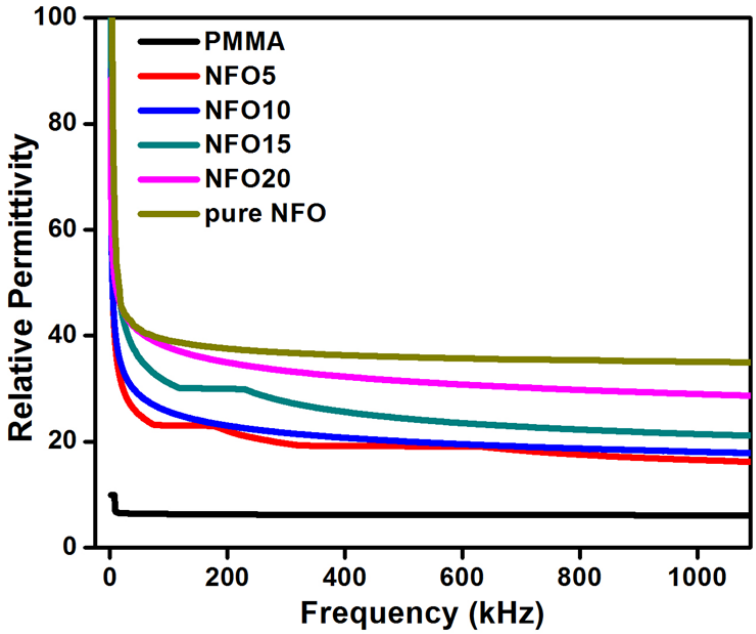

Figure 3.7: Variation of relative permittivity of developed samples with respect to frequency.

From the figure, it is clear that relative permittivity decreases with increase in frequency. Usually in low frequency region, the net polarization will be contributed by interfacial, dipolar, ionic and electronic polarizations whereas interfacial one being the dominant. But when frequency increases, the contribution from different polarization mechanisms separates out. Due to this, net polarization will decrease as a function of

frequency which in turn decreases the relative permittivity of material. The values of relative permittivity measured at 1 MHz are given in table 3.3.

For normal intrinsic dielectrics, the dielectric properties are unaltered even if a magnetic field is applied, whereas for MDs, they do. Look at the variation of dielectric permittivity with the application of 3 kOe magnetic field in figure 3.8. Here, one can observe a decrease in the values of relative permittivity for all the composites developed when a magnetic field of 3 kOe is applied. This confirms the existence of magnetocapacitance in the developed composites, which can occur due to several reasons like chemical inhomogeneity and electrical heterogeneity.

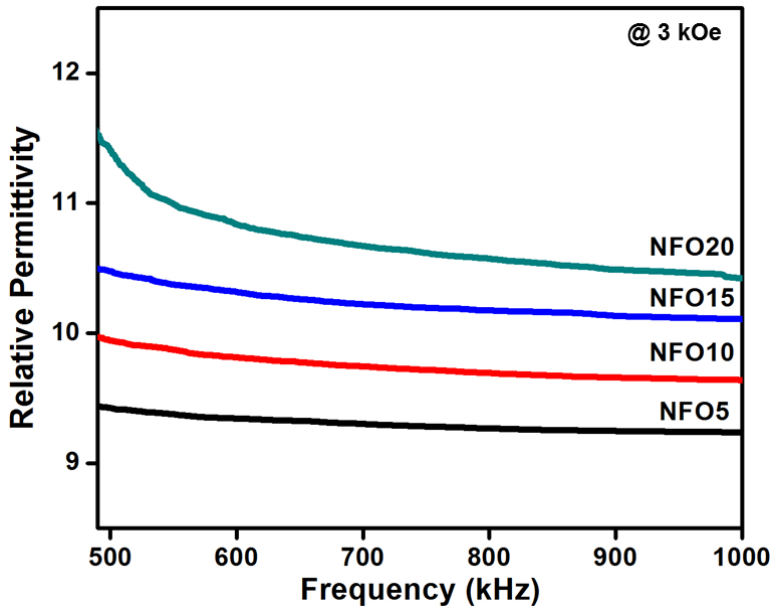

Figure 3.8: Variation of relative permittivity of developed PMMA-NFO composites under the application of 3 kOe magnetic field.

The coupling between magnetic and electric polarization is to be understood more profoundly, which is usually estimated qualitatively by measuring the variation in relative permittivity under the application of an external magnetic field. This change in

relative permittivity with magnetic field is termed as MD coupling which is defined as in equation 1.17.

PMMA is a known diamagnetic material, and hence it will not show any variation of relative permittivity with magnetic field. Here, all composites show a variation in relative permittivity when magnetic field is applied, which is summarized in table 3.3. As shown, the samples show a decrease in relative permittivity under field and hence result in negative value for MD coupling coefficient. It should be noted that the composite samples exhibit high level of MD coupling which can happen due to the magnetostrictive strain produced by multiferroic spinel, NFO. This strain in turn induce variations in the dipolar order within the polymer, giving rise to different dipolar mobility when a magnetic field is applied.[13] Thus the permittivity of NFO-PMMA system decreases with the application of a strong magnetic field.

Table 3.3: MD properties of PMMA-NFO composites developed.

Composition	Relative permittivity at 1 MHz		-MC (%) at 1 MHz
	without field	with 3 kOe field	
PMMA	6.0	_	_
NFO5	16.5	9.2	44.2
NFO10	18.1	9.6	46.7
NFO15	21.4	10.1	52.8
NFO20	28.0	10.4	62.7
NFO	35.0	_	_

In case of non-ferroelectric MD systems, usually second derivative of Ginzburg–Landau free energy is taken with respect to polarization and is proportional to M^2, where M is the magnetization.[29,30] It is clear that the magnetization value increases with increase in filler loading, as per table 3.1. Hence, MD coupling increases as the volume fraction of NFO is increased from 0.05 to 0.2 in PMMA matrix.

Figure 3.9 represents the variation of magnetocapacitance as a function of applied magnetic field at 1 MHz. Here, the magnetocapacitance shows an increasing trend as magnetic field is increased. However, no signature of the existence of an electromechanical resonance frequency is visible anywhere in the frequency range we examined.

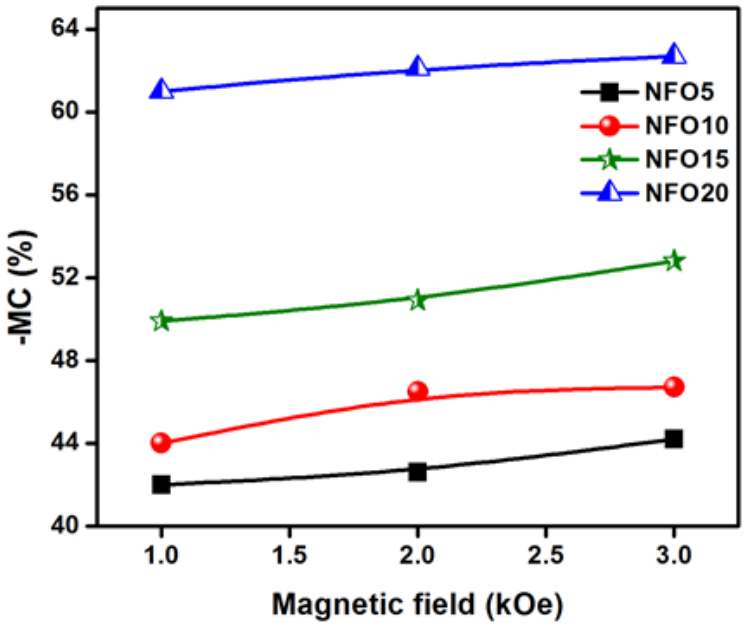

Figure 3.9: Variation of magnetocapacitance with the application of different magnetic fields in the PMMA-NFO composites

As the MD properties show promising results, they can be further used for the benefit of antenna miniaturization. Our idea is to explore whether the developed

composites can be used as substrates for antenna miniaturization, as they have agreeing values for both relative permittivity and magnetic permeability. This will in turn reduce the resonant wave length of half wave patch antennas and hence miniaturize them. For achieving this, the dielectric and magnetic properties of the material has to be tuned carefully without compromising the low loss behaviour. Tailoring the properties of such a single layer MD substrate is inappropriate for a wide spectrum of operational frequencies and the size reduction also quenches the bandwidth, S_{11}, directivity of the antennas compared with a dielectric substrate due to field confinement.[31] Graded composites are recently evolving as a solution to this problem and they can effectively improve the antenna charecteristics.[32] Additional miniaturization is also reported for uniaxially graded composites as the top to down reduction in functionality imparts a blue shift in the resonant wavelength.[33]

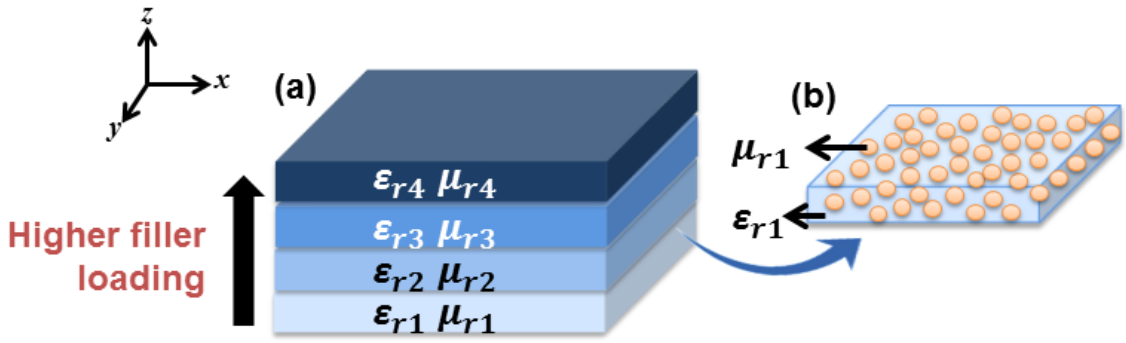

Figure 3.10: Schematic showing (a) developed functionally graded MD substrate and (b) single layer of composite that contain magnetic filler in the PMMA matrix.

Hence we developed a functionally graded anisotropic substrate in which the properties like ε_r and μ_r varies in the z plane (figure 3.10(a)), through polymer hot pressing technique. This can be conveniently realized by stacking the four developed composites together with single layer consisting of NFO fillers embedded in PMMA

matrix (figure 3.10(b)). The composite having minimum filler loading is kept near ground plane and then arranging the rest with increase in filler loading to the patch will result in a functionally graded substrate as shown in figure 3.10(a).

For understanding the values of ε_r and μ_r, in composites with different volume fraction of NFO ($0.05V_f$, $0.1V_f$, $0.15V_f$, $0.2V_f$), waveguide measurements in X band using Nicolson-Ross-Weir method[34] were taken, which are shown in figure 3.11.

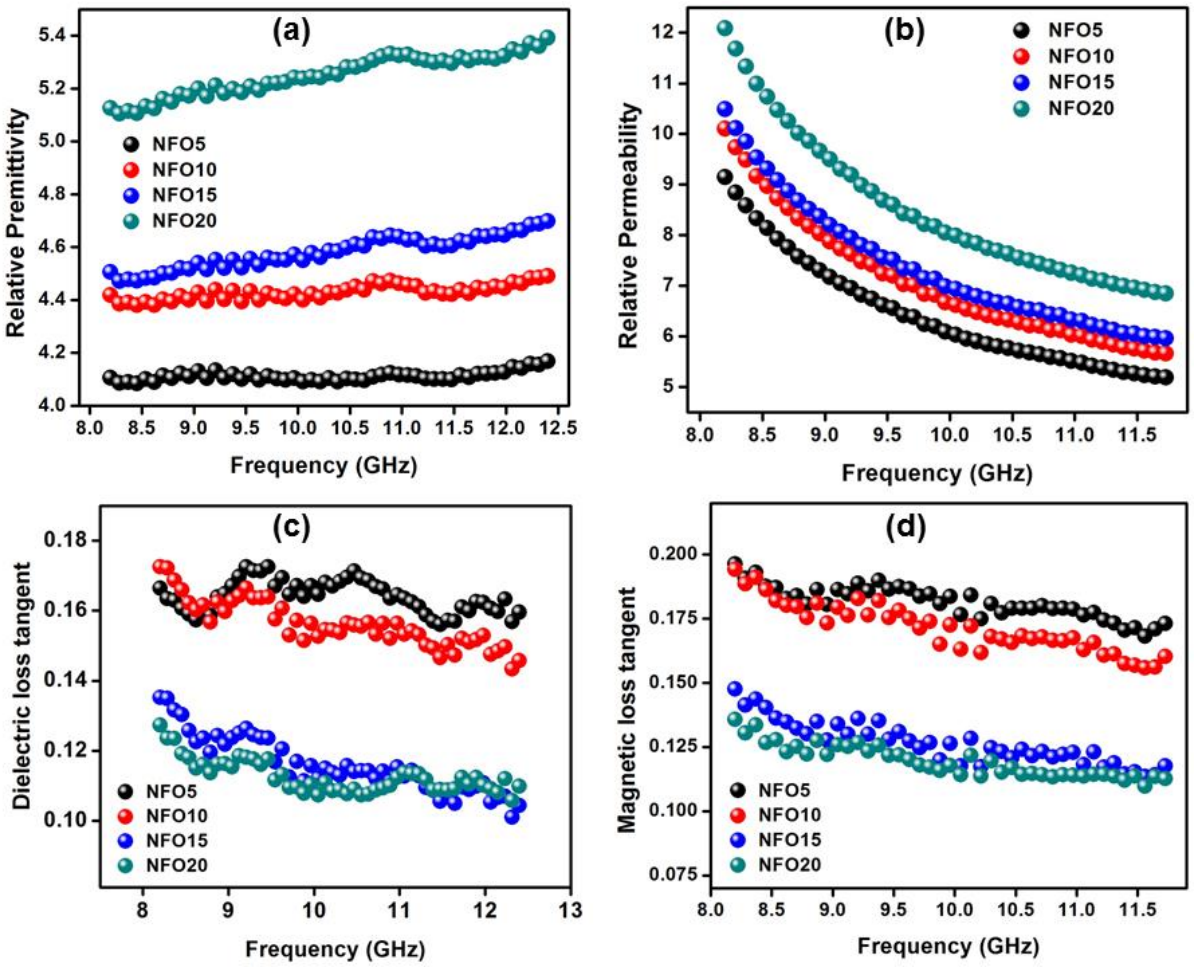

Figure 3.11: Variation of (a) relative permittivity, (b) relative permeability, (c) dielectric loss tangent and (d) magnetic loss tangent as a function of frequency in X band.

The variation of real part of relative permittivity and relative permeability with respect to frequency is shown in figure 3.11(a) and (b) respectively. The real part in dielectric and magnetic property is attributed to the ability of dipoles and spins to store electric and magnetic energy, respectively.[35] The relative permittivity of the composite increases with increase in filler content. This is due to the incorporation of higher amount of NFO which is having a higher relative permittivity (due to higher polarizability) than PMMA matrix. Marginal variation is seen for the values of relative permittivity with respect to frequency. In case of relative permeability, the value increases with increase in filler content and is obviously due to the higher amount of magnetic component in the composite. The dielectric loss tangent and magnetic loss tangent are shown in figure 3.11(c) and (d) respectively. The ratio of imaginary to real part of relative permittivity and relative permeability is given by dielectric as well as magnetic loss tangents. The loss values are in the order of 10^{-1} for all composites and show a marginal dispersion which is only within the error limits of the waveguide measurement setup. The applicability of the developed functionally graded composite as an antenna substrate is challenging here, due to its slightly lossy dielectric behavior. Rather, this developed composite can be used as a loading in low loss substrate, beneath the patch, so as to reduce the antenna dimensions effectively without compromising the antenna performance.[36,37] One has to carefully choose the geometry of such a loading, as it is reported to control the characteristics of the radiation pattern.

Herein, microstrip patch antenna (MPA) on a low loss Arlon substrate loaded with the functionally graded composite beneath the patch was theoretically designed and modeled to operate at 830 MHz. If one could fabricate an MPA operating at this

frequency employing a dielectric substrate (ε_r = μ_r = 1), the dimensions of its patch will be 175.01 mm in length and 180.72 mm in width which gives an area of 31627. 8 mm^2 for the patch. But when we use a MD material as a loading in the antenna substrate the dimensions of patch were reduced to 38.67mm in length and 73.32mm in width. Interestingly, this modification will eventually reduce the area of patch to 2835.38 mm^2. For identifying the impact of the developed substrates in the field of antenna size miniaturization we have to find the miniaturization factor. Miniaturization factor is defined by the expression,

$$n = \sqrt{\varepsilon_{reff}\, \mu_{reff}} \tag{3.1}$$

where ε_{reff} and μ_{reff} represents the effective relative permittivity and effective relative permeability of the developed material respectively. The miniaturization factor obtained for the present antenna is 4.96.

The percentage miniaturization attained for a MD antenna is calculated by the equation 3.2.

Percentage minaturization

$$= \left\{ \frac{\text{Area of patch}_{(\varepsilon_r = \mu_r = 1)} - \text{Area of patch}_{(\varepsilon_r,\ \mu_r)}}{\text{Area of patch}_{(\varepsilon_r = \mu_r = 1)}} \right\} \text{x } 100\ \% \tag{3.2}$$

For the current MD antenna, percentage miniaturization was calculated to be 91.03%. In next generation communication devices aiming for huge antenna miniaturization, the figures obtained in the present research is significant. Hence we can conclude that the newly developed MD functionally graded composite with PMMA-

$NiFe_2O_4$ is a potential candidate in the field of antenna miniaturization. Figure 3.12 is a schematic representation that shows a normal dielectric substrate antenna that can be replaced by a functionally graded anisotropic antenna with 91% size reduction.

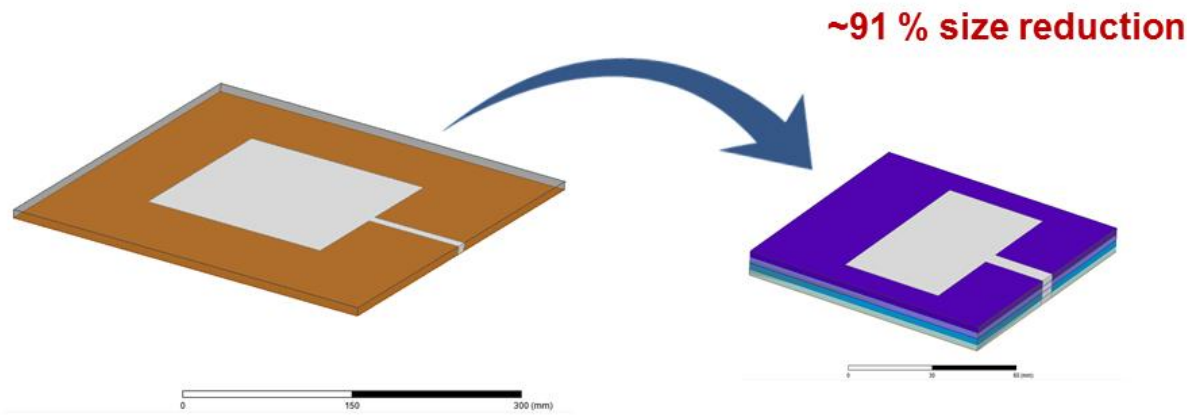

Figure 3.12: Schematic showing the reduction in size of antenna using the MD substrate developed from a dielectric only substrate.

3.5 Conclusions

In comparison to dielectric only substrates, the employing of MD materials as substrates for antenna miniaturization offers many advantages in addition to impedance matching and reduced capacitive coupling. In the present study, polymer composites consisting of $NiFe_2O_4$ as magnetic phase and PMMA as dielectric phase were used for fabricating MD substrate. NFO was synthesized via polymer pyrolysis method. The structural as well as the magnetic studies were performed for the developed NFO. Composites based on PMMA and NFO were synthesized using solution blending technique, using DMF as the solvent. The structural, microstructural and magnetic characterizations were performed over various volume fractions NFO loaded samples (0.05 V_f, 0.1 V_f, 0.15 V_f and 0.2 V_f). The MD measurements showed that maximum filler

loaded sample has got an impressive magnetocapacitance value of -62.7%. A functionally graded anisotropic composite was made by horizontally stacking the different filler loaded samples together in functionally gradient way, since such a design can bring about a blue shift in the resonant wavelength. An antenna was theoretically designed to operate at 830 MHz using the properties of developed anisotropic composite as loading in the substrate. It was observed that a whopping 91% size reduction can be attained using the present functionally graded composite when compared to a substrate material having ($\varepsilon_r = \mu_r = 1$). Hence, the developed composite is a potential candidate for its application in the field of antenna miniaturization.

3.6 References

(1) Mosallaei, H.; Sarabandi, K. Magneto-Dielectrics in Electromagnetics: Concept and Applications. *IEEE Trans. Antennas Propag.* **2004**, *52* (6), 1558–1567.

(2) Hur, N.; Park, S.; Sharma, P. A.; Guha, S.; Cheong, S. Colossal Magnetodielectric Effects in $DyMn_2O_5$. *Phys. Rev. Lett.* **2004**, *93* (September), 3–6.

(3) Folen, V. J.; Rado, G. T.; Stalder, E. W. Anisotropy of the Magnetoelectric Effect in Cr_20_3. *Phys. Rev. Lett.* **1961**, *6* (11), 607–608.

(4) Huang, Z.; Cao, Y.; Sun, Y.; Xue, Y.; Chu, C. Coupling between the Ferroelectric and Antiferromagnetic Orders. *Phys. Rev. B - Condens. Matter Mater. Phys.* **1997**, *56* (5), 2623–2626.

(5) Tokunaga, Y.; Furukawa, N.; Sakai, H.; Taguchi, Y.; Arima, T. H.; Tokura, Y. Composite Domain Walls in a Multiferroic Perovskite Ferrite. *Nat. Mater.* **2009**, *8* (7), 558–562.

(6) Subramanian, M. A.; He, T.; Chen, J.; Rogado, N. S.; Calvarese, T. G.; Sleight, A. W. Giant Room-Temperature Magnetodielectric Response in the Electronic Ferroelectric $LuFe_2O_4$. *Adv. Mater.* **2006**, *18* (13), 1737–1739.

(7) Lisnevskaya, I. V.; Bobrova, I. A.; Lupeiko, T. G.; Agamirzoeva, M. R.; Myagkaya, K. V. $Y_3Fe_5O_{12}$/Na,Bi,Sr-Doped PZT Particulate Magnetoelectric Composites. *J. Magn. Magn. Mater.* **2016**, *405*, 62–65.

(8) Wu, Y.; Li, J.; Zhang, Z. Q.; Chan, C. T. Effective Medium Theory for Magnetodielectric Composites: Beyond the Long-Wavelength Limit. *Phys. Rev. B -*

Condens. Matter Mater. Phys. **2006**, *74* (8), 1–9.

(9) Naveed Ul-Haq, M.; Yunus, T.; Mumtaz, A.; Shvartsman, V. V.; Lupascu, D. C. Magnetodielectric Effect in Relaxor/Ferrimagnetic Composites. *J. Alloys Compd.* **2015**, *640*, 462–467.

(10) Yao, Y. P.; Hou, Y.; Dong, S. N.; Li, X. G. Giant Magnetodielectric Effect in Terfenol-DPZT Magnetoelectric Laminate Composite. *J. Appl. Phys.* **2011**, *110* (1).

(11) Han, Y.; Li, L.; Guo, D.; Ren, X.; Xia, W. Magnetodielectric Effect in $NaNbO_3$-$NiFe_2O_4$ Particulate Composite. *Mater. Lett.* **2013**, *98*, 19–21.

(12) Martins, P.; Lanceros-Méndez, S. Polymer-Based Magnetoelectric Materials. *Adv. Funct. Mater.* **2013**, *23* (27), 3371–3385.

(13) Martins, P.; Silva, D.; Silva, M. P.; Lanceros-Mendez, S. Improved Magnetodielectric Coefficient on Polymer Based Composites through Enhanced Indirect Magnetoelectric Coupling. *Appl. Phys. Lett.* **2016**, *109* (11), 1–20.

(14) Ramesh, S.; Wen, L. C. Investigation on the Effects of Addition of SiO_2 Nanoparticles on Ionic Conductivity, FTIR, and Thermal Properties of Nanocomposite PMMA-$LiCF_3SO_3$-SiO_2. *Ionics (Kiel).* **2010**, *16* (3), 255–262.

(15) Demir, M. M.; Koynov, K.; Akbey, Ü.; Bubeck, C.; Park, I.; Lieberwirth, I.; Wegner, G. Optical Properties of Composites of PMMA and Surface-Modified Zincite Nanoparticles. *Macromolecules* **2007**, *40* (4), 1089–1100.

(16) Nasr, G. M.; Mousa, E.; Haroun, M. M. Lithium Ferrite ($LiFe_5O_8$)/Polymethyl Methacrylate (PMMA) Nano-Composite Used in High Dielectric Constant Capacitor and Electromagnetic Applications. *Egypt. J. Pet.* **2019**.

(17) Maji, P.; Choudhary, R. B. Facile Synthesis, Dielectric Properties and Electrocatalytic Activities of PMMA-$NiFe_2O_4$ Nanocomposite. *Mater. Chem. Phys.* **2017**, *193*, 391–400.

(18) Wang, J.; Ren, F.; Yi, R.; Yan, A.; Qiu, G.; Liu, X. Solvothermal Synthesis and Magnetic Properties of Size-Controlled Nickel Ferrite Nanoparticles. *J. Alloys Compd.* **2009**, *479* (1–2), 791–796.

(19) Liu, X.; Yang, G.; Fu, S. Mass Synthesis of Nanocrystalline Spinel Ferrites by a Polymer-Pyrolysis Route. *Mater. Sci. Eng. C* **2007**, *27*, 750–755.

(20) Hessien, M. M.; Mostafa, N. Y.; Abd-Elkader, O. H. Influence of Carboxylic Acid Type on Microstructure and Magnetic Properties of Polymeric Complex Sol-Gel Driven $NiFe_2O_4$. *J. Magn. Magn. Mater.* **2016**, *398*, 109–115.

(21) Zhang, Z.; Liu, Y.; Yao, G.; Zu, G.; Wu, D.; Hao, Y. Synthesis and Characterization of Dense and Fine Nickel Ferrite Ceramics through Two-Step Sintering. *Ceram. Int.* **2012**, *38* (4), 3343–3350.

(22) Nabiyouni, G.; Fesharaki, M. J.; Mozafari, M.; Amighian, J. Characterization and Magnetic Properties of Nickel Ferrite Nanoparticles Prepared by Ball Milling Technique. *Chinese Phys. Lett.* **2010**, *27* (12).

(23) Yang, N.; Xu, C.; Hou, J.; Yao, Y.; Zhang, Q.; Grami, M. E.; He, L.; Wang, N.; Qu, X. Preparation and Properties of Thermally Conductive Polyimide/Boron Nitride Composites. *RSC Adv.* **2016**, *6* (22), 18279–18287.

(24) Wang, F.; Yao, Y.; Zeng, X.; Huang, T.; Sun, R.; Xu, J.; Wong, C. P. Highly Thermally Conductive Polymer Nanocomposites Based on Boron Nitride Nanosheets Decorated with Silver Nanoparticles. *RSC Adv.* **2016**, *6* (47), 41630–41636.

(25) Nelson, A. T.; White, J. T.; Andersson, D. A.; Aguiar, J. A.; McClellan, K. J.; Byler, D. D.; Short, M. P.; Stanek, C. R. Thermal Expansion, Heat Capacity, and Thermal Conductivity of Nickel Ferrite ($NiFe_2O_4$). *J. Am. Ceram. Soc.* **2014**, *97* (5), 1559–1565.

(26) Nan, C. W.; Birringer, R.; Clarke, D. R.; Gleiter, H. Effective Thermal Conductivity of Particulate Composites with Interfacial Thermal Resistance. *J. Appl. Phys.* **1997**, *81* (10), 6692–6699.

(27) Sebastian, M. T.; Jantunen, H. Polymer-Ceramic Composites of 0-3 Connectivity for Circuits in Electronics: A Review. *Int. J. Appl. Ceram. Technol.* **2010**, *7* (4), 415–434.

(28) Holliday, L.; Robinson, J. Review: The Thermal Expansion of Composites Based on Polymers. *J. Mater. Sci.* **1973**, *8* (3), 301–311.

(29) Lawes, G.; Ramirez, A. P.; Varma, C. M.; Subramanian, M. A. Magnetodielectric Effects from Spin Fluctuations in Isostructural Ferromagnetic and Antiferromagnetic Systems. *Phys. Rev. Lett.* **2003**, *91* (25), 1–4.

(30) Lawes, G.; Kimura, T.; Varma, C. M.; Subramanian, M. A.; Rogado, N.; Cava, R. J.; Ramirez, A. P. Magnetodielectric Effects at Magnetic Ordering Transitions. *Prog. Solid State Chem.* **2009**, *37* (1), 40–54.

(31) Ikonen, P.; Rozanov, K. N.; Osipov, A. V; Tretyakov, S. A. Magneto-Dielectric Substrates in Antenna Miniaturization : Potential and Limitations. *IEEE Trans. Antennas Propag.* **2006**, *54* (11), 3391–3399.

(32) Sarmah, D.; Bhattacharyya, N.; Bhattacharyya, S. Study of Graded Composite (LDPE/TIO_2) Materials as Substrate for Microstrip Patch Antennas in X-Band. *IEEE Trans. Dielectr. Electr. Insul.* **2013**, *20* (5), 1845–1850.

(33) Bouttout, F.; Benabdelaziz, F.; Benghalia, A.; Khedrouche, D.; Fortaki, T. Uniaxially Anisotropic Substrate Effects on Resonance of Rectangular Microstrip Patch Antenn. *Electron. Lett.* **1999**, *35* (4), 255–256.

(34) Larsson, C.; Sjöberg, D.; Elmkvist, L. Waveguide Measurements of the Permittivity

and Permeability at Temperatures up to 1000 ˚C. *Tech. Rep. LUTEDX/(TEAT-7196)* **2010**.

(35) Arora, A.; Bindra, S. Tuning of Microwave Absorptive Behavior of Double Substituted Barium Hexaferrites with Change in Thickness in 26 . 5 – 40 . 0 GHz Band. *Appl. Phys. A* **2017**, *123*, 0–5.

(36) Hansen, R. C.; Burke, M. Antennas with Magneto-Dielectrics. *Microw. Opt. Technol. Lett.* **2000**, *26* (2), 75–78.

(37) Ikonen, P. M. T.; Maslovski, S. I.; Simovski, C. R.; Tretyakov, S. A. On Artificial Magnetodielectric Loading for Improving the Impedance Bandwidth Properties of Microstrip Antennas. *IEEE Trans. Antennas Propag.* **2006**, *54* (6), 1654–1662.

Chapter 4

UNUSUAL MAGNETOELECTRIC COUPLING IN ALL-PRINTED LAYERED COMPOSITES OF Pr DOPED $SrTiO_3$ AND $SrRuO_3$ THICK FILMS

4.1 Abstract

Magnetoelectric materials (ME) always draw attention of researchers since it find numerous applications in the field of magnetic/ferroelectric storage media, non-volatile memory devices, sensors etc. Among various kinds of ME composites, (2-2) connectivity is an area of key interest because of its large interfacial area between the phases, which will further result in an enhanced ME coefficient when compared to other connectivity schemes. In line with them, a novel screen printable ME ceramic based composite was investigated in detail in this paper. A magnetoelectric composite with Pr doped $SrTiO_3$ (STO) as ferroelectric component and $SrRuO_3$ (SRO) as ferromagnetic component was successfully developed via screen printing technique. The all printed ME composite exhibited a maximum ME voltage coefficient of 655 mV/cm.Oe at room temperature for dc magnetic field. All properties of STO and SRO both in bulk as well as in ink form were studied in detail. The ferroelectric, ferromagnetic nature together with ME behaviour associated with the present composite demonstrate its suitability in the fields of sensors, actuators, energy harvesters etc.

4.2 Introduction:

Ferroic materials with multiple memory states and heterogeneous read/write capacity has always fascinated scientific world for decades.[1,2,3,4] Existing technologies for memory applications include magnetic random access memory (MRAM) and ferroelectric random access memory (FeRAM). MRAM usually utilize ferromagnetic materials for data writing, but it holds slow writing speed. Also overheat is produced in device due to high current that generates the magnetic field and thereby it consumes

high energy for its operation.[5] FeRAM is a candidate for memory applications which can overcome the drawbacks of MRAM by offering faster writing speed via switching the electrical polarization states.[6] This has got a disadvantage of slower reading rates which is linked to destructive read operations.[7,8] Hence, the greatest challenge is to develop novel smart magnetoelectric (ME) devices that possess of advantages of both FeRAM and MRAM.[9,10,11]

Single phase ME materials are scare in nature due to rules pertaining to crystal symmetry and electronic configuration that restrict simultaneous occurrence of ferroelectricity and ferromagnetism in same system.[12,13] Besides, such systems usually show low magnetoelectric response.[14] In comparison with single phase materials, composite ME materials exhibit a magnetoelectric coupling which is 3-5 orders higher than single phase multiferroics, at ambient temperatures.[15,16] In heterogeneous ME composites, the magnetoelectric coupling arises as a result of strain transfer happening at phase boundaries.[17] Therefore, larger interfacial area will give a maximum strain transfer which in turn gives rise to better magnetoelectric response in the composite.[10] Exploring innovative pathways to develop ME composites is more significant due to their ability to synchronize with the IoT (Internet of Things) concept.[18] They will help in engineering the devices that can develop sustainable as well as wireless interconnected smarter devices[19] having long battery life[20], communication devices with miniaturized ME antennas[21], smart energy harvesters[22] etc.

Usually ME composites are labelled by the dimensionality of components present in the system. Of all the composite connectivity schemes proposed by Newnham[23], (2-2) configuration has got the advantages of providing more flexibility for material design

aspect, control over composition of layers in the composite and lower leakage currents.[11] Interfacial area will be larger in case of (2-2) composite which will facilitate better strain transfer between the two phases. Layered composites in miniaturized size find its application in the field of ultra-sensitive room temperature magnetic field sensors.[24] Moreover, layered (2-2) laminates yielded the highest ever magnetoelectric coupling in comparison to (1-3) and (0-3) composites.[25] Tape casting is the widely used technique for making miniaturised devices like capacitors, FeRAM etc.[26] There are numerous literatures available in which ME composites were fabricated using tape casting technique.[27,28,29,30,31] Another method of production for a (2-2) laminate type composite is screen printing of one layer over another. Printing of smart materials is more environmentally friendly and it offers several advantages like high speed, low cost and large scale production.[32] Even though there are so many advantages involved in printing of smart devices there are only two reports are available in literatures regarding the printing of ME composites.[18,33] But both these reports are concentrated on the development of polymer based ME composites via printing technique. This chapter reports an all printed ceramic ME composite. Among the various printing techniques available, we focus on screen printing technique which the most widely used one for the development of smart materials production.[34,35]

Strontium ruthenate ($SrRuO_3$) is a popular conductive perovskite ferromagnetic oxide, which has been traditionally used as an itinerant ferromagnetic and also as a buffer layer for thin film ferroelectrics. In such itinerant magnets, since the number of electrons in a unit cell can be uncertain at high temperatures where their magnetic moment is not well-defined.[36] However, a slight structural distortion of the corner-

sharing RuO_6 in $SrRuO_3$, could drastically change the electric and magnetic transport properties of this strongly correlated system. For example magnetic moment of $SrRuO_3$ films are predicted to increase under tensile strain[37] and so is its Curie temperature.[38] However, not many investigations were reported on observance of such effects in thick films.

On the other hand, $SrTiO_3$ is an incipient ferroelectric perovskite that shows saturation of dielectric constant below Curie temperature, in contrast to well-known ferroelectrics whose dielectric constant just peaks at transition. Interestingly, the ferroelectricity of $SrTiO_3$ can be tailored by tensile and compressive strains in thin films.[39] Besides strain, presence of intrinsic defects and extrinsic dopants may lead to alterations in their electronic structure. It was shown that low concentration of aliovalent dopants can bring about lattice instability that can induce ferroelectricity.[40] In 2005, Duran et al. observed that a small amount of Pr doping at Sr site leads to mixed Pr^{3+}/Pr^{4+} valence at A site, resulting in strain induced ferroelectric transition at about 238 °C.[41] Other researchers also observed giant dielectric tenability and peculiar dielectric relaxation with high polarization response to applied electric field in Pr doped $SrTiO_3$.[42,43]In fact, the paraelectric to relaxor ferroelectric phase transition in $Sr_{1-x}Pr_xTiO_3$ is believed to be a phenomenon driven by random polarizability instability.[44] Later, it was revealed that the charge compensation in Pr doped $SrTiO_3$ should have originated from Sr defects and not from the reduction of Ti^{3+} ions.[45] Ever since, the dielectric anomaly in the doped $SrTiO_3$ and unprecedented occurrence of ferroelectricity has been an active area of research.

Our attempt is to explore whether extrinsic $SrTiO_3$ as a ferroelectric can contribute towards magnetoelectric coupling when is in close contact with an incipient ferromagnet. Thus, the present paper presents the first fully printed ceramic based magnetoelectric composite with doped $SrTiO_3$ as the ferroelectric component and $SrRuO_3$ as ferromagnetic component. The inks of both these materials were developed which was screen printed on top of another in order to obtain a (2-2) laminate type ME composite.

4.3 Experimental Section

4.3.1 Materials

Titanium isopropoxide ($C_{12}H_{28}O_4Ti$, >99%, Sigma Aldrich), praseodymium nitrate hexahydrate ($Pr(NO_3)_3{\cdot}6H_2O$), acetyl acetone ($C_5H_8O_2$, 99%, Sigma Aldrich), ethylene glycol ($C_2H_6O_2$, >99%, Sigma Aldrich), strontium acetate ($C_4H_6O_4Sr$, >99.5%, Sigma Aldrich), Ruthenium(III) nitrosyl nitrate ($Ru(NO)(NO_3)_3$, 99%, Alfa Aesar), 2-Methoxyethanol, $C_3H_8O_2$ (99%, Sigma Aldrich)

4.3.2 Pr:STO synthesis

The Pr doped strontium titanate is synthesized using a sol-gel synthesis route. For this, titanium itanium isopropoxide, $C_{12}H_{28}O_4Ti$ was added to acetyl acetone, $C_5H_8O_2$ in a round bottomed flask at 120˚C for 30 minutes at constant stirring. After 30 minutes ethylene glycol, $C_2H_6O_2$ was added to the solution. At the same time, in another RB, sufficient quantity of strontium acetate, $C_4H_6O_4Sr$ and praseodymium nitrate hexahydrate $Pr(NO_3)_3{\cdot}6H_2O$ (Sr:Pr= 0.925:0.075) were dissolved in ethylene glycol, $C_2H_6O_2$, and were kept at 120˚C kept under constant stirring. After 1 h of mixing, both

these solutions were mixed together and allowed to stir together again at 120°C. After 4 h of mixing 3ml deionized water was added to the above mixture to form the stable solution of $SrTiO_3$. This solution was then dried in an oven kept at 100°C until all the solvents evaporate. So obtained powder was ground well calcined and qualified for ink preparation.

4.3.3 SRO synthesis

A 0.2 M strontium ruthanate solution was made by separately dissolving $Ru(NO)(NO_3)_3$ in 10ml 2-Methoxyethanol and $C_4H_6O_4Sr$ in 10 ml acetic acid at room temperature. These two individual solutions were then mixed together for 2 h at 100 °C to obtain a uniform brown solution. The obtained solution was dried in an oven which was then ground well and calcined at an elevated temperature.

4.3.4 Ink formulation and magnetoelectric composite preparation

A screen printable ink usually consists of filler, solvent, binder as well as dispersant. Here, the fillers are $SrTiO_3$ and $SrRuO_3$. A binary solvent system is used in the present ink formulation. Equal volumes of xylene and ethanol were chosen as solvents in order to provide fast curing for the proposed inks.

(i) In the first step, Triton X-100 (TCI, Tokyo, Japan), the dispersant, was dissolved in solvent mixture for 30 min in an ultrasonic bath.

(ii) Respective fillers ($SrTiO_3$/$SrRuO_3$) was added to the solution and stirred continuously for 4 h in a magnetic stirrer.

(iii) Ethyl cellulose (binder) was added and stirred for another 24 h to get a homogenous ink with desired viscosity.

For the production of hybrid ME composites, these inks were screen printed on desired substrates one over another and was kept at 100 ˚C for 24 h in an oven.

4.3.5 Characterizations

Thermogravimetry/ differential thermal analysis (TG/DTA) of the powders were carried out from room temperature upto 1000 ˚C in air atmosphere using a thermogravimetric analyser (TGA/DTA instrument, Shimadzu, Japan). Phase purity of the calcined powder was analysed using X-ray diffraction (XRD) analysis with Cu Kα radiation (X'Pert PRO diffractometer, PANalytical, Almelo, The Netherlands). The particle size of ceramics prepared was characterized using high-resolution transmission electron microscopy (HRTEM) (FEI Tecnai G2 30S-TWIN, FEI Co., Hillsboro, OR, USA). Viscosity of inks developed was measured using a Rheo plus32 rheometer (Anton Paar, Ashland, VA, USA). Screenprinting of prepared ink was done using an XPRT2 semiautomatic screen-printer (EKRA, Germany). Microstructural analysis of the printed film was done by scanning electron microscopy (SEM) using a JSM 5600LV instrument (JEOL, Tokyo, Japan). The adhesion strength of the printed ink on the substrate was carried out by tape test analysis based on modified ASTM standard D3359-09 and were analysed using optical microscopy (MRDX, Leica Microsystems, Wetzlar, Germany). The surface roughness of printed thick films was estimated using atomic force microscopy (AFM) (Multimode, Bruker, Germany), in tapping mode. The ferroelectric properties of bulk as well as printed inks were analysed using a ferroelectric tester (aixACCT-TF2000E, GmbH, Aachen, Germany). Magnetic properties were measured using a Vibration Sample Magnetometer (VSM) attached to Physical Property Measurement System (PPMS Quantum Design, USA). Magnetoelectric

measurements were carried out in ac as well as dc magnetic fields. The ac magnetic field was applied with the help of a pair of Helmholtz coils and dc field dependence of magnetoelectric coupling was studied using a setup consisting of dc electromagnet having bipolar power supply with GPIB integrated gauss meter. Both these fields were applied along the direction of thickness of the printed heterostructure. The data acquisition was performed using LabVIEW software.

4.4 Results and Discussion

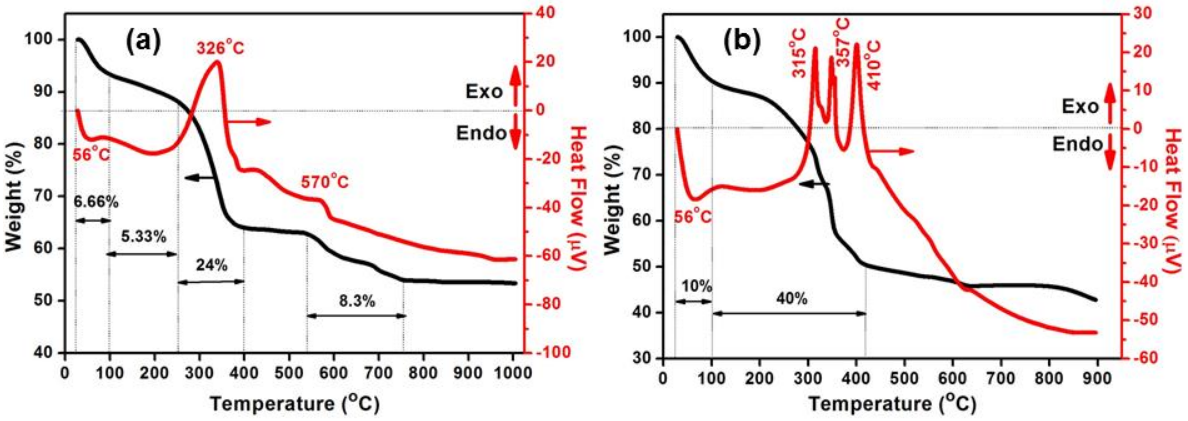

Figure 4.1: TG/DTA analysis of (a) STO, (b) SRO.

As hinted before, the present research was organized into studies pertaining to individual FE and FM components at first and then the properties of their 2-2 composite. In order to understand the thermal evolution history of the precursor powder of Pr doped $SrTiO_3$ (Pr:STO) and $SrRuO_3$ (SRO), a combined thermogravimetric (TGA)/differential thermal (DTA) analysis was performed, whose results in terms of weight loss and heat flow as a function of temperature is shown in figure 4.1(a) and (b). The TG curve was recorded for the STO sample in oxygen atmosphere with 5 ˚C/min heating velocity from 30 ˚C-1000 ˚C which is shown in figure 4.1(a). As suggested by the

TG curve, thermal decomposition profile of STO can be divided into four stages. In the first stage, the weight loss starts from 30 ˚C and shows a sharp decrease up to 100 ˚C indicating a total weight loss is around 6.66%. This can be attributed to the removal of planar water and ethylene glycol present in the respective powder. In DTA curve, an endothermic peak is observed around 56 ˚C, corresponding to the foresaid weight loss. In the following stage, a steady weight loss of about 5.33% is observed up to 260 ˚C. A sharp weight loss of around 24% is observed after 260 ˚C to 400 ˚C. This may be due to the removal of most of the organic residues present in the powder sample. The sharp exothermic peak at around 326 ˚C corresponds to the removal of alkoxides and acetates which were added as reagents during the reaction process. A TG weight loss of about 8.3% is observed from 550 ˚C to 750 ˚C and thereafter no considerable weight loss is observed. The loss of weight in this particular region is implied to the burn out of surface hydroxyls and carbon residues. An exothermic peak around 570 ˚C is attributed to this weight loss. Based on this TG-DTA result, the prepared powder was calcined over a temperature range from 500 ˚C to 900 ˚C.

TG was carried out on precursor SRO powder by heating them up to 900 ˚C in air with a heating rate of 5 ˚C/min to develop the mechanistic understanding behind the weight loss to form the resultant powder (Figure 4.1(b)). An initial weight loss of about 10% was observed from 30 ˚C to 100 ˚C which is due to removal of planar water from the precursor powder. An endothermic peak of around 56 ˚C corresponds to this weight loss. A major weight loss of almost 40% happened in the temperature range from100 ˚C to 420 ˚C. This weight loss occurred due the formation of Sr and Ru complex hydroxides. Three sharp exothermic peaks at 315 ˚C, 357 ˚C and 410 ˚C are observed in

this region. No considerable weight loss is observed after 600 ˚C. Hence the precursor powder was calcined from 600 ˚C.

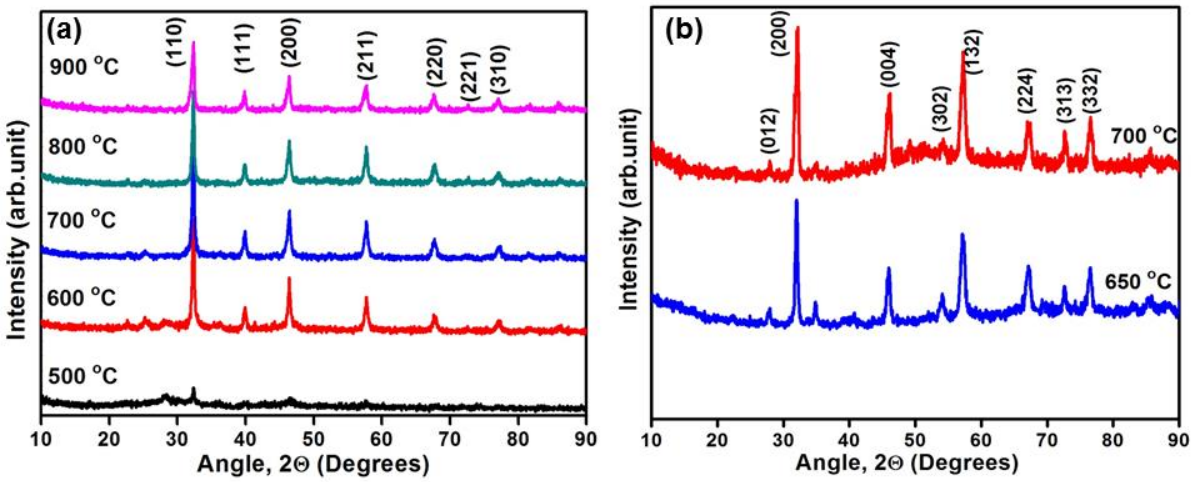

Figure 4.2: XRD patterns of (a) STO, (b) SRO.

X-ray was used in the present study as a primary tool to check the phase purity of ferroic materials since the presence of any inorganic impurity or additional phase in the compound may drastically affect their performance. The XRD pattern of $SrTiO_3$ was recorded, as shown in figure 4.2(a). The precursor powder was calcined from 500 ˚C to 900 ˚C for 4 h in a muffle furnace. The resultant XRD patterns indicate that the phase formation starts at 600 ˚C and is complete at 900 ˚C. All the peaks in the XRD pattern can be indexed using the standard JCPDS file 89-4934. The crystal structure belongs to I4/mcm space group with tetragonal symmetry. The sharpness of the diffraction peaks indicates the better homogeneity and crystallisation of samples. On the other hand, the XRD pattern of $SrRuO_3$ recorded for samples calcined at 650 ˚C and 700 ˚C for 4 h is plotted in figure 4.2(b). From the XRD pattern, it is clear that the phase formation of SrRuO3 is complete at 700 ˚C and all the peaks can be indexed using the JCPDS file 89-

5713. The crystal structure of $SrRuO_3$ belongs to Pnma space group with orthorhombic symmetry.

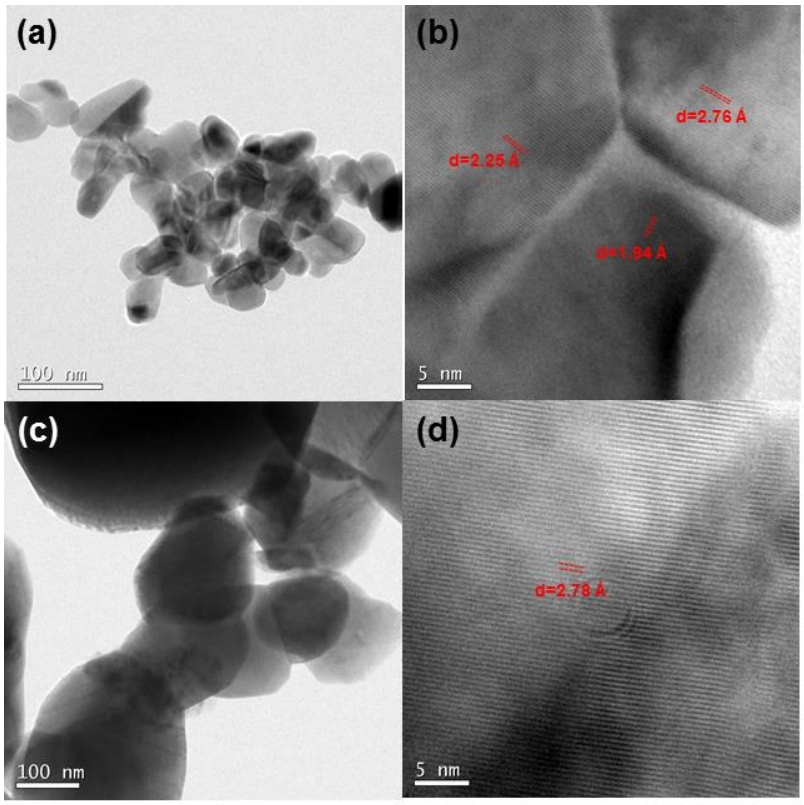

Figure 4.3: (a) and (b) HRTEM images of STO, (c) and(d) HRTEM images of SRO.

The nanocrystalline nature of STO as well as SRO was tested using TEM analysis. Figure 4.3(a) represent the morphology as well as particle size of calcined STO. It is evident from the figure that STO has an average particle size ranging from 30 nm to 60 nm. The crystalline nature of prepared powder is clear from the lattice image shown in figure 4.3(b). The value of d-spacing between adjacent fringes is measured to be 1.94 Å, 2.25 Å and 2.76 Å which corresponds to [200], [111] and [110] planes respectively. Similarly, TEM was recorded for SRO samples that were calcined at a higher temperature (~900°C). The average particle size of SRO is around 100 nm- 300 nm (figure 4.3(c)) than STO nanoparticles. The higher particle size can be attributed to the grain growth

occurred at elevated temperature. As shown in the lattice fringe image in figure 4.3(d), SRO appears to be highly crystalline. Here, the d spacing value between two fringes is calculated to be 2.82Å which represents [110] plane of SRO crystal. Since our ultimate objective is making thick film heterostructures using ferroic inks, the individual particle size plays crucial role, which controls the ink viscosity. The results obtained from TEM analysis indicates that the resultant powders will go well with developing inks out of it.

The doping of trivalent rare earth ion can happen in different ways. The first possibility is a partial substitution of Ti^{4+} by trivalent Pr^{3+} maintains charge neutrality by excluding the formation of Sr vacancies. Alternatively, planar faults of the host are compensated by the trivalent impurity, through radiative recombination.[45] Figure 4.4(a) shows the room temperature variation of polarization (P) with respect to electric field (E) of STO thick films which were printed on platinized silicon substrates. It can be shown that the switched charge (Q) of a real dielectric is given by,

$$Q = 2P_r A + \sigma EAt \qquad (4.1)$$

where P_r is the remanent polarization, A is the area of the capacitor, σ is the electrical conductivity of the real dielectric, E is the applied field and t is the measurement time.[46]

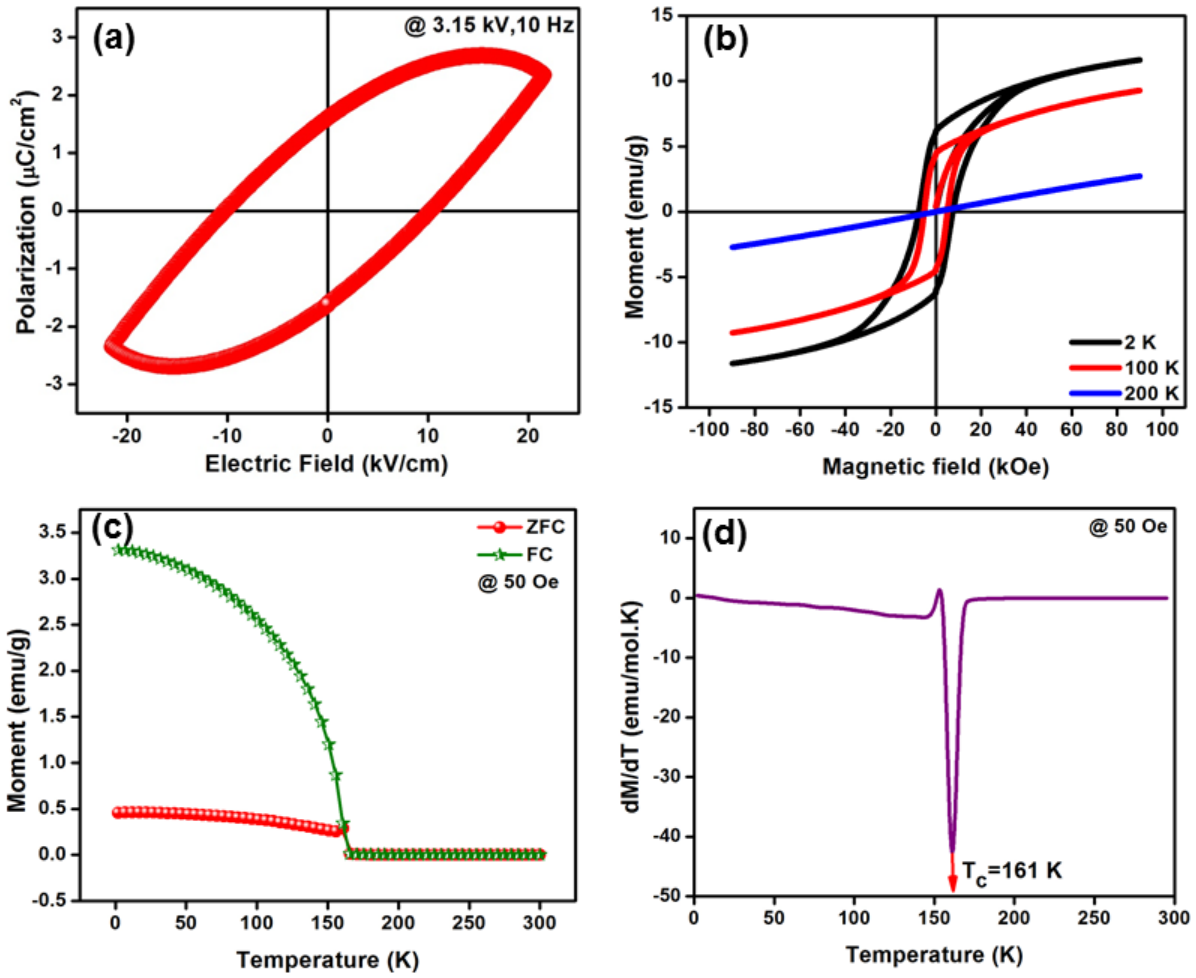

Figure 4.4: (a) Room temperature P-E hysteresis curve of STO, (b) M-H plot of SRO at different temperatures, (c) M-T plot of SRO at a magnetic field of 50 Oe, (d) dM/dT plot to determine T_c.

In the case of a quasi linear dielectric,

$$Q = \sigma EAt \qquad (4.2)$$

which means that it has finite leakage and is lossy, since σ is proportional to dielectric loss (tanδ). Here the leakage current may be originated from the oxygen vacancies, that may likely to form by the partial substitution of Ti^{4+} by Pr^{3+}. The P-E hysteresis loop in the present case indicates that it not a perfect ferroelectric, but more like a quasi-ferroelectric or lossy dielectric, even though there were earlier reports indicating the

room temperature ferroelectricity in Pr doped $SrTiO_3$.[41] The sample was able to bear an electric field up to 20 kV/cm without any break down, but it was observed that even with the application of such a high electric field, the P-E loop obtained was not fully saturated, typical of quasi ferroelectrics. The remanent polarization (P_r) and coercive field (E_c) obtained are 1.61 μC/cm^2 and 10.3 kV/cm respectively. Beyond 20 kV/cm the sample undergoes break down.

M-H hysteresis measured at 2 K, 100 K and 200 K for powder SRO is shown in figure 4.4(b). The magnetic moment of the sample was measured for magnetic field ranging from -90 kOe to +90 kOe. Here, hysteresis loop looks like ferromagnetic in nature. But even after the application of 90 kOe, the loops are not saturated. This is due to the presence of antiferromagnetic interaction along with the ferromagnetic interaction in respective material.[47] The remanance (M_r) and coercivity (H_c) decreases as temperature is increased from 2 K to 100 K. Finally, the M-H curve shows a linear behaviour which represents the paramagnetic nature of SRO at 200 K. In paramagnetic state the H_c and M_r shows zero value. Figure 4.4(c) shows the magnetization versus temperature (M-T) curve recorded using zero field cooled (ZFC) and field cooled (FC) modes at 50 Oe. There is a bifurcation in ZFC and FC curves which arises mainly due to the magnetocrystalline anisotropy of SRO in the measurement techniques used. Under ZFC condition, SRO sample was cooled from room temperature (300 K) down to 2 K, without the application of an external magnetic field while the actual measurement was recorded during warming up of the sample from 2 K to 300 K where the magnetic field was 50 Oe. On the other hand, FC measurement was recorded on cooling the sample from 300 K to 2 K under the external magnetic field. Usually the response of spins to the

applied magnetic field depends on the competition between the externally applied magnetic field strength and magnetocrystalline anisotropic energy in the material. If the applied field is small, then all the spins may not orient in the direction of field. When the applied magnetic field overcomes anisotropy field, the spins will be forced to align in the direction of external magnetic field. So when the applied field is high, then bifurcation between ZFC and FC curves will be less.[48] While analysing figure 4.4(c), one can see that, ZFC and FC plots meet at Curie temperature T_c, beyond which they show a paramagnetic nature. Curie temperature can be accurately determined from dM/dT versus T plot which is given in figure 4.4(d). The ferromagnetic transition is indicated by the sharp decrease of magnetization in ZFC data at 50 Oe and was measured to be 161 K, which is in agreement with previously report.[49]

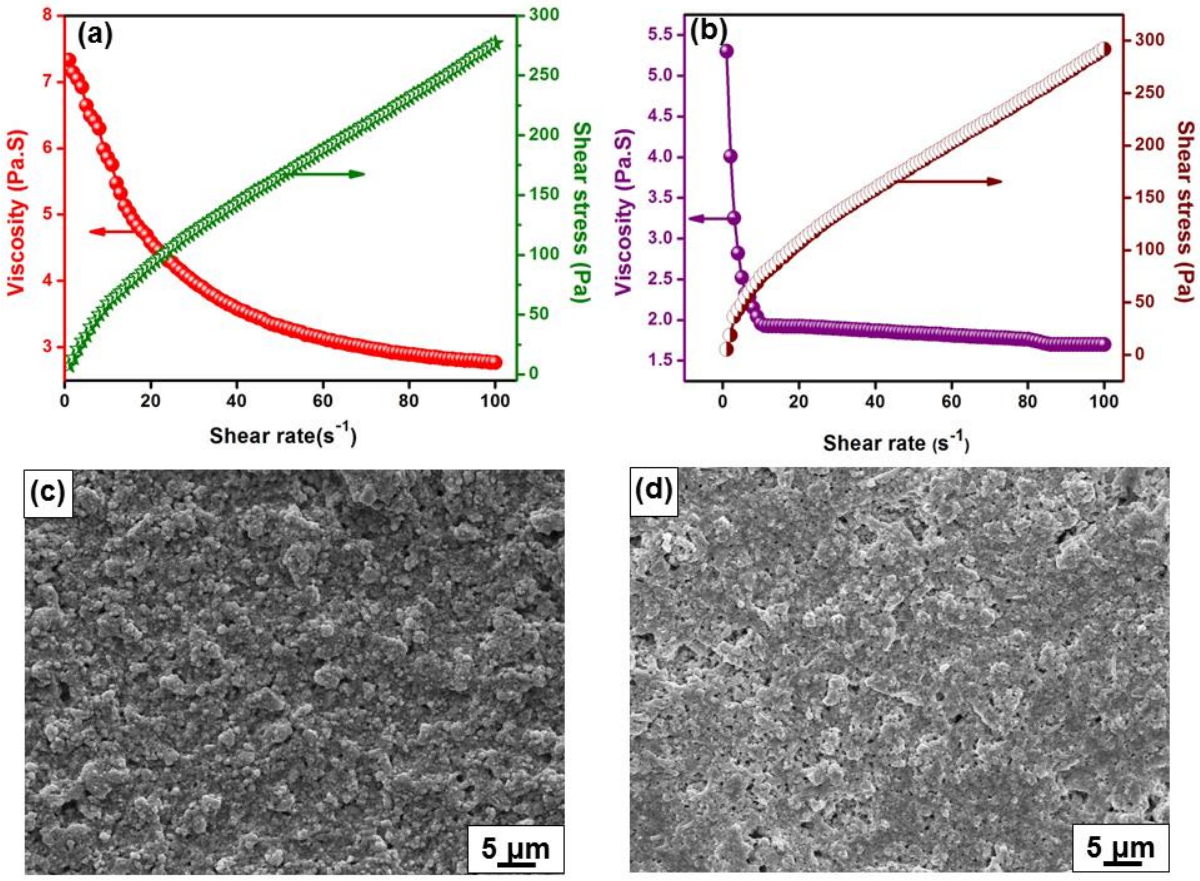

Figure 4.5: Variation of viscosity and shear stress with shear rate of (a) STO, (b) SRO (c) surface SEM of STO ink, (d) surface SEM of SRO ink printed on top of mylar® substrate.

Since we are employing screen printing technique to make thick film out of the qualified STO and SRO powders, the flow characteristics of the constituent inks have to be studied. In order to make a smooth and uniform printing, the ink slurry composition should be optimized to get minimum viscosity. Here, the quantity as well as quality of organic components that are needed for formulating the ink should be chosen judiciously, so as to facilitate room temperature evaporation curing after printing. As briefed in the Experimental section, xylene-ethanol mixture was used as the solvent, Triton X-100 as the dispersant while ethyl cellulose served as the binder in the ink synthesis. Figures 4.5(a) and (b) represent the rheological behaviour of the ready-to-print slurry of STO and SRO respectively. In both the cases one can observe a decrease in viscosity with the increase in shear rate. This is normally known as shear thinning behaviour, which is the essential criterion for a screen printing ink. As the shear rate increases the ink becomes thinner which in turn facilitate the free flow of ink through the screen mesh. Viscosity value of 1-20 Pa.s at lower shear rates are considered to be the ideal value for screen printing. For STO, the viscosity has gone below 3 Pa.s while for SRO, the value is less than 2 Pa.s which indicates that the developed inks qualify for screen printing. Further in figures 4.5(a) and (b) are the shear stress curves in both STO and SRO rheology profile, that further attest nature of pseudoplasticity in the inks. Usually pseudoplasticity is required to prevent bleeding of ink to flow beyond the print boundaries. Figures 4.5(c) and (d) represents the scanning electron microscopic images recorded from the surface of STO and SRO printed film respectively. A uniform

distribution of particles is seen throughout the microstructure with minimum porosity. This porosity is unavoidable factor in these cases because of fast volatilization of organic solvents present in the ink formulation, and the fact that we do not employ a post printing sintering. Thus the printed films are likely to contain a trace volume of the binder, ethyl cellulose, while other organic matter evaporates during post printing drying at ambient conditions.

Surface morphology of the printed patterns as viewed using AFM, is shown in figure 4.6. Surface smoothness plays an important role in determining the quality and adhesion of the printed pattern. As the solvents in used in ink formulation escapes at room temperature, there includes some porosity in the dried printed patterns we developed. AFM micrographs were recorded from the surface of double stroke printed samples. Figures 4.6(a) and (b) represents 2D and 3D images of STO samples respectively. The average surface roughness (R_a) and root mean square roughness (R_q) of STO samples were analysed to be 91.7±5 nm and 117±5 nm respectively, which is comparable with previously reported values for printed films. Two important parameters obtained from AFM images are kurtosis topography and skewness. In the present case for STO, kurtosis value is observed to be 2.72. Usually kurtosis value < 3 indicates that the distribution curve is platykurtoic, which means that scan surface consists of relatively few high peaks and low values. In case of printed films, skewness is a measure of variation of surface. Here, for STO skewness is measured to be -0.443. The negative value for skewness generally indicates that surface distribution has a longer lower valley at the measurement areas when compared to reference plane.

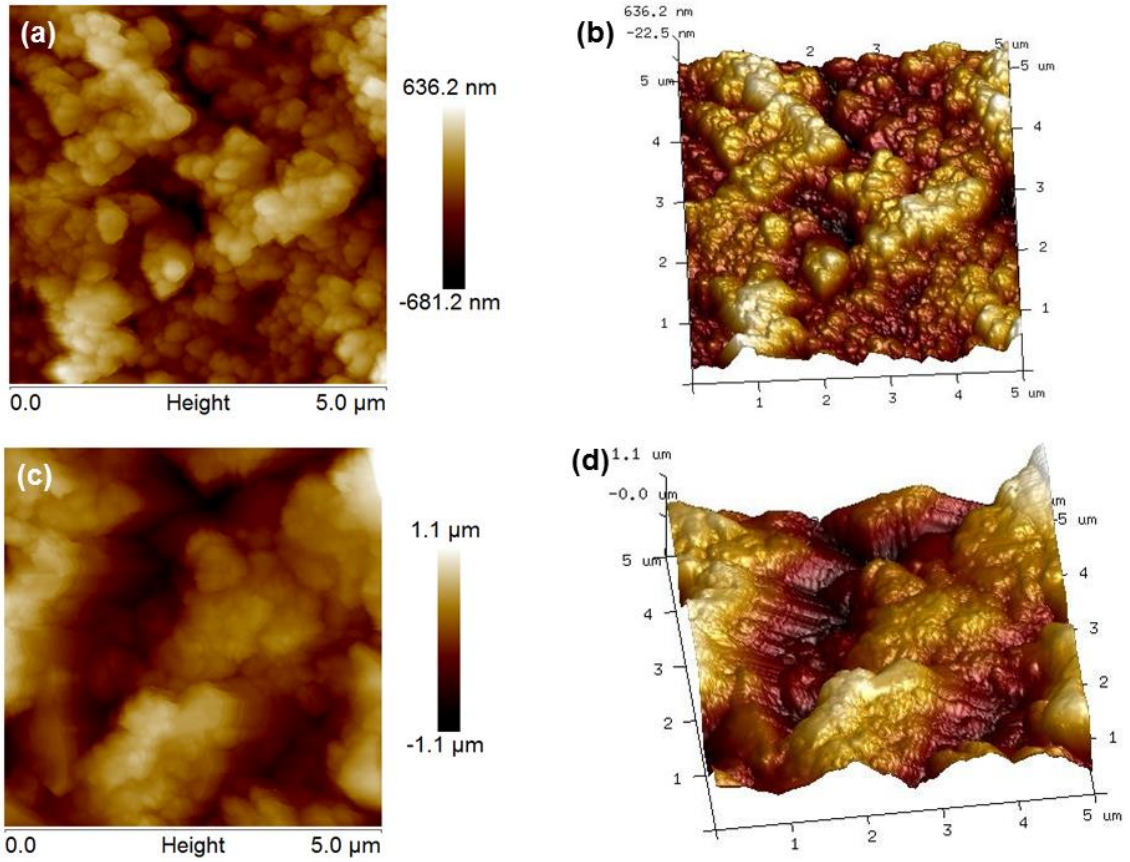

Figure 4.6: (a) 2D, (b)3D AFM images of printed STO film and (c) 2D, (d)3D AFM images of printed SRO film.

The 2D and 3D AFM images of SRO is shown in figure 4.6(c) and (d) respectively. The average surface roughness was measured to be 117±5 nm and root mean square roughness was identified to be 145±5 nm. In fact, these values are greater than that for STO, but still lower when compared to earlier reports on room temperature curable inks.[50,51]

Figure 4.7(a) and (b) represents the P-E hysteresis loop of STO thick film and M-H hysteresis of SRO counterpart respectively. The P-E loops show that they were not saturated even after the application of 10 kV/cm. The remanent polarization (P_r) and coercive field (E_c) were decreased from the case of STO bulk when comes to printed

thick films. This deviation from ferroelectric hysteresis may be due to the presence of organic vehicles present in the ink composition. The effect of substrate clamping in the case of printed pattern is unavoidable owing to the mismatch in thermal expansion between STO film and platinized silicon substrate. The electric dipoles in STO will be unable to align in same degree as in case of bulk STO which in turn restrict the polarization to happen by the substrate. This can be another reason for the decrease in Pr value of STO ink.

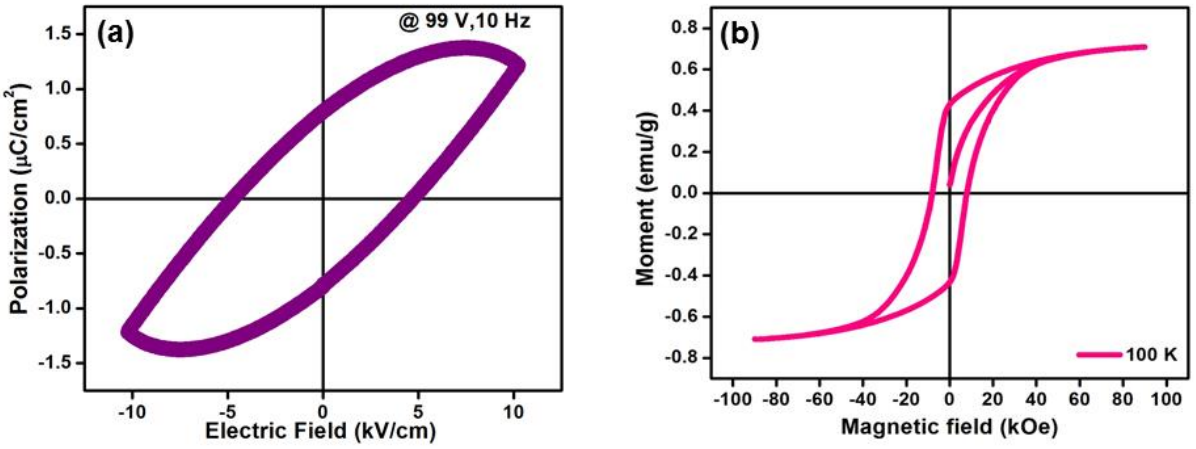

Figure 4.7: (a) Room temperature P-E curve for printed STO film, (b) M-H curve for printed SRO film at 100 K.

The M-H hysteresis curve of SRO ink shows that there is a considerable decrease in Mr value when compared to SRO bulk. At 100 K, bulk SRO had a M_r value of 4.409 emu/g which was reduced to 0.4273 emu/g in SRO thick films. The reason for this decrease in M_r can be attributed to the presence of external components in the ink formulation as well as substrate clamping effect. But interestingly, the ferromagnetic nature of SRO was retained even in printed form too, when measured below Curie temperature. This confirms that the printing process has no adverse effect on ferromagnetic property of SRO. Once the properties of individual $SrTiO_3$ and $SrRuO_3$ inks were optimized

independently, we proceeded to develop heterostructural (2-2) magnetoelectric composites using these ferroic inks. For that, we screen printed STO ink on top of a Si(100)/SiO_2/TiO_2/Pt substrate, annealed at 60°C for 15 min and thereafter screen printed SRO ink on top of annealed STO to form (2-2) bilayer magnetoelectric composite.

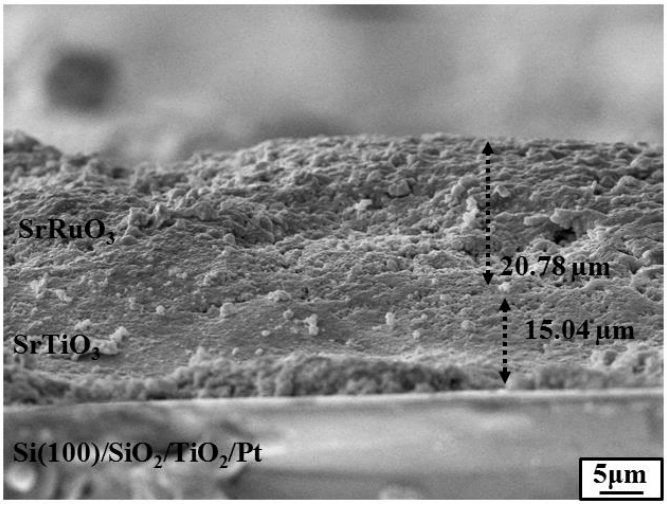

Figure 4.8: Cross sectional SEM image of STO-SRO printed 2-2 composite.

The cross-sectional SEM image of screen printed composite is shown in figure 4.8. From the image the average thickness of STO and SRO was identified to be 15.04 µm and 20.78 µm respectively. No microstructural defects like delamination or cracks can be observed here. This confirms the compatibility of STO and SRO layers with each other and also with the substrate. A dense microstructure can be observed for both ceramic thick films in this figure.

Room temperature ferroelectric hysteresis curve for composite multilayer STO-SRO is shown in figure 4.9(a).

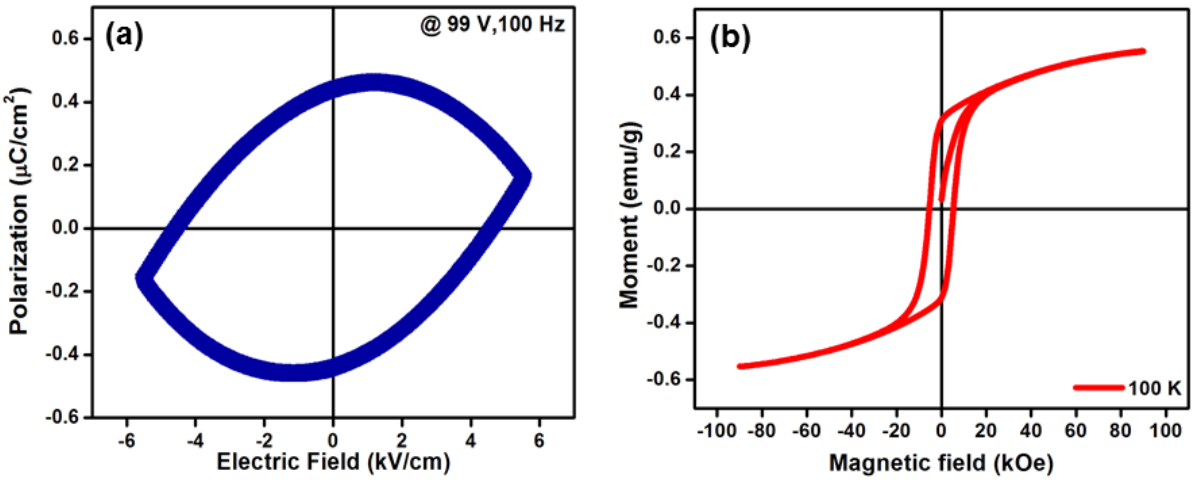

Figure 4.9: (a) P-E curve of printed STO-SRO bilayer at 300 K, (b) M-H curve of printed STO-SRO bilayer at 100 K.

This measurement was carried out at a voltage of 99 V and frequency of 100 Hz. A visible decrease in the value of P_r is evident, which may due to the presence of ferromagnetic layer, SRO. Here we may notice that the multiferroic bilayers are rigidly clamped each other and also with the substrate, which will limit the intensity of poling field to a diminished polarization. Earlier reports suggest that clamped films are likely to suffer inferior magnetoelectric coupling.[52] There occurred a marginal drop in the VSM magnetic moment measurement as well (figure 4.9(b)) at 100 K, which is attributed to the spin-charge interaction at the magnetoelectric interface. Anyhow, ferromagnetic nature is retained even in the bilayer composite but M_r value diminished from screen printed SRO alone.

The magnetoelectric coupling in layered FE-FM heterostrctures occurs mainly due to strain mediation between the hetero phases. That is, the magnetostrictive strain of the ferromagnetic layer is transferred to the ferroelectric layer across the film interface, giving rise to an electric polarization. The second possibility is through charge

screening effect, where charge accumulates at the FE-FM interface that modulates the interface magnetization through spin-dependent screening.[53]

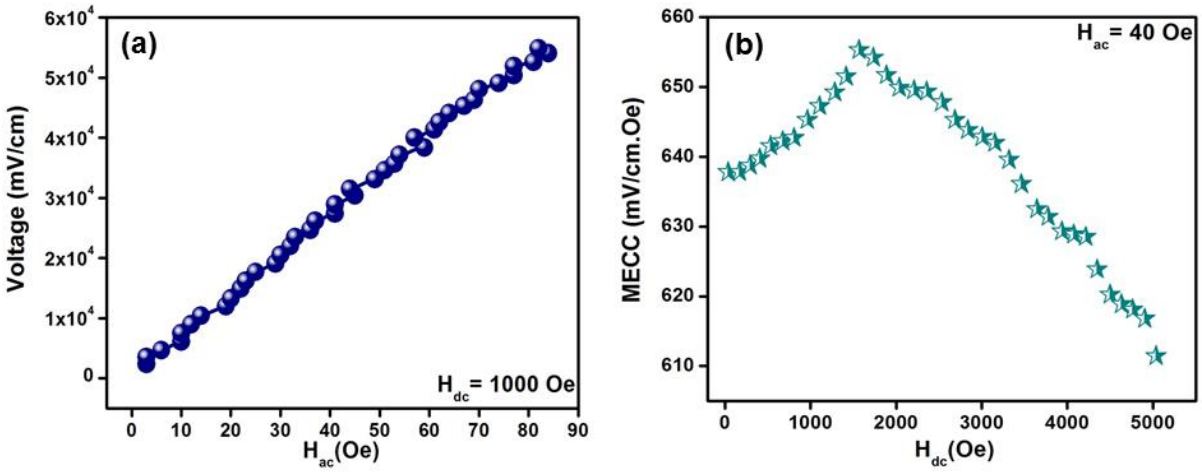

Figure 4.10. The variation of ME coupling coefficient under the application of (a) ac, (b) dc magnetic field for STO-SRO bilayer screen printed sample.

In the present case, the magnetoelectric coupling coefficient for both ac and dc magnetic field were measured. When the layered composite is placed in a magnetic field, the field will mechanically induce an alteration in electric polarization and strain, which will further induce a magnetoelectric voltage in the composite. Here, for the MECC measurement 35 μm thick sample was used. For ac magnetoelectric measurement, the voltage across the sample increases with respect to magnetic field as shown in figure 4.10(a). The MECC for this measurement is calculated from equation (1.18) and was obtained to be 657 mV/cm.Oe. Figure 4.10(b) depicts the dc measurement taken for the composite at an ac field of 40 Oe with a frequency of 850 Hz. Here one can see that, the MECC value increases up to a particular d.c magnetic field and decreases thereafter. The maximum MECC value obtained for STO-SRO bilayer composite is 655 mV/cm.Oe. The ME effect in the current bilayer screen printed composite originated from the elastic

interaction between the two phases present in the system. As there are two separate layers for ferroelectric and ferromagnetic materials, there occurs an interface that separates them. When a magnetic field is applied to the composite system, the strain developed in the magnetic phase will be effectively transferred to attached ferroelectric layer which is in contact with. This will cause an invariable electric polarization at the output. Since this is a layer by layer structure with thickness in the range of μm, the domain walls under the application of external magnetic field will progress much easily when compared to other tape casted laminates. It should be noted that the ME measurements were done at ambient temperatures where $SrTiO_3$ showing piezomagnetic properties is unusual, which can be due to effects of lattice strain induced by the ferroelectric phase. However, more studies are required to assess the underlying reasons resulting in the piezomagnetic effect in ferroelectrically coupled incipient ferromagnets while remaining in the paramagnetic state.

4.5 Conclusions

The Pr:$SrTiO_3$ and $SrRuO_3$ powders were synthesized using wet chemical methods. Phase purity and particle size of the developed ceramics were confirmed using XRD and TEM analysis. The ferroelectric properties of STO and ferromagnetic properties of SRO were investigated in detail. Room temperature curable inks based on these materials were developed using binary solvent system (Xylene: ethanol), ethyl cellulose as binder and Triton X-100 as dispersant. Microstructure, surface roughness, ferroelectric property and ferromagnetic property of the developed inks were studied. After exploring individual properties, a (2-2) composite was developed via screen printing one ink over another on to a substrate. The cross sectional SEM micrograph revealed a

crack free microstructure for the composite. Ferroelectric as well as ferromagnetic nature of the hetero structure was confirmed. Magnetoelectric studies showed that the composite exhibited a MECC value of 657 mV/cm.Oe for ac magnetic field and 655 mV/cm. Oe for dc magnetic field. These promising results confirm its suitability in the fields of sensors, actuators and energy harvesters etc. Still, further studies are needed to confirm the magnetoelectric performance of this bilayer system in which $SrRuO_3$ stays in paramagnetic state at ambient temperatures.

4.6 References

(1) Eerenstein, W.; Mathur, N. D.; Scott, J. F. Multiferroic and Magnetoelectric Materials. *Nature* **2006**, *442*, 759–765. https://doi.org/10.1038/nature05023.

(2) Nan, C. W.; Bichurin, M. I.; Dong, S.; Viehland, D.; Srinivasan, G. Multiferroic Magnetoelectric Composites: Historical Perspective, Status, and Future Directions. *J. Appl. Phys.* **2008**, *103*, 031101–1–35. https://doi.org/10.1063/1.2836410.

(3) Spaldin, N. A.; Cheong, S.; Ramesh, R. Multiferroics: Past, Present, and Future Additional Resources for Physics Today. *Cit. Phys. Today* **2010**, *63* (10), 38. https://doi.org/10.1063/1.3502547.

(4) Vaz, C. A. F.; Hoffman, J.; Ahn, C. H.; Ramesh, R. Magnetoelectric Coupling Effects in Multiferroic Complex Oxide Composite Structures. *Adv. Mater.* **2010**, *22* (26–27), 2900–2918. https://doi.org/10.1002/adma.200904326.

(5) Hu, J. M.; Li, Z.; Chen, L. Q.; Nan, C. W. Design of a Voltage-Controlled Magnetic Random Access Memory Based on Anisotropic Magnetoresistance in a Single Magnetic Layer. *Adv. Mater.* **2012**, *24* (21), 2869–2873. https://doi.org/10.1002/adma.201201004.

(6) Roy, A.; Gupta, R.; Garg, A. Multiferroic Memories. *Adv. Condens. Matter Phys.* **2012**, *2012*. https://doi.org/10.1155/2012/926290.

(7) Ishiwara, H. Ferroelectric Random Access Memories. *J. Nanosci. Nanotechnol.* **2012**, *12* (10), 7619–7627. https://doi.org/10.1166/jnn.2012.6651.

(8) Garcia, V.; Bibes, M. Ferroelectric Tunnel Junctions for Information Storage and Processing. *Nat. Commun.* **2014**, *5*, 1–12. https://doi.org/10.1038/ncomms5289.

(9) Ortega, N.; Kumar, A.; Scott, J. F.; Katiyar, R. S. Multifunctional Magnetoelectric

Materials for Device Applications. *J. Phys. Condens. Matter* **2015**, *27* (50). https://doi.org/10.1088/0953-8984/27/50/504002.

(10) Erdem, D.; Bingham, N. S.; Heiligtag, F. J.; Pilet, N.; Warnicke, P.; Vaz, C. A. F.; Shi, Y.; Buzzi, M.; Rupp, J. L. M.; Heyderman, L. J.; et al. Nanoparticle-Based Magnetoelectric BaTiO3-CoFe2O4 Thin Film Heterostructures for Voltage Control of Magnetism. *ACS Nano* **2016**, *10* (11), 9840–9851. https://doi.org/10.1021/acsnano.6b05469.

(11) Lu, X.; Kim, Y.; Goetze, S.; Li, X.; Dong, S.; Werner, P.; Alexe, M.; Hesse, D. Magnetoelectric Coupling in Ordered Arrays of Multilayered Heteroepitaxial BaTiO3/CoFe2O4 Nanodots. *Nano Lett.* **2011**, *11* (8), 3202–3206. https://doi.org/10.1021/nl201443h.

(12) Ramesh, R.; Spaldin, N. A. Multiferroics: Progress and Prospects in Thin Films. *Nat. Mater.* **2007**, *6*, 21–29.

(13) Hill, A. N. Why Are There so Few Magnetic Ferroelectrics? *J. Phys. Chem. B 2000,* **2000**, *104*, 6694–6709. https://doi.org/10.1021/JP000114X.

(14) Yang, T. N.; Hu, J. M.; Nan, C. W.; Chen, L. Q. On the Elastically Coupled Magnetic and Ferroelectric Domains: A Phase-Field Model. *Appl. Phys. Lett.* **2014**, *104* (20). https://doi.org/10.1063/1.4875719.

(15) Vaz, C. A. F. Electric Field Control of Magnetism in Multiferroic Heterostructures. *J. Phys. Condens. Matter* **2012**, *24*, 333201. https://doi.org/10.1088/0953-8984/24/33/333201.

(16) Bichurin, M. I.; Petrov, V. M. Magnetoelectric Effect in Magnetostriction-Piezoelectric Multiferroics. *Low Temp. Phys.* **2010**, *36* (6), 544–549. https://doi.org/10.1063/1.3456999.

(17) Nan, C. W.; Bichurin, M. I.; Dong, S.; Viehland, D.; Srinivasan, G. Multiferroic Magnetoelectric Composites: Historical Perspective, Status, and Future Directions. *J. Appl. Phys.* **2008**, *103* (3). https://doi.org/10.1063/1.2836410.

(18) Lima, A. C.; Pereira, N.; Policia, R.; Ribeiro, C.; Correia, V.; Lanceros-Mendez, S.; Martins, P. All-Printed Multilayer Materials with Improved Magnetoelectric Response. *J. Mater. Chem. C* **2019**, *7* (18), 5394–5400. https://doi.org/10.1039/c9tc01428d.

(19) Akyildiz, I. F.; Pierobon, M.; Balasubramaniam, S.; Koucheryavy, Y. The Internet of Bio-Nano Things. *IEEE Commun. Mag.* **2015**, *53* (3), 32–40. https://doi.org/10.1109/MCOM.2015.7060516.

(20) Mundy, J. A.; Brooks, C. M.; Holtz, M. E.; Moyer, J. A.; Das, H.; Rébola, A. F.; Heron, J. T.; Clarkson, J. D.; Disseler, S. M.; Liu, Z.; et al. Atomically Engineered Ferroic Layers Yield a Room-Temperature Magnetoelectric Multiferroic. *Nature* **2016**, *537* (7621), 523–527. https://doi.org/10.1038/nature19343.

(21) Nan, T.; Lin, H.; Gao, Y.; Matyushov, A.; Yu, G.; Chen, H.; Sun, N.; Wei, S.; Wang, Z.; Li, M.; et al. Acoustically Actuated Ultra-Compact NEMS Magnetoelectric Antennas. *Nat. Commun.* **2017**, *8* (1), 1–7. https://doi.org/10.1038/s41467-017-00343-8.

(22) Chu, Z.; Annapureddy, V.; Pourhosseiniasl, M.; Palneedi, H.; Ryu, J.; Dong, S. Dual-Stimulus Magnetoelectric Energy Harvesting. *MRS Bull.* **2018**, *43* (3), 199–205. https://doi.org/10.1557/mrs.2018.31.

(23) Newnham, R. E., Skinner, D. P., Cross, L. E. Connectivity and Piezoelectric Pyroelectric Composites. *Mater. Res. Bull* **1978**, *13* (5), 525–536.

(24) Prokhorenko, S.; Kohlstedt, H.; Pertsev, N. A. Ferroelectric-Ferromagnetic Multilayers: A Magnetoelectric Heterostructure with High Output Charge Signal. *J. Appl. Phys.* **2014**, *116* (11). https://doi.org/10.1063/1.4896189.

(25) Palneedi, H.; Annapureddy, V.; Priya, S.; Ryu, J. Status and Perspectives of Multiferroic Magnetoelectric Composite Materials and Applications. *Actuators* **2016**, *5* (1), 9. https://doi.org/10.3390/act5010009.

(26) Jantunen, H.; Hu, T.; Uusimäki, A.; Leppävuori, S. Tape Casting of Ferroelectric, Dielectric, Piezoelectric and Ferromagnetic Materials. *J. Eur. Ceram. Soc.* **2004**, *24* (6), 1077–1081. https://doi.org/10.1016/S0955-2219(03)00552-1.

(27) Premkumar, S.; Varadarajan, E.; Rath, M.; Rao, M. S. R.; Mathe, V. L. Ferroelectric and Piezoelectric Properties of PSLZT Multilayer/NZFO Co-Sintered Magnetoelectric Composite Fabricated by Tape Casting. *J. Eur. Ceram. Soc.* **2019**, *39* (16), 5267–5276. https://doi.org/10.1016/j.jeurceramsoc.2019.08.010.

(28) Santa-Rosa, W.; Venet, M.; M'Peko, J. C.; Moreno, R.; Amorín, H.; Algueró, M. Environmentally-Friendly Magnetoelectric Ceramic Multilayer Composites by Water-Based Tape Casting. *J. Eur. Ceram. Soc.* **2019**, *39* (4), 1065–1072. https://doi.org/10.1016/j.jeurceramsoc.2018.10.009.

(29) Zhou, D.; Hao, L.; Gong, S.; Fu, Q.; Xue, F.; Jian, G. Magnetoelectric Effect of the Multilayered CoFe2O4 /BaTiO3 Composites Fabricated by Tape Casting. *J. Mater. Sci. Mater. Electron.* **2012**, *23* (12), 2098–2103. https://doi.org/10.1007/s10854-012-0706-9.

(30) Hao, L.; Zhou, D.; Fu, Q.; Hu, Y. Multiferroic Properties of Multilayered BaTiO3-CoFe 2O4 Composites via Tape Casting Method. *J. Mater. Sci.* **2013**, *48* (1), 178–185. https://doi.org/10.1007/s10853-012-6726-2.

(31) Park, C. S.; Priya, S. Cofired Magnetoelectric Laminate Composites. *J. Am. Ceram. Soc.* **2011**, *94* (4), 1087–1095. https://doi.org/10.1111/j.1551-2916.2010.04213.x.

(32) Oliveira, J.; Correia, V.; Castro, H.; Martins, P.; Lanceros-Mendez, S. Polymer-Based Smart Materials by Printing Technologies: Improving Application and Integration.

Addit. Manuf. **2018**, *21*, 269–283. https://doi.org/10.1016/j.addma.2018.03.012.

(33) Chlaihawi, A. A.; Emamian, S.; Narakathu, B. B.; Ali, M. M.; Maddipatla, D.; Bazuin, B. J.; Atashbar, M. Z. Novel Screen Printed Flexible Magnetoelectric Thin Film Sensor. *Procedia Eng.* **2016**, *168*, 684–687. https://doi.org/10.1016/j.proeng.2016.11.247.

(34) Søndergaard, R. R.; Hösel, M.; Krebs, F. C. Roll-to-Roll Fabrication of Large Area Functional Organic Materials. *J. Polym. Sci. Part B Polym. Phys.* **2013**, *51* (1), 16–34. https://doi.org/10.1002/polb.23192.

(35) Sousa, R. E.; Oliveira, J.; Gören, A.; Miranda, D.; Silva, M. M.; Hilliou, L.; Costa, C. M.; Lanceros-Mendez, S. High Performance Screen Printable Lithium-Ion Battery Cathode Ink Based on C-LiFePO4. *Electrochim. Acta* **2016**, *196*, 92–100. https://doi.org/10.1016/j.electacta.2016.02.189.

(36) Chandra, P.; Lonzarich, G. G.; Rowley, S. E.; Scott, J. F. Prospects and Applications near Ferroelectric Quantum Phase Transitions: A Key Issues Review. *Reports Prog. Phys.* **2017**, *80* (11). https://doi.org/10.1088/1361-6633/aa82d2.

(37) Gan, Q.; Rao, R. A.; Eom, C. B.; Garrett, J. L.; Lee, M. Direct Measurement of Strain Effects on Magnetic and Electrical Properties of Epitaxial SrRuO3 Thin Films. *Appl. Phys. Lett.* **1998**, *72* (8), 978–980. https://doi.org/10.1063/1.120603.

(38) Terai, K.; Ohnishi, T.; Lippmaa, M.; Koinuma, H.; Kawasaki, M. Magnetic Properties of Strain-Controlled SrRuO3 Thin Films. *Japanese J. Appl. Physics, Part 2 Lett.* **2004**, *43* (2 A). https://doi.org/10.1143/jjap.43.l227.

(39) Pertsev, N.; Tagantsev, A.; Setter, N. Phase Transitions and Strain-Induced Ferroelectricity in Epitaxial Thin Films. *Phys. Rev. B - Condens. Matter Mater. Phys.* **2000**, *61* (2), R825–R829. https://doi.org/10.1103/PhysRevB.61.R825.

(40) Martínez, E.; García, S.; Marin, E.; Vasallo, O.; Peña-Rodríguez, G.; Calderón, A.; Siqueiros, J. M. Dielectric and Thermal Properties of XPbTiO3-(1-x)SrTiO3 Polycrystals. *J. Mater. Sci.* **2004**, *39* (4), 1233–1239. https://doi.org/10.1023/B:JMSC.0000013880.59790.a3.

(41) Durán, A.; Martínez, E.; Díaz, J. A.; Siqueiros, J. M. Ferroelectricity at Room Temperature in Pr-Doped SrTiO3. *J. Appl. Phys.* **2005**, *97* (10). https://doi.org/10.1063/1.1903100.

(42) Wei, T.; Song, Q. G.; Zhou, Q. J.; Li, Z. P.; Chen, Y. F.; Qi, X. L.; Guo, S. Q.; Liu, J. M. Giant Dielectric Tunable Behavior of Pr-Doped SrTiO3 at Low Temperature. *Funct. Mater. Lett.* **2012**, *5* (1), 1–5. https://doi.org/10.1142/S179360471250018X.

(43) Wang, X.; Lu, X.; Weng, Y.; Cai, W.; Wu, X.; Liu, Y.; Huang, F.; Zhu, J. Improved Electrical Properties of Pr-Doped SrTiO3 Films. *Solid State Commun.* **2010**, *150* (5–6), 267–270. https://doi.org/10.1016/j.ssc.2009.11.010.

(44) Dwij, V.; De, B. K.; Tyagi, S.; Sharma, G.; Sathe, V. G. Raman Spectroscopic Investigation of Relaxor Behavior in Pr Doped SrTiO3 and Origin of Fano Resonance. 1–11.

(45) Sluchinskaya, I. A.; Lebedev, A. I.; Erko, A. Crystal Structure, Local Structure, and Defect Structure of Pr-Doped SrTiO 3. *J. Appl. Phys.* **2012**, *112* (2). https://doi.org/10.1063/1.4737586.

(46) Scott, J. F. Ferroelectrics Go Bananas. *J. Phys. Condens. Matter* **2008**, *20* (2), 22–23. https://doi.org/10.1088/0953-8984/20/02/021001.

(47) Ganeshraj, C.; Mahato, R. N.; Divyaa, D.; Santhosh, P. N. Magnetic, Electrical Transport and Structural Investigations of Orthorhombic Perovskite Pr2 MnFeO6. *J. Appl. Phys.* **2010**, *107* (9), 7–10. https://doi.org/10.1063/1.3359441.

(48) Joy, P. A.; Anil Kumar, P. S.; Date, S. K. The Relationship between Field-Cooled and Zero-Field-Cooled Susceptibilities of Some Ordered Magnetic Systems. *J. Phys. Condens. Matter* **1998**, *10* (48), 11049–11054. https://doi.org/10.1088/0953-8984/10/48/024.

(49) Chang, Y. J.; Kim, C. H.; Phark, S. H.; Kim, Y. S.; Yu, J.; Noh, T. W. Fundamental Thickness Limit of Itinerant Ferromagnetic SrRuO3 Thin Films. *Phys. Rev. Lett.* **2009**, *103* (5), 2–5. https://doi.org/10.1103/PhysRevLett.103.057201.

(50) Varghese, J.; Teirikangas, M.; Puustinen, J.; Jantunen, H.; Sebastian, M. T. Room Temperature Curable Zirconium Silicate Dielectric Ink for Electronic Applications. *J. Mater. Chem. C* **2015**, *3* (35), 9240–9246. https://doi.org/10.1039/c5tc01388g.

(51) Varghese, J.; Kuzhichalil Peethambharan, S.; Sebastian, M. T. Room Temperature Curable Silica Ink. *RSC Adv.* **2014**, *4*, 47701–47707. https://doi.org/10.1039/c4ra06479h.

(52) Bichurin, M.; Petrov, V.; Zakharov, A.; Kovalenko, D.; Yang, S. C.; Maurya, D.; Bedekar, V.; Priya, S. Magnetoelectric Interactions in Lead-Based and Lead-Free Composites. *Materials (Basel).* **2010**, *4* (4), 651–702. https://doi.org/10.3390/ma4040651.

(53) Chu, Z.; Pourhosseiniasl, M.; Dong, S. Review of Multi-Layered Magnetoelectric Composite Materials and Devices Applications. *J. Phys. D. Appl. Phys.* **2018**, *51* (24). https://doi.org/10.1088/1361-6463/aac29b.

Chapter 5

MAGNETOELECTRIC (2-2) COMPOSITES REALIZED THROUGH SCREEN PRINTING OF $CoFe_2O_4$ ON Pr DOPED $SrTiO_3$: EXPERIMENT Vs THEORY

5.1 Abstract

Thick film multiferroics continue to enthuse researchers due to their wide range of applications in fields of memory, sensing and transduction. With an aim of improving the magnetoelectric property, in the current chapter, we developed another ME composite using $CoFe_2O_4$ (CFO), with Pr doped $SrTiO_3$ (Pr:STO) and tried to correlate its ME properties through a theoretical model. As widely known, CFO is a well-known magnetostrictive material. Nanoceramics based on both the materials were developed. These inks were screen printed one on top of other, yielding a (2-2) layered magnetoelectric heterostructure. The all printed ME composite exhibited a better magnetoelectric response under the application of dc magnetic field with MECC value, α=779 mV/cm.Oe. Relevant properties of individual ferroic layers as well as the composite form were studied in detail. The ferroic properties along with magnetoelectric coupling were simulated using finite element methods, and are in reasonably good agreement with experimental results. Apparent properties of thick film composites indicate their suitability in next generation sensors and energy harvesters.

5.2 Introduction

The increasing need of multimedia storage has always fascinated researchers and therefore constant efforts are done world over, to develop techniques for higher writing/reading speed and storage density. Multiferroic based memory can store more than two states, which in turn improve storage density, that can revolutionize next

generation storage techniques.[1,2] In multiferroics, this is achieved by the cross coupling of electric and magnetic orders, through magnetoelectric (ME) coupling.[3]

As elaborated in chapter 4, ME effect is the induction of electric polarization P, under the application of an external magnetic field H, and vice versa.[4] The past century has witnessed an evolution of ME materials from single phase to particulate composite to laminate composite from the perspective of material dimensions and constituents.[5] Single phase ME materials needs long range ordering and doesn't possess high inherent ME coupling near room temperature.[6] This difficulty can be circumvented by developing ME multiphase composites. Here, ferroic orders are electromagnetically coupled to each other via stress mediation resulting in enhanced ME coupling.[7,8] Massive attempts have been devoted to develop composites with various phase connectivity schemes like (0-3), (1-3), (3-3) etc. Later by 2001, researchers developed ME laminate composites with (2-2) connectivity where layer-by-layer architecture comprising of alternate ferromagnetic (FM) and piezoelectric phases.[9,10] These thick film laminates are advantageous due to minimal interfacial damping and low leakage currents, resulting in enhanced ME coupling[11].

In fact the phase connectivity has got significant influence on the ME response in a composite material. In laminated composites, the ME coupling is dictated by three factors such as;

(i) material parameters of constituent phases like dielectric permittivity, magnetic permeability, elastic constants, piezoelectric as well as piezomagnetic coupling coefficients,[12,13]

(ii) volume-to-thickness ratio of layers associated,[14] and

(iii) orientation of constituent phases and applied magnetic field.[15]

An important parameter that determines the ME response in laminate type composites is the interfacial coupling. Strain transfer happening at phase boundary is the key factor that determines the ME coupling. Still, there lacks a clarity on the theory of ME coupling in bulk laminates, which will be attempted in this chapter. Larger the interfacial area, maximum will be the strain transfer which in turn results in an enhanced value of ME coupling coefficient for laminate type (2-2), when compared to ME particulate type (0-3).

A bilayer composite with ferroelectric (FE)/piezoelectric layer and ferromagnetic/magnetostrictive layer having a free boundary is the simplest (2-2) composite. They are usually prepared by cofiring the corresponding layers together at high temperatures. Tape casting technique is widely employed for making individual layers has got some disadvantages. In multilayer tape casted heterostructures, the principal challenges are differential shrinkage caused by the mismatch in thermal expansion of individual layers and inter-diffusion and chemical reaction happening between the layers. In order to avoid these issues, hot-pressing technique has been employed instead of high temperature treatment.[16] Since the latter being cumbersome and expensive, researchers have been looking for a facile technique to generate high coupling ME composites.

Screen printing is a convenient method, where a magnetostrictive layer is printed over a FE layer at ambient conditions, thereby avoids post printing heat

treatment. Further, since the printed structures being porous and flexible, they can be realized on flexible substrates as well, say conductive tapes (or fabrics). Printing is performed using inks formulated out of constituent phases which should be cured at ambient temperature and pressure. Printing also possesses an additional advantage of less quantity of material requirement too. Hence, the present chapter focuses on developing a ceramic based ME composite via screen printing technique, similar to chapter 4 and tries to correlate the experimental properties with theory.

The ME effect in laminate composites depends on the microstructure and coupling interaction across the FE-FM interface.[17] The average or macroscopic field applied to a ME composite would permeate the material microstructure and would spread unequally into different points owing to heterogeneity of the material. The anisotropy due to the underlying crystalline nature of constituent phases contributes to this phenomenon. The local or microscopic fields are composed of external applied fields (which are designated as "average fields") and local variables and are related by governing equations. This chapter also focuses on analyzing the distribution of local fields in a (2-2) laminate ME composite. A homogenization method is developed in this chapter for composites of lowest crystallographic symmetry through a two-scale asymptotic analysis. The unit cells are so chosen that they can encompass the heterogeneity of composite comprehensively.

The ME material chosen in the present chapter is Pr doped $SrTiO_3$ (Pr:STO, where Sr:Pr=0.925:0.075) as in chapter 4. On the other hand, the FM material chosen is $CoFe_2O_4$ (CFO) which is a well-known magnetostrictive material. This material also

possesses high piezomagnetic coupling coefficient.[18] Hence a better ME coupling coefficient is expected at room temperature for Pr:STO-CFO bilayer ME (2-2) composites screen printed on conductive substrates, which is thoroughly investigated experimentally and theoretically, in the following sections.

5.3 Experimental Section

5.3.1 Materials

Cobalt acetate ($Co(CH_3CO_2)_2.4H_2O$, Sigma Aldrich), Iron nitrate ($Fe(NO_3)_3.9H_2O$, Sigma Aldrich), Titanium isopropoxide ($C_{12}H_{28}O_4Ti$, Sigma Aldrich), Praseodymium nitrate hexahydrate ($Pr(NO_3)_3{\cdot}6H_2O$), Acetyl acetone ($C_5H_8O_2$, Sigma Aldrich), Ethylene glycol ($C_2H_6O_2$, Sigma Aldrich), Strontium acetate ($C_4H_6O_4Sr$, Sigma Aldrich), 2-Methoxy ethanol (2-MOE, Sigma Aldrich) and Diethanolamine (DEA, Sigma Aldrich) were used as the starting materials.

5.3.2 Synthesis of CFO

About 0.02 mol of ($Co(CH_3CO_2)_2.4H_2O$ and 0.01 mol of ($Fe(NO_3)_3.9H_2O$ were mixed in 2-MOE and DEA in a round bottomed flask, using an ultra sonicator. Vigorous sonication was performed for 2 h till a uniform mixture of precursor was obtained. This solution was kept in an oil bath at 70 ˚C and continued heating for 12 h under constant stirring with refluxing in order to avoid evaporation of the solvents. After 12 h, the solution was allowed to dry. The dried powder was then taken for further characterizations. Pr doped STO (Sr:Pr=0.925:0.075) was synthesized using the same procedure as mentioned in section 4.3.2

5.3.3 Ink Formulation

After the phase formation of Pr:STO and CFO were confirmed and powders were qualified, our next aim was to develop a viscous ink out of the developed powder. As discussed in chapter 4, the solvents chosen here is binary solvent system consisting of xylene and ethanol, Triton X-100 as dispersant and ethyl cellulose as binder. The ink formulation steps are elaborated well in chapter 4.

5.3.4 Characterization

TG/DTA was performed using a thermo gravimetric analyzer from room temperature upto 1000 ˚C in oxygen atmosphere (TGA/DTA instruments, Shimadzu, Japan). Phase purity of calcined powder was confirmed using X-ray diffraction technique with Cu Kα radiation (X'Pert PRO diffractometer, PANalytical, Almelo, The Netherlands). High resolution TEM was used for analyzing the particle size of developed CFO powder (FEI Tecnai G2 30S-TWIN, FEI Co., Hillsboro, OR, USA). The rheological behavior of the ink was done using Rheo plus32 rheometer (Anton Paar, Ashland, VA, USA). The screen printing of ink on different substrates were performed using XPRT2 semiautomatic screen-printer (EKRA, Germany). Scanning electron microscopy was used for the microstructural analysis of printed films using JSM 5600LV model (JEOL, Tokyo, Japan). Surface roughness of thick film was estimated with the help of atomic force microscopy (AFM) in tapping mode (Multimode, Bruker, Germany). Magnetic measurements were performed using an oven setup attached to the physical property measurement system (PPMS, Quantum Design, USA). ME measurements were carried out in ac as well as dc magnetic fields. The ac magnetic

field was applied with the help of a pair of Helmholtz coils using which, a suitable magnetic field was applied across the sample and the ME output voltage was estimated by recording the induced polarization (P). The working principle is that the electric dipoles inside the sample align themselves with the ac magnetic field, resulting a drop in ac voltage across the sample which is measured via Faraday Effect. Thus it is clear that the apparent output voltage is purely due to the ME coupling effect. For measuring the dc field dependence of ME coupling, a setup consisting of dc electromagnet having bipolar power supply with GPIB integrated gauss meter. Both these fields were applied along the direction of thickness of the printed heterostructure. The data acquisition was performed using LabVIEW software.

5.4 Results and Discussion

The characteristic features of the Pr:STO powder is explained in detail, in chapter 4 and hence is not repeated here.

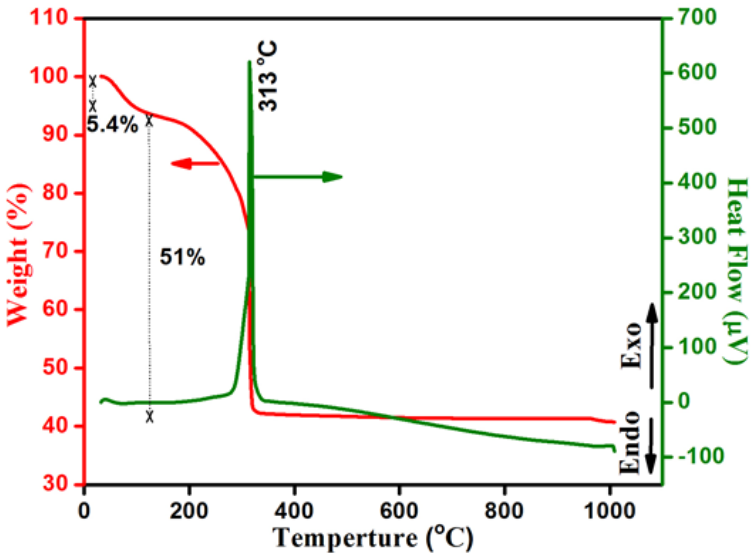

Figure 5.1: TG/DTA profile of as synthesized CFO powder.

The thermal decomposition of prepared CFO powder was investigated using TG/DTA analysis, as shown in figure 5.1. Two apparent weight losses are observed in the TG profile, one minor and the other major. First one is a weight loss of around 5.4%, observed upto 100 ˚C. The prominent weight loss of around 51% is observed between 150 ˚C and 350 ˚C for which a sharp exothermic peak at 313 ˚C in the DTA curve. This may be the signature of decomposition of acetates and nitrates to oxides. It should be noted that the weight loss is negligible after the decomposition temperature which indicates that the decomposed products are now formed into ferrites.

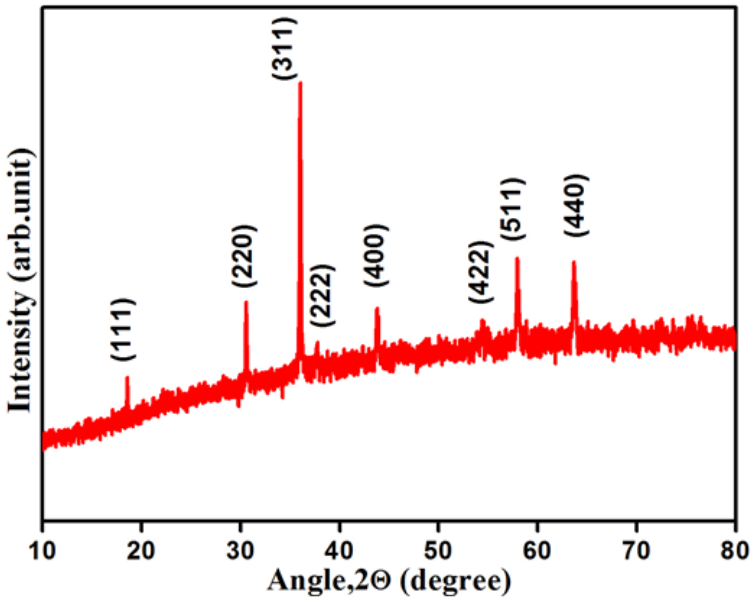

Figure 5.2: XRD pattern obtained for CFO powder calcined at 900 ˚C for 4 h.

The XRD pattern of post heat treated CFO at 900 ˚C is shown in figure 5.2. All the peaks in the pattern can be indexed to single phase spinel cobalt ferrite structure [JCPSD File Card No. 22-1086]. No intermediate or additional peaks can be observed in the obtained pattern within the sensitivity of experimental technique.

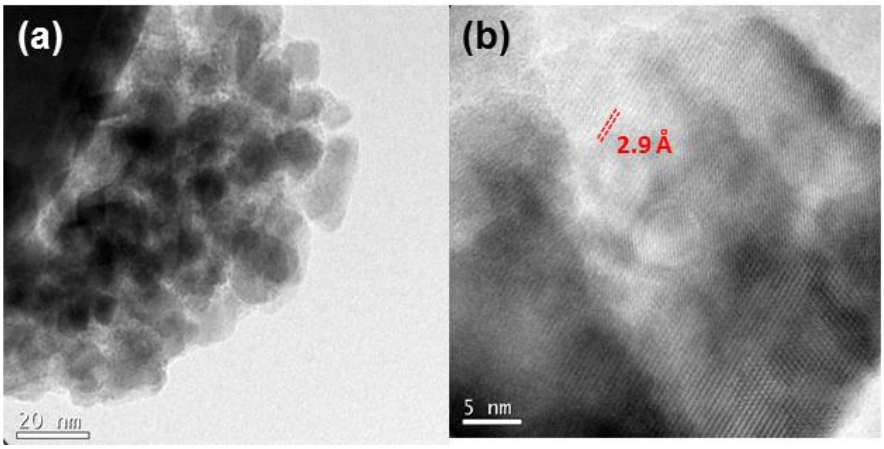

Figure 5.3: (a) TEM micrograph of CFO powder and (b) HRTEM showing the lattice plane.

The TEM micrograph of temperature treated CFO and its high resolution image is shown in figures 5.3(a) and (b) respectively. Most of the particles show a distorted spherical morphology as shown in figure 5.3(a). The particles are highly agglomerated since the CFO particles show room temperature magnetic property. These particles act like tiny magnets, attract together to form cluster which is clearly visible in the TEM micrograph. The average particle size is around 20 nm. The high resolution image shows crystal lattice with d spacing value 2.9 Å which corresponds to (220) plane.

The M-H loop of CFO at different temperatures are recorded and shown in figure 5.4(a). This reveals that the sample show ferromagnetism at 300 K, 500 K, 700 K while exhibit a paramagnetic behavior at 800 K. So at some temperature between 700 K and 800 K, the material changes its nature from ferromagnetic to paramagnetic behavior and hence Curie temperature lies in between these two temperatures. Also, one can observe a decrease in saturation magnetization (M_S) when temperature is increased from 300 K to 700 K. This is possibly due to the rearrangement of cation distribution, i.e., there will be a degree of inversion in CFO wherein an exchange of Co^{2+} and Fe^{3+}

from octahedral to tetrahedral sites and vice versa can happen when temperature is increased. [19,20]

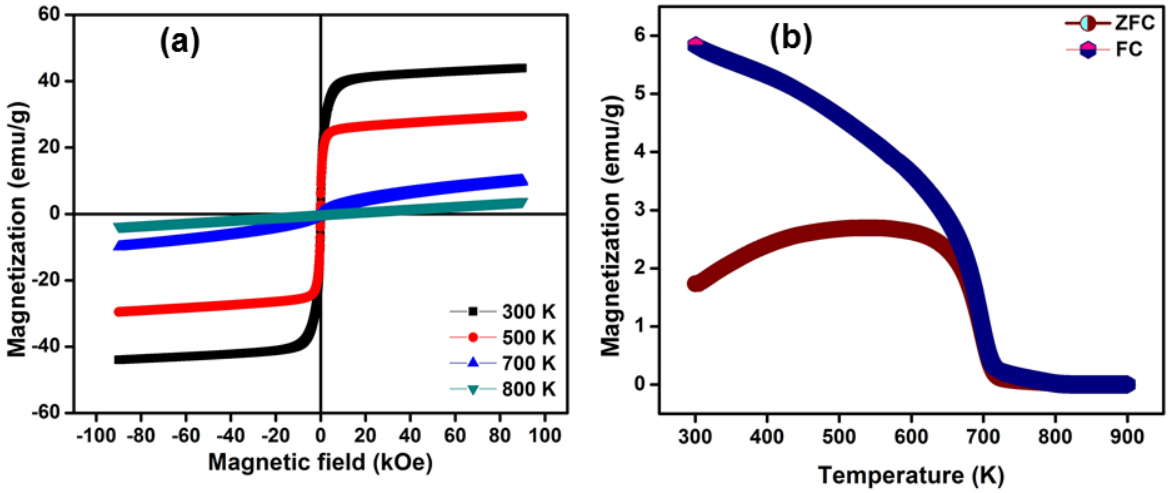

Figure 5.4: (a) M-H curves of CFO at different temperatures and (b) M-T curve at 50 Oe.

At room temperature, M_s value is around 40 emu/g which is lower than the reported value for bulk CFO (74 emu/g).[21] This deviation can be attributed to the super paramagnetic nature of the magnetic nanoparticles. Here, the density of magnetization will be less in the case of magnetic nanoparticles when compared to bulk materials which depend upon surface defects as well as morphology of the particles.[22] The surface defects in nanoparticles occur as a result of finite scaling of nanocrystallites which will induce a non- collinearity in the magnetic moments on the surface of magnetic particles. These effects are prominent in the magnetic nanoparticles having FM nature.[23] The measured M-T curve is shown in figure 5.4(b). A sudden drop in the curve is observed with increase in temperature, which indicates the magnetic transition from FM state to paramagnetic state. In case of CFO, the transition temperature is found to be 713 K in the present study.

After studying the material properties of CFO, a viscous ink that facilitates screen printing was developed, using finely ground powders. The study of flow characteristic of the ink is mandatory while developing a screen printable ink because minimum viscosity should be the optimum condition chosen for obtaining a smooth as well as uniform printed pattern. In order to facilitate room temperature curing, the solvent vehicle system has to be selected judiciously. Ethanol-xylene mixture has proven as one of the best solvent system that allow fast curing of ink.[24,25,26]

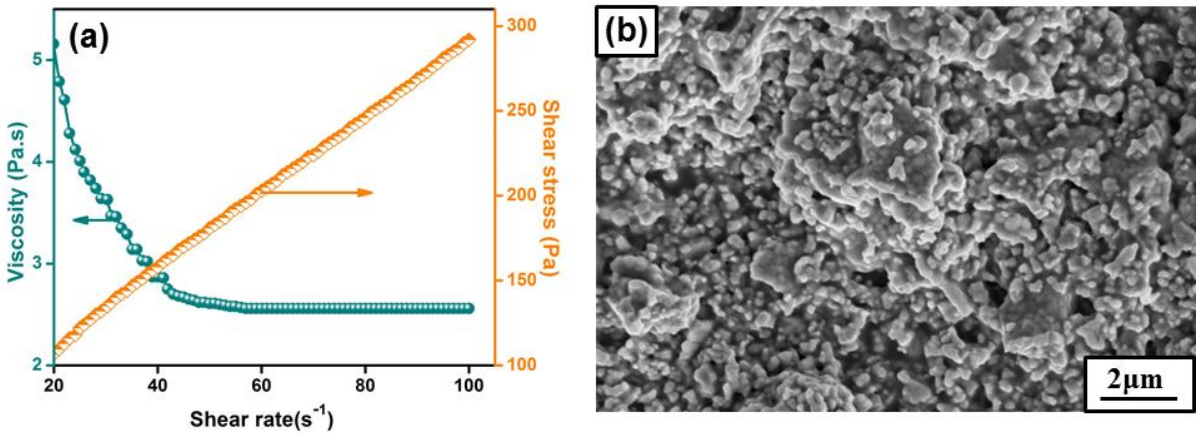

Figure 5.5: (a) Variation of viscosity and shear stress of CFO ink with shear rate and (b) SEM micrograph of printed CFO surface.

The rheological behavior of CFO ink is shown in figure 5.5(a). The viscosity curve shows a shear thinning nature. i.e., as shear rate increases, viscosity decreases and reaches a minimum value. Here the minimum value obtained is less than 3 Pa.s, which is feasible for screen printing of an ink. This optimal viscosity is needed for the free flow of ink through the mesh opening of the screen, at higher shear rates. The shear stress curve was also plotted and one can observe a pseudoplastic nature for developed ink. This nature helps in preventing the bleeding of ink beyond the boundaries after printing. This effect usually arises due to the aggregation of suspended particles.

Aggregation in a colloidal ink is usually caused by the attractive force like van der Waals and imbalanced repulsive force due to the steric and electrostatic effect of particles in the suspension. This will eventually help in preventing the particles in ink from approaching each other and create a weak bond between them. When a force is applied, these bonds will break and thereby reduces the viscosity.[27,28,29] The optimized ink was screen printed on cleaned platinized silicon [$Pt/Ti/SiO_2/Si(100)$]. The surface SEM was recorded for the printed film and is shown in figure 5.5(b). Some particles appear to be joined end to end may be due to the binding by ethyl cellulose. A uniform distribution of filler particle (CFO) is observed with a minimum amount of porosity. Porosity is an unavoidable in case of printed thick films as it arises from the volatilization of solvent system present in the ink formulation.

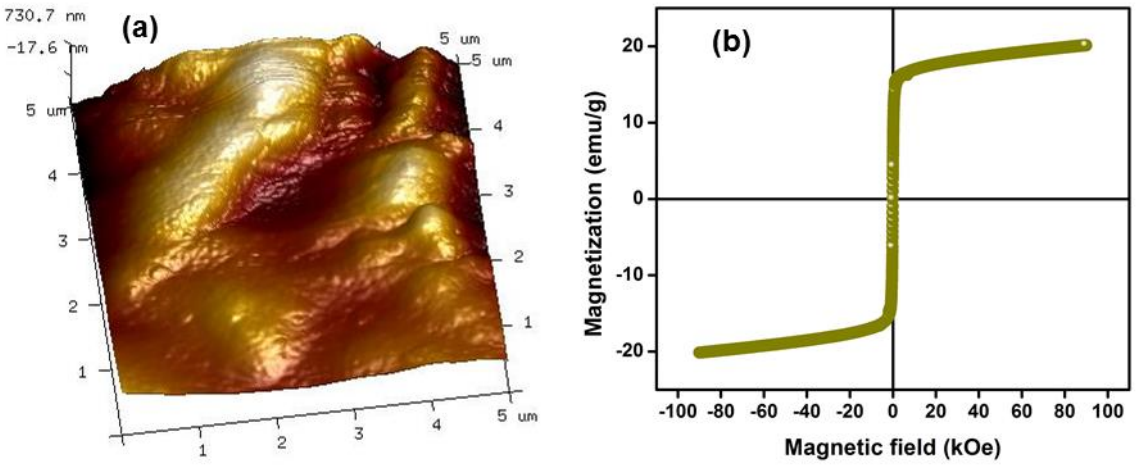

Figure 5.6: (a) 3D AFM image of double stroke screen printed CFO and (b) M-H curve taken for printed pattern at 100 K

Surface roughness of printed layer is an important parameter since the fabrication of printed electronic device involves various steps. Hence the surface roughness of screen printed CFO ink was studied using AFM working in tapping mode.

Surface smoothness depends greatly on the particle size distribution of filler, post printing leveling as well as the porosity created due to the evaporation of organic solvents, constituting the ink. The 3D AFM image of the printed pattern after double stroke printing is shown in figure 5.6(a). The average surface roughness (R_a) is obtained as 139±5 nm. The printed film shows a root mean square roughness (R_q) value of 183±5 nm. These values are lower than the values reported for screen printed inks used for printed electronic applications.[25,26] It shows that the developed ink can yield good quality printed patterns. Kurtosis value that indicates the unevenness of printed pattern was also calculated from the obtained 3D pattern and the value is obtained as 2.49. Any value less than 3 for kurtosis indicates that the surface has relatively few mountains and low valleys and this is termed as platykurtoic. These mountains and valleys arise due to the evaporation driven porosity. Skewness is a measure of asymmetry of the surface. Skewness for the present pattern was found to be -0.979. Usually negative value for skewness indicates that the surface distribution possess long tails than valleys at the measurement area.[24]

Figure 5.6(b) shows the M-H curve of CFO printed pattern at 300 K. There is a decrease in M_s value when compared to the synthesized CFO which is 40 emu/g. This can be attributed to the external components like binder as well as dispersant present in the ink formulations. These can arrest the spins at least on the surface, to align in the direction of magnetic field, which in turn reduces the magnetic property in case of thick films. Still, the FM property is retained in thick film state too which is important to expect a ME nature in composite, at room temperature.

On the other hand, a complete set of characterization was done Pr doped $SrTiO_3$ nanopowder and its quasi-ferroelectric printed pattern, which is described in chapter 4. In order to get an idea regarding the ME property of the composite developed with Pr doped STO and CFO, first screen printed one over another on top of a platinized silicon wafer. The cross sectional SEM was taken for the composite and is shown in figure 5.7.

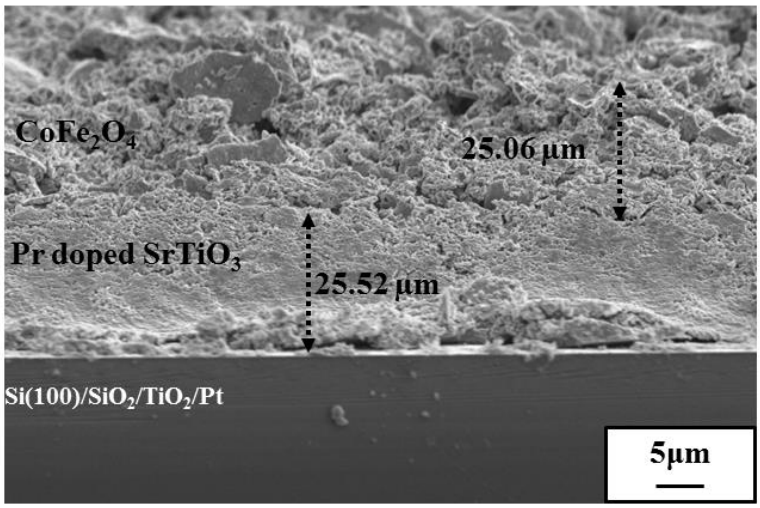

Figure 5.7: Cross sectional SEM image of Pr:STO and CFO (2-2) composite.

The SEM image reveals compatibility between the Pr:STO and CFO layers since no visible delamination and cracks between these two layers is observed. The average thickness for the Pr:STO layer is found to be 25.52±0.03 µm and for CFO layer it is 25.06±0.03 µm. Seemingly dense microstructure is also observed in both the layers.

The P-E curve of Pr:STO-CFO bilayer composite at room temperature is shown in figure 5.8(a). A leaky dielectric behavior is observed which shows a lower value of remanence (P_r) when compared to Pr:STO printed thick film alone. This is due to the presence of CFO layer in between the electrodes which is attached to Pr:STO layer. The CFO is clamped with the Pr:STO layer which in turn delimits the electric field to polarize

the dipoles close to it. This will result in a lower polarization value as reflected in the FE curve.

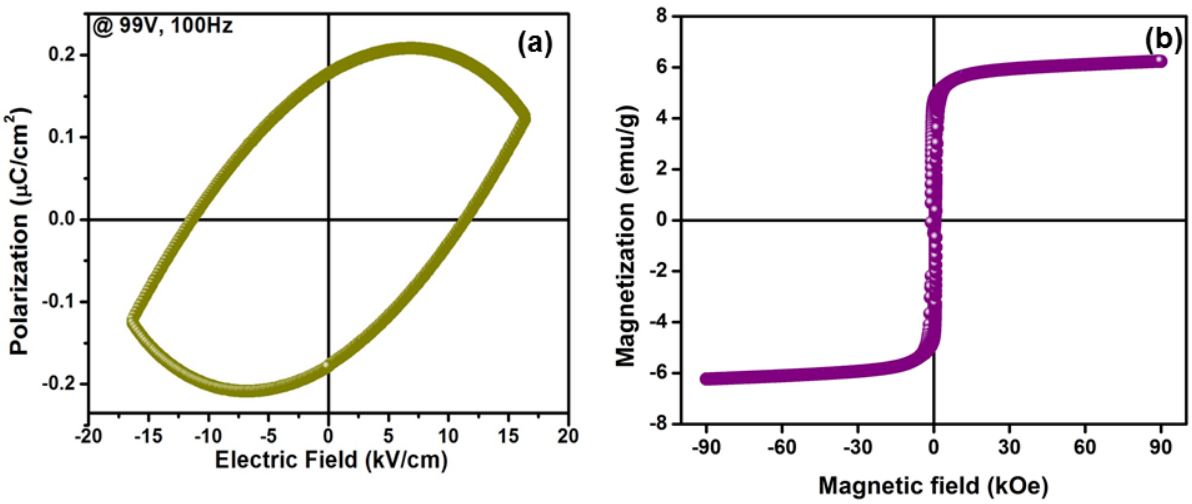

Figure 5.8: (a) P-E loop and (b) M-H loop of Pr:STO-CFO bilayer composite at 300 K.

The M-H hysteresis curve at room temperature of bilayer composite is shown in figure 5.8(b). Even though the FM nature is retained in the composite, M_s value decreased considerably. This can be attributed to the interaction of Pr:STO with CFO. The dipoles in Pr:STO due to the influence of ME coupling at the interface (or due to demagnetization field), will restrict the spins to align in the applied magnetic field which will result in a lower value of M_s. The quasi-FE and FM nature present in the composite shows the presence of a spin-charge interaction in the composite that may give rise to ME coupling in the composite.

Now let us examine the peculiar ME coupling of the bilayer laminates. The coupling in ME heterostructures arises due to the strain transfer between the phases. The interface that separates two layers are well defined in this case, which is clear from the cross sectional SEM (Figure 5.7).

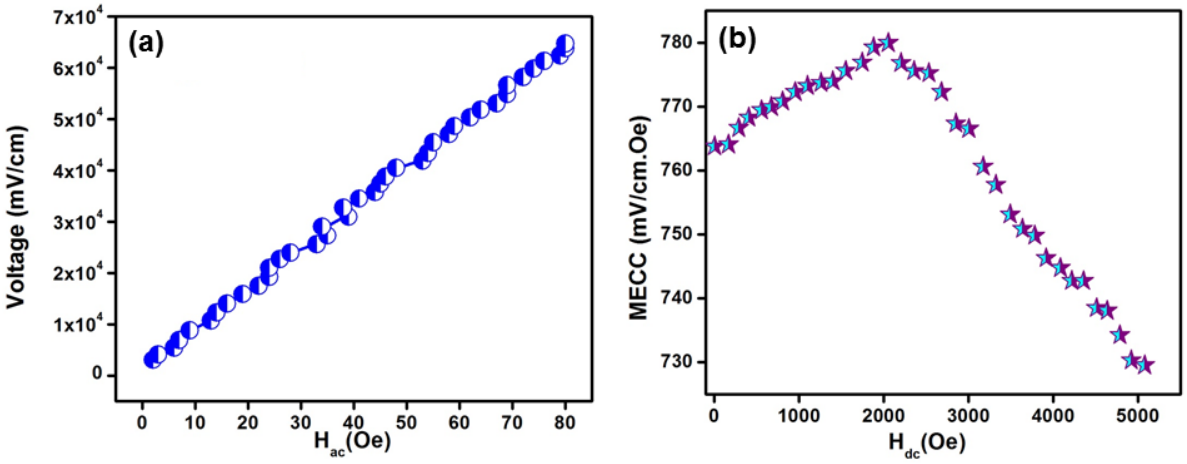

Figure 5.9: Variation of ME coupling coefficient under the application of (a) DC field and (b) AC field for the Pr:STO-CFO bilayer composite at room temperature.

When a magnetic field is applied against the bilayer heterostructure, a strain will be generated in the magnetostrictive phase which will further transferred to the attached FE layer at the interface. So at the output, there will be an electric polarization generated from the FE layer. Hence, the ME coupling in these kinds of layered heterostructures occurs from the elastic interaction between the FE-FM phases.

The ME coupling in the Pr:STO-CFO composite was studied for both ac and dc magnetic fields. The strain induced ME voltage at the output is given by equation (1.18). Here, for the MECC measurement was taken for 30 μm thick sample. When ac magnetic field was applied, voltage increases linearly as shown in figure 5.9(a). The MECC for this ac response was calculated from equation (1.18) and was obtained to be very impressive at 780 mV/cm.Oe. The dc response was also recorded for the composite (figure 5.9(b)). The MECC value increases up to a maximum value at a dc magnetic field and decreases thereafter. The maximum MECC value obtained for dc response in the Pr:STO-CFO bilayer composite is 779 mV/cm.Oe. Since this is a layer-by-layer structure

with thickness in the range of microns, the domain walls under the application of external magnetic field will progress much easily when compared to other tape casted laminates.

A theoretical analysis will throw more light into the microscopic phenomena occurring in layered multiferroics, when a magnetic field is applied. Hereafter, we try to model the average polarization and magnetization in a magnetoelectric thick film against magnetic and electric fields respectively, and understand the electric-to-magnetic energy conversion occur in them through the transmission of an electric field induced elastic stress from the FE to FM phase.

5.4.1 Theoretical Modelling

High magnetoelectric coupling between the Pr:STO and CFO layers can occur in response to an applied magnetic field and also by the confluence of magnetostrictive effects and piezoelectricity to give rise to an electrical response This has been analyzed through homogenization method utilizing the separation of scales and combining variational formulation. Herein, we model the distribution of local fields in the Pr:STO and CFO based ME composite of (2–2) connectivity, due to the application of external magnetic and electric fields. We developed a homogenization method for multiferroics through a two-scale asymptotic analysis of the microscopic electric, magnetic and force fields to profile the impact on each of them, by an external field at microscopic scale.

5.4.1.1 Constitutive Equations and Homogenization

The ME effect is described by a term in the thermodynamic potential $\emptyset_{me}$ that is linear both in the magnetic (H) and electric (E) field, such that,

$$\emptyset_{me} = -\alpha_{ik} E_i H_k \tag{5.1}$$

where the ME coupling coefficient α_{ik} is an unsymmetrical tensor.[30] When H = 0, the electric field generates a magnetization,

$$M_k = \alpha_{ik} E_i \tag{5.2}$$

and when E = 0, the magnetic field generates an electrical polarization,

$$P_i = \alpha_{ik} H_k \tag{5.3}$$

A two-scale asymptotic homogenization analysis combined with a variational formulation is developed for determination of the equivalent material properties of a periodic multiferroic ME composite. Local and average (global) electrical, magnetic, and mechanical constitutive behaviour are computed. The model takes into account the FE, FM, and the composite ME phases by treating the constitutive behaviour. For a linear magneto- electro-elastic solid, constitutive equations are governed by the electrical, mechanical and magnetic fields. The model quantifies the local electrical and magnetic potential, displacements, electrical and magnetic fields, stress and strain fields, magnetization (through magnetic flux density) and polarization (through electric displacement) and von-Mises stress, besides the effective magneto-electro-mechanical properties.

The general homogenization method applied to multiferroics has no limitations regarding volume fraction or shape of the constituents involved and is based upon assumptions of periodicity of the microstructure and the separation of the microstructure scale through a proper asymptotic expansion.[31] The mathematical

theory of homogenization accommodates the phase interaction in characterizing both the macro- and micro-mechanical behaviours of the composite material. i.e., the method permits the introduction of different field equations in a microscopic scale to each constituent of a composite while following the representative volume element (RVE) notion. This study considers multiferroic materials that respond linearly to changes in the electric field, electric displacement, mechanical stress, strain as well as magnetic field. Let Ω be a fixed domain in x space. We consider an auxiliary y space divided into parallelepiped periods Y. For a linear anisotropic ME material, generated through the periodic repetition of a unit cell representing the smallest sample of heterogeneity of the material domain Ω, the governing equations are given below;

force equilibrium equation,

$$\sigma_{ij,j} + b_i = \rho \ddot{u}_i \tag{5.4}$$

strain-mechanical displacement relation,

$$\epsilon_{ij} = \frac{1}{2}\left(u_{i,j} + u_{j,i}\right) \tag{5.5}$$

electrical (magnetic) field-electrical (magnetic) potential relations,

$$\left.\begin{aligned} E_i &= -\varphi_{,i} \\ H_i &= -\psi_{,i} \end{aligned}\right\} \tag{5.6}$$

and the quasistatic steady-state Maxwell's equations for electromagnetic phenomena,

$$\left.\begin{aligned} D_{i,i} &= 0 \\ B_{i,i} &= 0 \end{aligned}\right\} \tag{5.7}$$

In a multiferroic solid, the mechanical, electrical and magnetic variables are related by constitutive relations. For small deformations, the linear constitutive laws of multiferroics in the absence of heat flux are given by,

$$\sigma_{ij} = C_{ijkl}^{EH}\epsilon_{kl} - e_{kij}E_k - e_{kij}^{M}H_k \tag{5.8}$$

$$D_i = e_{ijk}\epsilon_{jk} + \kappa_{ij}^{\epsilon H}E_j + \alpha_{ij}H_j \tag{5.9}$$

$$B_i = e_{ijk}^{M}\epsilon_{jk} + \alpha_{ji}E_j + \mu_{ij}^{\epsilon E}H_j \tag{5.10}$$

Here σ, ϵ, u, b, ρ, D, B are stress, strain, displacement, body force, mass density, electric displacement vector, and magnetic flux density respectively.C^{EH}, e, e^{M}, $\kappa^{\epsilon H}$ and $\mu^{\epsilon E}$ are stiffness, strain to (electric, magnetic) field coupling constants (or piezo-electric and -magnetic coefficients), permittivity (dielectric) and (magnetic) permeability respectively (It should be noted that the notation used for dielectric permittivity in the theory $\kappa^{\epsilon H}$ is equivalent to the term ε_r used elsewhere in the thesis).

Considering the standard homogenization procedure, the material functions C^{EH}, e, e^{M}, $\kappa^{\epsilon H}$ and $\mu^{\epsilon E}$ are considered to be Y-periodic functions in the unit cell domain defined as,

$$Y = [0, Y_1]\times[0, Y_2]\times[0, Y_3].^{31}$$

If $y = x/\varepsilon$ where ε is the asymptotic scale factor representing the microstructure scale, the displacement (u), electric potential (φ) and magnetic potential (ψ) are expanded asymptotically up to the first-order variation terms, giving,

$$\left.\begin{aligned} u^{\varepsilon}(x) &= u^{0}(x,y) + \varepsilon u^{1}(x,y) \\ \varphi^{\varepsilon}(x) &= \varphi^{0}(x,y) + \varepsilon \varphi^{1}(x,y) \\ \psi^{\varepsilon}(x) &= \psi^{0}(x,y) + \varepsilon \psi^{1}(x,y) \end{aligned}\right\} \quad , y=x/\varepsilon, \qquad (5.11)$$

where $u^1(x,y)$, $\varphi^1(x,y)$ and $\psi^1(x,y)$ are functions to be determined which are Y periodic in y. Here the two scales x and y are spatial variables where x is a macroscopic quantity and y is a microscopic one.[32] The functions involved in this expansion are assumed to be dependent on these two variables, where one (i.e., x) describing the "global" or average response of the structure and the other (i.e., y) describing the "local" or microstructural behaviour. Here, the two variables x and x/ε take into account the two scales of the homogenization; the x variable is the macroscopic variable, whereas the x/ε variable takes into account the microscopic geometry.

Applying calculus of variations, passing through the limit ε→0 and advance using asymptotic analysis one obtains the effective magneto-electro-elastic moduli, viz., the homogenized elastic stiffnesses $\tilde{C}_{ijkl}^{EH}$, piezoelectric coefficients $\tilde{e}_{ijk}$, piezomagnetic coefficients $\tilde{e}_{ijk}^{M}$, dielectric permittivities $\tilde{\kappa}_{ij}^{\epsilon H}$, magnetic permeabilities $\tilde{\mu}_{ij}^{\epsilon E}$ and the ME coupling coefficients $\tilde{\alpha}_{ij}$ of the ME multiferroic. In other words one could get a good approximation of the macroscopic behaviour of such a heterogeneous material by letting the parameter ε which describes the fineness of the microscopic structure, tend to zero (ε→0) in the equations describing phenomena. And for a homogeneous material, the physical properties do not depend on x. The detailed theoretical analysis is given elsewhere.[31] (In all the expressions of this chapter, it may be noticed to discern the difference in notations of asymptotic scale factor ε and the mechanical strain ϵ. All the

microscopic quantities will carry the notation of ε to identify their local character, which should not be mistaken for ε_r which is used to describe dielectric permittivity, elsewhere in the thesis).

5.4.2 Homogenization of ME Composite

A general homogenization method was applied to ME composites based on several assumptions that includes periodic boundary conditions on microstructure as well as separation of microstructure scale through asymptotic expansion. The product property of homogenized ME coupling based on the asymptotic analysis of an ME material is given by,[31,33]

$$\tilde{\alpha}_{ij} = \frac{1}{|Y|}\int_Y e_{pkl}(x,y)\frac{\partial \Gamma_k^m}{\partial y_l} - \kappa_{pj}^{\epsilon H}(x,y)\frac{\partial \Psi^m}{\partial y_j} - \alpha_{pj}(x,y)(\delta_{jm} + \frac{\partial Q^m}{\partial y_j})] \times (\delta_{np} + \frac{\partial R^n}{\partial y_p})dY \quad (5.12)$$

Here, R and Q, are characteristic electric and magnetic displacements. Γ and Ψ are the characteristic coupled functions satisfying a set of microscopic equations. Due to the microstructure inhomogeneity, these characteristic functions will appear in the microscopic displacement, electric and magnetic perturbations namely, $u^1(x,y)$, $\varphi^1(x,y)$ and $\psi^1(x,y)$ respectively. Their macroscopic spatial derivatives namely, $u^0(x,y)$, $\varphi^0(x,y)$ and $\psi^0(x,y)$ will bridge the macroscale as well as microscale through characteristic function as shown in 5.12. The piezoelectric coefficient is indicated by e_{pkl} and dielectric permittivity is shown by $\kappa_{pj}^{\epsilon H}$ at constant strain and magnetic field (H). $i, j, k, \ldots = 1,2,3, \ldots$ are the 3-cordinate indices and δ_{ij} is Kronecker delta.

Here in the present case, ME composite is a heterogeneous body which is assumed to be obtained by the translation of microstructure of size, Y. For a homogenized laminate type ME composite, its physical properties have no effect on the global frame of reference, x. But here the composite is heterogeneous and hence the magneto-electro-mechanical properties has a dependence on x. The material properties like $\kappa^{\epsilon H}, e, \alpha$ etc. and R, Q, Γ and Ψ are Y periodic functions that depends on the microscopic coordinates y. The efficiency of voltage controlled magnetization state is measured by effective $\tilde{\alpha}$ value. So the key objective in ME composite research lies in the maximization of its value by which they can be sought in potential applications.[34]

5.4.2.1 Microscopic and Average Fields

The microscopic fields (or local fields) pertaining to the electrical, magnetic, and spatial degrees of freedom and their coupling interactions at an arbitrary point in the unit cell can be obtained by the asymptotic analysis.[35] The microscopic fields at an arbitrary point of the unit cell can be determined using the equations Eq. 5.6 and 5.11. The displacement field $u^{\varepsilon}(x)$, the electric potential field $\varphi^{\varepsilon}(x)$ and the magnetic potential field $\psi^{\varepsilon}(x)$ involving details of the microstructure are given

$$u^{\varepsilon}(x) = u^{0}(x) + \varepsilon[\chi_k^{mn}(x,y) \times \epsilon_{mn}\big(u^{0}(x)\big) + \Phi_k^{m}(x,y)\frac{\partial \varphi^{0}(x)}{\partial x_m} + \Gamma_k^{m}(x,y)\frac{\partial \varphi^{0}(x)}{\partial x_m} \tag{5.13}$$

$$\varphi^{\varepsilon}(x) = \varphi^{0}(x) + \varepsilon[\eta^{mn}(x,y) \times \epsilon_{mn}\big(u^{0}(x)\big) + R^{m}(x,y)\frac{\partial \varphi^{0}(x)}{\partial x_m} + \Psi^{m}(x,y)\frac{\partial \varphi^{0}(x)}{\partial x_m} \tag{5.14}$$

$$\psi^{\varepsilon}(x) = \psi^{0}(x) + \varepsilon[\lambda^{mn}(x,y) \times \epsilon_{mn}\left(u^{0}(x)\right) + \theta^{m}(x,y)\frac{\partial \varphi^{0}(x)}{\partial x_m} + Q^{m}(x,y)\frac{\partial \varphi^{0}(x)}{\partial x_m} \quad (5.15)$$

Here, χ, R and Q are microscopic characteristics material, electric and magnetic displacements. $\Phi, \Gamma, \Psi, \lambda, \theta, \eta$ are characteristic coupled functions. u^0 is a constant with respect to x and have dependence only on y. This is valid for fields like ψ^0 and φ^0.[32]

For the complete knowledge about that state of electrical as well as magnetic field impacts within the body (state of stress), one must have an idea regarding stress and other fields at every point in the body. The microscopic stress, $[\sigma_{ij}^{\varepsilon}(x)]$, electrical displacement $[D_i^{\varepsilon}(x)]$ and magnetic flux densities $[B_i^{\varepsilon}(x)]$ at each point of the domain can be computed using equations 5.8-5.10 as well as field equations 5.5 and 5.6. The flux normally represents the product of average normal component of field and the surface area. Here also, same definition is applicable for flux density, B. The electrical displacement, D is a measure of polarization P to the applied electric field, E. The equivalence of average stress and homogenized stress can be expressed by applying average operator $\langle . \rangle$ denoting $\left(\frac{1}{|Y|}\int_Y . dY\right)$, where Y is the domain size.

Average fields can be computed by the following equations,

$$\langle \sigma_{i,j} \rangle = \tilde{C}_{ijkl}^{EH}\left(\frac{\partial u_k^0(x)}{\partial x_l}\right) + \tilde{e}_{kij}\left(\frac{\partial \varphi^0(x)}{\partial x_k}\right) + \tilde{e}_{kij}^{M}\left(\frac{\partial \psi^0(x)}{\partial x_k}\right) \quad (5.16)$$

$$\langle D_i \rangle = \tilde{e}_{ijk}\left(\frac{\partial u_j^0(x)}{\partial x_k}\right) - \tilde{\kappa}_{ij}^{\epsilon H}\left(\frac{\partial \varphi^0(x)}{\partial x_j}\right) - \tilde{\alpha}_{ij}\left(\frac{\partial \psi^0(x)}{\partial x_j}\right) \quad (5.17)$$

$$\langle B_i \rangle = \tilde{e}_{ijk}^{M} \left(\frac{\partial u_j^0(x)}{\partial x_k} \right) - \tilde{\alpha}_{ji} \left(\frac{\partial \varphi^0(x)}{\partial x_j} \right) - \tilde{\mu}_{ij}^{\epsilon H} \left(\frac{\partial \psi^0(x)}{\partial x_j} \right) \qquad (5.18)$$

These are macroscopic equations because they does not contains y. These can be computed using the homogenized solutions for u^0, φ^0, ψ^0 and that of corresponding fields namely, $\left(\frac{\partial u_j^0(x)}{\partial x_k} \right), \left(\frac{\partial \varphi^0(x)}{\partial x_j} \right), \left(\frac{\partial \psi^0(x)}{\partial x_j} \right)$ are prescribed. This postulate is applicable in the case of microscopic fields, microscopic stress, electrical displacements and flux densities.

5.4.3 Numerical Implementation

The methodology used to obtain the average and local fields is based on the software POSTMAT (*material post processing*) developed by Guedes and Kikuchi.[35] It is to be noticed that the homogenized coefficients only depend on the local (microscopic) structure of the medium, and is obtained by the numerical solution of the boundary value problem, where the boundary conditions being of the periodic type. The homogenization method gives relevant information on the local and global behaviours in contrast to majority of problems in mechanics where the micro- and macro-processes are of very different nature.[32] Microscopic cell problems are solved prior to the macroscopic homogenized ones, and the finite element approximations related to the microscopic problem are defined to evaluate the homogenized coefficients subjected to periodic boundary conditions. Details of numerical implementation of homogenization ME composite are briefed below. Once the homogenized solutions for u^0, ψ^0 and φ^0 are known, then one can compute, the local displacement, potentials,

fields, strains, stresses, and equivalent von-Mises stresses for each element and at each integration point. (The equivalent von-Mises stress at the nodes is an average of the values at the Gauss points of the surrounding elements with same material properties.)

ME multiferroic composite, in general, can be considered as an aggregate of several single crystalline crystallites/grains and hence the system altogether would be polycrystalline nature. The unit cell or the representative volume element (RVE) conceived in this work is a volume containing a sufficiently large number of crystallites or grains that its properties can be considered as equivalent to that of the macroscopic sample. The electric polarization *P*as well as the magnetization *M* interspersed inside the crystallites could be mapped using some coordinate system. In a sense the underlying crystal orientation can encompass the orientations of *P* or *M*. Thus we introduce the Euler angles (ψ^0,φ^0,θ) to quantify the crystal orientations of a multiferroic polycrystal, as the crystallites in an as-grown sample are randomly oriented in the lattice space and hence require three angles to describe its orientation with reference to a fixed coordinate system. Here we use the so called *x-convention*, where the first and third rotation is through the *y* axis and the second rotation is through intermediate *x* axis. Thus all physical quantities like $\lambda'_{ijklmn\ldots}(y')$ expressed in a crystallographic coordinate system y′will be coordinate transformed to local coordinate system *y* according to the following scheme:

$$\lambda_{ijkl\ldots}(y) = e_{im}e_{jn}e_{kp}e_{lq}\ldots\widetilde{\lambda'}_{mnpq\ldots}(y') \tag{5.19}$$

before it is introduced for homogenization. (i.e., the FE and FM materials' electromechanical property data entered into the homogenization program are

obtained with respect to the crystallographic coordinates.) Here $e_{\mu v}$ are the Euler transformation matrices.[36]

In the finite element (FEM) simulation of the homogenization, a multiferroic crystallite is represented by a finite element in the unit cell. Thus we have a polycrystalline unite cell having as much number of crystallites as the number of finite elements by which it is discretized. As-grown FE (or for that matter FM) polycrystal (here printed film), often ends up in a near complete compensation of polarization (or magnetization) and the material consequently exhibit very small, if any, electric (or magnetic) effect until they are poled by the application of an electric (magnetic) field. The orientation distribution of the crystallites (grains) in such a polycrystalline material would be uniform with a standard deviation $\sigma \rightarrow \infty$ before poling (application of electric/magnetic field) and that after poling would best be represented by a distribution function with $\sigma \rightarrow 0$. Thus, any pragmatic configuration of orientation distribution of grains in multiferroic material would fit in a Gaussian distribution defined by the probability distribution function

$$f(\propto |\mu, \sigma) = \frac{1}{\left(\sigma\sqrt{2\pi}\right)} exp - \left[\frac{(\alpha - \mu)^2}{2\sigma^2}\right] \qquad (5.20)$$

where $\mu$and σ are the mean and standard deviation of angle α, which corresponds to Euler angle. The convergence of ME properties with unit cell size allows us to determine the simulation-space independent, equivalent ME properties of the composite. Convergence analyses on ME composite reveal the accuracy one derives from discretizing the unit cell (sampling of unit cells with more or less number of grains) is minimal above 1000 elements/grains.[37] Consequently, in this study, we kept unit cell

sizes greater than 1000 finite elements. In order to solve the microscopic system of equations resulting from homogenization, FEM formulation was developed and its details are given elsewhere.[31] A three dimensional ($3D$) multiferroic FEM is conceived with five degrees of freedom (DOF), three DOF for spatial displacement and one each for electric and magnetic potentials. Eight-noded isoparametric elements with 2×2×2 Gauss-point integration are used obtain solutions. Altogether there were nine microscopic equations that should be solved for as much number of unknowns namely the characteristic functions χ_i^{mn}, η^{mn}, λ^{mn},R^m,Φ_i^m,θ^m,Q^m,Ψ^m and Γ_k^m, where the indices m, n=1,2,3.[31] The problem is reduced to standard variational FEM, after the usual approximations of finite element formulation and can be expressed concisely as,

$$\boldsymbol{Ku} = \boldsymbol{f} \tag{5.21}$$

where $\boldsymbol{K}$ is the global stiffness matrix, $\boldsymbol{u}$ is the vector of unknown functions and $\boldsymbol{f}$ is the load vector.

5.4.4 Numerical results

5.4.4.1 Homogenized values

Here we model a system of (2-2) ME composite consisting of layer of FE material (Pr:STO, where Sr:Pr=0.925:0.075) glued into a laminate with a layer of FM material (CFO). Both the constituents of composite are of equal volume. We use, single crystalline data for tetragonal STO[38] (which resembles Pr doped STO) and polycrystalline data for CFO[39] the resulting system would be a single-crystal FE–polycrystal (or ceramic) FM composite. First we have run the homogenization to evaluate the equilibrium effective properties of the composite to discern the ME coupling. We introduced an orientation distribution for the Pr:STO layer of the laminate

to render it polycrystalline nature with a texture. The grains constituting the polycrystal are assumed to be single crystalline and each of them are assigned with an orientation picked up randomly from a normal distribution. The results are summarized in Table 5.1 along with the experimental results of Pr:STO–CFO. Since the individual phases of the composite being devoid of any multiferroic property, they lack the property of ME coupling as such. Since we do not have experimental characterization of full FE data, we have used computational data for STO from Erba et al., where they used *ab initio* theoretical simulation.[38] However, the deviation of computational value of ME voltage coupling ($\tilde{\alpha}_{E33}$) is expected mainly due to the paucity of Pr:STO data to be used for simulation. Since the computational model does not take the porosity of the composite thick film sample into account, its influence can affect the ME coupling data and can contribute to the deviation. Notwithstanding this, the effective values given in Table 5.1 for ME composite would provide a guide to the comprehensive experimental characterization of Pr:STO–CFO composite.

Table 5.1: Values of the homogenized piezoelectric stress coefficients $\tilde{e}_{i\mu}$ (in C/m^2), piezomagnetic coefficients $\tilde{e}^{M}_{i\mu}$ (in N/Am) dielectric permittivity $\tilde{\kappa}^{\epsilon H}_{ij}$ (in κ_0) and ME voltage coefficient (absolute value) $|\tilde{\alpha}_{Eij}|$ (in mV/cm.Oe) of ME composite.

Method	$\tilde{e}_{31}$	$\tilde{e}_{33}$	$\tilde{e}_{24}$	$\tilde{e}^{M}_{31}$	$\tilde{e}^{M}_{33}$	$\tilde{e}^{M}_{24}$	$\tilde{\kappa}^{\epsilon H}_{11}$	$\tilde{\kappa}^{\epsilon H}_{33}$	$\tilde{\alpha}_{E11}$	$\tilde{\alpha}_{E33}$
Simul.	0.02	0.18	0.80	23.8	36.3	397.9	127.2	20.3	3418.6	96
Expt.	_	_	_	_	_	_	_	_	_	779

5.4.4.2 Application of Electric and Magnetic Field on Printed ME Thick Film

Here we model the above system of (2-2) ME composite consisting of polycrystalline FE material (Pr:STO) and FM layer of CFO upon applying an external

electric field E. It is interesting to notice the distribution of microscopic fields computed at every nodal points of the FEM mesh constructing the microstructure. The distribution of some of the significant local physical quantities across the microscopic material upon applying a global external electric field $\mathbb{E}$, large enough to saturate the electric response, is as shown in figure 5.10. Here the volume fraction of the FE (Pr:STO) component in the ME composite is kept at v_f = 50% (or equivalently v_f of CFO is 50%) conforming the experiment. The lower layers in the subplots shown in Fig. 5.10 refers to the Pr:STO layer and the top layer is CFO. The spread of local fields provide an indication of the response of the material microstructure to the applied electric field. The magnetic scalar potential ψ^{ε} exhibits the emergence of magnetism consequent to the application of electric field, obviously due to the ME coupling appearing in the composite. It is a vital parameter that the ψ^{ε} and its distribution can provide information regarding the magnetic field (equation 5.6) and its distribution across the composite. The electric potential φ^{ε} as well as magnetic potential ψ^{ε} show a concentration near and across the interface. Since the ME coupling resulting from E in ME composites is facilitated through stress/strain transfer due to piezoelectric effect in the FE phase and the consequent straining of the FM layer. This would result in the generation of a magnetic potential and hence the magnetization of the composite.

The microscopic stress profile $\sigma_{ij}^{\varepsilon}$shown in figure 5.10 exhibits the distribution of this stress and its values provide a measure of the strength of the coupling. It is seen that the components $\sigma_{11}^{\varepsilon}$ and $\sigma_{22}^{\varepsilon}$ characterizing the distribution along the xy plane of the composite show stress contraction along the magnetic layer (-ve values). The shear components ($\sigma_{12}^{\varepsilon}$ and $\sigma_{13}^{\varepsilon}$) show nearly uniform distribution. Similar is the spread of

longitudinal stress component $\sigma_{33}^{\varepsilon}$ along z axis of the composite. Expansive strain along the z-axis across the FE layer $\epsilon_{33}^{\varepsilon}$ results in an overall negative magnetic field H_3^{ε} in that direction. This is in accordance with equation 5.6.

Table 5.2: Values of average polarization and magnetization of ME composite.

Method	P_r (μC/cm²)	M_r (emu/g)
Simulated	0.2164	1.72
Experimental	0.1767	4.69

We have computed the average polarization ($\langle P_r \rangle$) and magnetization ($\langle M_r \rangle$) of the composite. The values are found to be $\langle P_r \rangle$=0.2164 μC/cm² and $\langle M_r \rangle$=1.72 emu/g, which are in the same order as that of experimental values (table 5.2). The slight deviation can be explained based on the non-ideal inclusion of porosity and presence of polymeric binder that wraps the grains in the printed ME films. Here the polarization and magnetization components are along z axis which is equivalent to y_3 axis of the microstructure.

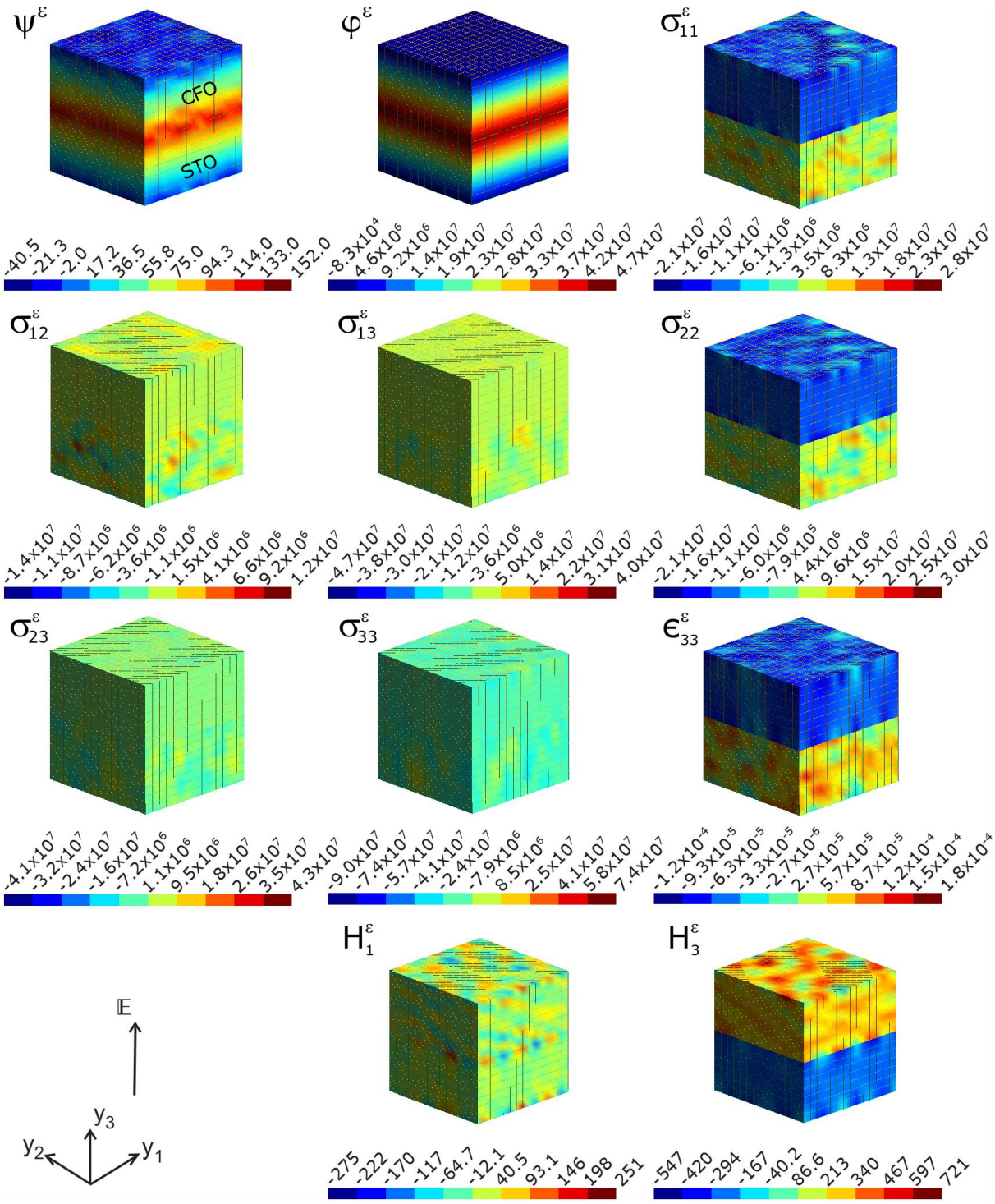

Figure 5.10: Map of local fields (computed at the nodal points of the FEM) of ME composite (Pr:STO-CFO) namely, magnetic scalar potential ψ^{ε}(in A), electric potential φ^{ε}(in V), stress $\sigma_{ij}^{\varepsilon}$ (in N/m^2) strain $\epsilon_{33}^{\varepsilon}$, magnetic field H_i^{ε} (in A/m) upon applying global electric field $\mathbb{E}$ on microstructure.

5.5 Conclusions

This chapter tried to understand the phenomena of magnetoelectric coupling in printed layered laminates with the help of a suitable theoretical model. The magnetic component, $CoFe_2O_4$ nanopowder was synthesized using sol-gel technique with the objective to make a bilayer ME composite with Pr-doped $SrTiO_3$. The phase purity of the former was confirmed with XRD analysis and particle size was measured to be in the range of 20 nm. The FM nature of CFO was confirmed from magnetic characterizations. A room temperature curable ink based on CFO was developed inorder to make a ME composite with Pr doped STO (whose properties were studied in detail in chapter 4). Ink properties of CFO ink were studied using various characterization techniques and noticed that even after the addition of external components like solvents, binder and dispersant, the FM nature was well retained. After exploring the properties of ink, a ME composite was developed by screen printing CFO over Pr:STO ink on $Pt/Ti/SiO_2/Si(100)$ substrates. The FE as well as FM nature of composites was confirmed in the bilayer laminates. ME studies revealed that a maximum value of 779 mV/cm.Oe was obtained under the application of dc magnetic field and 780 mV/cm.Oe under ac magnetic field at room temperature. A homogenization method for laminar multiferroics through a two-scale asymptotic analysis of the microscopic electric, magnetic and force fields, was developed and implemented numerically using finite element analysis. The experimental ferroic properties are in reasonably good agreement with theoretical model. These results show that the developed composite finds promising application in the field of next generation memories, sensors and energy harvesters.

5.6 References

(1) Shi, Z.; Wang, C.; Liu, X.; Nan, C. A Four-State Memory Cell Based on Magnetoelectric Composite. *Chinese Sci. Bull.* **2008**, *53* (14), 2135–2138.

(2) Eerenstein, W.; Mathur, N. D.; Scott, J. F. Multiferroic and Magnetoelectric Materials. *Nature* **2006**, *442*, 759–765.

(3) Bibes, M.; Barthélémy, A. Multiferroics: Towards a Magnetoelectric Memory. *Nat. Mater.* **2008**, *7* (6), 425–426.

(4) Spaldin, N. A.; Fiebig, M. The Renaissance of Magnetoelectric Multiferroics. *Science.* **2005**, *309* (July), 391–392.

(5) Wang, Y.; Li, J.; Viehland, D. Magnetoelectrics for Magnetic Sensor Applications: Status, Challenges and Perspectives. *Mater. Today* **2014**, *17* (6), 269–275.

(6) Ma, J.; Hu, J.; Li, Z.; Nan, C. W. Recent Progress in Multiferroic Magnetoelectric Composites: From Bulk to Thin Films. *Adv. Mater.* **2011**, *23* (9), 1062–1087.

(7) Nan, C. W.; Bichurin, M. I.; Dong, S.; Viehland, D.; Srinivasan, G. Multiferroic Magnetoelectric Composites: Historical Perspective, Status, and Future Directions. *J. Appl. Phys.* **2008**, *103* (3), 031101.

(8) Jin, J.; Lu, S. G.; Chanthad, C.; Zhang, Q.; Haque, M. A.; Wang, Q. Multiferroic Polymer Composites with Greatly Enhanced Magnetoelectric Effect under a Low Magnetic Bias. *Adv. Mater.* **2011**, *23* (33), 3853–3858.

(9) Ryu, J.; Carazo, A. V.; Uchino, K.; Kim, H. E. Magnetoelectric Properties in Piezoelectric and Magnetostrictive Laminate Composites. *Japanese J. Appl. Physics, Part 1 Regul. Pap. Short Notes Rev. Pap.* **2001**, *40* (8), 4948–4951.

(10) Ryu, J.; Priya, S.; Uchino, K.; Kim, H. E. Magnetoelectric Effect in Composites of Magnetostrictive and Piezoelectric Materials. *J. Electroceramics* **2002**, *8*, 107–119.

(11) Srinivasan, G.; Priya, S.; Sun, N. X. *Composite Magnetoelectrics Materials, Structures, and Applications*; Elsevier: London, 2015.

(12) Li, M.; Berry, D.; Das, J.; Gray, D.; Li, J.; Viehland, D. Enhanced Sensitivity and Reduced Noise Floor in Magnetoelectric Laminate Sensors by an Improved Lamination Process. *J. Am. Ceram. Soc.* **2011**, *94* (11), 3738–3741.

(13) Gao, J.; Das, J.; Xing, Z.; Li, J.; Viehland, D. Comparison of Noise Floor and Sensitivity for Different Magnetoelectric Laminates. *J. Appl. Phys.* **2010**, *108* (8), 084509.

(14) Bichurin, M. I.; Petrov, V. M.; Averkin, S. V.; Liverts, E. Present Status of Theoretical Modeling the Magnetoelectric Effect in Magnetostrictive-Piezoelectric Nanostructures. Part I: Low Frequency and Electromechanical Resonance Ranges.

J. Appl. Phys. **2010**, *107* (5), 053904.

(15) Petrov, V. M.; Srinivasan, G.; Bichurin, M. I.; Galkina, T. A. Theory of Magnetoelectric Effect for Bending Modes in Magnetostrictive- Piezoelectric Bilayers. *J. Appl. Phys.* **2009**, *105* (6).

(16) Srinivasan, G.; Devreugd, C. P.; Flattery, C. S.; Laletsin, V. M.; Paddubnaya, N. Magnetoelectric Interactions in Hot-Pressed Nickel Zinc Ferrite and Lead Zirconante Titanate Composites. *Appl. Phys. Lett.* **2004**, *85* (13), 2550–2552.

(17) Nan, C. W.; Liu, G.; Lin, Y.; Chen, H. Magnetic-Field-Induced Electric Polarization in Multiferroic Nanostructures. *Phys. Rev. Lett.* **2005**, *94* (19), 1–4.

(18) Khaja Mohaideen, K.; Joy, P. A. High Magnetostriction and Coupling Coefficient for Sintered Cobalt Ferrite Derived from Superparamagnetic Nanoparticles. *Appl. Phys. Lett.* **2012**, *101* (7).

(19) Senthil, V. P.; Gajendiran, J.; Raj, S. G.; Shanmugavel, T.; Ramesh Kumar, G.; Parthasaradhi Reddy, C. Study of Structural and Magnetic Properties of Cobalt Ferrite ($CoFe_2O_4$) Nanostructures. *Chem. Phys. Lett.* **2018**, *695*, 19–23.

(20) Mohamed, R. M.; Rashad, M. M.; Haraz, F. A.; Sigmund, W. Structure and Magnetic Properties of Nanocrystalline Cobalt Ferrite Powders Synthesized Using Organic Acid Precursor Method. *J. Magn. Magn. Mater.* **2010**, *322* (14), 2058–2064.

(21) Gonzalez-Sandoval, M. P.; Beesley, A. M.; Miki-Yoshida, M.; Fuentes-Cobas, L.; Matutes-Aquino, J. A. Comparative Study of the Microstructural and Magnetic Properties of Spinel Ferrites Obtained by Co-Precipitation. *J. Alloys Compd.* **2004**, *369* (1–2), 190–194.

(22) George, T.; Sunny, A. T.; Varghese, T. Magnetic Properties of Cobalt Ferrite Nanoparticles Synthesized by Sol-Gel Method. *IOP Conf. Ser. Mater. Sci. Eng.* **2015**, *73* (1), 2–5.

(23) Caizer, C.; Stefanescu, M. Magnetic Characterization of Nanocrystalline Ni-Zn Ferrite Powder Prepared by the Glyoxylate Precursor Method. *J. Phys. D. Appl. Phys.* **2002**, *35* (23), 3035–3040.

(24) Pullanchiyodan, A.; Surendran, K. P. Formulation of Sol-Gel Derived Bismuth Silicate Dielectric Ink for Flexible Electronics Applications. *Ind. Eng. Chem. Res.* **2016**, *55* (26), 7108–7155.

(25) Varghese, J.; Kuzhichalil Peethambharan, S.; Sebastian, M. T. Room Temperature Curable Silica Ink. *RSC Adv.* **2014**, *4*, 47701–47707.

(26) Varghese, J.; Teirikangas, M.; Puustinen, J.; Jantunen, H.; Sebastian, M. T. Room Temperature Curable Zirconium Silicate Dielectric Ink for Electronic Applications. *J. Mater. Chem. C,* **2015**, *3* (35), 9240–9246.

(27) Alias, R.; Mohd, S. *Rheological Behaviors and Their Correlation with Printing Performance of Silver Paste for LTCC Tape*; InTech Open, 2012.

(28) Neidert, M.; Zhang, W.; Zhang, D.; Kipka, A. Screen-Printing Simulation Study on Solar Cell Front Side Ag Paste. *Conf. Rec. IEEE Photovolt. Spec. Conf.* **2008**, 14–17.

(29) Wu, S. P.; Zhao, Q. Y.; Zheng, L. Q.; Ding, X. H. Behaviors of ZnO-Doped Silver Thick Film and Silver Grain Growth Mechanism. *Solid State Sci.* **2011**, *13* (3), 548–552.

(30) Landau, L. D.; Lifshitz, E. . *Electrodynamics of Continous Media*; Pergamon Press: Oxford, **1960.**

(31) Jayachandran, K. P.; Guedes, J. M.; Rodrigues, H. C. A Generic Homogenization Model for Magnetoelectric Multiferroics. *J. Intell. Mater. Syst. Struct.* **2014**, *25* (10), 1243–1255.

(32) Sanchez-Palencia, E. *Non-Homogeneous Media and Vibration Theory:Lecture Notes in Physics*; Springer-Verlag: Berlin, **1980**.

(33) Jayachandran, K. P.; Guedes, J. M.; Rodrigues, H. C. Solutions for Maximum Coupling in Multiferroic Magnetoelectric Composites by Material Design. *Sci. Rep.* **2018**, *8* (1), 1–9.

(34) Fiebig, M.; Lottermoser, T.; Meier, D.; Trassin, M. The Evolution of Multiferroics. *Nat. Rev. Mater.* **2016**, *1* (8).

(35) Guedes, J. M.; Kikuchi, N. preprocessing and Postprocessing for Materials based on Homogenization method with Adaptive Finite Element Methods. *Comput. Methods Appl. Mech. Eng.* **1990**, *83*, 143–198.

(36) Goldstein, H. *Classical Mechanics*; Addison-Wesley, Reading, MA, **1978**.

(37) Jayachandran, K. P.; Madeira, J. F. A.; Guedes, J. M.; Rodrigues, H. C. Laminate Composite Magnetoelectric Multiferroics Optimized by Global Derivative-Free Optimization Method. *Comput. Mater. Sci.* **2018**, *148*, 190–199.

(38) Erba, A.; El-Kelany, K. E.; Ferrero, M.; Baraille, I.; Rérat, M. Piezoelectricity of SrTiO3: An Ab Initio Description. *Phys. Rev. B - Condens. Matter Mater. Phys.* **2013**, *88* (3), 1–10.

(39) Pan, E.; Heyliger, P. R. Free Vibrations of Simply Supported and Multilayered Magneto-Electro-Elastic Plates. *J. Sound Vib.* **2002**, *252* (3), 429–442.

Chapter 6

CONCLUSIONS AND FUTURE PERSPECTIVES

6.1 Thesis Conclusions

Smart materials are class of materials in which a variety of researches are going on in the current era inorder to facilitate new dimensions in electronic devices. The field of wireless communication system is growing rapidly and the microelectronic industry is constantly looking for pathways in finding exemplary technologies that can facilitate circuit miniaturization. Despite of its faster and high performance, the current generation electronic industry is looking for miniaturized devices. Also, improving the memory states is a hurdle facing in electronic industry for the better functionality of devices. Integrating multiple components in a single module can make tremendous changes in the current scenario for circuit miniaturization and increasing the memory states of devices. Thus, multifunctional materials are a promising aspect for exploring better functionality over devices in our day to day life.

Against this background, the present thesis entitled as "***Multilayer composites for magnetodielectric and magnetoelectric applications***" is an authentic record on developing several multifunctional materials for practical applications. The thesis is focused on developing magnetodielectric and magnetoelectric materials. The main objective of this thesis was to develop (2-2) layered composites out of several kinds of materials developed for better functionalities, through energy efficient techniques. A systematic study on developing multilayer composites realized through LTCC technology, hot pressing of polymer ceramic composites and screen printing has been explored. The major scientific outcome of present thesis is summarized below.

A novel approach of realizing screen printed magnetic layer on an LTCC substrate was introduced. The LTCC substrate was developed using typical glass ceramic composite based on $BiSmMoO_6$-2 wt.% BBSZ, sinterable at 875 ˚C. Through all the possible characterization techniques available, we concluded that the developed tape composition has got potential impact in the field of LTCC technology. Single phase $BiFeO_3$ was developed using wet chemical method and developed a screen printable ink out of it. Magnetodielectric composite was realized through screen printing $BiFeO_3$ ink on the developed LTCC tape. This composite marked a promising negative magnetocapacitance value upto 15% under the application of 3 kOe magnetic field at room temperature which shows its suitability in the field of antenna miniaturization as well as electronic band gap structures.

Polymer composites based on PMMA-$NiFe_2O_4$ were developed by varying the filler content (5, 10, 15 and 20 vol.%) . Each composite individually marked good values of magnetocapacitance. The composites were stacked together by employing hot pressing technique to make anisotropy along the *z* direction. The permittivity as well as permeability values will vary in that direction since the filler content is varying in all layers. Inorder to validate its applicability in the field of antenna miniaturization, a theoretical antenna was designed for operating at 830 MHz. An impressive 91% size reduction was achieved using this anisotropic layered structure which marks its identity as magnetodielectric substrate material.

Another remarkable emphasis of present thesis was given for developing magnetoelectric composites via screen printing technique. Screen printable inks of Pr

doped $SrTiO_3$ as well as $SrRuO_3$ were used for making a (2-2) composite. Despite of using conventional tape casting technique, this method finds enormous advantages like room temperature processing, cost effectiveness etc. The developed ceramic ink compositions were screen printed one over another for making a bilayer heterostructure that could yield a magnetoelectric coupling coefficient of 655 mV/cm.Oe when a dc magnetic field is applied. This room temperature coupling between the chosen FE-FM interactions is quite unusual. Yet, promising value of MECC is offering its practical applications in the field of sensors, actuators, memory devices etc.

To give a new direction for ME composites, effort was taken for improving the MECC value in present thesis. For that, $CoFe_2O_4$ was used as FM component with Pr doped $SrTiO_3$. Room temperature curable inks based on both ceramics were developed. A bilayer composite was developed using screen printing technique. The composite showed a maximum dc MECC of 780 mV/cm.Oe which is the highest ever in literatures based on printed ME composites. This composite can be a promising candidate for next generation memory applications.

6.2 Future Perspectives

The studies carried out and results obtained in the present thesis provide an excellent scope for interesting future studies as mentioned below.

- As the present thesis only cover upto magnetocapacitance study based on LTCC composition, a more detailed study on the permeability and permittivity factors

can be incorporated. This will give an insight to the practical realization of a miniaturized antenna over the developed substrate.

- Fabrication of antenna on the anisotropic polymer ceramic substrate can be practically made possible. More efforts have to be taken care to minimize the loss tangents in the composite for better gain and efficiency values.
- Though the room temperature magnetoelectric coupling of Pr doped STO and SRO bilayer heterostructure has been studied and there needs more studies to explain the unusual behavior of SRO which is in paramagnetic state at room temperature. Cryogenic studies are needed to confirm the ferroelectricity in Pr doped STO too. These studies will help in explaining more science behind the unusual coupling observed in the present bilayer composite. Also, theoretical studies can be performed in composite for substantiating the results obtained.
- The Pr:STO-CFO composite was realized in bilayer form only. This study can be extended by incorporating more layers and study its effect in the MECC value.

List of Publications

1. **Deepa Rajendran Lekshmi**, Kuzhichalil Peethambharan Surendran, Ultra-Low Dielectric Loss $BiSmMoO_6$ Flexible Tapes for Hybrid Integrated Circuits, *Journal of the European Ceramic Society*, 39 (**2019**), 1819-1826.
2. **Deepa Rajendran Lekshmi**, Thomas Letang, Kuzhichalil Peethambharan Surendran, High permittivitty $(La_{0.5}Sr_{0.5})CoO_{3-\delta}$ - $La(Co_{0.5}Ti_{0.5})O_{3-\delta}$ ceramic composites for next generation MIM capacitors, *Journal of the European Ceramic Society*, 38 (**2018**), 3853-3860.
3. Yogita Bist, Richa Tomar, Pullanchiyodan Abhilash, **Deepa Rajendran Lekshmi**, M Thirumal, Microwave dielectrics: solid solution, ordering and microwave dielectric properties of $(1-x)Ba(Mg_{1/3}Nb_{2/3})O_3-xBa(Mg_{1/8}Nb_{3/4})O_3$ ceramics, *Bulletin of Material Science*, 40 (**2017**), 1165-1170
4. Yogita Bist, Pullanchiyodan Abhilash, **Deepa Rajendran Lekshmi**, M Thirumal, Microwave dielectric properties of $(1-x)Ba(Mg_{1/3}Ta_{2/3})O_3-xBa(Mg_{1/8}Ta_{3/4})O_3$ ceramics, *Ferroelectrics*, 558 (**2020**), 92-103
5. **Deepa Rajendran Lekshmi**, Nandakumar Kalarikkal, Kuzhichalil Peethambharan Surendran, Unusual magnetoelectric coupling characteristics in all-printed layered composites of $SrRuO_3$ and Pr doped $SrTiO_3$ thick films, (to be communicated).
6. **Deepa Rajendran Lekshmi**, Nandakumar Kalarikkal, Kuzhichalil Peethambharan Surendran, Characteristics of screen printed 2-2 composites of $CoFe_2O_4$ and Pr-doped $SrTiO_3$ (manuscript to be communicated).
7. **Deepa Rajendran Lekshmi**, Adarsh S. Pillai, Swapna S. Nair, Kuzhichalil Peethambharan Surendran, Functionally graded layered magnetodielectric substrates for microstrip patch antenna miniaturisation (manuscript to be communicated).
8. **Deepa Rajendran Lekshmi,** Swapna S. Nair, Kuzhichalil Peethambharan Surendran, Magnetodielectric based on $BiFeO_3$ screen printed on BiSmMoO6 based LTCC tapes (manuscript to be communicated)

List of Conference Proceedings

Contributory Talk:

1. **Deepa Rajendran Lekshmi**. and K.P. Surendran, "Screen Printable Ink of $BiFeO_3$ Nanoparticles For Electronic Applications", of International Conference on Nanotechnology: Ideas, Innovations and Initiatives-2017 (ICN3I-2017) held at IIT Roorkee.

Poster Presentations:

1. **Deepa Rajendran Lekshmi.,** Induja. I. J., Dr. Subodh G, Dr. M. T. Sebastian, Dr. K. P. Surendran, "Novel Functional Dielectrics for Microwave Applications", Second International Conference on Advanced Functional Materials (ICAFM 2014), Trivandrum. ***(Best Poster Award)***

2. **Deepa Rajendran Lekshmi,** Dr. M. T. Sebastian, Dr. K. P. Surendran, "Radio Frequency and Thermal Characterization of a Novel Functional Dielectric System", International Conference on Science, Technology and Applications of Rare Earths (STAR 2015), Trivandrum.

3. **Deepa Rajendran Lekshmi,** Sneha Joy, Dr. K. P. Surendran, "Magneto-Electric Heterostructures Based on $SrTiO_3$-$SrRuO_3$ Thick Films Developed Using Screen-Printing Technique", Second International Conference on Recent Trends in Materials Science and Technology (ICMST 2018), Thiruvananthapuram.

4. **Deepa Rajendran Lekshmi**, Sivan Pillai Adarsh, Swapna Nair, Kuzhiclail P. Surendran, "PMMA Based Magnetodielectric Composites for Antenna Miniaturization", Third International Conference on Advanced Functional Materials (ICAFM 2019), Thiruvananthapuram.